University of Glasgow

Sprott, Mark Robert (2019) *Surface functionalisation of poly L-lactic acid to control protein organisation and growth factor presentation in tissue engineering*. PhD thesis.

https://theses.gla.ac.uk/74292/

Copyright and moral rights for this work are retained by the author

A copy can be downloaded for personal non-commercial research or study, without prior permission or charge

This work cannot be reproduced or quoted extensively from without first obtaining permission in writing from the author

The content must not be changed in any way or sold commercially in any format or medium without the formal permission of the author

When referring to this work, full bibliographic details including the author, title, awarding institution and date of the thesis must be given

Enlighten: Theses
https://theses.gla.ac.uk/
research-enlighten@glasgow.ac.uk

Surface Functionalisation of Poly L-Lactic Acid to Control Protein Organisation and Growth Factor Presentation in Tissue Engineering

Mark Robert Sprott

(BSc (Hons), MSc)

Submitted in fulfilment of the requirements for the

Degree of Doctor of Philosophy (PhD)

School of Science and Engineering

College of Engineering

University of Glasgow

Glasgow, G12 8LT

May 2019

Abstract

Poly L-Lactic acid (PLLA) is a versatile established biodegradable polymer used in biomedical engineering. The characteristic properties (stiffness, topology and biodegradation) of PLLA are ideal for regeneration applications *in vivo*, providing a biocompatible microenvironment to *in situ* cells and allowing for gradual transfer of mechanical stress to the engineering tissue via controllable polymer degradation. However, inefficient adsorption of key biological factors, including the extracellular matrix component fibronectin (FN), hinder its use as a cellular microenvironment. Poly(ethyl acrylate) (PEA) has been shown to induce spontaneous organisation of FN into physiological-like fibrils, exposing binding motifs critical for cell adhesion, differentiation and the binding of growth factors (GF). Thus, here we present a novel chemical process to polymerise functional PEA brushes, able to drive FN fibrillogenesis, onto PLLA. The produced surface initiated atomic transfer radical polymerisation system (SI-ATRP), allows control of surface biofunctionality while maintaining PLLA bulk properties such as degradability profile and mechanical strength. Production of a molecularly thin PEA brush coating onto PLLA providing additional functionality to the widely utilised backbone biomaterial. The process outlined is shown to be highly tuneable, taking place in 3 distinct optimized steps; aminolysis, initiator immobilisation and polymerisation. Initial functionalisation via aminolysis and subsequent immobilisation of the bromine based initiator occur in 2 separate reaction processes, named as a 2-pot system. Here we also present initial production of a streamlined 1-pot SI-ATRP system, performing aminolysis and initiator immobilisation within the same reaction vessel, a 1-pot system. These processes, alongside further potential variations to the system, highlight the resilience and highly modifiable nature of this surface modification technology. Neither of these processes are shown to significantly impact on the bulk physical properties of the backbone PLLA, as measured primarily via enzymatic degradation with proteinase K and atomic force microscopy (AFM) nanoindentation. Alongside surface characterisation utilising AFM, X-ray photoelectron spectroscopy (XPS) and water contact angle (WCA) to measure PEA grafting, we investigated the biological activity of modified surfaces in

terms of FN adsorption and cellular response. Produced PEA brushes were shown to retain the functionality of driving fibrillogenesis triggering FN organisation into physiological-like fibrils, which allow for enhanced cellular adhesion, growth factor binding and differentiation of myoblast C2C12 cells and human mesenchymal stem cells. Translation of this system into 3D, by printing medical grade PLLA scaffolds and modifying their surface, has shown that this process is scalable and functional for use in implantable biomaterials. The results demonstrate the potential of this technology to engineer controlled microenvironments to tune cell fate via biologically active surface modification of an otherwise bioinert biodegradable polymer gaining wide use in tissue engineering applications.

Table of Contents

List of Figures and Tables.

Presentations

(2018) Oral presentation at the European Society for Artificial Organs (ESAO), Madrid, Spain. M R Sprott, G Gallego-Ferrer, M J Dalby, M Cantini, M Salmerón-Sánchez. Functionalization of PLLA with Polymer Brushes to Trigger the Assembly of Fibronectin into Nanonetworks.

(2016) Poster presentation at the British Orthopaedic Research Society (BORS), Glasgow, UK: M R Sprott, M Cantini, M J Dalby, M Salmerón-Sánchez. Synthetic Microenvironments to Control Stem Cell Growth.

(2016) Poster presentation at the Bioengineering for Cancer workshop held in conjuncture with the Beatson Cancer Institute. Glasgow, Scotland: M R Sprott, M Cantini, M J Dalby, M Salmerón-Sánchez. Synthetic Microenvironments to Control Stem Cell Growth.

Publications

Functionalization of PLLA with Polymer Brushes to Trigger the Assembly of Fibronectin into Nanonetworks (2019) M R Sprott, G Gallego-Ferrer, M J Dalby, M Salmerón-Sánchez, M Cantini. Advanced Healthcare Materials 8, 3, e1801469

3D Printed Biodegradable Scaffolds Functionalised Via Surface Initiated Atomic Transfer Radical Polymerisation To Enhance Cellular Adhesion And Osteogenic Differentiation. (2019) M R Sprott, M J Dalby, M Cantini, M Salmerón-Sánchez. To be submitted.

Characterisation of 1- And 2-Pot Surface Initiated Atomic Transfer Radical Polymerisation Mechanism for Surface Modification of PLLA Films. (2019) M R Sprott, G Gallego-Ferrer, M J Dalby, M Cantini, M Salmerón-Sánchez. To be submitted

Acknowledgements

First, I would like to thank my funders, with their funding we are attempting to improve knowledge, understanding and hopefully lives.

Foremost I would like to acknowledge and thank all of my supervisors; Manuel Salmerón-Sánchez, Mathew J Dalby and Marco Cantini. I am extremely grateful to them for giving me the opportunity to work within their group, learn from them and for their guidance. They are not only great supervisors but also inspirations. I feel incredibly lucky and fortunate to have been able to work through my PhD under each of their tutelage, let alone all three of them. Thank you, from the depth of my heart, for everything.

I feel it prudent to highlight my thanks to Marco Cantini, for his constant, day to day, hour to hour, by-the-minute, almost inhuman, incessant mentoring. His incredible knowledge on EVERYTHING is awe-inspiring. I am very grateful for his willingness to help and talk through any aspect of the work at any given time. Without doubt he has been instrumental in maintaining my sanity and keeping me focused through this entire project. I honestly cannot thank him enough for his help and support.

I am incredibly grateful to know each and every person in the group, each one is an amazing person and I am thankful to be able to work alongside each of them. It truly is such a friendly and lovely group of people to work with. However, there are far too many to thank individually.

I would like to thank everyone at CBIT and in Valencia for being so welcoming, especially Gloria and Carmen for their motivational words, kindness and constant support.

A special thanks has to go out to Hilary J. Anderson, contractually, for so many things over the years and for years to come! Coincidentally, I would like to thank her fiancé Jake, Mark#2 (not everyone is perfect), Ricky, Doug, Eleni, Nadira and Sara for being so amazing to me when I started in the lab and even now. While I am grateful for meeting everyone in MiMe, other noted alumni have to be recognised; my thanks to the basement office team old and new, without whom I wouldn't have been able to see the light at the end of the tunnel.

My loving thanks to my family; my parents for literally and figuratively making me the man I am today. Both of you have moulded such a distinct part of my being that I will never forgive either of you. My Granny for always humouring me and believing in me, even when I didn't. I need to thank my brother, Joshua, for legitimately always smiling and pushing me to be a better person. Please keep smiling, you are the best of us. You are all amazing people that I am proud to be related to.

Also I am very thankful for the family I chose, those friends who were understanding and always had a nice word while I hid away writing. While there are many of you I feel the need to thank; Ped, Becca and Caitlin, I honestly do not nor do I want to know what life is like without each of you anymore.

I am eternally grateful to my partner, Iona, for putting up with me despite the all-nighters in the lab, the write-up and generally me. I am so lucky to be with you. She has been so supportive and understanding when I needed it most. Thank you for being so clever, smart and funny. I would also like to thank her family for cheering me up, making me laugh and generally supporting me through this.

With all my heart I dedicate this work to those that came before and people who couldn't be with us. In particular, my Grandpa Robert Wardrope, Nana Nancy Mulcahy and Mia Sprott amazing beings who were taken too soon.

Author’s declaration

I hereby declare that the research presented within this thesis is my own work unless otherwise stated, and has not been submitted elsewhere for any other academic degree.

List of Abbreviations	
º	Degrees
2D	2 Dimensional
3D	3 Dimensional
µl	Micro Litre
µm	Micro Metre
A	Ampere
AC mode	Alternating Contact (regarding AFM)
ACA	Advancing Contact Angle
AFM	Atomic Force Microscopy
ANOVA	Analysis of Variance
ARGET	Activator Regenerated Electron Transfer
AsAc	Ascorbic Acid
ASC	Adult Stem Cell
BCA	Bicinchoninic Acid
BIBB	α-Bromoisobutyryl Bromide
BME	Biomedical Engineering
BMPs	Bone Morphogenic Proteins
BSA	Bovine Serum Albumin
Ca	Calcium
CaCl	Calcium Chloride
CuBr	Copper Bromide
DAPI	4’6-diamidino-2-phenylindole
DSC	Differential Scanning Calorimetry
DMA	Dynamic Mechanical Analysis
DMEM	Dulbecco’s modified eagle’s medium
DMF	Dimethylformamide
DMSO	Dimethyl Sulfoxide
DPBS	Dulbecco’s Phosphate Buffered Saline
DRS	Dielectric Relaxation Spectroscopy
EA	Ethyl Acrylate
ECM	Extracellular Matrix
ESC	Embryonic stem cells
ERK	Extracellular Signal-regulated Kinase
FAs	Focal Adhesions
FAK	Focal Adhesion Kinase
FBS	Foetal Bovine Serum
FITC	Fluorescein
FN	Fibronectin
FT-IR	Fourier-Transform Infrared Spectroscopy
GFs	Growth Factors
HCl	Hydrochloric Acid
hr	Hours
hMSCs	Human Mesenchymal Stem Cells
HMDS	Hexamethyldisilazane
Hz	Hertz
ICW	In-Cell Western
HA	Hydroxyapatite
iPSCs	Induced pluripotent stem cells
LDH	Lactose Dehydrogenase

MA	Methyl Acrylate
MSC	Mesenchymal stem cells
N_2	Nitrogen
nm	Nanometres
OCN	Osteocalcin
OPN	Osteopontin
Pa	Pascals
PBS	Phosphate Buffer Solution
PCL	Poly(Caprolactone)
PEA	Poly(Ethyl Acrylate)
PEG	Poly (Ethylene Glycol)
PHSRN	Pro-His-Ser-Arg-Asn amino acid sequence
PLLA	Poly(L-lactic acid)
PMA	Poly(Methyl Acrylate)
P/S	Penicillin/Streptomycin
py	Pyridine
RCA	Receding contact angle
RGD	Arg-Gly-Asp amino acid sequence
rpm	Rotations Per Minute
s	Seconds
SAMs	Self-assembled monolayers
SCA	Static Contact Angle
SI-ATRP	Surface Initiated Atomic Transfer Radical Polymerisation
TGA	Thermogravimetric Analysis
TPMA	Tris(2-pyridylmethyl)amine
UV	Ultraviolet
USD	United States Dollars
V	Volts
W	Watts
WCA	Water Contact Angle
XPS	X-ray Photoelectron Spectroscopy

1. Introduction

1.1. Tissue engineering

Tissue engineering, being an interdisciplinary field, requires the utilisation of several disciplines, including engineering and biological principles, for the maintenance or replacement of tissue function (Howard, Buttery et al. 2008). Synergy of techniques from these disciplines allows for the ability to mimic *in vivo* cellular environments, allowing for controlled cellular differentiation post implantation and regeneration of damaged tissues (Langer and Vacanti 1993). In fact, by employing interdisciplinary modification techniques materials can be developed that are able to mimic biological environments, regulating cellular interactions on and in these materials. Biomimicry, the recreation or imitation of biological systems, utilises the physical characteristics of bulk materials, such as polymers, and the functionality of biological systems for modelling or modulation of cellular interactions for use in tissue engineering. These biomimetic materials vary considerably in application, specificity and complexity, but predominantly aim to improve material-cellular interactions *in vivo* or provide an *in vitro* model for tissues found within the body (Green and Elisseeff 2016).

1.1.1. Bone fracture healing

Bone fractures and other tissue defects are a prevalent issue in medicine throughout the world (Perez, Kouroupis et al. 2018). There are approximately >6 million fractures per year in the US and >3.5 in the six largest European countries (France, Germany, Italy, Spain, Sweden and the UK) (Einhorn 1995, Hernlund, Svedbom et al. 2013). In the EU, it is estimated that in 2010 26,300 life-years were lost due to incidental fractures and the total number of fractures in the future will rise by 28% to 4.5 million by 2025 (Hernlund, Svedbom et al. 2013). In 2010 the mortality rate associated with bone defects was estimated to be 43,000 people in the European Union, highlighting the severity and the need for the development of improved treatments of these issues in our current age (Hernlund, Svedbom et al. 2013).While certain bone tissue defects, such as simple fractures, can be treated by the host over time or by medical professionals, other conditions such

as critical bone defects, generally a fracture of more than 2 cm in length or over half the circumference of the bone (Watanabe, Harada et al. 2016), require more extensive medical intervention to regenerate form and function of the broken bone. Generally, fracture healing takes place within the first 2 months post-injury; however, contributing factors can inhibit or even fully stop this process, resulting in delayed union or even stopping of any bone union forming. Non-union defects result from approximately 10% of fractures (Einhorn 1995); the risk of these developing can be increased from a variety of factors; dietary habits, pre-existing ailments, fracture site movement or the location of the break, all have contributing factors to the severity and thus level of treatment required to regenerate the tissue (Castillo, Bosse et al. 2005, Tzioupis and Giannoudis 2007, Kostenuik and Mirza 2017, Westrick, Hamilton et al. 2017). In some situations a combination of these issues can contribute to delaying the union of the bone during medical treatment, which can result in infection, or fracture site polytrauma and non-union of the fractured bone, in these cases loss of function or the appendage can be the only option for conventional medicine (Gomez-Barrena, Rosset et al. 2015, Cheng, Alba-Perez et al. 2019). Typically non-union fractures require an increased level of medical care to treat and healthcare resources (Morshed 2014), therefore the development and optimisation of regenerative medicine treatments for critical bone defects are vital.

Treatments for non-union breaks include synthetic grafts, autographs and allographs; these are the current standard for replacement of bone defects of such a size that inhibits natural regrowth. Generally, the gold standard for critical bone defect repair involves grafting bone from another unaffected area of the patient to replace the lost tissue. This is due to these bone fragments possessing inherent osteoinductive and osteoconductive properties while avoiding any histocompatibility issues. Allografts, tissue grafts from non-genetically identical donors, can result in rejection of the implanted tissue or even disease transmission. While autografts are predominantly utilised, they still present distinct issues post implantation such as donor site morbidity, limited availability, infection, nerve damage and surgical complications (Younger and Chapman 1989, Perez, Kouroupis et al. 2018). These issues cumulate in a total graft rejection rate

of 60% (Soucacos, Dailiana et al. 2006), resulting in non-unions and subsequent late grafting fractures; this highlights the need for improved tissue engineering alternatives to improve biocompatibility, availability and osteo-regeneration of synthetic grafts.

Bone tissue engineering has produced a variety of regenerative medicine products, synthetic grafts, aiming to facilitate regeneration of growth and function caused by a variety of ailments. Polymer products are commercially used as a clinical bone fixation scaffold, such as FIXSORB® (Takiron Co.) or NEOFIX (Gunze Ltd.), due to the high modulus, long controllable degradation time and gradual transfer of mechanical stress to the *in situ* cellular system while removing the need for a secondary operation to remove conventional metal pins, sutures or anchors (Ulery, Nair et al. 2011). However these materials, while providing mechanical support over controllable time-points, do not encourage cellular regeneration of the bone tissue, as autografts or allografts would. These systems also have the potential for treatment of degradative bone tissue diseases, such as osteoporosis, allowing for implantation and regeneration or strengthening of defective areas (Yu, Tang et al. 2015). Therefore there is the need for development of tissue engineering solutions and augmentations to establish material treatments for bone tissue defects or fractures.

1.2. Biomaterials

Biomaterials offer an approach to treating damage or loss of tissues by providing a framework for the replacement and regeneration of functions of the affected biological systems (Rincon Lasprilla, Rueda Martinez et al. 2011). Biomaterials have been used in many aspects of regenerative medicine from the creation of artificial organs to implanted drug delivery systems (Khandare and Minko 2006, Zadpoor and Malda 2017). Typically three types of biomaterial are used in tissue engineering: ceramics, natural and synthetic polymers. Generally ceramics, characterised by their high Young's modulus and brittle topography, are used for osteogenic regeneration. Ceramic biomaterials, such as scaffolds utilising hydroxyapatite (HA) and tri-calcium phosphate, possess chemical compositions

and structures very similar to those of natural mineral deposits and are therefore highly biocompatible (Hench 1993, Ambrosio, Sahota et al. 2001). However, the inherent rigidity of ceramics limits their utilisation in tissue regeneration; the brittleness and handling issues impact on the processability and variability for defined application for a given implantation. Also bone produced in established ceramic scaffolds are unable to facilitate the same degree of mechanical loading or biodegradability as native *in situ* tissue (Wang 2003). Polymer-based biomaterials are a growing field of research due to their wide array of physical properties and potential biomedical applications (Iaquinta, Mazzoni et al. 2019). Biomedical research utilises a wide range of polymers, either biodegradable or biostable, for a variety of applications due to the versatility, availability and established modification techniques. Naturally derived polymers, such as collagen or alginate scaffolds, are inherently biodegradable, biologically active and exhibit very good cellular interactions, however poor processability and reproducibility produce scaffolds with small control over the mechanical properties and translation into clinical use (O'Brien 2011). Synthetic polymers, such as poly lactic acid (PLA) or poly (ethylene glycol) (PEG), are more readily processed than natural polymers providing a greater control of degradability, mechanical properties and presentation of functional groups. In general, biomaterials provide a highly tuneable and expandable alternative to current regenerative medical technologies, having an approximate market value of 134.3 billion USD (Prasad, Bazaka et al. 2017), which is ever growing and developing.

1.2.1. Synthetic polymers

The use of synthetic polymers provides the most variable and controllable platform for tissue engineering. Biomedical polymers should have appropriate mechanical properties mimicking the surrounding tissue for the intended use, degrade in a predicted timeframe so as to transfer mechanical and biological function to the recovering tissue and ideally have a high affinity for or express biological signals relevant to the intended use (Ulery, Nair et al. 2011). These definitions are not fully comprehensive and certain exceptions are present in

specific circumstances; one example is in the use of biostable materials which are non-degradable within the body that are able to provide long-term structural and functional support (Lozano Picazo, Perez Garnes et al. 2015). One established characteristic is that as a biomaterial the polymer must not provoke an inflammatory or harmful response from the surrounding tissue and should produce non-toxic degradation products which are readily excreted naturally by the host.

1.2.2. Biomaterials for tissue engineering

Biomaterials are often utilised as cellular scaffolds or mechanical support systems within the body to facilitate regeneration of tissue function (O'Brien 2011). Cells have been shown to respond to three main factors within implanted systems: mechanical forces, micro/nanoscale topographical features and biochemical signalling (Figure 1.1). These factors directly influence initial adhesion, differentiation, viability and functionality of cells (Mason, Califano et al. 2012, Anderson, Sahoo et al. 2016). Modulation of specific material characteristics such as stiffness can drastically alter the application of biomimetic materials, from silk-based gels for soft tissue regeneration to stiffer polymer scaffolds for bone regeneration (Polo-Corrales, Latorre-Esteves et al. 2014, Wang, Wang et al. 2016). Mimicry of physiological elastic moduli, as found *in vivo,* has been shown to directly mediate cellular responses. Materials with different stiffness induce differentiation of cells to different linages: 0.1-1 kPa neurogenic, 8-17 kPa myogenic or 25-40 kPa osteogenic (Discher, Janmey et al. 2005, Zhang 2012). Therefore, appropriate materials and modification techniques must be employed when designing materials for specific tissue-associated regenerative medicine approaches.

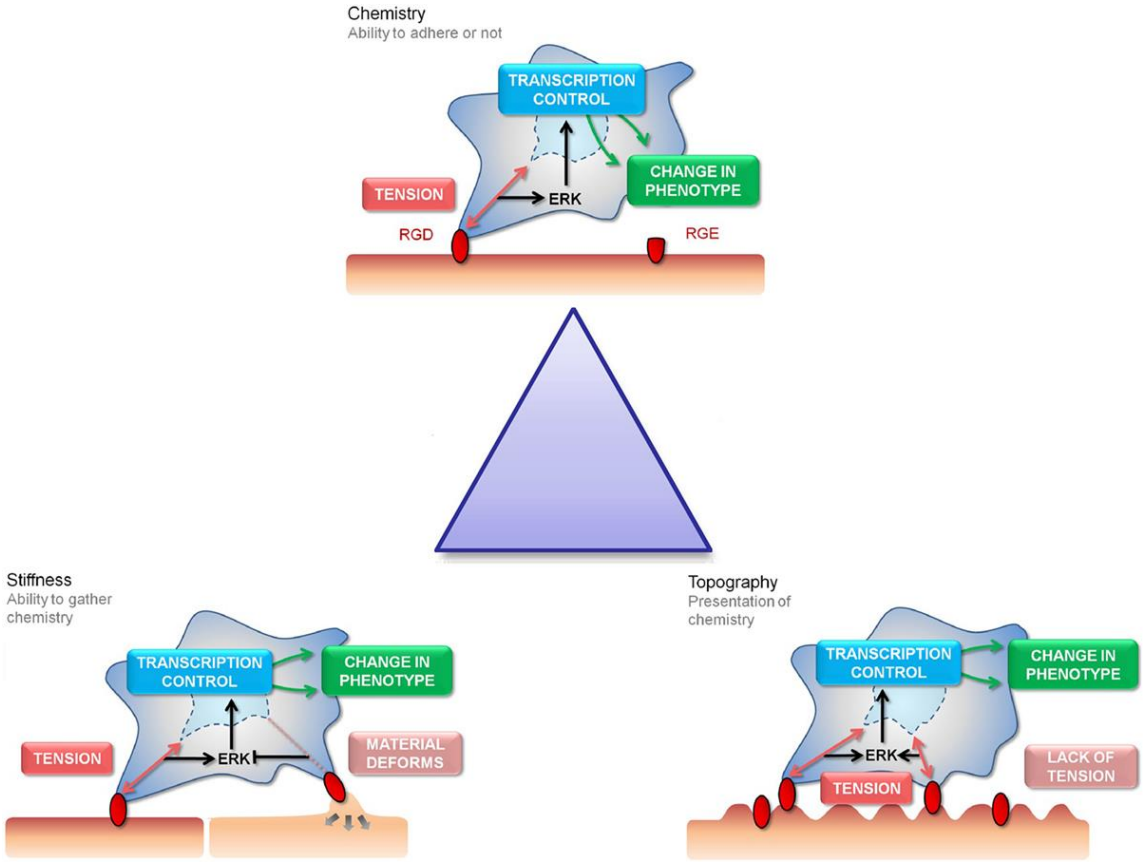

Figure 1.1. Material surface interactions. Chemistry, stiffness and topography control cellular interactions; focal adhesion formation is shown here. Red shows cellular adhesion sites and stimuli resulting in either high adhesive (blue) or low adhesive (green) phenotypes. From Anderson et al, 2016, Mesenchymal Stem Cell Fate: Applying Biomaterials for Control of Stem Cell Behaviour.

The physical properties of biomaterials are dependent on their chemical structure and their constituent functional groups. Through controlled chemical reactions and the introduction of biological factors, the surface activity and chemical properties of a given biomaterial can be refined and attuned for desired applications (Khan, Tanaka et al. 2015). Therefore, current biomedical research utilises modification of biodegradable polymers to manufacture implantable microenvironments for cells; these microenvironments present selected biochemical signals (Xu, Yang et al. 2011), optimal topologies and mechanical properties corresponding to the tissue damaged (Dalby, Gadegaard et al. 2007, Mason, Califano et al. 2012, Mpoyi, Cantini et al. 2016). Cell-material interactions have been shown to be modulated by the inclusion and presentation of simple chemical functional groups on biomaterials (Curran, Chen et al. 2005, Curran, Chen et al. 2006, Benoit, Schwartz et al. 2008, Phillips, Petrie et al. 2010),

highlighting the potential for improvement of already established biomaterials via chemical modification techniques. However, certain methodologies of processing polymers so as to alter the surface properties can indirectly change the chemical characteristics of the original material, therefore altering the effectiveness of the biomaterial for the intended application (Zhu, Gao et al. 2004). Hence, careful consideration must be used in the surface modification of biomaterials to induce favourable chemical reactions.

Nanoscale topographical surface features have been shown to influence cellular phenotypes, both genomic and proteomic, when presented on biomaterials (Xiao, Jiang et al. 2002, Dalby, Hart et al. 2008). For example, research has shown that by presenting surfaces with nano-pits of varying degrees of symmetry or disorder cell differentiation can be influenced in a tuneable manner (Dalby, Gadegaard et al. 2007). This topographical influence has been shown to translate to influence protein interactions with cells, where ECM components adsorbed onto these disordered surface features are able to induce a higher degree of cellular adhesion and differentiation (Mpoyi, Cantini et al. 2016).

One of the first vital interactions for any biomaterial is the initial contact and adhesion of the cultured cells; for example, it has been shown that without proper material-cell interfaces stem cells undergo apoptosis through a process known as anoikis (Dalby, Gadegaard et al. 2014). Cellular adhesion dictates the tensile signalling pathways, such as extracellular signal-regulated kinase (ERK), and is able to directly regulate cellular transcription and subsequently phenotype (Anderson, Sahoo et al. 2016). Therefore, a major consideration when developing biomaterials for biomedical applications must be to facilitate cell adhesion to ensure high viability and functionality of cells. Thus, it is vital that biomaterials are developed or modified to facilitate cellular adhesion via chemical, topographical and stiffness mechanisms.

In general, biomaterials present the potential to create a vast array of tissue engineering solutions and models. Their myriad of modern uses, such as structurally supportive sutures, cellular-filled implants or model systems for drug discovery, are constantly evolving and, by way of surface modification, continually improving. Research and development of polymer surface modification techniques

is a growing field of biomedical engineering (Khan, Tanaka et al. 2015, Khan and Tanaka 2017), one key aspect of this being the improvement of current processing techniques, modifying or adding functionality to materials while maintaining other favourable material properties.

1.2.3. 2D vs. 3D

Traditionally the majority of cellular cultures utilised for tissue engineering has been performed on 2D biomaterials, however more modern research has aimed to translate this work to 3D microenvironments (Li and Kilian 2015). The aim is to improve the currently poor translatability of *in vitro* cellular treatments performed within laboratories to clinical applications in regenerative medicine (Hollister and Murphy 2011). *In vivo*, the cellular microenvironment consists of the 3D surroundings of the cells, including the extracellular matrix, which the traditional 2D *in vitro* cell culture models are unable to accurately re-create; this results in misleading or non-predicted results when this form of 2D biomedical research is applied *in vivo* (Edmondson, Broglie et al. 2014). Therefore, by adapting established techniques to facilitate cellular interactions with biomaterials, such as adhesion, from flat 2D biomaterial surfaces to 3D scaffolds, the degree of biomimicry can be improved by better simulating the *in situ* microenvironments as would be sensed by cells. Through this translation several 2D techniques have been utilised in 3D systems including; *in vitro* modelling of the central nervous system for therapeutically drug development (Hopkins, DeSimone et al. 2015), lithographic patterning for micro-engineering extracellular matrices (Li and Kilian 2015) and modelling of cancer mechanotransduction mechanisms (Lee, Chang et al. 2019). These types of studies have shown that 2D methodologies can be successfully translated into 3D systems and this is able to improve the accuracy, effectiveness and reliability of these techniques. Indeed, It has been shown that cell morphology and physiology are drastically altered when cultured in 3D comparatively to 2D culture environments (Benya and Shaffer 1982, Baharvand, Hashemi et al. 2006), due to the increased dimension of cellular interactions with other cells, ECM and material surfaces.

The use of hydrogels and 3D polymer scaffolds has emerged as a methodology to culture cells within 3D microenvironments. These hydrogels consist of crosslinked networks of hydrophilic polymers possessing binding domains for cells within a hydrated 3D environment (El-Sherbiny and Yacoub 2013). However, their intrinsic hydrated composition in certain cases limits their propensity for higher stiffness osteogenic regenerative applications (Caliari and Burdick 2016). To solve this, several hydrogel systems for increasing hydrogel stiffness and osteogenic differentiation have been developed (Engler, Sen et al. 2006, Khetan, Guvendiren et al. 2013, Wen, Vincent et al. 2014, Tozzi, De Mori et al. 2016). 3D polymer scaffolds can be produced via several methodologies: electrospinning, extrusion or 3D printing to name a few (Barry, Silva et al. 2005, Corey, Gertz et al. 2008, Serra, Mateos-Timoneda et al. 2013, Frydrych, Roman et al. 2015, Ravi, Shiakolas et al. 2017). These scaffolds made primarily of bulk polymer are able to maintain similar physical characteristics as their 2D counterparts while presenting cells with a 3D surface area to interact with. 3D printing in particular provides the potential for fine control of fibre size, pore volume and architecture, allowing for controlled mechanical properties that support cell growth post implantation and tuneable degradation times (Carletti, Motta et al. 2011). In fact, synthetic polymer scaffolds have been proposed as alternatives to allograft and autografts, (Takahashi and Tabata 2004, Li, Liu et al. 2012, Polo-Corrales, Latorre-Esteves et al. 2014) providing similar osteogenic regeneration.

1.3. Extracellular matrix

Within tissue cells are surrounded by a complex 3D extracellular matrix (ECM) which regulates both cell viability and differentiation state (Frantz, Stewart et al. 2010, Mason, Califano et al. 2012). ECMs can vary in chemical and physical properties that in turn alter the growth and activity of the cells they encompass. Typically ECMs are composed of a selected recipe of water, proteins and polysaccharides, dictated biochemically and mechanically by the cellular component and surrounding microenvironments, producing a specialised cellular environment optimised for the tissue it inhabits. This extracellular microenvironment can possess an intricate variety of topographical, biochemical and physical areas within the same region and dictates the properties of the tissue and even the organ.

The ECM regulates a variety of cellular behaviours through four main pathways; biophysical anchorage of the cell, mechano-transduction, biochemical receptor binding and presentation of growth factors (Figure 1.2). The composition of the ECM dictates the surrounding stiffness and elasticity, and it provides the ability to regulate water and homeostasis not only of the cellular environment, but also of the produced tissue. ECM factors are also able to directly control cellular function by presenting biochemical signals, such as growth factors, which interact with cell-surface receptors to induce intercellular signal transduction and regulate gene transduction (Frantz, Stewart et al. 2010). Through these mechanical, biological and chemical signals, cell functionality and differentiation state can be regulated. Conversely cells are able to remodel and mediate the composition and characteristics of the ECM to further mediate cellular and tissue function. This process involves the degradation of the ECM, primarily by matrix metalloproteinases (MMPs), produced as either soluble or cell-membrane-anchored proteinases by cells which function within the extra-cellular space to enzymatically degrade ECM proteins.(Bonnans, Chou et al. 2014) This allows for these matrix components to be replaced, in most cases by *in situ* cells to remodel their surrounding ECM.

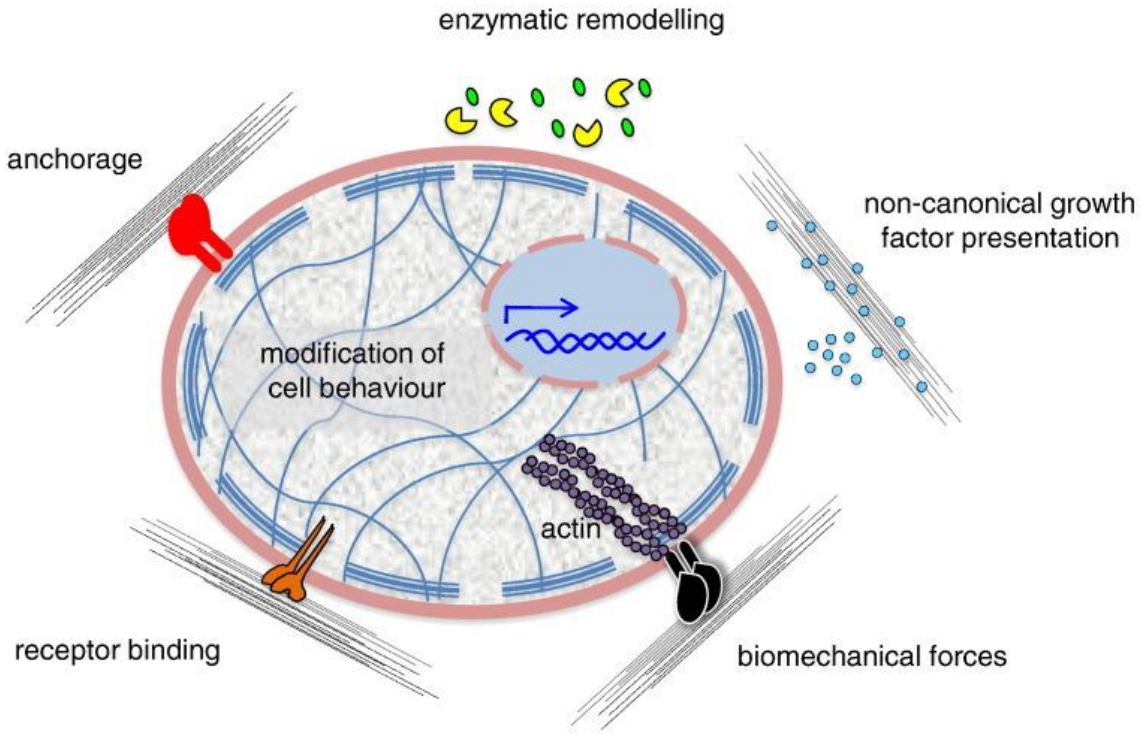

Figure 1.2. Extracellular matrix-mediated regulation of cellular behaviour. This figure shows various ways by which the ECM can modulate cell behaviour and fate, depending on the characteristics and composition of surrounding ECM. Cells can bind different ECM-bound receptors or co-receptors receiving mechanical stimuli (red, orange and black). Cellular anchorage (red) influence various biological functions by directing positionality of the given cell. Focal adhesion formation (black) and subsequent actin filament formation provides mechano-transduction between cells and the ECM. Growth factors bound to ECM components or soluble within the ECM can chemically signal cells (orange and cyan). Cells themselves can remodel the ECM via producing enzymes. From Gattazzo F, Urciulo A, Bonaldo P., 2014, Extracellular matrix: A dynamic microenvironment for stem cell niche.

Genetic abnormalities of the ECM result in a range of syndromes that can be incredibly harmful to the host tissue (Jarvelainen, Sainio et al. 2009). Research has shown that without the structural support and biochemical signalling provided by the ECM, cells *in vitro* become de-differentiated and lose viability, making them unsuitable for tissue engineering purposes. Due to these issues, different bioreactor and synthetic support scaffold approaches have been developed to emulate the ECM *in vitro* (Xu, Yang et al. 2011, Fourel, Valat et al. 2016). These

studies have shown that with the addition of key ECM proteins, a degree of the physical and chemical functions as found *in situ* can be maintained and developed *in vitro*. These advancements in biomimetics have developed more sustainable cellular populations which maintain differentiation states for longer. Biomimetic materials have also been developed to drive cellular differentiation, expressing selected biological factors to signal cells to differentiate to specific lineages (Liu and Roy 2005, Liu, Tian et al. 2010, Wang, Wang et al. 2016). Within tissue engineering applications 3D environments, such as polymeric scaffolds or hydrogels, are utilised to provide cells with provisional ECM environments for modelling or regeneration of tissue. Therefore, the understanding and characterisation of ECM properties is vital in the development and improvement of biomimetic tissue engineering systems.

1.4. Fibronectin

One vital extracellular matrix component is fibronectin (FN); this protein has been shown to control many cellular functions including adhesion, migration, differentiation and growth (Pankov and Yamada 2002). Fibronectin is a glycoprotein with the molecular weight of ~250 kDa and is generally found as dimers consisting of a number of three variations of spliced functional domains (FN I, II and III) (Figure 1.3). The constituents of the dimer regulate cellular and ECM component interactions, which in turn greatly influence cellular adhesion, viability and differentiation state. FN contains multiple binding domains implicated in interactions with ECM components such as collagen ($FNII_{1-2}$) and FN matrix forming complexes (FNI_{1-5}) (Pankov and Yamada 2002, Singh, Carraher et al. 2010). FN possesses binding sites for many functional proteins such as integrins and growth factors. Integrin binding sites such as the RGD (Arg-Gly-Asp) domain found at $FNIII_{10}$ and the PHSRN (Pro-His-Ser-Arg-Asn) synergy domain ($FNIII_9$) can induce cell mediated FN assembly which produce focal adhesion with cells producing a favourable binding site for cell attachment (Cantini, González-García et al. 2012). Binding sites for growth factors, such as Bone Morphogenic protein 2 (BMP-2), are located in the $FNIII_{12-14}$ sequence and can drive cellular proliferation and osteogenic differentiation (Zhao, Harris et al. 2002, Llopis-Hernandez, Cantini et al. 2016). These GF regions are able to directly influence cellular interactions and therefore cell fate. The availability of these binding sites on FN is regulated by the physical conformation of the molecule, as explained in the following paragraphs (sections 1.4.1. and 1.4.2.).

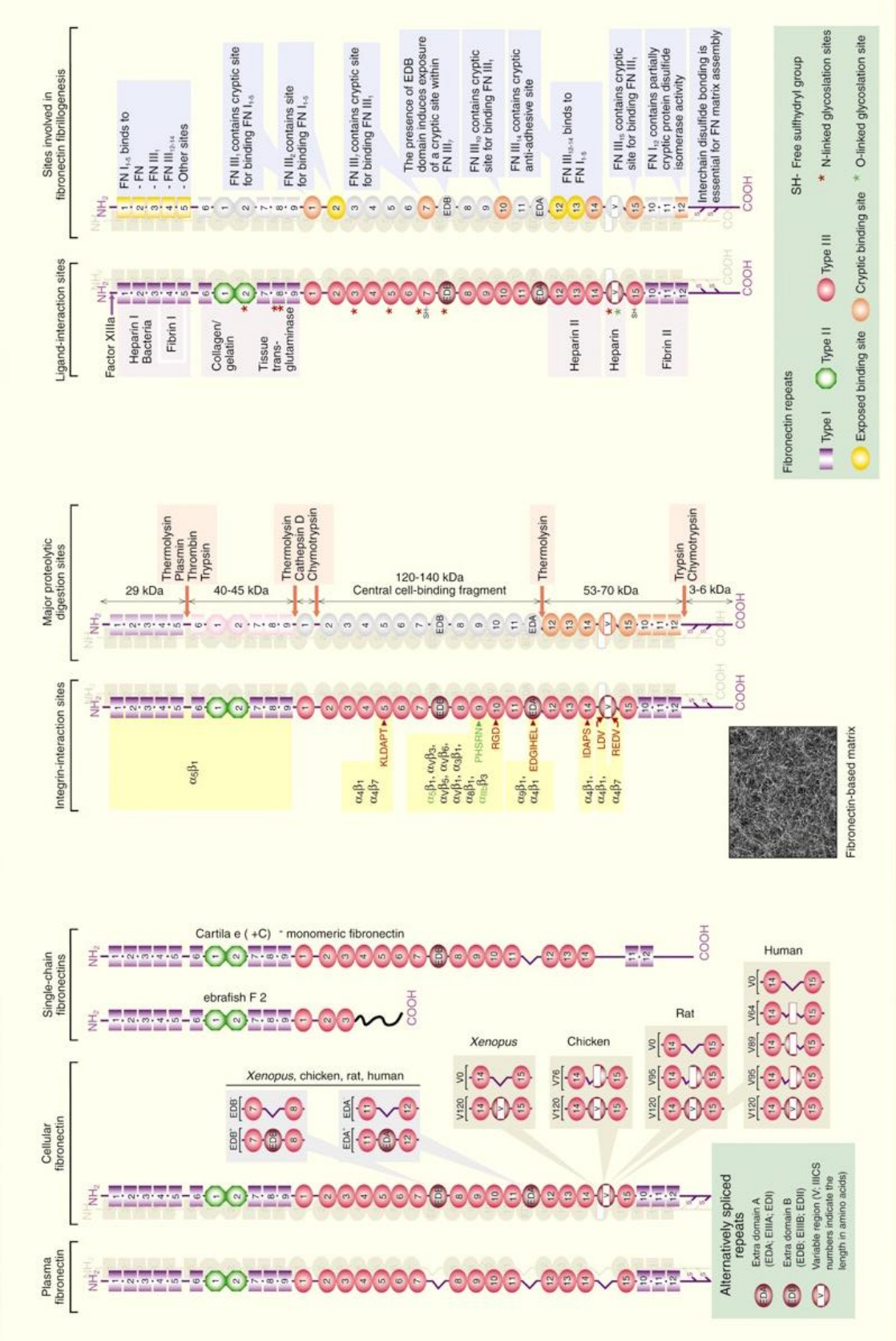

Figure 1.3. Fibronectin molecule deconstructed. The diagram shows the different FN molecules and their corresponding integrin-interacting, enzymatic

degradation, ligand interacting and fibrillogenesis sites. From Pankov and Yamada, 2002, Fibronectin at a glance.

1.4.1. Cell-mediated fibrillogenesis

FN has been observed to exist in either a globular or fibril conformation and these secondary structures of FN directly regulate the availability and activation of the functional domains. The majority of FN found within the body is found within ECMs in fibril form, deposited via cell-mediated fibrillogenesis; however, other FN molecules found circulating in blood plasma are found in globular or "closed" conformation, which is regarded as its non-active form (Pankov and Yamada 2002) (Figure 1.4). Cell-mediated fibrillogenesis has been described as a "knitting" function of cells to assemble an FN-rich ECM around themselves (Hynes 1999); this refers to the direct cell-surface receptor mediated reorganisation of the ECM in general and more specifically to the reorganisation of ECM-bound FN fibrils. Usually, cell-mediated fibrillogenesis initiates due to α5β1 integrin binding of the FN RGD and PHSRN synergy sites with cell receptors. Multiple integrins binding on a single cell; causes contractile clustering of FN therefore producing high local concentrations of FN. This promotes self-association and fibrillogenesis while translating mechano-transduction via receptor cytoplasmic domain interactions to the actin cytoskeleton (Schwarzbauer and Sechler 1999, Mao and Schwarzbauer 2005, Singh, Carraher et al. 2010, Schwarzbauer and DeSimone 2011, Lemmon and Weinberg 2017). While this is the most common mechanism by which cells mediate fibrillogenesis, other processes have been shown to support this matrix formation (Wierzbicka-Patynowski, Mao et al. 2004).

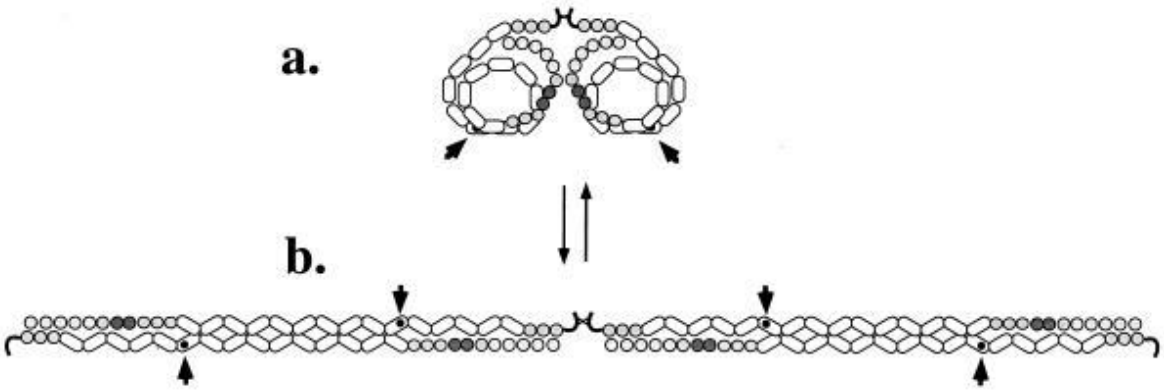

Figure 1.4. Fibronectin secondary structure. A) Globular FN, in solution, showing a series of independently folded domains coiled into a compact composition. **B)** FN assembled into extended filaments, the elongated fibrils exposing the RGD domain (labelled by arrows on both A and B) for recognition by cells. Taken from Hynes, 1999, the dynamic dialogue between cells and matrices: Implications of FN's elasticity. Copyright 1999 National Academy of Sciences.

1.4.2. Cell-free fibrillogenesis

FN fibrillogenesis can be induced in the absence of cells via a variety of methodologies; chemical, physical or surface-mediated assembly has been shown to form artificial FN matrices. Chemical treatment of plasma FN by reducing agents such as dithiothreitol (DTT) has been shown to stimulate decoupling of the disulphide-stabilized globular domains and induction of non-covalent assembly of FN networks (Williams, Janmey et al. 1983). Lower concentrations of DTT and strong oxidants have also shown the ability to induce intramolecular bonding of FN through the type I and II repeats and sulphide terminal region respectively (Vartio 1986, Sakai, Fujii et al. 1994). Other chemical-based methodologies to disrupt or denature the globular conformation of FN have been shown to drive self-assembly. For example the addition of guanidine as a denaturant or of the anionic molecule heparin show that the disruption of globular FN molecule either by chemical denaturing or electrostatic interactions is able to drive the favourable formation of FN fibrils (Cantini, González-García et al. 2012, Llopis-Hernandez, Cantini et al. 2015). This process

of unfolding, and predominantly subsequent fibril formation, can be further demonstrated by the application of mechanical tension onto FN globular molecules (Brown, Blunn et al. 1994, Zhong, Chrzanowska-Wodnicka et al. 1998, Ulmer, Geiger et al. 2008). Studies have shown that by mechanically disrupting the globular conformation, for example by domain separation of lipid bilayers or creating regions of extreme hydrophobicity differences (Baneyx and Vogel 1999, Ulmer, Geiger et al. 2008), the physical elongation of the FN molecule can expose the cryptic binding domains required for self-assembly, producing FN fibrils.

Material-driven fibrillogenesis occurs upon adsorption of FN on selected material surfaces (Salmeron-Sanchez, Rico et al. 2011, Cantini, González-García et al. 2012, Llopis-Hernandez, Cantini et al. 2016); this is dependent on the ability of the surface chemistry to disrupt the globular conformation of FN, as with the other synthetic methodologies. The adsorption of FN onto hydrophilic or negatively charged surfaces has been shown to facilitate the elongation of globular FN molecules (Nelea and Kaartinen 2010). Certain polymer surfaces, such as poly (ethyl acrylate), possess highly molecularly mobile, functional side chains which favour adsorption of FN in an extended conformation and consequent fibril formation (Salmeron-Sanchez, Rico et al. 2011). This is thought to occur due to the hydrophobic regions of FN interacting with the ethyl side chains of PEA, supplemented by the net negative charge of the bulk polymer, producing physical disruption of the globular conformation allowing FN molecules to orientate themselves into a favourable fibril conformation (Cantini, Gonzalez-Garcia et al. 2012). As previously described in cell-mediated and other synthetic fibrillogenesis mechanisms, the non-globular single elongated strands of FN would then be able to interact freely to form fibrils and networks enabling the favourable cellular interactions with FN binding motifs such as the PHSRN or growth factor binding domains. Material-driven fibrillogenesis presents the ability to develop biomaterial surfaces able to drive the re-organisation of the secondary structure of FN and therefore the expression of multiple cryptic binding domains that allow for enhanced cellular interactions.

1.4.3. Integrin binding

Cells sense their immediate environment via biochemical and physical cues, which lead to signalling-regulated cell function, differentiation and viability. Signal transduction of these cues is instigated by cell adhesion receptors known as integrins. These transmembrane heterodimeric proteins interact with ECM components and cells, translating external mechanical cues to intracellular structures (Schwartz 2010) (Figure 1.5). Integrin binding is dictated by the composition and combination of two type I transmembrane glycoproteins, α and ß. These proteins generally consist of extracellular elongated stalks that traverse cellular membranes, globular ligand binding domains (Xiong, Stehle et al. 2001) and cytoplasmic tails which predominantly binds cytoskeletal and signalling proteins (Hughes, DiazGonzalez et al. 1996, Calderwood, Fujioka et al. 2003). High variability in the amino acid make-up of each individual α and ß subunit, their components and different combinations of each subunit allow for a vast array of specific cellular binding to be dictated by integrins. Typically, α and ß extracellular globular regions bind specific domains in the ECM, transmitting precise signals through the cytoplasmic tail, potentially to recruit actin binding filaments or produce a signalling cascade to the nucleus.

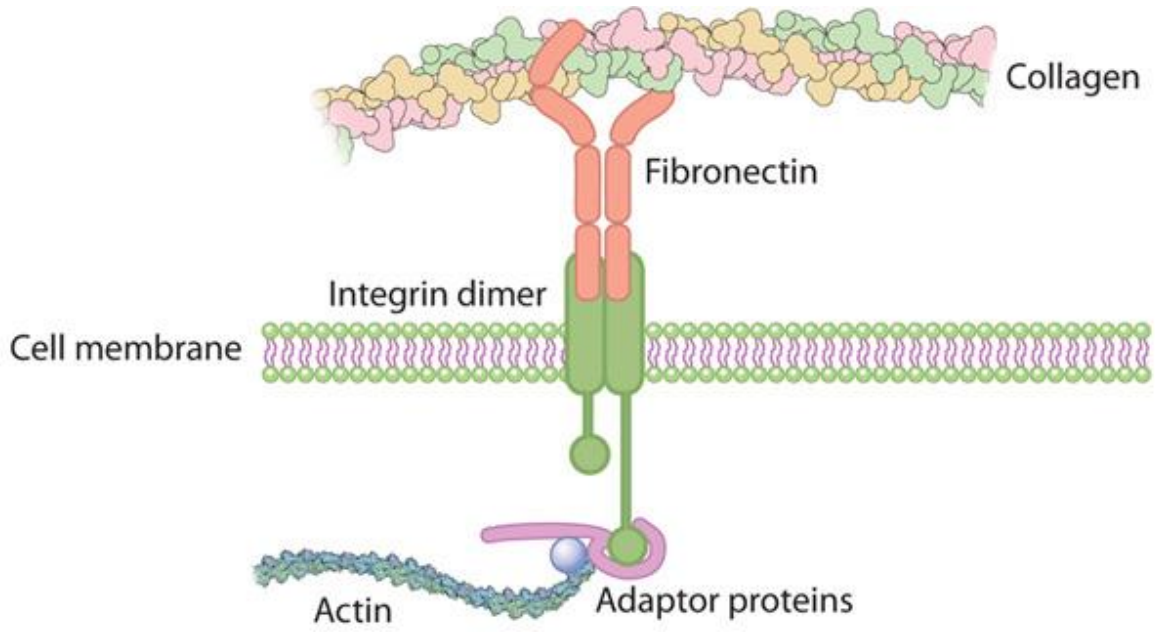

Figure 1.5. Integrin binding extracellular matrix components initiating focal adhesion complexes and actin filament formation. From Cell Adhesion, Cell Communication, Nature Education, 2010, found at https://www.nature.com/scitable/topicpage/cell-adhesion-and-cell-communication-14050486. (Last accessed 24/04/19)

As one of the most abundant ECM proteins, FN has been shown to possess amino acid sequences corresponding to dozens of these integrin receptor families (Plow, Haas et al. 2000). These FN cell recognition sequences are found at several sites (Figure 1.3.); some of these sites include RGD on cellular $FNIII_{10,}$ LDV and REDV on alternatively splices variant FNV and an EDGIHEL sequence found on EDA alternatively spliced FN (Pankov and Yamada 2002). Generally the best known of these sequences is the RGD domain, which interacts with, e.g., α5β1 integrins; this domain is not exclusively presented by FN, but can be found in other extracellular membrane proteins such as vitronectin and fibrinogen. The R residue fits into the cleft of a β-propeller inserted into the α subunit while the D residue is cationically bound within a von Willebrand factor A-domain in the β subunit (Humphries, Byron et al. 2006). This binding domain-integrin interaction has been shown to be important in controlling cellular adhesion. The binding of this domain is dependent on the FN secondary structure, regulating the 3D presentation of the RGD motif, and promoted and enhanced by secondary site

binding of the synergy domain. The synergy site is able to promote RGD binding of cells by interacting with the α5 subunit; although this synergistic binding of both domains enhances cellular adhesion, it is not required (Redick, Settles et al. 2000). In fact, it has been shown that while the PHSRN synergy site has no integrin binding activity of its own, it is able to synergistically improve RGD-mediated cellular binding 100 fold (Obara, Kang et al. 1988, Kimizuka, Ohdate et al. 1991, Aota, Nomizu et al. 1994, Redick, Settles et al. 2000). The exposure of these two binding domains for α5β1 integrin interactions is dependent on their relative distance and orientation to each other as well as the secondary conformation of FN (Bachman, Nicosia et al. 2015). These cryptic sites are favourably presented by FN fibrils.

α5β1 integrin recognition of the RGD and PHSRN FN motifs allows mechano-transduction of force stimuli from the ECM to the cell, producing contractile dependant cellular phenotypes. Upon integrin receptor binding and clustering, the accumulation of integrins at sites of high concentrations of RGD domains, as would be present with FN fibril networks (Takagi and Springer 2002, Calderwood 2004, Takahashi, Leiss et al. 2007), occurs and the assembly of intracellular multiprotein structures is triggered (Figure 1.6). These structures are generally referred to as focal adhesions (FAs). Initially, the N-terminal region of talin, an antiparallel homodimeric actin cross-linking protein (Critchley 2004), interacts with the intracellular component of the β integrin subunit, while the C-terminal actively binds to actin (Anthis and Campbell 2011). This interaction, and subsequent employment of kindlin proteins (Meves, Stremmel et al. 2009), which have been shown to aid in the activation of integrins (Calderwood, Campbell et al. 2013), provide a protein "anchor" that both stabilize the integrin and provide a biological initiator for protein recruitment. Other stabilizing proteins such as vinculin, which possesses a globular head N-terminal domain able to interact with the rod structure of talin and α-actinin and a tail region that can bind F-actin (Critchley 2004), are able to bind to this "anchor". The presence of vinculin has been shown to increase the size of FAs and reduce their rate of turnover. Inhibition of contractility induces loss of vinculin co–localised with FAs (Humphries, Wang et al. 2007, Wolfenson, Bershadsky et al. 2011). The C-terminal tail of vinculin is able to bind actin, strengthening the interactions with talin, acting as a bridge or

molecular clutch, transducing forces from the ECM-bound integrins to the actin cytoskeleton (Elosegui-Artola, Oria et al. 2016). Focal adhesion kinases (FAKs) are subsequently recruited to further stabilize and control the turnover of the FAs. The presence of FAK, recruited due to phosphorylation of Tyr397 in response to integrin clustering, and the subsequent binding with another kinase protein Src are able to phosphorylate and dephosphorylate key focal adhesion proteins (Webb, Donais et al. 2004). Through this mechanism, FAK is able to regulate the adhesion dynamics in response to alterations in ECM and signalling via growth factors. Focal adhesions transmit traction force between cells and ECMs: through these focal points the actin cytoskeleton of the cells is able to directly respond to and exert force on the ECM (Wozniak, Modzelewska et al. 2004). These structures range from small immature sites, less than 1 micron in size, to more mature FAs which can be from 1 to 10 microns long.

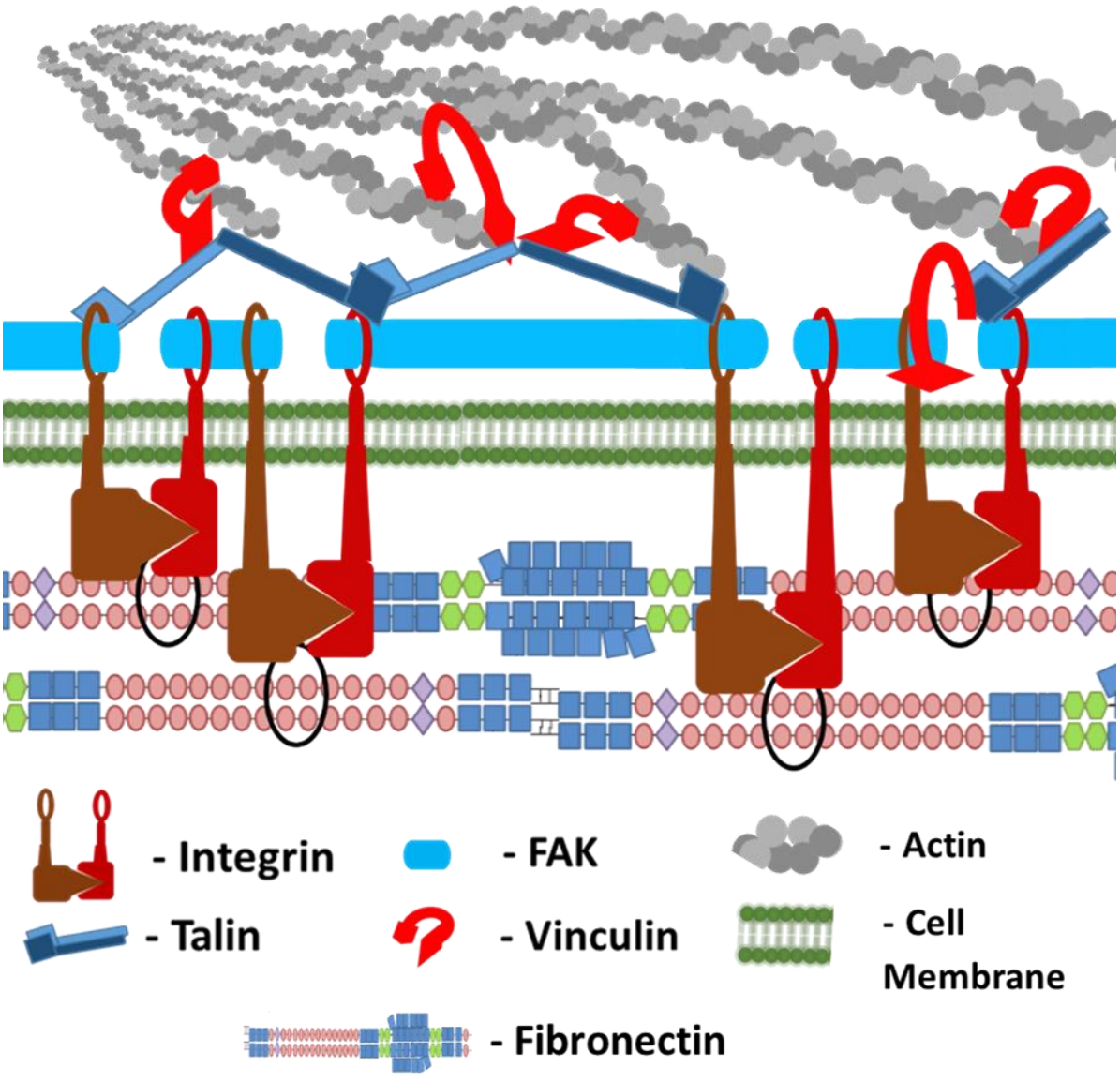

Figure 1.6. Focal adhesion and subsequent actin filament formation induced by RGD binding of α5β1 integrins (circled in black). Inspired by educational images from Mechanobiology Institute National University of Singapore (MBI), Sruthi Jagannathan, MBInfor sponsored by Mechanobiology Institute, National University of Singapore. Found at https://www.mechanobio.info/what-is-mechanosignaling/what-is-the-extracellular-matrix-and-the-basal-lamina/what-are-focal-adhesions/what-are-mature-focal-adhesions-composed-of/. (last accessed 24/04/19)

1.4.4 Growth factors

Growth factors (GFs) are signalling proteins that stimulate cell growth, differentiation, survival and tissue repair. FN has been found to bind and present growth factors to cells, predominantly occurring on the 12^{th} – 14^{th} type III repeats (Martino and Hubbell 2010). These domains possess high affinity heparin-binding domains (Pankov and Yamada 2002), which many growth factors, such as fibroblast growth factors and vascular endothelial growth factors have been found to bind to through their affinity to heparin and heparin sulfate (Bossard, Van den Berghe et al. 2004, Wijelath, Rahman et al. 2006, Kirkpatrick and Selleck 2007). Growth factor binding to various ECM components produces similar transduction pathways to integrin binding (Hynes 2002, Lin, Ren et al. 2011), the function of this binding can vary. In certain cases ECM components act as a reservoir of soluble growth factors, able to locally release these morphogens upon degradation, allowing for an established gradient within the ECM (Hynes 2002, Zhu and Clark 2014). However, some ECM bound GFs maintained as solid-phase ligands induce different cellular signals compared to their soluble counterparts (Mohammadi, Olsen et al. 2005, Zhu and Clark 2014). Both these methodologies locally release or present GF to associated cellular receptors to induce morphogenesis.

In certain cases it has been shown that bound GF is able to stabilize and actively present GFs to cells more favourably than when these morphogens are in solution (Kuhl and GriffithCima 1997, Llopis-Hernandez, Cantini et al. 2016). In particular cases, these tethered GFs are not internalized by the cell upon contact,

restricting the area of interaction to the surface and allowing prolonged cellular signalling (Platt, Roman et al. 2009, Rodrigues, Blair et al. 2013, Zhu and Clark 2014). Additionally, growth factor binding domains have been shown to synergies with integrin binding to enhance cellular viability and interactions (Hynes 2002, Lin, Ren et al. 2011, Donnelly, Dalby et al. 2018), even facilitating additional integrin-dependant signalling pathway activation (Fourel, Valat et al. 2016, Donnelly, Salmeron-Sanchez et al. 2018). These cross talk interactions may be dependent on membrane proximity interactions or cooperative downstream signal transduction pathways (Lin, Ren et al. 2011, Zhu and Clark 2014). It has been reported that certain GFs, e.g. Vascular endothelial growth factor (VEGF), require both integrin binding (α5β1) proximal to growth factor receptor binding (VEGFR2) on FN to facilitate full activation of the GF (Borges, Jan et al. 2000). Therefore by either the absorption or presentation of GF in collaboration with integrin-mediated interaction, FN is able to regulate and drive cellular morphogenesis via GF cellular signalling pathways (Dalby, Garcia et al. 2018).

1.5. Stem cells

Stem cells are characterised by their ability to self-renew and capacity to differentiate into a variety of cell lineages. Within this subset of cells there are further classification definitions which correlate to the differentiation potential of the cells; for example embryonic stem cells (ESCs) are able commit to any lineage (pluripotency), while adult stem cells (ASCs) or progenitor cells are more lineage-defined and can only differentiate into specific cell types (multipotency) (Nadig 2009). These stem cells are naturally found within defined biological niches (Figure 1.7), which either induce retention of these cells stem-like characteristics via quiescence or stimulate differentiation to specific lineages via signalling (Donnelly, Salmeron-Sanchez et al. 2018). Stem cell niches are specialized microenvironments with defined extrinsic physical and functional factors that regulate stem cell behaviour (Schofield 1978, Donnelly, Salmeron-Sanchez et al. 2018). Many ASC subsets have distinct niches: haematopoietic stem cells close to endosteum and/or sinusioidal blood vessels within bone

marrow, epithelial stem cells in the bulge of hair follicles, and neural stem cells within subgranular and subventricular zones of the central nervous system to name a few (Morrison and Spradling 2008). Stem cell populations within these niches are either maintained or driven to differentiate for tissue development or regeneration in response to a diverse range of signals. Certain characteristics of stem cell niches are conserved by most stem cell microenvironments; such as certain heterologous cell-cell interactions, cellular responses to tissue damage or ligand and mechanical properties presented by ECM components can be observed in several, if not all, stem cell niches (Lane, Williams et al. 2014). Through this tight regulation, the stem cell populations can be utilised by the body to compensate for and repair local damaged tissues or can be maintained in a state of propagation or quiescence (Jones and Wagers 2008).

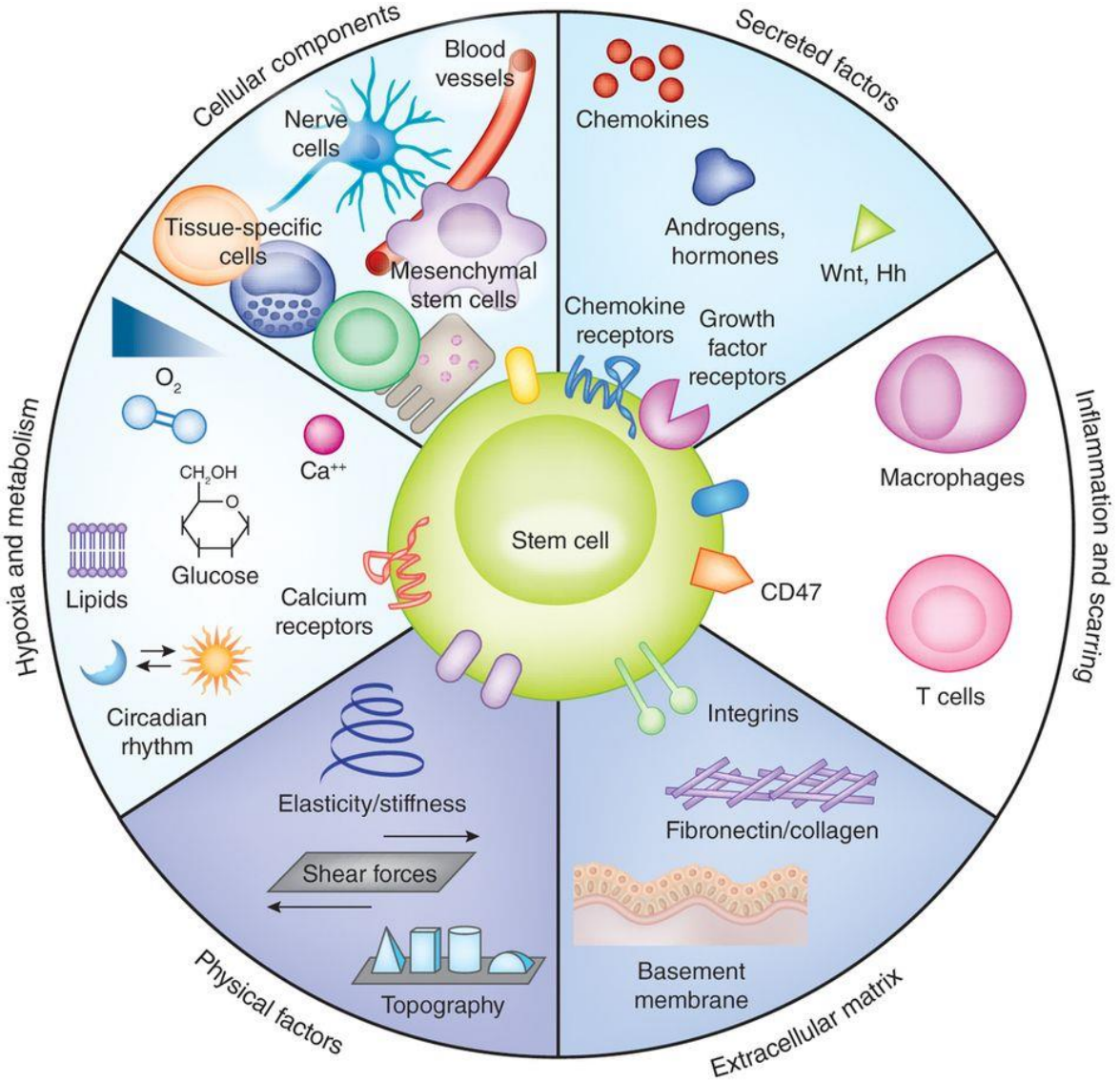

Figure 1.7. Stem cell niche factors shown to regulate cell fate. Stem cell population maintenance and cues to differentiate are tightly controlled by their inhabited niches; the niches themselves are specifically made-up of a variety of complex heterotypic, dynamic structures which provide physical, ECM, inflammatory, secretory cellular hypoxia and metabolic factors. From Lane et al, 2014, Modulating the stem cell niche for tissue Regeneration Nature, 32; 8

1.5.1. Mesenchymal stem cells

Tissue engineering has utilised a variety of stem cells for many years, primarily due to their pluripotency and ability to regenerate damaged tissues, and their propensity for signal-induced responses, be it to mechanical, biological or chemical cues. In bone tissue repair, stem cells allow full regeneration of the damaged tissue and intracellular signalling to surrounding tissue to promote healing. The most commonly utilised stem cell types are Mesenchymal stem cells (MSCs); these cells are found within a variety of different stem cell niches, including bone marrow, adipose tissue and within the eye close to the corneal limbus (Donnelly, Salmeron-Sanchez et al. 2018). These adherent fibroblast-like cells are able to differentiate into a variety of cells, including osteoblasts, adipose, myoblasts, myocytes and chondrocytes both *in situ* and *in vitro* (Dominici, Le Blanc et al. 2006, Phinney and Prockop 2007) (Figure 1.8).

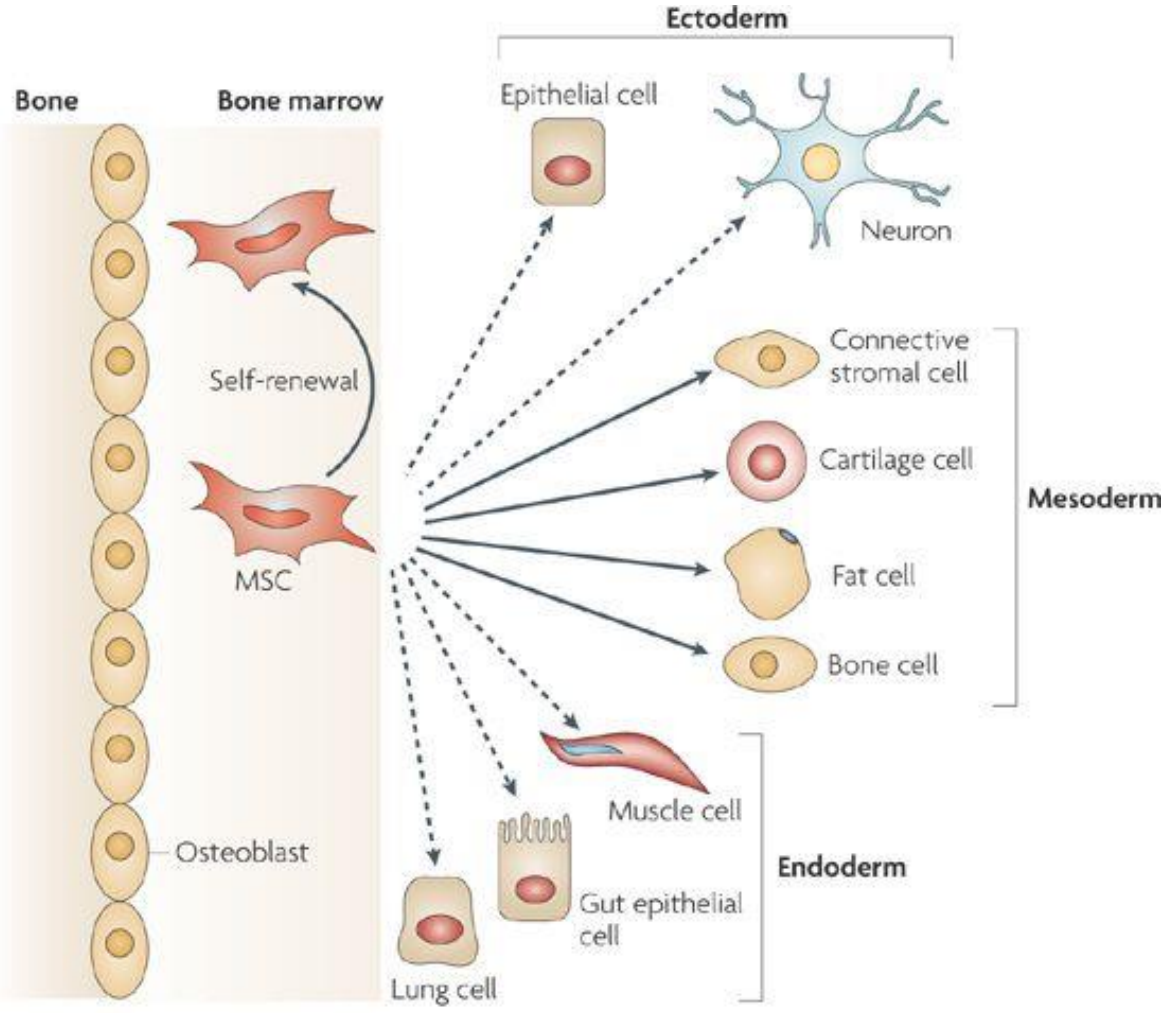

Figure 1.8. MSC within bone marrow is able to self-renew or differentiate into a variety of cell types through ectoderm, mesoderm or endoderm lineages. From Uccelli and Pistoia, 2008, Mesenchymal stem cells in health and disease, Nature Reviews Immunology volume 8, pages 726–736 (2008)

1.5.2. Osteogenic differentiation

The fate of MSCs is tightly regulated by factors of their niche; hence, modern biomedical engineering has employed several methodologies to emulate these factors and use MSCs in tissue engineering. These biomimicry approaches can be chemical (e.g. presentation of selected chemical groups to cells on self-assembled monolayers (Ulman 1996, Badia, Lennox et al. 2000, Sotiropoulou, Perez et al. 2006, Phillips, Petrie et al. 2010, Greenbaum, Hsu et al. 2013)), topographical/spatial (e.g., presenting varying densities of cellular binding domains (Kilian, Bugarija et al. 2010, Fernandez-Yague, Abbah et al. 2015)), or mechanical (e.g. culturing stem cells within hydrogels of controlled stiffness (Mayer 2005, Engler, Sen et al. 2006, Bhushan 2009, Huh, Torisawa et al. 2012, Donnelly, Smith et al. 2017)) and have shown that, by modifying established biomaterials, MSC fate can be driven and controlled for specific applications in tissue engineering, such as bone regeneration. For example, topographical modulation via roughness of poly caprolactone (PCL) surfaces was used to probe the relationship between cell fate and surface smoothness in basal media, not containing any growth factors or osteogenic inducers. The modified surface conformation was shown to increase COL1 synthesis and alkaline phosphatase (ALP) expression, an effector protein responsible for the mineralization of the ECM (Marom, Shur et al. 2005), comparatively to flat controls (Faia-Torres, Charnley et al. 2015). ALP acts as a metalloenzyme in the hydrolysis of phosphomonoesters, forming a serine phosphate intermediate which reacts with water at high pHs releasing inorganic phosphate from the enzyme (E Golub and Boesze-Battaglia 2007). The enzyme is found bound to the plasma membrane by its C-terminal via a phosphatidyl inositol-glycophospholipid (Harrison, Shapiro et al. 1995). The

process of mineralization or calcification of the ECM represents a major stage in osteoblast activity in primary bone formation (Schindeler, McDonald et al. 2008). This process highlights the presence of mature osteoblasts that allow this ECM remodelling, indicating the successful differentiation of osteoprogenitors (MSC) cells. Therefore by staining or quantifying the mineralization of the ECM surrounding stem cells grown *in vitro* MSC differentiation into osteoblasts can be determined (Al-Jarsha, Moulisova et al. 2018, Hay, Rodrigo-Navarro et al. 2018). Other markers of osteogenic differentiation of MSC cells include osteopontin (OPN), an early stage marker, and osteocalcin (OCN), a late stage marker (Aubin 2001). These non-collagenous proteins have been shown to be present in bone matrix and due to the high density of aspartic acid and glutameric acid residues within their primary amino sequence are able to bind calcium ions with a high affinity (Oldberg, Franzen et al. 1988). Therefore, it is thought that these bone matrix proteins are selectively produced by osteoblasts as a bridge to hydroxyapatite, a naturally occurring mineral found in bone, during different stages of bone formation (Hauschka, Lian et al. 1989, Sodek, Ganss et al. 2000, Noda and Denhardt 2008).

Growth factors are also able to drive differentiation of MSCs. One key subset of growth factors known to regulate osteogenic differentiation are bone morphogenic proteins (BMPs). These GFs are found throughout the body and have been shown to be critical for all organ systems (Wang, Green et al. 2014). However, they were first discovered due to the ability of certain BMPs to induce bone formation; for example bone morphogenic protein 2 (BMP-2) is a dimeric member of the transforming growth factor-ß (TGF-ß) family of proteins, excreted by cells and bound to components of the ECM, such as FN. MSCs are able to bind dimeric BMP-2 through cell surface BMP-receptors (BMPRI and BMPRII) forming heterotetrameric complexes, which initiate osteogenic signal transduction. BMP-2 treatment has successfully been utilised for bone regenerative tissue engineering purposes (Lee, Silva et al. 2011), however due to low efficiency of this GF in solution, a result of ineffective GF presentation to cells, high concentrations of BMP-2 are required. These high concentrations of BMP-2 used with conventional biomaterials are costly and have been shown to have potential adverse side effects within these systems. Therefore, current research aims to optimise the presentation of BMP-2 therefore lowering the concentrations

required for successful osteogenesis in tissue engineering. (James, LaChaud et al. 2016).

1.6. Poly L-Lactic Acid

Poly L-Lactic acid (PLLA) is a hydrophobic semi-crystalline polyester with a melting point of 174-184ºC and a glass transition temperature of 60-65ºC (Auras 2010, Rincon Lasprilla, Rueda Martinez et al. 2011). The PLLA polymer is made of L-lactic acid (LA) monomers (Figure 1.9), whereas poly D-lactic acid (PDLA), its optimal isomer and poly L/D-lactic acid (PLDLA) a blend are either, comprise solely or partially of D-lactic acid monomers. The polymer can be manufactured at different molecular weights and processing temperatures which allow the production of different forms of PLLA with diverse physical properties (Nampoothiri, Nair et al. 2010, Savioli Lopes, Jardini et al. 2012). These variations allow for a wide range of poly lactic acid polymers to be produced for different applications. PLLA degrades within the human body to produce the non-toxic degradation products; water, carbon dioxide and lactic acid which are processed by the Krebs cycle and excreted through urine. The reagents required to synthesis PLLA are widely available and cost effective, allowing PLLA to be a very accessible biomaterial.

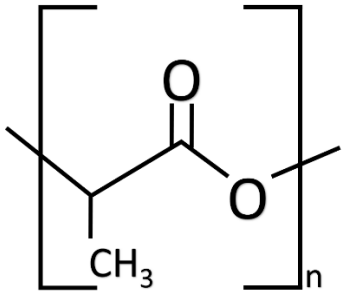

Figure 1.9. Structural formula of poly L-lactic acid.

1.6.1. Properties

PLLA has been used as a biodegradable polymer for many years (Zhu, Gao et al. 2004); key characteristics of this polymer, its biocompatibility, availability and controllable degradation within the body, make it a versatile and useful resource for regenerative medicine (He, Wang et al. 2013). PLLA is able to maintain certain aspects of its characteristic mechanical properties, such as high tensile strength (4.8 GPa), even after alterations and processing. However, it can alternatively be processed to produce a soft or elastic materials, therefore it can be used as both a rigid and a plastic biomaterial (Farah, Anderson et al. 2016). This flexibility has allowed it to be used in many different types of biomaterial. The mechanical characteristics of PLLA can be changed by altering the molecular weight of the pure polymer, by co-polymerising it with other polymers or by adding chemical reagents such a plasticisers. The mechanical properties and chemical composition regulate the appropriate use as a biomaterial and biodegradation of PLLA devices; for example, PLLA can be processed to have a degradation time of between 6 months to 5 years (Suuronen, Pohjonen et al. 1998). This variation allows for a wide scope of PLLA applications within the body, from drug delivery applications to long-term bone fixation. In some cases improved mechanical properties such as impact strength and tensile strength are needed for bone fixation; in these instances PLLA can be strengthened with copolymerisation with D-lactide or other polymers, such as co-polymerisation with glycolic acid to form Poly Lactic-co-glycolic acid (PLGA) (Haers, Suuronen et al. 1999, Makadia and Siegel 2011). PLLA can also be used in polymer-based hydrogel scaffolds used for regeneration of tissues (Hiemstra, Zhong et al. 2006); in this case lactide is usually co-polymerised with other more hydrophilic polymers to produce the water swollen 3D structure (Basu, Kunduru et al. 2016). These variations have allowed PLLA to be applied in various tissue engineering applications, from rigid scaffolds for bone regeneration to soft tissue regeneration for cartilage repair (Rosenzweig, Carelli et al. 2015).

1.6.2. PLLA in cell culture

While PLLA is incredibly useful as mechanical support for regeneration, one obstacle in utilising PLLA as a cellular environment for implantation is the limited cellular adhesion due to poor adsorption and expression of key biological signals. Implantable porous scaffolds usually contain pluripotent cells or biological signalling molecules to enlist cells to the site of regeneration (Zhu, Gao et al. 2004, Auras 2010, Rincon Lasprilla, Rueda Martinez et al. 2011, Savioli Lopes, Jardini et al. 2012, He, Wang et al. 2013, Frydrych, Roman et al. 2015, Liu, Tian et al. 2015). Due to inefficient ECM protein adsorption, PLLA is often modified before surgical implantation for regenerative medicine purposes (Zhu, Gao et al. 2004, Xu, Yang et al. 2011). For example, PLLA scaffolds can either be pre-seeded with donor cells before implantation or be preloaded with relevant proteins corresponding to the tissue surrounding the intended implant. These steps to improve cell-surface interactions are necessary, as this is the first point of contact with the *in vivo* environment of the body (Zhu, Gao et al. 2004). However, PLLA is not an ideal biomaterial for adhesion of certain ECM components, such as FN, as it is unable to drive the formation of protein fibrils that would facilitate enhanced cellular interactions (Zhu, Gao et al. 2004). Therefore, several surface modification techniques have been proposed to improve this initial interaction and the subsequent cell adhesion and growth. These methods include UV irradiation (Zhu, Zhang et al. 2002), plasma treatment (Chen and Su 2011, Jacobs, Declercq et al. 2013) , surface entrapment (Meng, Wang et al. 2004), alkaline treatment (Kramer, Kunkemoeller et al. 2014) and SI-ATRP (Xu, Yang et al. 2011). The aim of these procedures is to directly add protein, alter the surface characteristics or co-polymerise more bioactive polymers onto the surface of PLLA to increase implant effectiveness.

1.7. Poly (Ethyl Acrylate)

Poly (Ethyl Acrylate) (PEA) is an acrylic ester polymer; it has a glass transition temperature of -23 ºC and tensile strength of 0.23 MPa (Figure 1.10). PEA is biostable *in vivo* and is non-degradable. Therefore it is able to provide long-term structural support to the mechanical properties of the tissue when PEA is utilised in copolymer systems as a non-degrading elastic polymer (Lozano Picazo, Perez Garnes et al. 2015).

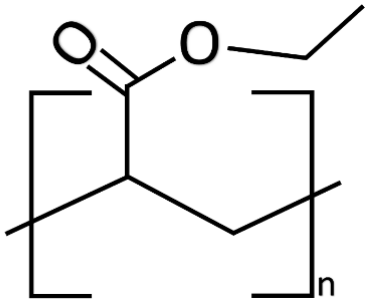

Figure 1.10. Structural formula of poly (ethyl acrylate).

1.7.1. PEA in biomedical engineering

PEA is hydrophobic, at physiological temperatures it is biostable and possess elastomeric characteristics. Another benefit of PEA in biomedical engineering is its good biological behaviour and protein interactions; when FN is coated onto the polymer, PEA is able to organise FN into physiological-like fibrillar networks; this facilitates initial cellular adhesion and the formation of focal adhesions (Salmeron-Sanchez, Rico et al. 2011, Cantini, González-García et al. 2012, Llopis-Hernandez, Rico et al. 2013, Vanterpool, Cantini et al. 2014). PEA is able to induce material-driven fibrillogenesis due to the mobility and

composition of functional groups in the polymer, which facilitate unfolding of the FN molecule. This exposes functional binding sites for cellular adhesion and growth factors binding such as BMP-2 (Bathawab, Bennett et al. 2016, Llopis-Hernandez, Cantini et al. 2016, Moulisova, Gonzalez-Garcia et al. 2017). Within our group we have shown that by plasma treating decellularized bone fragments with PEA, fibrillogenesis of FN is able to favourably increased presentation of the $FNIII_{12-14}$ growth factor and $FNIII_9$ synergy binding domains, allowing for ultralow doses of growth factors for critical bone defect regeneration (Cheng, Alba-Perez et al. 2019). This control over the conformation and activity of FN allows for the selective adhesion and phenotypical responsiveness of a variety of cells types (Lozano Picazo, Perez Garnes et al. 2015, Donnelly, Dalby et al. 2018). However, PEA has been shown to be non-biodegradable (Lozano Picazo, Perez Garnes et al. 2015), which is a limiting factor in its use in biomedical engineering applications. Therefore, strategies are needed to produce nanometrically thin functional PEA coatings on biodegradable substrates; this thin layer has to maintain its ability to induce FN fibrillogenesis, without altering the degradation profile of the underlying material. The inclusion of thin layers of PEA, produced by plasma polymerisation and spin-coating has been shown to provide additional functionality to glass and poly caprolactone (Llopis-Hernandez, Cantini et al. 2015, Llopis-Hernandez, Cantini et al. 2016, Cheng, Alba-Perez et al. 2019). In turn, this thin polymer layer, as small as a couple of nanometers, can be subsequently metabolized (Kreyling, Abdelmonem et al. 2015, Muellner, Dodds et al. 2015, Schulz, Gojzewski et al. 2018). Techniques currently utilised to produce these thin layers of PEA include plasma and spin coating (Llopis-Hernandez, Cantini et al. 2016, Cheng, Alba-Perez et al. 2019). These processed have been shown to retain the functionality of PEA, however they can result in modified polymer chain chemistry or ineffective translation to 3D systems (Cantini, Gonzalez-Garcia et al. 2012). Plasma polymerisation has been utilised in coating bone chips pre-implantation *in vivo*, these PEA coated bone chips were observed to enhance osteogenic regeneration in critical bone defect models through enhanced presentation of ultra-low doses of BMP-2 (Cheng, Alba-Perez et al. 2019). While plasma has been utilised to coat the internal architecture of 3D scaffolds, this coating has been shown to be heterogeneous (Barry, Silva et al. 2005, Canal, Khurana et al. 2016). Additionally plasma coating does not produce PEA chemically bound to the coated surface

and therefore “peeling” may occur. Therefore further advances in developing treatments for the inclusion of homogenous thin layers of PEA within 3D scaffolds is required.

1.8. Surface modification of polymer substrates

Polymers are vastly useful as biomaterials, primarily because of their versatility and potential to be modified to produce substrates with specific properties, attuned to the desired application. Therefore, there have been vast amounts of research into methodologies to tune polymer characteristics for specific biomedical uses. In particular, surface modification strategies predominantly focus on the addition of a functional layer to the surface of the polymer, modulating the interface where the majority of the interactions with the biological milieu occur. These approaches aim at optimising the biological performance of the polymer, tuning its surface to control its interfacial properties. Surface modification strategies include plasma treatment, including plasma polymerisation (Chu, Chen et al. 2002, Chen and Su 2011, Jacobs, Declercq et al. 2013, Cheng, Alba-Perez et al. 2019), addition of topographical features (Dalby, Gadegaard et al. 2007, Costa Martinez, Rodriguez Hernandez et al. 2008), or inclusion of functional chemical groups or polymer brushes (Xu, Yang et al. 2011, Gonzalez-Garcia, Moratal et al. 2012, Khetan, Guvendiren et al. 2013, Yu, Johnson et al. 2014). The aim of these modifications is to add a certain biological functionality to the polymer; such as immobilisation of GFs, addition of non-fouling properties or improving biocompatibility (Zhu, Gao et al. 2004, Siegwart, Oh et al. 2012, Nemani, Annavarapu et al. 2018), while generally maintaining its bulk properties.

1.8.1. Surface Initiated-Atomic Transfer Radical Polymerisation (SI-ATRP)

While many surface modification techniques have been developed over the years, surface-initiated atomic transfer radical polymerisation (SI-ATRP) has emerged as a widely used methodology for controlled alteration of surface properties for biomedical applications (Xu, Yang et al. 2011). In SI-ATRP, the surface intended to be altered is initially functionalised or primed and an initiator molecule is then immobilised. This initiator is activated in the presence of the intended monomer for a specified time (Matyjaszewski, Dong et al. 2007, Matyjaszewski 2012), and the monomer is therefore polymerised in place of the anchored initiator and bound to the surface (Datta, Bhowmick et al. 2008) (Figure 1.11). The polymerisation can be supplemented with other catalysts: for example an activators regenerated by electron transfer (ARGET) protocol utilises non-radical forming reducing agents to facilitate the activation and substitution of the initiator; in this way the reaction kinetics are lowered and less catalytic activator is required (Simakova, Averick et al. 2012).

Compared to other surface modification polymerisation techniques SI-ATRP is tolerant of slight impurities (Matyjaszewski, Dong et al. 2007), such as oxygen in the system, and does not require the same extreme experimental conditions required for ionic and ring opening metathesis polymerisation (Datta, Bhowmick et al. 2008). Due to the versatility and variability of SI-ATRP it can be carried out in many different solvents in different conditions, which make it a widely utilised surface modification methodology in biomedical research (Datta, Bhowmick et al. 2008, Xu, Yang et al. 2011, Siegwart, Oh et al. 2012, Simakova, Averick et al. 2012). The specificity of the reaction also allows for refined control of molecular weight and functionality of polymers produced from SI-ATRP on many different surfaces, including proteins, inorganic materials and organic surfaces (Siegwart, Oh et al. 2012).

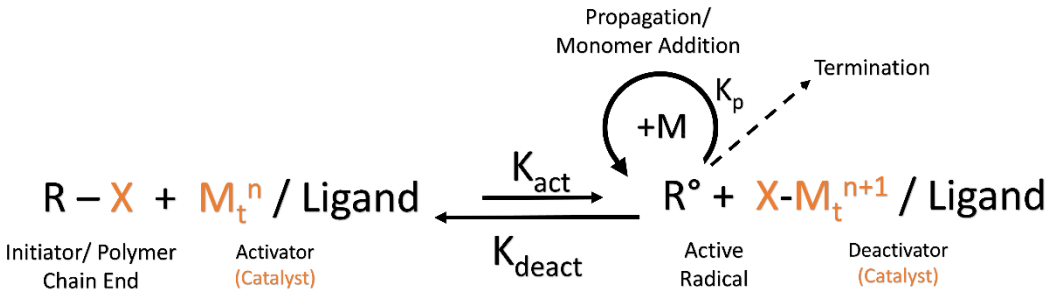

Figure 1.11. General mechanism by which atomic transfer radical polymerisation occurs. The base polymer (X) is bound to a functional initiator molecule (R), this complex is generally referred to as the "initiator". The initiator can have one or several reactive side chains, providing high degrees of attenuation in designing ATRP processes. This "initiator" reacts with the ligand to be bound in a complex with a strong transition metal catalyst (M_t^n) in the lower oxidation state, transferring the atom or group from the initiator to create a free radical (R) and an oxidized transition metal halide complex (X-M_t^{n+1}/Ligand). The radical propagates polymerisation of the introduced monomer (M), further reacting with the oxidized transition metal halide complex rejuvenating the catalyst. This process can repeat itself and is reversible, requiring the control of the temperature and atmospheric conditions as introduction of air or other free radicals will stop the reaction. Adapted with permission from Krzysztof Matyjaszewski and Jianhui XiaAtom (2001) Transfer Radical Polymerization. Chem. Rev. 2001, 101, 9, 2921-2990. Copyright 2001 American Chemical Society.

The SI-ATRP reaction allows for the incorporation of functional polymer chains onto surfaces without significantly altering the chemical characteristics of the host material. Moreover, the mechanical characteristics of the substrate can be maintained, which is incredibly useful in biomedical applications (Xu, Yang et al. 2011). This technique allows for the incorporation of functional polymer chains onto surfaces in a robust, efficient, cost-effective and controllable manner (Simakova, Averick et al. 2012). Due to the accessibility and

versatility of SI-ATRP it has being utilised in many aspects of biomedical research, including drug delivery methodologies (altering or encapsulating drugs) and surface functionalisation for improved cellular interactions (Khandare and Minko 2006, Datta, Bhowmick et al. 2008, Xu, Yang et al. 2011).

1.9. Objectives

The aim of the research outlined in this doctoral dissertation is to develop an implantable and degradable polymeric scaffold with optimised protein and cellular interactions for application in tissue engineering. The system will consist of a biodegradable rigid backbone (PLLA) and of biologically active brushes (PEA) able to induce the organisation of the ECM component, fibronectin (FN) into physiological-like fibrils (Figure 1.12).

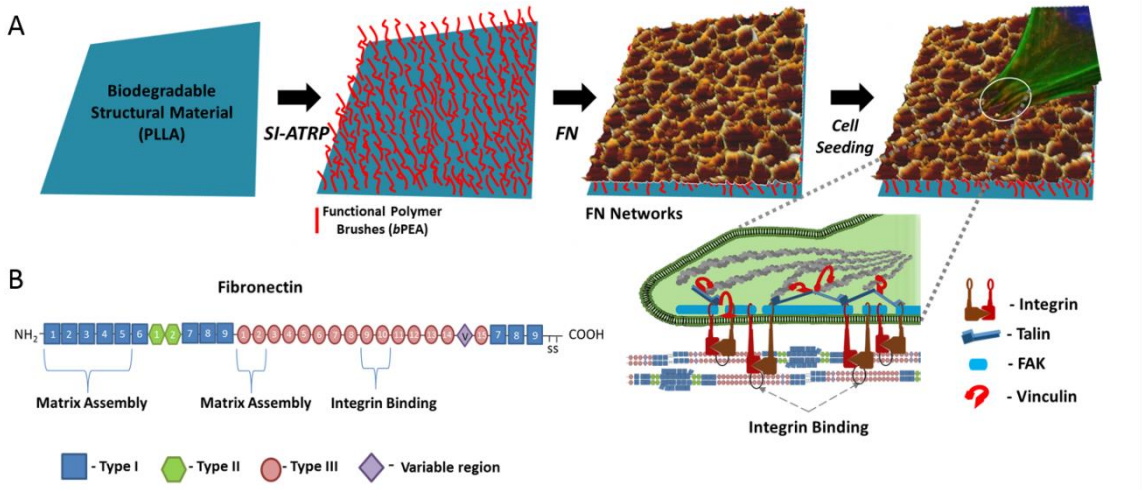

Figure 1.12. Surface modification of PLLA with PEA brushes to induce material-driven assembly of fibronectin into nanonetworks. (A) PLLA modified via SI-ATRP to present PEA brushes (*b*PEA) on its surface; PEA drives the assembly of FN into physiological-like nanonetworks that facilitate cell adhesion and differentiation. **(B)** Sketch of FN outlining main matrix assembly and cell binding domains, and representation of the nanofibrils formed upon adsorption on PEA, which expose integrin binding domains and therefore facilitate the formation of focal adhesions by cells. Taken from Sprott et al, 2019.

To this end, we will first develop a SI-ATRP based methodology to produce PEA brushes on PLLA surfaces:

1. We aim to optimise each step in this SI-ATRP process to achieve minimal alterations to any physical properties of PLLA so as to preserve its favourable characteristics (mechanical strength, degradability), whilst introducing nanometric PEA brushes on the substrate (*Chapter 2*).
2. We will characterise the interfacial properties of the synthetized polymer brushes, with attention to the retention of their ability to support the formation of biologically active FN assembly into nanonetworks, and we will test the ability of our surface modification to enhance cell adhesion and support cell differentiation using a model cell line (*Chapter 3*).
3. We will compare alternative SI-ATRP protocols and their biological interactions (*Chapter 4*).
4. Then, we will further characterise the ability of our system to recruit and successfully present growth factors to mesenchymal stem cells. We will show the translation potential of the surface modification strategy developed in this thesis by applying it to a 3D scaffold designed for bone tissue engineering applications (*Chapter 5*).
5. In the final chapter, we will present an overall discussion of our results and future perspectives for the materials and methodologies developed in this thesis (*Chapter 6*).

2- Synthesis via ARGET SI-ATRP and physico-chemical characterisation of PLLA-*b*PEA

2.1 Introduction

Poly L-lactic acid (PLLA) is a well-established and widely used polymer in tissue engineering applications; however, it does not possess an inherent biological activity. In this chapter, we propose a methodology to introduce functional poly (ethyl acrylate) (PEA) brushes on its surface. The chosen methodology for surface modification is an atomic transfer radical polymerisation technique. This system has been used for many years, but the polymerisation of acrylate brushes onto PLLA has not been documented. Therefore, we aim to develop a novel protocol for this procedure. Initially, production of these brushes onto PLLA samples was performed on 2D films. Each step of the activator regenerative electron transfer (ARGET) surface-initiated atomic transfer radical polymerisation (SI-ATRP) (Figure 2.1) was optimised so as to ensure efficient functionalisation of the surface while maintaining the favourable characteristics of the bulk substrate.

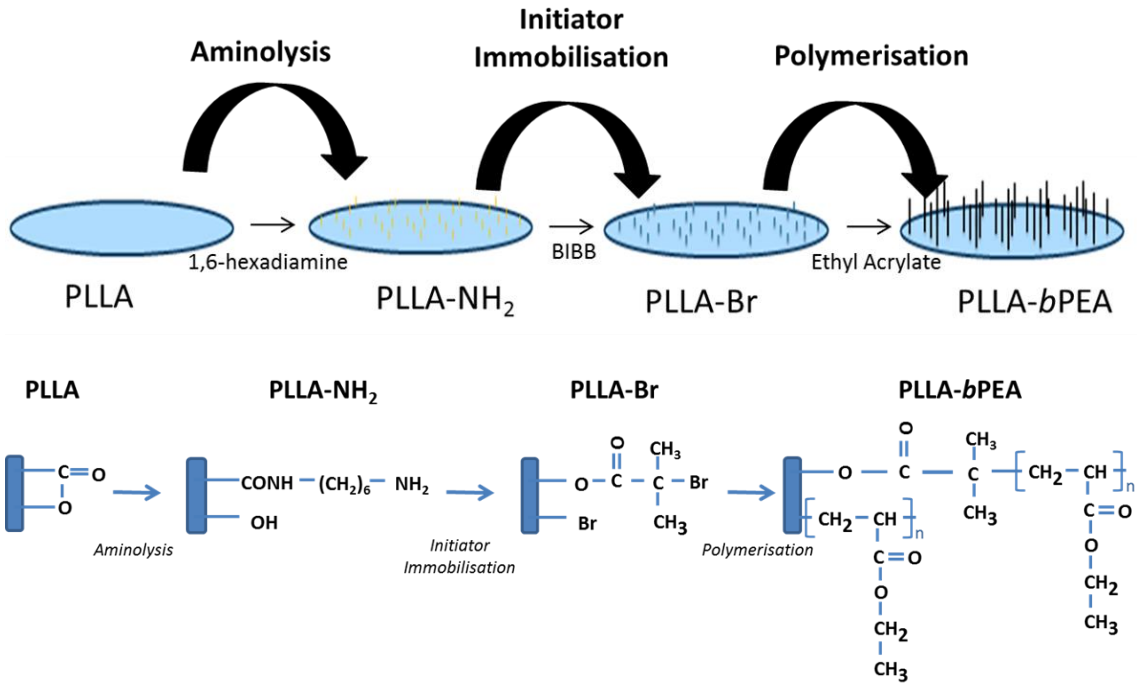

Figure 2.1. SI-ATRP process. Characterisation of the key steps of SI-ATRP on PLLA and the surface chemical reactive groups produced from each step. Adapted from (Sprott, Gallego-Ferrer et al. 2019).

2.2 Materials and methods

2.2.1 Materials: Poly (L-Lactide) films (thickness 50 µm) were purchased from Goodfellow (Huntingdon, UK). 1,6-hexanediamine (98%), 2-propanol (≥99.5%), 2-bromoisobutyryl bromide (BIBB, 98%), anhydrous pyridine (Py, 99.8%), anhydrous hexane (95%), copper(I) bromide (CuBr,99.999 %), Tris(2-pyridylmethyl)amine (TPMA, 98%), ethyl acrylate (EA, 99.5%), methanol (99.99%), ascorbic acid (AsAc) were purchased from Sigma Aldrich, Dorset, UK. Glass reaction vessels were custom-made. Spin-coated PEA controls (PEA) were prepared on 12 mm glass coverslips from 4% solutions in toluene of bulk PEA, obtained via polymerisation of EA using 1% benzoin (Sigma, St. Louis, MO) as a photonitiator, spun at 3000 rpm with acceleration of 3000 rpm s^{-1} and vacuum dried at 60ºC for 2 hours to remove excess toluene.

2.2.2 Preparation of PLLA-bPEA films: The developed SI-ATRP system takes place in three steps: priming (aminolysis), initiator immobilisation (bromination) and polymerisation (Figure 2.1.); these processes take place sequentially and separately within different reaction vessels (Figure 2.2.). PLLA films were cut into 13.8 mm circles, with an area of 1.9 cm^2. The aminolysis protocol was carried out according to the method described in (Zhu, Gao et al. 2004). Briefly, PLLA films were immersed in 1, 6-hexanediamine and 2-propanol at 40ºC for 10 minutes. Samples were then washed in deionised water at RT for 24 hours with constant agitation to remove excess 1, 6-hexanediamine and then vacuum dried at room temperature to a constant weight.

For initiator immobilisation, aminolysed PLLA films were placed on shelves within a 3-necked sealed reaction vessel, which was then degassed with oxygen-free nitrogen gas. 3.5 mL BIBB and 70 mL anhydrous hexane were degassed within a side-arm and added to the reaction vessel to fully cover the samples. 1.4 mL pyridine was then dropped slowly into the reaction vessel as the reagents were stirred vigorously with a magnetic stirrer. The overall ratio of the reagents was hexane: BIBB: pyridine (20:1:0.4). The reaction was maintained at 0˚C with an ice

bath for 2 hours and then subsequently kept at room temperature (24°C) for 22 hours. A nitrogen flow was maintained throughout the entire 24 hour protocol. The initiator immobilised PLLA samples were then removed from the reaction vessel and washed with 2:1 deionised water: methanol solution in a soxhlet apparatus for ≥72 hours and then vacuum dried to constant weight. Polymerisation of initiator immobilised PLLA samples was carried out within a separate reaction vessel in a nitrogen atmosphere at room temperature. 1.95 mg CuBr and 12.8 mg TPMA powder were added to the bottom of the reaction vessel containing the PLLA samples. 16.65 g of ethyl acrylate and 16mL of methanol were then placed in a side arm of the reaction apparatus and the whole vessel was purged with nitrogen. Once all samples were immersed in this solution and thoroughly mixed through, 123.28 mg ascorbic acid dissolved in 16 mL methanol was introduced dropwise (over 1 to 4 hours). The final ratio of the reactants was EA: CuBr: TPMA: AsAc (96:0.005:1:0.4). The polymerisation was stopped by flooding the vessel with oxygen and the samples (PLLA-*b*PEA) were then washed in 2:1 deionised water: methanol solution within a soxhlet apparatus for ≥72 hours and vacuum dried to constant weight. For the measurement of grafting yield samples were weighed before and after SI-ATRP treatment using an Ohaus Pioneer balance; grafting yield was calculated as $(W_{PLLA\text{-}bPEA}\text{-}W_{PLLA})/A$, where A is the film area (30 samples of ~1 cm^2).

Figure 2.2. Experimental set-up. The reaction vessels are on the left and in the centre, connected to condenser and dropper side arm; on the right is a soxhlet set-up for washing of the samples post reaction. Each reaction vessel consists of either a 3 or 4-necked lid and vessel, sealed with a Teflon O-ring and vacuum grease. Each neck is further connected to a condenser to retain all reagents within the vessel, a dropper arm with controllable drip rate regulated by a rotating stopper or an airtight rubber stopper with a needle pumping 0-grade nitrogen into the system(not shown) (nitrogen outlet was monitored via a bubbling apparatus downstream from the condenser). Each reaction vessel was placed within a glass water bath (not shown) on a magnetic stirrer enabled bench heater, so as to allow for control over general temperature and agitation of the reagents during reaction. Within each glass reaction vessel were perches for glass shelves used to maintain samples within the centre of the reaction and separate them from the magnetic stirrer. A basic soxhlet apparatus was set up, with a boiling vessel for solvents and glass boiling beads and a collection soxhlet tube with a Teflon sieve to ensure samples were not dropped into boiling solvents. A water system was set

up connecting flow between the condensers of all three apparatus so as to condensate reaction vapours.

2.2.3. Atomic force microscopy: Atomic Force Microscopy was used to quantify surface roughness and visualise topology in dry conditions. Height and lock-in phase images were taken in AC mode using a Nanowizard 3 Bioscience AFM (JPK, Berlin Germany). Scans were made using cantilevers with a resonance frequency of 75 kHz and a force constant of 3 N m^{-1} (MPP-21120 from Bruker, Billerica, MA). Surface area scans (n=3) of 5x5 µm (0.5Hz) were used to analyse surface roughness of each sample from any given condition. The R_{rms} was calculated using the JPK DP software after image levelling to remove variations or tilts in the background. Scans of 2x2 µm (0.7Hz), 1x1 µm (0.8Hz) and 0.5x0.5 µm (1Hz) were used to identify features and qualitatively assess surface topology.

Force spectroscopy curves were obtained, after calibration of cantilever sensitivity and spring constant, using ~30 Nm^{-1} cantilevers with a 20 µm diameter spherical silica tip. The cantilever was approached to the surface with a constant speed of 2.0 µm s^{-1}, at room temperature in water or ambient conditions, and the Young's modulus was calculated using a Hertz model (JPK DP software), with an indentation depth of 30 nm.

2.2.4 Dynamic mechanical analysis: Dynamic mechanical analysis (DMA) was performed on a DMA 8000 (Perking-Elmer) apparatus at a frequency of 1Hz in tension mode, the temperature range was -150 to 100°C at a rate of 1°C min^{-1}. Young's modulus was determined at 36-38°C on sample of 10 mm x ~6 mm x 0.05 mm.

2.2.5 Water contact angle: Water contact angle measurements were undertaken on PLLA and functionalised samples. Static contact angles (SCA) were measured by dropping 3 µL of deionised water onto the samples (Figure 2.3). Advancing (ACA) and receding (RCA) contact angles were measured by the addition or removal of water to the droplet until an increase or decrease in the length of the baseline was observed. Contact angle hysteresis was calculated from the

difference between ACA and RCA. Analysis was conducted using a Theta optical tensiometer (Biolin Scientific, Stockholm, Sweden).

Figure 2.3. WCA images. Showing 3 µl water drop on PLLA, PEA and PLLA-*b*PEA surfaces.

2.2.6. Ninhydrin assay: A ninhydrin colorimetric method was utilised to quantify the amount of available amine groups bonded onto the surface of the aminolysed PLLA samples. Samples were immersed in 1 ml of ninhydrin solution, prepared by mixing 40 ml of 0.35M hydrinatin dihydrate and 4.49M ninhydrin in ethylene glycol with 10 ml of 0.04M lithium acetate buffer at pH 5.2. The samples were then heated to 90°C for 20 minutes and subsequently diluted with 9 ml of 1:1 2-propanol: deionised water solution. The vials containing the samples were vigorously vortexed to include any chromatic sediments, elutes were pipetted into a 96 well plate and absorbance was read at 566 nm using Tecan NanoQuant Infinite M200 Pro plate reader (Männedorf, Switzerland). A calibration curve was obtained using solutions containing glycine of known concentrations.

2.2.7. Enzymatic degradation: Individual samples were dried to constant weight under vacuum for a minimum of 2 days, samples were then submerged in 0.2 mg mL^{-1} proteinase K enzyme (Sigma, St. Louis, MO) in Tris-HCL buffer (pH 8.6) with 0.2 mg mL^{-1} sodium azide (Sigma, St. Louis, MO). Incubated samples were kept at 37°C with agitation. The degradation solution was replaced every 24 hours to maintain enzymatic activity. Samples were dried under vacuum to constant weight before final weight was established.

2.2.8. X-ray photoelectron spectroscopy: X-ray Photoelectron Spectroscopy (XPS) was used to identify the surface chemical composition of samples. All X-ray photoelectron spectra were obtained at the National EPSRC Users' Service (NEXUS) at Newcastle University (found at: http://www.ncl.ac.uk/nexus/). Each sample was analysed at three points with a maximum beam size (400 µm x 800 µm) with a K-alpha XPS apparatus (Thermo Scientific) equipped with a monochromatic Al-K-alpha source for Carbon, Oxygen, Nitrogen, Bromine and overview spectra. X-ray energy was 1486.68 eV at a voltage of 12 kV, current of 3 mA and power of 36 W. Analysis of the XPS results was conducted with CasaXPS version 2.3.16 (Casa Software Ltd) with adjustments for transmission and escape depth included in the VAMAS block provided by NEXUS.

2.2.9 Statistical analysis: Pre-processing and normalization of data are stated in the individual methods sections. Analysis of statistical differences was conducted using student T-test (Graphpad) for two sample comparison and One-way ANOVA for different groups using a Turkey HSD *post hoc* test to compare different groups. Differences were considered significant *$p < 0.05$, **$p < 0.01$, ***$p < 0.001$, ****$p < 0.0001$. All data presented are mean values, error bars are standard deviation and n numbers are noted in the figure captions.

2.3 Results

2.3.1 Surface characterisation

Surface modification of PLLA films was conducted via an optimized ARGET SI-ATRP process. This system consists of three separate steps, each allowing for further controlled optimization and customization of desired products. Briefly, surfaces are functionalized during initial aminolysis procedures; this primes the PLLA for immobilisation of bromine based initiators. Upon bromination of these surfaces ethyl acrylate chains can be polymerised at these initiation points

producing PEA brushes onto the surface of the PLLA. Due to the high degree of variability in these steps, optimization at each stage can lead to dramatically altered properties of the PLLA-*b*PEA samples, ranging from PEA brush density to PLLA bulk mechanical stiffness. Therefore we initially aimed to optimize each step in the SI-ATRP system so as to maintain substrate properties such as surface roughness and stiffness, while maximizing the surface functionalization. As the first step of SI-ATRP, aminolysis represents a vital process in surface modification, determining the homogeneity and density of priming sites for initiation and subsequently polymer brushes. However, as this reaction chemically breaks polymer backbones to incorporate functional amine groups, it has been shown that longer durations and temperatures of aminolysis are degradative to PLLA films (Zhu, Gao et al. 2004). Therefore it is vital to optimize this step to maintain the originally desirable mechanical properties of PLLA. Aminolysis of PLLA samples, performed with 0.06 mg mL^{-1} 1,6-hexanediamine at 40 °C, showed that increasing time while decreasing the hydrophobicity of the surfaces (Figure 2.4B) produced samples with a significantly increased RMS roughness (Figure 2.4A). The decrease of contact angle is representative of the inclusion of hydrophilic amine groups onto the surface, as observed via ninhydrin assay (Figure 2.4C). The available amine groups on the surface were observed to increase relative to time and temperature of aminolysis, however the dramatic chemical alterations to PLLA films aminolysed at 50°C resulted in structurally inviable films, which would crumble upon handling. Samples produced at 40°C for either 10 or 20 minutes were observed to have similar available surface amine densities and increased surface hydrophilicity relative to 5 minute aminolysed samples. However, 10 minute samples were not observed to have significantly rougher surfaces than pristine PLLA, therefore in order to maintain physical characteristics, 10 minutes of aminolysis with 0.06 mg mL^{-1} 1, 6-hexanediamine at 40 °C was concluded to be the optimum protocol for initial functionalization. With this methodology, a surface density of $-NH_2$ functional groups (~1.6×10^{-7} mol cm^{-2}) was calculated via ninhydrin assay.

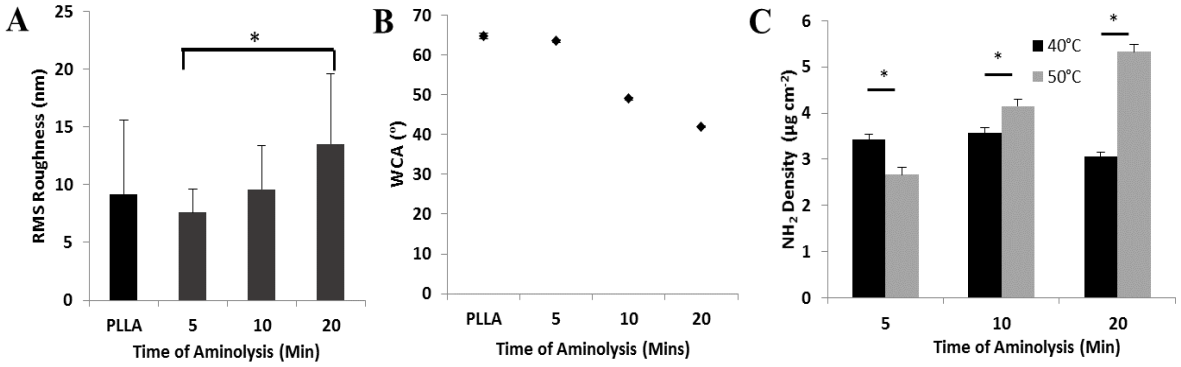

Figure 2.4. Aminolysis of PLLA. (A) Surface root mean squared roughness measurements of PLLA samples aminolysed for 5, 10 and 20 minutes with 0.06 mg mL^{-1} 1, 6-hexanediamine at 40 °C. The PLLA samples were washed with deionised water. A minimum of 12 measurements were taken from 5x5 μm^2 AFM scans of each sample. **(B)** Static water contact angle characterisation of PLLA films aminolysed for either 5, 10 or 20 minutes. **(C)** NH_2 density on PLLA surfaces aminolysed for 5, 10 and 20 minutes with 0.06 mg mL^{-1} 1, 6-hexanediamine at 50 °C compared to PLLA aminolysed at 40 °C. Graphs show mean values and standard deviation. *$p < 0.05$.

Characterisation of samples treated further through the SI-ATRP procedure, with subsequent 24 hours of initiator immobilisation and 4 hours of polymerisation, showed that topological and chemical alterations had been implemented (Figure 2.5). Surface roughness was measured to increase progressively through each step after aminolysis (Figure 2.45A). While untreated PLLA and PLLA-NH_2 had similarly smooth surfaces (R_{RMS} ~ 10.9 nm), initiator immobilisation was observed to increase this to ~ 19.5 nm and polymerisation to ~ 26.0 nm. Static contact angle was observed to recover to similar levels of hydrophobicity as PLLA post bromination (~90°) (Figure 2.5B), potentially due to the loss of amine groups and addition of initiator. PLLA-*b*PEA samples were measured to have similar hydrophobic surfaces to bulk PLLA and PEA, however dynamic contact angle measurements suggest distinctly altered surface chemistries on PLLA-*b*PEA compared to pristine PLLA. Receding contact angle was measured to drop on PLLA-*b*PEA samples to levels resembling PEA (Figure 2.5C), resulting in these samples presenting surfaces of similar chemical mobility to bulk PEA (Figure 2.5D).

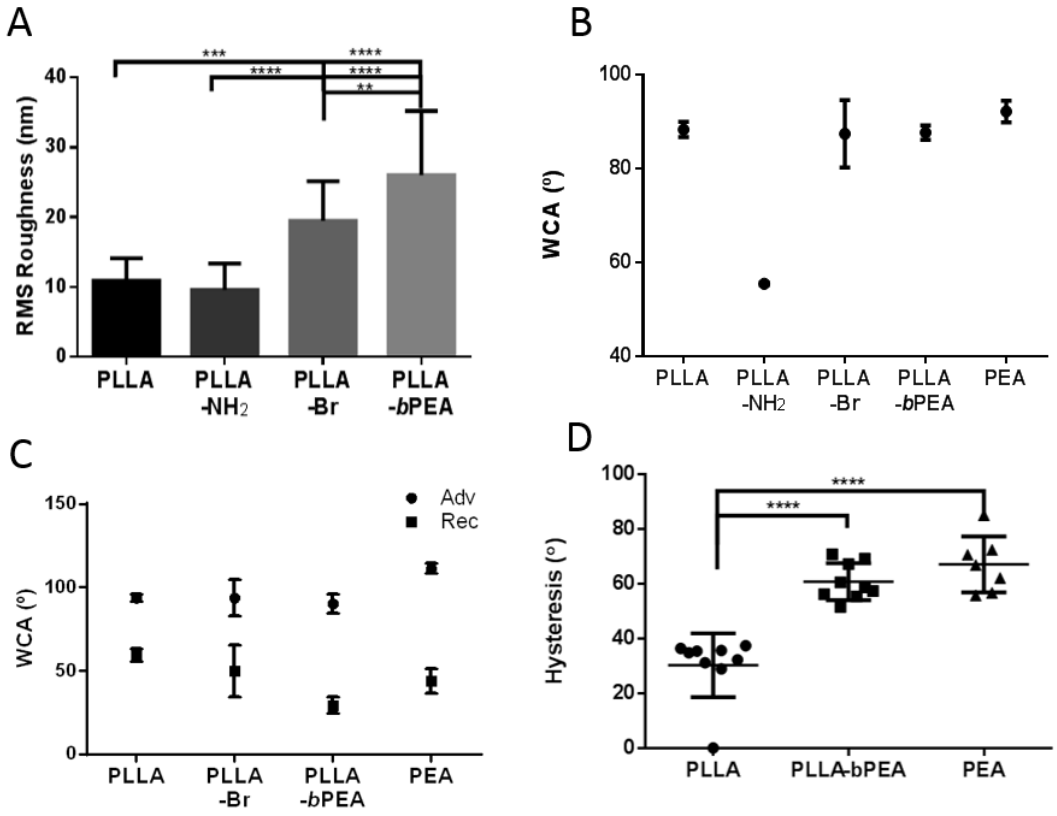

Figure 2.5. Surface characterisation (A) Surface root mean squared roughness measurements of PLLA samples through the entire SI-ATRP process. A minimum of 12 measurements were taken from 5x5 μm^2 AFM scans of each sample **(B)** Static water contact angle characterisation of PLLA, aminolysed PLLA, initiator immobilised PLLA, polymerised PLLA-*b*PEA and spin-coated PEA controls. **(C)** Advancing (Adv) and Receding (Rec) contact angles of spin-coated PLLA, PLLA-Br, PLLA-*b*PEA and PEA. **(D)** Water contact angle hysteresis of pristine PLLA, PLLA-*b*PEA and spin-coated PEA samples. Graphs show mean values and standard deviation. **p < 0.01, ***p < 0.001, ****p < 0.0001.

Having shown that surface modification had successfully altered the chemical composition of the sample surface, it was important to ensure the maintenance of bulk PLLA properties. Enzymatic degradation was investigated using proteinase K; SI-ATRP treated samples were observed to maintain similar percentage weight loss to untreated PLLA after 72 and 96 hours. This highlights that the surface modification does not impact on the bulk hydrolytic degradation and is able to maintain the degradative property of PLLA. Sample stiffness was

measured by a variety of methodologies in either ambient or liquid conditions; these characterisations were performed to ensure that SI-ATRP did not impact the mechanical properties in either of these conditions. Generally mechanical properties were measured to be maintained within the sample MPa range on all PLLA-*b*PEA samples respectively to their PLLA controls: the Young's modulus as measured by DMA (Figure 2.6D) was observed to be 141 MPa (PLLA) and 63 MPa (PLLA-*b*PEA). However as this procedure is performed on whole samples this value may be influenced by fissures or macroscale imperfections of the films. Nanoindentation was performed on the samples, both in air and liquid (Figure 2.6 B and C), to establish the Young's modulus of the polymer without the influence of macroscopic factors. Nanoindentation performed in ambient conditions presented higher Young's modulus values for PLLA (690 MPa) and PLLA-*b*PEA (240 MPa), whereas in liquid they were observed to be similar to those measured by DMA (159 MPa and 91 MPa respectively). This suggests that nanoindentation in air conditions does not account for liquid diffusion and swelling of the polymer, as found in liquid conditions. In any case from these Young's modulus data and enzymatic degradation we can observe that SI-ATRP does not critically impact on the mechanical properties of the bulk PLLA films.

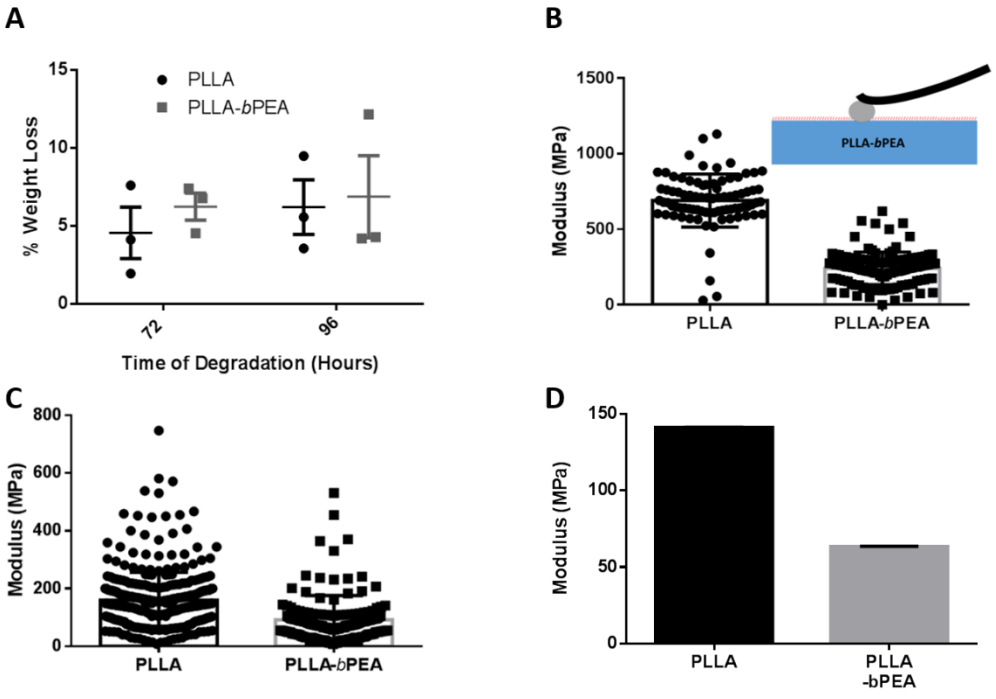

Figure 2.6. Bulk characterisation (A) Percentage weight loss of PLLA and PLLA-*b*PEA samples after 72 and 96 hours of degradation with 0.2 mg mL^{-1} proteinase K at 37°C. **(B)** Elastic modulus of PLLA and PLLA-*b*PEA measured via nanoindentation in air using AFM. Inset shows AFM nanoindentation technique. **(C)** Nanoindentation in liquid. **(D)** Elastic modulus of PLLA and PLLA-*b*PEA at 37 °C measured from dynamic mechanical analysis (DMA) using a DMA 8000 (Perking-Elmer) apparatus at a frequency of 1Hz in tension mode; the temperature range was -150 to 100°C at a rate of 1°C min^{-1}. Young's modulus was determined at 37°C on sample of 10 mm x ~6 mm x 0.05 mm. Graphs show mean values and standard deviation. Graphs show mean values and standard deviation.

2.3.2 Surface chemical composition

X-ray photoelectron spectroscopy was performed to characterise the surface chemical composition of the top <10nm of the samples to confirm functionalization through each step of the SI-ATRP. Carbon (C1s), oxygen (O1s), nitrogen (N1s) and bromine (Br3D) scans were collected from PLLA, PLLA-NH_2, PLLA-Br, PLLA-*b*PEA and spin-coated PEA (Figure 2.7 A-E). Each carbon and oxygen spectra have been fitted with peaks corresponding to binding conformations of the relevant atoms within these samples; the spectra of the intermediate aminolysis and initiator elements show the presence of these elements on the surface of the samples (Figure 2.7 B and C). These scans confirm the incorporation of nitrogen peaks after aminolysis (Figure 2.7 B) and subsequent immobilisation of the bromine based initiator, BIBB (Figure 2.7 C). Bromine to carbon ratios were found to be $3.4 \times 10^{-3} \pm 1.0 \times 10^{-3}$, which indicates a sufficient surface density of initiator to allow for continuous brush coverage after polymerisation (Xu, Yang et al. 2011). It can also be noted that both these elements are removed post polymerisation on PLLA-*b*PEA (Figure 2.7 D), suggesting that these intermediates are removed or masked by the PEA brushes formed on the surface. Observation of the carbon spectra confirm the maintenance of PLLA carbon spectra compositions (Figure 2.7 A), a distinct 3 peak composition (1:1:2) relating to the carbon backbone bonding, carboxyl and ester groups, on PLLA, PLLA-NH_2 and PLLA-Br. This maintenance highlights the specificity of both the aminolysis and initiator

immobilisation reaction, as they are able to incorporate nitrogen and bromine during functionalisation while not significantly altering the chemistry of the bulk PLLA backbone. This is also confirmed by observing the oxygen binding conformation on these samples. PLLA-*b*PEA is observed to have a significantly altered carbon and oxygen spectra comparatively to bulk PLLA (Figure 2.7 D); these spectra possess binding domains similar to control and theoretical PEA (Figure 2.7 E). In fact, PLLA-*b*PEA surfaces was calculated as having similar carbon binding domain ratios as spin-coated PEA, suggesting that PEA has been successfully polymerised onto these samples.

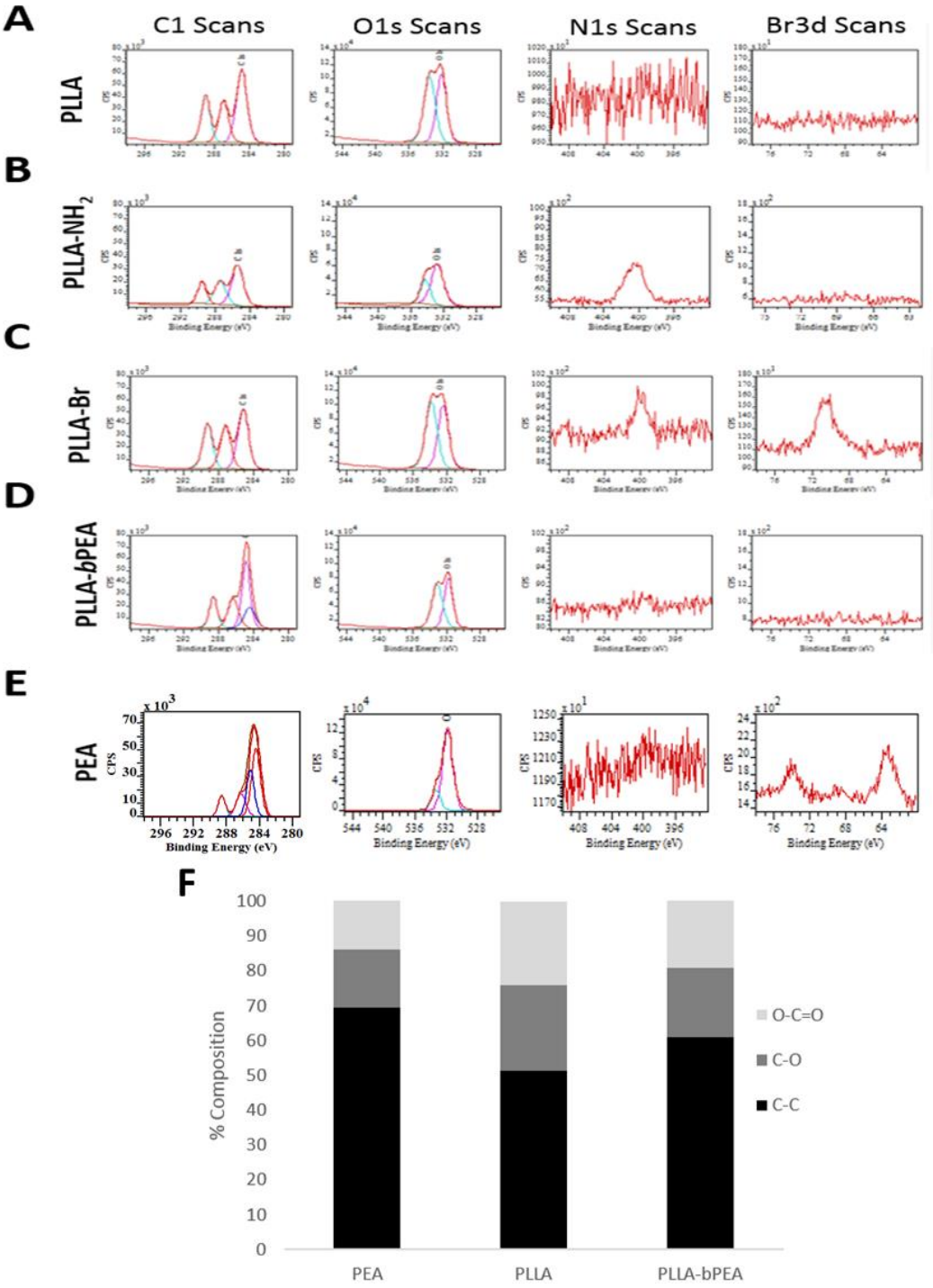

Figure 2.7. C 1s, O1s, N1s and Br3d core-level spectra of all SI-ATRP steps, taken by XPS analysis. (A) Shows the initial untreated PLLA series of spectra. **(B)** Shows the aminolysed sample, a peak can be observed in the nitrogen spectra showing the presence of nitrogen. **(C)** Shows the spectra of PLLA-Br samples. Peaks can be observed in both the bromine and nitrogen spectra indicating the

presence of these elements on the surface of this sample. **(D)** Shows the spectra of PLLA-*b*PEA polymerised for 4 hours. **(E)** Shows the spectra of PEA spin-coated onto glass coverslips. **(F)** Percentage of different binding environments for carbon and oxygen.

Further XPS characterisation confirms the presence of PEA on the surface of PLLA-*b*PEA. Comparing the PLLA, PLLA-*b*PEA and PEA spectra (Figure 2.8 A) illuminates how significant the similarities between PLLA-*b*PEA and PEA spectra are. While PLLA possesses three similar carbon binding peaks (1:1:2 carboxyl group (COO): ester bond (CO): carbon to carbon peaks (CC)), both PLLA-*b*PEA and PEA possess 4 distinct chemical binding domains; these almost identical spectra possess a tertiary carbon to carbon binding peak not present in PLLA. The presence of this PEA sidechain peak on PLLA-*b*PEA, as well as the distinctive binding ratios of the other carbon peaks, confirm the successful polymerisation of PEA brushes onto the surface of PLLA. The oxygen peaks found on PLLA-*b*PEA signify that the underlying PLLA backbone remains and that this coverage of PEA is not 100% over the top 10nm. This was further confirmed by analysing the changes in surface chemical composition during polymerisation (Figure 2.8 B). Peak fitting PLLA-*b*PEA spectra produced at two time points of polymerisation (2 or 4 hours) with control PLLA and PEA spectra allows for the estimation of the amount of each polymer on each surface. These results show increased estimated PLLA ratios on 2 hour PLLA-*b*PEA and conversely a higher concentration of PEA than PLLA on 4 hour PLLA-*b*PEA. In fact, it was calculated that increased time of polymerisation directly increased the PEA percentage, 40% at 2 hours and 60% at 4 hours (Figure 2.8 C). Therefore from these XPS scans we are able to confirm the successful polymerisation of PEA brushes onto the PLLA surface and we have identified that increased time of polymerisation directly regulates the density of acrylate brushes on these samples.

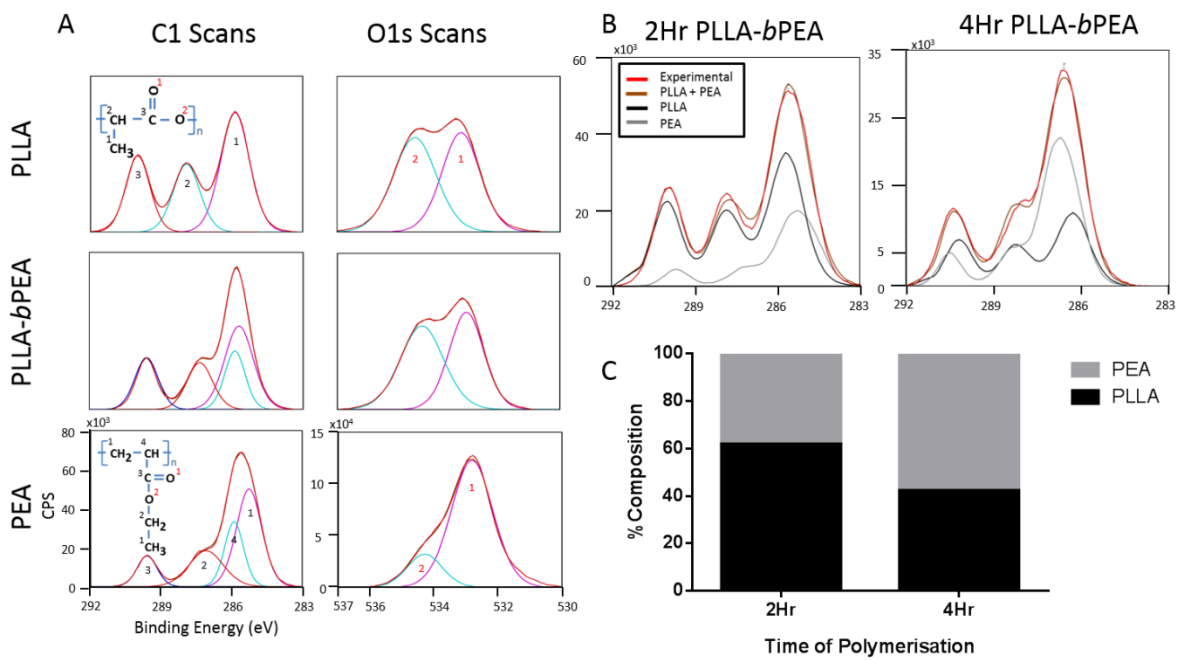

Figure 2.8. Chemical composition of the surface. (A) C 1s and O1s core-level spectra of PLLA, PLLA-*b*PEA (after 4 hours of polymerisation) and spin-coated PEA taken by XPS analysis. Each fitted peak represents a binding conformation of carbon atoms on the top 10 nm of the sample surface. From left to right the carbon peaks represent carboxyl group (COO), ester bond (CO) and carbon to carbon peaks (CC), PEA and PLLA-*b*PEA possess two C-C peaks which represent the polymer backbone carbons with and without sidechains. From left to right the oxygen peaks correspond to the ester bond and carboxyl group within the polymers. Peaks are numerically labelled corresponding to representative chemical structure insets. **(B)** C 1s core-level showing quantification of polymer line-shape elements for PLLA-*b*PEA after a 2 hour or 4 hour polymerisation, using the spectra obtained from control PLLA and PEA as components during line fitting. The bright red line corresponds to the experimental spectra for each sample. The line shapes are as follows: black line shows the PLLA carbon spectra, the grey line represents the PEA spectra, brown is the combined spectra of PLLA, PEA. **(C)** The calculated percentage of each polymer component (PEA or PLLA) in PLLA-*b*PEA samples acquired from polymer component peak fitting analysis software.

2.4 Discussion

A developing field in biomedical engineering research is the improvement of established biomaterials through methodologies of surface modification (Roach, Eglin et al. 2007, Khan, Tanaka et al. 2015, Khan and Tanaka 2017). These investigations aim to provide additional functionality to the surface through a variety of techniques (Zhu, Gao et al. 2004, Dalby, Gadegaard et al. 2014); however a significant challenge in this task is the maintenance of desirable bulk characteristics of the modified biomaterial. Here we present the development and optimisation of a tuneable, scalable and potentially translatable surface modification technique for the addition of advanced functionality to PLLA via the addition of PEA brushes. The inclusion of these PEA brushes via SI-ATRP was developed to provide optimal functionalization while maintaining desirable PLLA properties. This will ideally provide a new platform for mimicry of *in vivo* cellular microenvironments for regenerative medicine applications.

The SI-ATRP protocol described here was designed to grow PEA brushes onto PLLA. The general SI-ATRP system is well documented and allows for production of a highly tuneable procedure, able to control a variety of properties, including initiator density, surface roughness and architecture (Liu and Roy 2005, Liu and Su 2005, Khabibullin, Mastan et al. 2016). This specific reaction was optimized via the addition of an activator regeneration electron transfer mechanism during polymerisation which provided reduction of time, temperature and concentration of reagents used, improving the efficiency of the produced reaction (Zoppe, Ataman et al. 2017). By utilising tris(2-pyridylmethyl)amine, a neutral tripodal nitrogen-based ligand, able to form complexes with both copper and bromine allowed for the stabilization, regeneration and increased reduction potential of the copper (I) oxidation state (Kaur, Ribelli et al. 2015). By optimizing the steps of SI-ATRP and the characteristics of the produced PLLA samples, we were able to obtain PLLA-*b*PEA samples of defined characteristics designed for regenerative medicine purposes.

Surface modification was characterised through several methodologies, to determine significant alterations to the bulk PLLA film. Initially it was noted that surface topology was significantly altered with elongated time of aminolysis (Figure 2.4A); however this step was optimized to minimize this variation. The optimization of aminolysis provided a well-defined, high concentration of amine groups on the surface to continue the SI-ATRP procedure (Figure 2.4). Initiator immobilisation was observed to drastically increase RMS surface roughness (Figure 2A), as the incorporation of bromine initiator was calculated as the primary SI-ATRP step to introduce surface roughening on PLLA. This was suspected to be a by-product of this exothermic reaction proceeding at undefined temperatures, potentially stressing the base polymer and resulting in degradation. While it has been shown that nanotopographical features are able to modulate cellular interactions (Dalby, Gadegaard et al. 2014, Mpoyi, Cantini et al. 2016), here we attempted to minimize unnecessary variations to bulk PLLA surfaces, hence the optimization of aminolysis time. While the surface roughness does significantly increase post initiator immobilisation, the inherent properties of this reaction produce a certain degree of heat to function therefore it would be detrimental to the overall efficacy of SI-ATRP to further optimize initiator immobilisation to reduce roughening. RMS roughness was observed to increase on PLLA-*b*PEA samples, as a results of the formation of PEA polymer brushes on the surface (Zhu, Zhang et al. 2002). While roughness was optimized, it may still present an issue in further characterisation of surface interactions via AFM and therefore for further protein characterisation (Chapter 3) spin-coated PLLA-*b*PEA samples were produced with initially lower RMS roughness than purchased PLLA films.

As designed and expected, PLLA surface chemistry was observed to vary significantly through the SI-ATRP process. Chemical priming of the surfaces, by aminolysis, incorporated hydrophilic amine groups into the PLLA backbone, reducing the hydrophobicity of these samples (Figure 2.4 B and C). Immobilisation of bromine based initiators was observed to remove this additional hydrophilicity, increasing the WCA, which was subsequently maintained upon polymerisation of hydrophobic PEA brushes (Figure 2.5B). The inclusion of PEA onto PLLA films was observed to increase the surfaces WCA hysteresis, indicating enhanced molecular mobility as result of the inclusion of polymer brushes and surface roughness (Zhu,

Gao et al. 2004, Liu, Du et al. 2007). These chemical modifications were further confirmed via chemical analyses utilising XPS. Analysis of each intermediate PLLA sample highlighted the efficacy of the 3 steps of SI-ATRP; clear nitrogen and bromine peaks were identified on aminolysed and initiator immobilised samples, respectively (Figure 2.7 B and C). The introduction of these elements showing successful surface modification and the subsequent utilisation and removal of these peaks on PLLA-*b*PEA are further proof of the efficacy of the polymerisation procedure (Figure 2.7 D). In fact, by calculating the amine density and bromination of the surfaces, in accordance with other studies demonstrating the tuneability of ATRP reactions for optimised brush length and density (Xiao and Wirth 2002, Ohno and Matyjaszewski 2006, Kang, Crockett et al. 2014), it is possible to further characterise the homogeneity of PLLA-*b*PEA surfaces. In accordance to these studies we can note that the PLLA-*b*PEA samples presented here possess a sufficient surface density of amine groups (~1.6×10^7 mol cm^{-2}) and subsequently of bromine-based initiator groups ((Br)/(C) of ~3.4×10^{-3}) to achieve continuous brush coverage (Xu, Yang et al. 2011).

Further XPS analysis of PLLA-*b*PEA surfaces show that PEA brushes formed through SI-ATRP, on the top 10 nm of the polymer, possess carbon binding spectra that closely resemble those of bulk PEA, polymerised via photoinitiated radical polymerisation (Figure 2.8 A). PLLA-*b*PEA surfaces present carbon binding conformations that, when peak-fitted, not only possess the same ratios of binding domains as PEA (1:1:3) as opposed to PLLA (1:1:2), but possess an additional peak corresponding to PEA sidechains. The inclusion of this sidechain and the spectra shape of PLLA-*b*PEA show that PEA is successfully polymerised onto the surface of PLLA samples during SI-ATRP. Additionally, the production of full PEA chains with no loss of individual binding environments upon polymerisation, which is indicative of fragmentation of the polymer chain (Yasuda and Yasuda 2000), suggests an improved surface modification from other established methodologies, such as plasma polymerisation (Chu, Chen et al. 2002, Cantini, Rico et al. 2012, Cheng, Alba-Perez et al. 2019). However, while the EA molecules are not fragmented during polymerisation, PLLA-*b*PEA samples do not possess identical spectra to PEA. Slight variations in the carbon spectra, lower densities of the tertiary carbon binding peak and altered oxygen spectra indeed correspond to the underlying PLLA

film, indicating that PEA brush thickness is <10 nm. This was observed to correlate directly to the duration of the polymerisation, as a longer time was shown to increase surface percentages of PEA relative to PLLA on the surface. Therefore here we have shown the successful incorporation of chemical elements via each step of SI-ATRP and the characterisation of a time-dependent production of grafted PEA chains onto PLLA films.

Investigation of the bulk mechanical properties and degradation rates were investigated and no significant variations from untreated PLLA were encountered, suggesting that PLLA treated with SI-ATRP is still a viable structurally supportive polymer. Degradation rates and Young's modulus were maintained within the same range between PLLA and PLLA-*b*PEA (Figure 2.6). Young's modulus was measured locally, via AFM nanoindentation, and macroscopically, via dynamic mechanical analysis, in either air or liquid conditions. While differences were noted between methodologies, accounting for macroscopic fractures potentially incorporated during aminolysis and swelling of the polymer (Zhu, Gao et al. 2004), the general behaviour confirmed no excessive variation of the Young's modulus before and after SI-ATRP. The retention of similar PLLA degradation rates imply that PLLA-*b*PEA samples, like the untreated biomaterial, are able to act as a supportive structural scaffold *in vivo*, gradually reintroducing physical function to cells during regeneration in a tuneable manner (Ulery, Nair et al. 2011). These properties are ideal for *in situ* bone regenerative purposes: retention of Young's' modulus and of the degradation rate, allowing to provide adequate structural support for a controllable time (Armentano, Dottori et al. 2010, Saito, Liao et al. 2013, Wang, Wang et al. 2016). Therefore, the SI-ATRP system outlined here is able to provide a highly specific surface modification which do not significantly alter the bulk characteristics of the structural PLLA backbone.

While PLLA is often modified in aid of improving cellular interactions and biological activity these modification techniques have been shown to impact on the mechanical properties of the bulk PLLA. Processes such as etching (Kramer, Kunkemoeller et al. 2014), chemical modification (Zhu, Gao et al. 2004), blending (Xiao, Wang et al. 2011) and UV treatment (Janorkar, Metters et al. 2007), have

been utilised to improve cellular interactions on PLLA. However, several of these processing techniques drastically alter the mechanical properties, such as poor mechanical strength and altered degradation rates. Processing techniques to improve the mechanical properties such as co-polymerisation with poly (glycolic acid), while improving the co-polymer strength present their own issue, such as stress shielding and decreased cellular proliferation (Athanasiou, Niederauer et al. 1996), and therefore require further processing (Gentile, Chiono et al. 2014). Therefore techniques such as the plasma treatment, which has been shown not to affect bulk structural mechanics (Xiao, Wang et al. 2011) and SI-ATRP as described within this thesis, present methodologies for modifying biological activity of PLLA while retaining bulk physical properties. These systems allow for the inclusion of thin polymer layers or brushes onto the surface of biodegradable polymers, without altering the mechanical properties. In this and previous studies, PEA has been incorporated onto the surface of biodegradable polymers, such as PCL (Cheng, Alba-Perez et al. 2019). The plasma polymerisation of PEA onto the surface of PCL was shown to improve protein interactions, driving FN fibrillogenesis, and facilities enhanced cellular adhesion and osteogenic differentiation (Cheng, Alba-Perez et al. 2019). However, a main disadvantage of plasma-based surface modification of PLLA is surface rearrangement of the bulk polymer chains caused by thermally activated macromolecular motion, potentially impacting on the degradation rate (Xiao, Wang et al. 2011). Additionally, PEA polymerised onto these surfaces were altered, via plasma fragmentation (Cantini, Rico et al. 2012), resulting in chemically modified PEA surfaces. Our system of SI-ATRP has been shown to successfully modify PLLA with nanoscale, chemically unmodified PEA brushes, without impacting on the bulk mechanical properties as would be found utilising other modification techniques.

2.5 Conclusion

This chapter has outlined the development of a novel SI-ATRP process, able to produce defined and controlled modifications of the surface of an established biomaterial, PLLA. While this system introduces functional PEA brushes onto the surface of PLLA, it does so while maintaining the bulk characteristics of the

backbone polymer, such as controlled degradability and mechanical strength. Hence, this SI-ATRP surface modification methodology provides a tuneable and scalable technique to enhance the interfacial interactions of established biomaterials.

3. Fibronectin organisation and cell response on PLLA-*b*PEA

3.1. Introduction

To establish the efficacy of the engineered PLLA-*b*PEA surfaces, the interaction of the PEA brushes with proteins, namely fibronectin (FN), and their ability to influence cellular interactions was investigated. The ability of PEA to drive fibrillogenesis of fibronectin, leading to the assembly of elongated fibrils and eventually nanonetworks, allows the exposure of cryptic cellular binding domains that favour cellular interactions (Schwarzbauer and Sechler 1999, Salmeron-Sanchez, Rico et al. 2011, Cantini, Gonzalez-Garcia et al. 2012, Llopis-Hernandez, Rico et al. 2013). Therefore, having confirmed the production of PEA brushes onto PLLA films via surface initiated atomic transfer radical polymerisation, we proceeded to investigate the ability of the produced polymer microenvironments to drive FN fibrillogenesis. Furthermore, the ability of the produced surfaces to facilitate cellular adhesion and differentiation upon coating with FN was investigated. Indeed, while the ability of FN nanonetworks formed on PEA surfaces to favourably expose binding domains (Vanterpool, Cantini et al. 2014) has been previously demonstrated, here we aim to determine whether PLLA-*b*PEA surfaces retain this ability of bulk PEA and the corresponding cellular behaviour. In particular, C2C12 murine mouse myoblast cells were utilised as a cell model as they have been shown to favourably bind to FN nanonetworks on PEA and possess the potential to differentiate through distinct lineages according to defined stimuli; more specifically, they have the ability to form myotubes *in vitro* (Salmeron-Sanchez, Rico et al. 2011, Bathawab, Bennett et al. 2016). Cellular adhesion, characterised by the formation and maturation of focal adhesion complexes, and contractile-dependent differentiation were utilised to determine the functionality of the PEA brushes and their ability to drive enhanced cellular interactions on PLLA. Ultimately, in this chapter we aim to provide a direct characterisation of the efficacy of SI-ATRP in producing enhanced biocompatible materials for regenerative medicine applications.

3.2 Materials and methods

3.2.1. Materials: Poly (L-Lactide) films (thickness 50 μm) were purchased from Goodfellow (Huntingdon, UK), PLLA granules (Cargill Dow) provided by prof. Gloria

Gallego Ferrer (CBIT, UPV). 1,6-hexanediamine (98%), 2-propanol (≥99.5%), 2-bromoisobutyryl bromide (BIBB, 98%), anhydrous pyridine (Py, 99.8%), anhydrous hexane (95%), copper(I) bromide (CuBr,99.999 %), Tris(2-pyridylmethyl)amine (TPMA, 98%), ethyl acrylate (EA, 99.5%), methanol (99.99%), ascorbic acid (AsAc) were purchased from Sigma Aldrich, Dorset, UK. Glass reaction vessels were custom-made. Spin-coated PEA controls (PEA) were prepared on 12 mm glass coverslips from 4% solutions in toluene of bulk PEA, obtained via polymerisation of EA using 1% benzoin (Sigma, St. Louis, MO) as a photonitiator, spun at 3000 rpm with acceleration of 3000 rpm s^{-1} and vacuum dried at 60ºC for 2 hours to remove excess toluene.

3.2.2. Spin-coating: Spin-coated PLLA samples (scPLLA) were prepared by first treating 12mm glass cover slips with hexamethyldisilazane (HMDS) and then a 2% PLLA solution in chloroform was spun at 2000 rpm with an acceleration of 3000 rpm s^{-1}. ScPLLA samples were then aminolysed as previously described and washed with milliQ water for 6 hours and subsequently air dried. Initiator immobilisation was performed for 6 hours without agitation, samples were then washed with gentle pipetting of water and methanol 2:1 mix and air dried. Polymerisation was performed as before with the exemption of soxhlet washing, instead spin-coated samples were washed carefully by hand. ScPLLA and scPLLA-*b*PEA were used to observe FN conformation via AFM (Figure 3.3 A).

3.2.3. Protein adsorption: Fibronectin (R&D Systems) solutions of 20 µg mL^{-1} in Dulbecco's phosphate buffered saline (DPBS) were adsorbed onto samples for 1 hour for all applications unless otherwise stated. Samples were rinsed with DPBS before use.

3.2.4. FITC-FN labelling: FN was labelled using the DyLight™ 488 NHS Ester (ThermoFisher), following manufacturer instructions. Briefly, 1 mg fibronectin powder (Sigma-Aldrich) was dissolved in 0.05 M sodium borate at pH 8.5 (Thermo Scientific). DyLight™ 488 NHS Ester was dissolved in 10 mg mL^{-1} DMF. The protein to be labelled was incubated with labelling ester at room temperature within a dialysis membrane chamber for 4 hours with 3 dialysis buffer replacements.

3.2.5 Atomic force microscopy: Atomic Force Microscopy was used to quantify surface roughness and visualise topology before and after FN coating in all conditions on dried samples in air. FN-coated samples were rinsed with water after FN adsorption and gently dried with a nitrogen flow. For AFM imaging of FN in liquid, sample were not dried, but rather washed with DPBS and MilliQ water before being fixed with 4% formaldehyde at room temperature for 20 minutes. Height and lock-in phase images were taken in AC mode using a Nanowizard 3 Bioscience AFM (JPK, Berlin Germany). Scans were made using cantilevers with a resonance frequency of 75 kHz and a force constant of 3 N m^{-1} (MPP-21120 from Bruker, Billerica, MA). Fractal dimension analysis was carried out on the 1x1 μm2 images of FN-coated samples using the ImageJ Fractal box count analysis tool, using box sizes of 2, 3, 4, 6, 8, 12, 16, 32, and 64 pixels.

3.2.6. Water contact angle: Water contact angle measurements were undertaken on PLLA and functionalised samples. Static contact angles (SCA) were measured by dropping 3 μL of deionised water onto the samples. Advancing (ACA) and receding (RCA) contact angles were measured by the addition or removal of water to the droplet until an increase or decrease in the length of the baseline was observed. Contact angle hysteresis was calculated from the difference between ACA and RCA. Analysis was conducted using a Theta optical tensiometer (Biolin Scientific, Stockholm, Sweden).

3.2.7. Micro-bicinchoninic acid protein quantification: The density of adsorbed protein was determined by measuring the amount of non-adsorbed FN. A standard curve was created via serial dilutions of a FN stock of known concentration. Samples were coated for 1 hour and the remaining FN solution was transferred to 96-well plates, where the bicinchoninic acid working reagent was added (Thermo Fisher Scientific, Waltham, MA). The plate was then agitated and incubated at 37°C for 2 hours. The absorbance was read at 562 nm with a Tecan NanoQuant Infinite M200 Pro plate reader (Männedorf, Switzerland).

3.2.8. In-Cell Western: Binding domain availability on samples was examined using in-cell western (ICW). Fibronectin coated samples were blocked with Odyssey blocking buffer (LICOR) and incubated with primary antibody, HFN7.1 (DSHB, Iowa City, IA) or mAb1937 (Millipore) in blocking buffer for 1 hour. Samples

were then washed 5 times with agitation in 0.1% v/v Tween20/PBS. IRDye® 800CW antibodies were then prepared in blocking buffer and samples were incubated for 1 hour. After washing as before and drying, measurements were made at 800 nm using an Odyssey® system.

3.2.9 C2C12 culture: Mouse C2C12 myoblasts were thawed and re-suspended in Dulbecco's modified Eagle's medium (DMEM, high glucose, without pyruvate) with 1% v/v penicillin/streptomycin and 20% v/v foetal bovine serum (FBS). Cells were incubated in 37°C, 5% CO_2, and harvested by trypsinisation at 70% confluency.

For adhesion experiments, samples were sterilized under a UV lamp for 40 minutes on each side, as the samples are opaque, and coated with 20 μg mL^{-1} FN; negative controls were coated with PBS for 1 hour. Samples were then washed with PBS and seeded with 5000 cells cm^{-2} for 4 hours and then fixed with 4% formaldehyde for 30 minutes at 4°C. The cells were then permeabilised with 0.1% triton X-100, washed and finally blocked (PBS/BSA1%) for 30 minutes at room temperature. Samples were first incubated with anti-vinculin primary antibody (1:400), hVIN-1 (Sigma-Aldrich), in blocking buffer for 1 hour at room temperature and subsequently washed with washing buffer, PBS/Tween 20 0.5%. Cy3-conjugated secondary antibodies (Jackson ImmunoResearch) and BODIPY FL Phallacidin (Thermo Fisher Scientific) were then added for 1 hour at RT. The samples were then washed and mounted with mounting medium containing DAPI (Vector Laboratories, Inc.) and visualised with a fluorescence microscope (Zeiss AxioObserver Z1). Images were merged using ImageJ to localise nuclei and actin. Focal adhesions were analysed using the vinculin stain images; the procedure is described in Horzum et al. Images were analysed with threshold area of 0.5 μm^2 and 0-0.99 circularity.

For differentiation assays, samples were UV sterilised; collagen controls were obtained by coating sterile coverslips with 1 mg mL^{-1} ColI (Stem Cell Technologies, Cambridge, UK) and subsequently all samples were coated with 20 μg mL^{-1} FN for 1 hour. Cells were then seeded on the samples at 20,000 cells cm^{-2} for 3 hours in DMEM +1%P/S. This was then replaced with differentiation media after 3 hours and again after 2 days (DMEM +1%P/S +1%ITS-X, Life Technologies). 10μM Blebbistatin was used as contractility inhibitor and added after 3 hours of

culture. After 4 days of culture the cells were washed and fixed with 20:2:1 EtOH 70%/formaldehyde 37% acetic acid for 10 minutes at 4°C. Cells were then washed with PBS and blocked with 5% goat serum in PBS. Cells were then incubated with MF20-b antibody (Developmental Studies Hybridoma Bank, University of Iowa, USA) for 1 hour and washed, blocked and stained with a Cy3-conjugated antibody for 1 hour at 37°C. Samples were then mounted with mounting medium containing DAPI and imaged. ImageJ was used to capture and merge the images. Cell density and cell differentiation were calculated using CellC image analysis software (http://www.cs.tut.fi/sgn/csb/cellc/, Selinummi et al., 2005).

3.2.10. Statistical analysis: Pre-processing and normalization of data are stated in the individual methods sections. Analysis of statistical differences was conducted using student T-test (Graphpad) for two sample comparison and One-way ANOVA for different groups using a Turkey HSD *post hoc* test to compare different groups. Differences were considered significant *$p < 0.05$, **$p < 0.01$, ***$p < 0.001$, ****$p < 0.0001$. All data presented are mean values, error bars are standard deviation and n numbers are noted in the figure captions.

3.3 Results

3.3.1. Surface characterisation

To determine the functionality of the PEA produced via SI-ATRP surface characteristics were investigated post treatment with 20 μg mL^{-1} fibronectin. PLLA and PLLA-*b*PEA surfaces were observed to have lower RMS surface roughness after FN treatment (Figure 3.1 A), due to the protein covering the surface and diminishing the measured roughness of the samples. Static water contact of FN-treated samples was measured to be maintained within the same range on all samples as before FN treatment (~90°) (Figure 3.1B), showing no distinct variation of hydrophobicity due to protein adsorption. However, dynamic water contact angle analysis presented an overall decrease of receding contact angle resulting in a similar surface hysteresis on all surfaces (Figures 3.1C and D). This suggests

that treatment with this concentration of FN is able to fully cover the surface of all the samples, which present a FN mediated surface mobility regardless of the surface type.

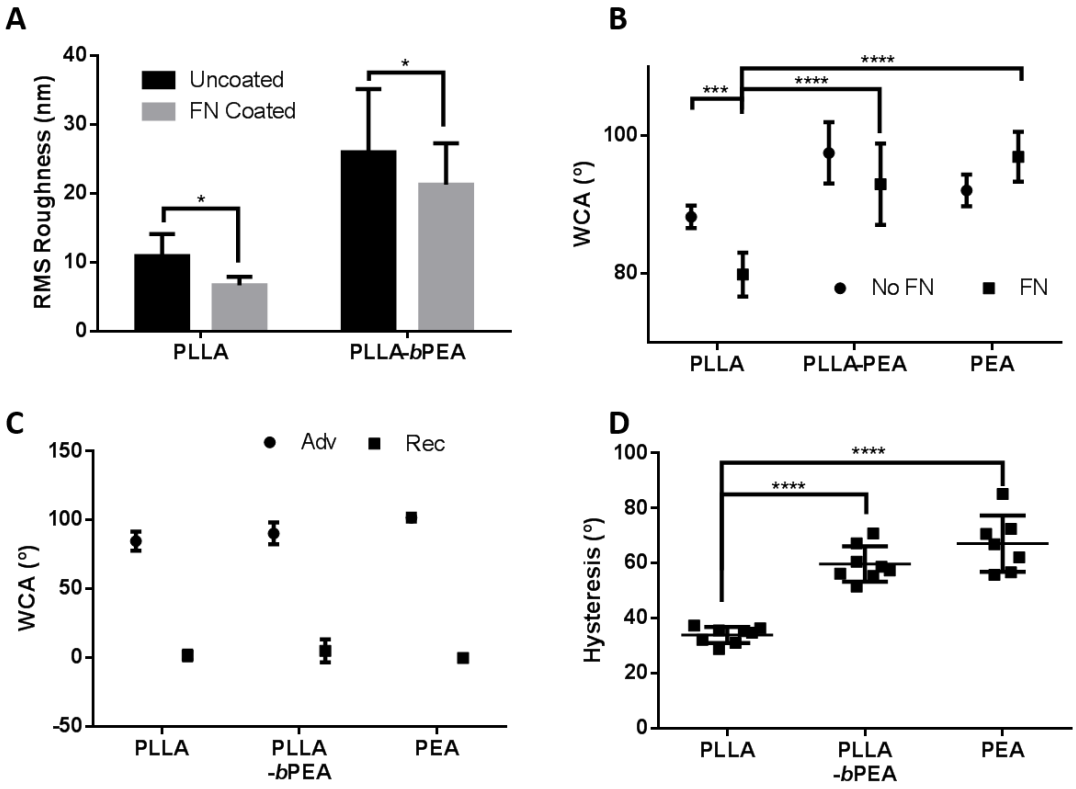

Figure 3.1. Comparison of FN treated surfaces (A) Surface root mean squared roughness measurements of PLLA and PLLA-*b*PEA samples with and without fibronectin coating. **(B)** Static water contact angle characterisation of spin-coated PEA controls, PLLA and polymerised PLLA-*b*PEA after FN adsorption. **(C)** Advancing (Adv) and Receding (Rec) contact angles of FN treated PLLA, PLLA-*b*PEA and PEA. **(D)** Water contact angle hysteresis of FN coated PLLA, PLLA-*b*PEA and spin-coated PEA samples. Graphs show mean values and standard deviation. *p < 0.05, ***p < 0.001, ****p < 0.0001.

3.3.2. FN assembly

To investigate FN organisation on the surfaces, fluorescently tagged FN was produced and adsorbed onto the samples. Homogeneous layers of fluorescent FN

were observed on PLLA surfaces, whereas PEA and PLLA-*b*PEA surfaces were observed to trigger the organisation of protein into fibrils interconnecting into network structures. Of these networks two different conformations can be noted; larger networks (Figure 3.2A), predominantly found on higher concentrations of FN, and smaller networks observed on lower concentrations (Figure 3.2B). The presence of FN networks on PLLA-*b*PEA suggests that PEA brushes on these surfaces are as functional as bulk PEA and able to drive fibrillogenesis. However, we have previously observed that SI-ATRP increases the surface roughness of PLLA and this underlying topology may contribute to the perceived microscopic conformation of FN on these surfaces.

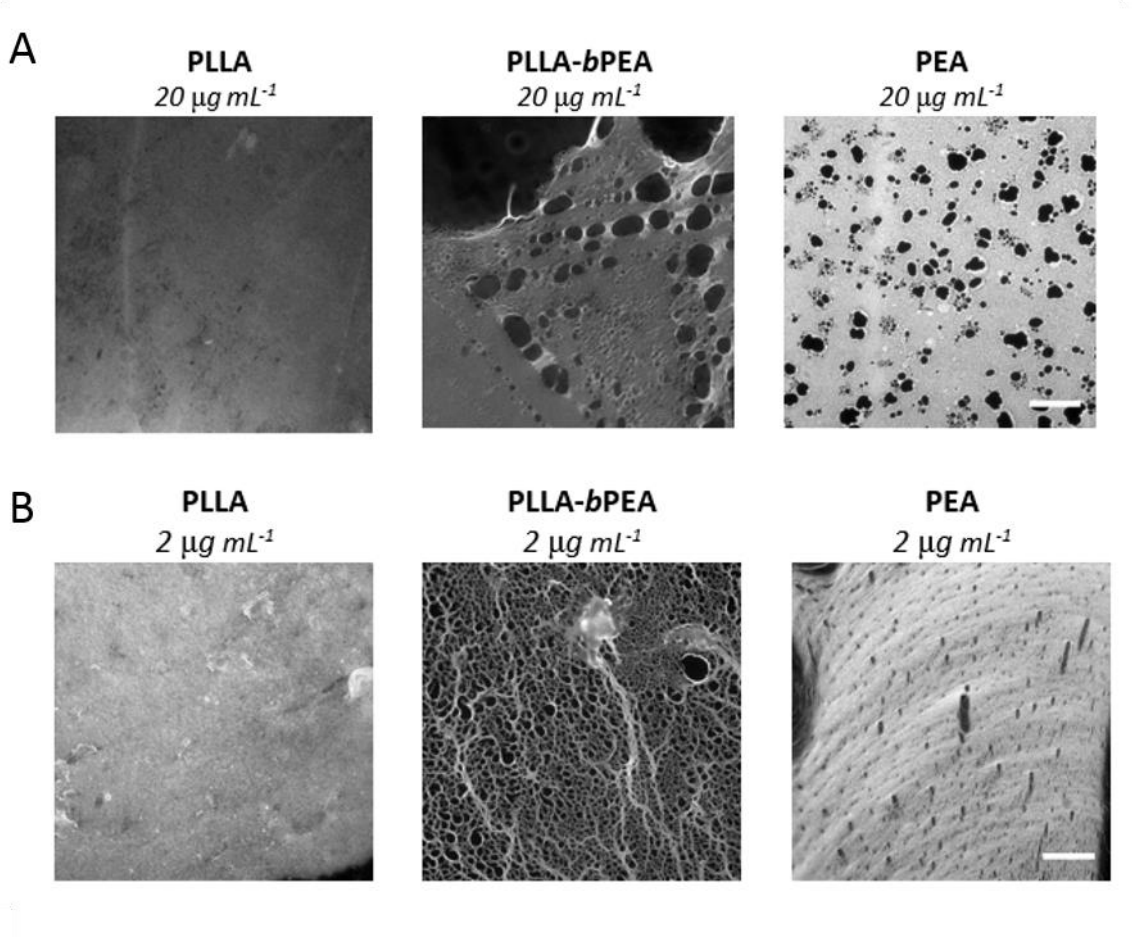

Figure 3.2. Adsorption of FITC-labelled FN. Samples of PLLA, PLLA-*b*PEA and PEA coated with **(A)** 20 μg mL^{-1} or **(B)** 2 μg mL^{-1}. Samples were coated with fibronectin-FITC in DPBS for 1 hour at room temperature, washed with DPBS and visualized under a fluorescent microscope after mounting. FN was labelled using the DyLight™ 488 NHS Ester (ThermoFisher), following manufacturer instructions.

Fibronectin networks can be observed throughout the samples with the exception of PLLA. Scale bar is 20μm.

Hence, to further confirm the presence of FN networks on the surface of SI-ATRP-treated PLLA samples atomic force microscopy was utilised, so as to visualise surfaces at the nanoscale and investigate more accurately the organisation and structure of the adsorbed FN molecules. Since we have previously noted increasing surface roughness on PLLA-*b*PEA samples (Figure 2.4 A), this roughness was speculated to prevent the ability to properly visualise the FN fibrils and nanonetworks via AFM. Indeed, the roughness in the same order of magnitude as the protein features to be visualised, both ~40 nm (Gugutkov, Gonzalez-Garcia et al. 2009), therefore FN features would be harder to distinguish via height scans. On flatter regions of PLLA-*b*PEA films small areas that resembled dense FN nanonetworks were observed in both height and phase scans, however these features could not be definitively distinguished due to surrounding surface roughness. The presence of these potential FN fibrils suggested that high RMS roughness was masking FN features on the PLLA-*b*PEA films. Therefore, spin-coated PLLA was instead treated with SI-ATRP. Spin-coated PLLA samples were initially smoother and, post polymerisation, these PLLA-*b*PEA samples possessed significantly lower RMS roughness than the films (5.77 nm ± 1.2 nm vs. 25.71 nm ± 8.16 nm). Therefore for all subsequent AFM imaging scPLLA and scPLLA-*b*PEA samples were used. AFM imaging confirmed that PLLA-*b*PEA surfaces were able to trigger FN assembly upon adsorption, similarly to PEA. FN fibrillogenesis, indicated by the presence of FN nanonetworks, was observed on PLLA-*b*PEA and PEA, whereas no such structures were present on PLLA, where FN remained in a flat monolayer (Figure 3.3 A). Nanonetworks formed on PLLA-*b*PEA were observed to be thicker and less interconnected, as confirmed by the decreased fractal dimension comparatively to FN on PEA. Fractal analysis of the AFM scans, used as a measure of connectivity of the protein network, showed that, while both PLLA-*b*PEA and PEA presented FN nanonetworks which possessed fractal properties, there were slightly lower levels of interconnection of on the PEA brushes compared to bulk PEA (Figure 3.3 B). The presence of FN nanonetworks on PLLA-*b*PEA proves that the PEA brushes retain the bio-functionality of bulk PEA to regulate FN secondary structure, through the same material driven fibrillogenesis

mechanism; however, due to the conformation and surface presentation of PEA in brush form, these nanonetworks possess altered characteristics.

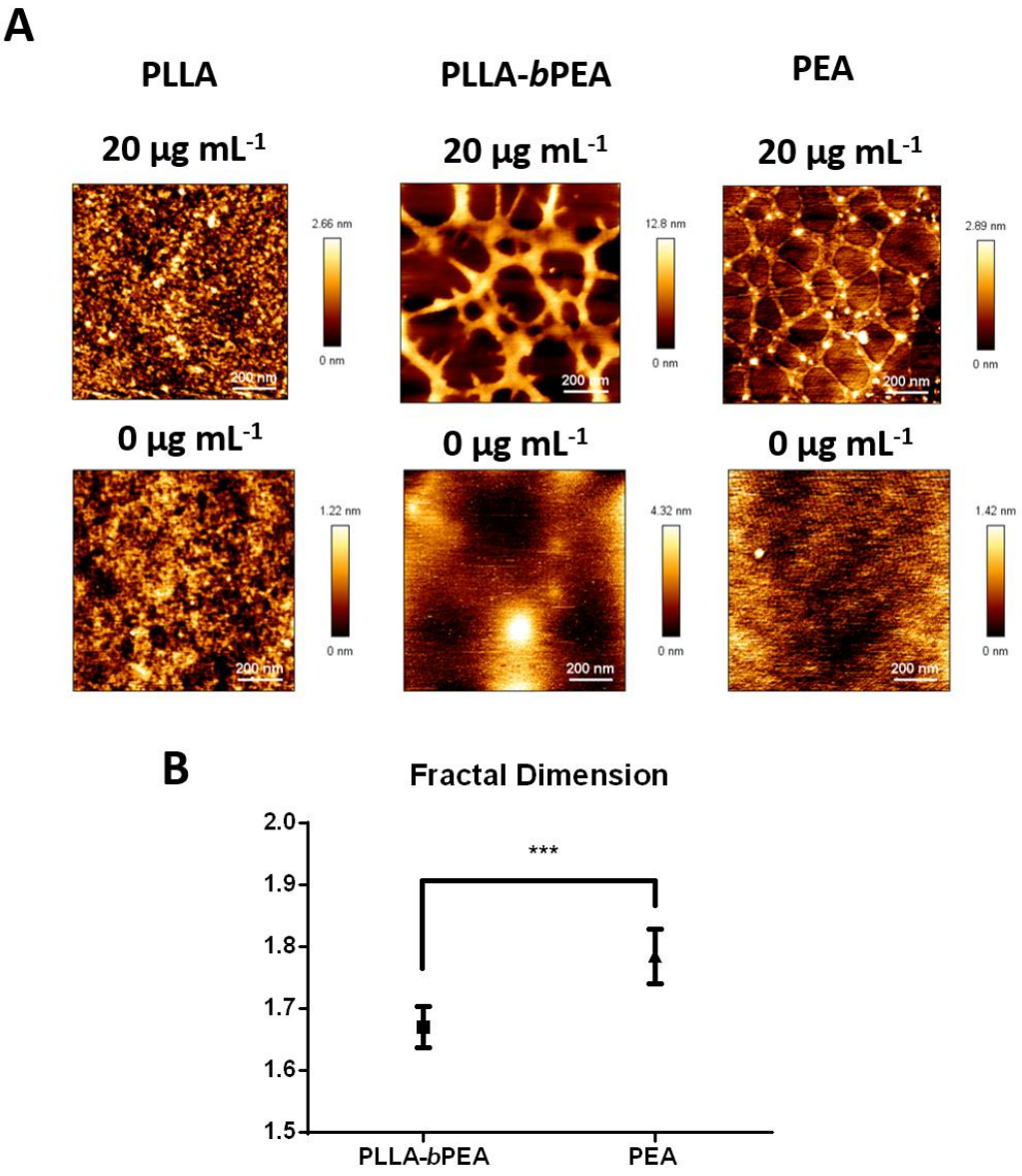

Figure 3.3. AFM Imaging of adsorbed FN on samples. (A) Height images from tapping mode AFM of spin-coated PLLA (scPLLA), scPLLA-*b*PEA and PEA coated with 20 and 0 µg mL^{-1} FN for 1 hour at room temperature. Scale bar is 200 nm. Please note that the colour scale is different for every image, as indicated, to allow clear visualisation of the surface features. **(B)** Fractal analysis of FN nanonetworks found on scPLLA-*b*PEA and PEA.

Further characterisation of the FN fibres produced on PEA brushes confirmed that these features as well as generally being thicker are also taller

than nanonetworks on PEA (Figure 3.4). Indeed, FN fibrils on PEA brushes presented increased average height and peak-to-valley roughness (Figure 3.4B and C).

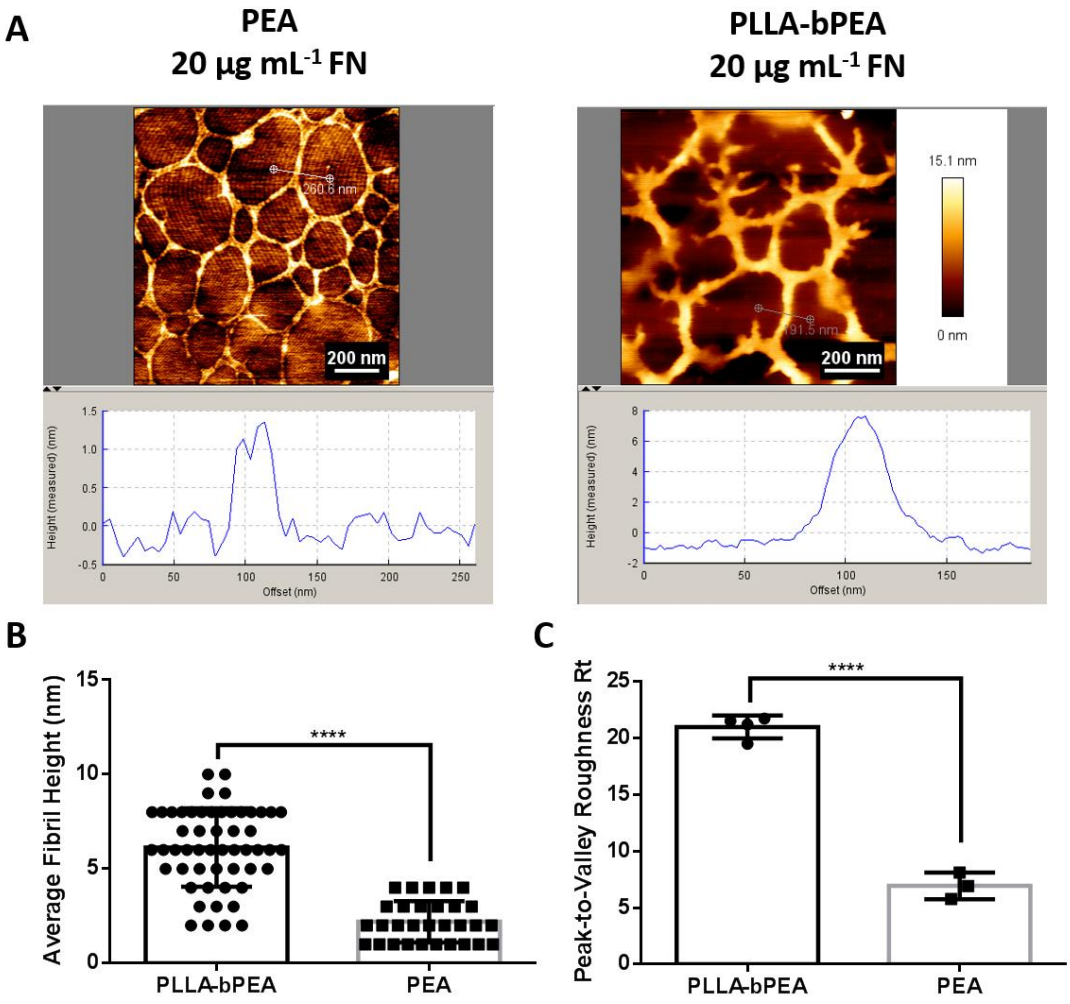

Figure 3.4. AFM analysis of FN Fibril conformation and thickness. **(A)** FN networks on PEA and PLLA-*b*PEA height scans as visualised via AFM, and corresponding cross-section which highlights the height of a FN fibril. **(B)** Average fibril height. **(C)** Peak-to-Valley Roughness. Graphs show mean values and standard deviation, n>3. ****p < 0.0001.

AFM imaging was predominantly performed in ambient conditions in air: samples were coated with FN, washed and dried gently with a nitrogen flow. However, FN fibrillogenesis was observed in both air and liquid on PEA; in the

latter case, samples were not dried but rather maintained in a liquid environment. FN nanofibrils were identified in liquid, highlighting that the protein-surface interactions occurring on these samples and the subsequent formation of protein nanonetworks are not a product of drying artefacts (Figure 3.5). Indeed, comparison of AFM performed in wet and dry conditions did show that improved definition of the FN nanonetworks could be obtained when imaging in dry conditions, due to improved tip-sample stability which allows a more accurate and easier scanning.

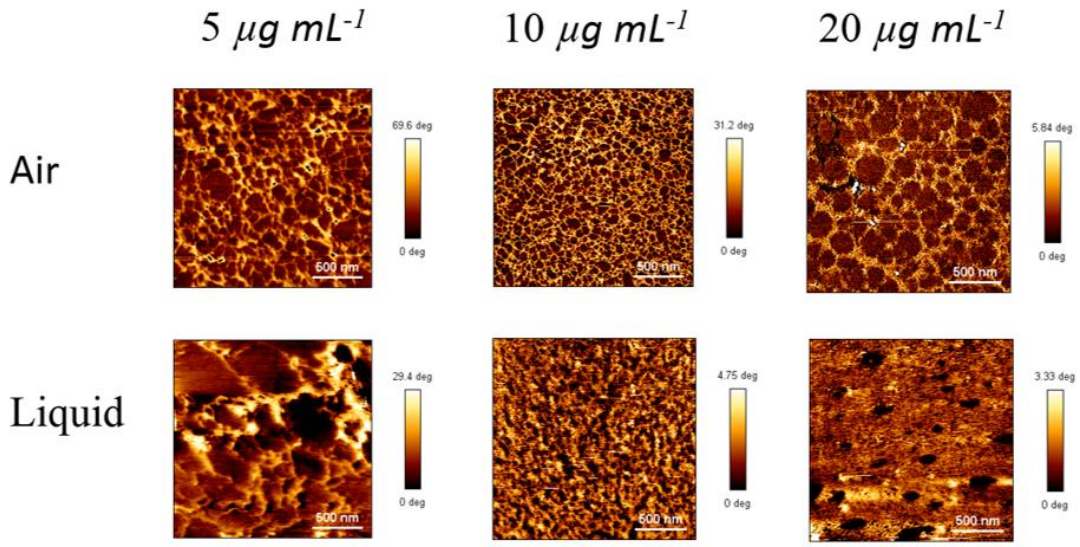

Figure 3.5. AFM phase images in liquid and dry conditions of spin-coated PEA coated with increasing concentration of fibronectin of 5, 10 and 20 μg mL^{-1} for 1 hour. FN nanofibrils are formed at the lower FN concentration as visible in liquid. After gentle drying, a similar fibrillary morphology is maintained and tip-sample stability is enhanced allowing easier scanning. This is confirmed at 10 μg mL^{-1}, whilst the increased protein density at 20 μg mL^{-1} makes distinguishing these structures in liquid more difficult due to higher surface coverage. Please note that the colour scale is different for every image, as indicated, to allow clear visualisation of the surface features.

3.3.3. Binding domain availability

Upon confirmation via AFM of the structural re-organisation of FN into nanonetworks at the molecular level on PLLA-*b*PEA, the biological functionality of these fibrils was investigated. The ability of PLLA-*b*PEA to adsorb and present FN in favourable orientations, therefore enhancing the availability of selected binding domains as found on PEA, was used to assess the potential of SI-ATRP for further cellular assays. It was observed that the total amount of FN absorbed on PLLA, PLLA-*b*PEA or PEA was similar, indicating no significant difference in protein surface density due to the formation of the nanonetwork (Figure 3.6A). This correlates with previous characterisation of material-driven fibrillogenesis, which, utilizing non-network forming acrylates and bulk poly (ethyl acrylate), showed similar densities of adsorbed FN independently of the protein structure (Vanterpool, Cantini et al. 2014). Regarding availability of integrin binding domains on adsorbed FN, this was measured using both the antibody HFN 7.1, which recognises to the RGD cell binding domain (Takahashi, Leiss et al. 2007, Vanterpool, Cantini et al. 2014), and the antibody mAb1937, which binds close to the PHSRN synergy domain (Garcia, Vega et al. 1999, Grigoriou, Cantini et al. 2017) (Figure 3.6D). While there was no significant upregulation of RGD presentation of FN adsorbed onto PLLA-*b*PEA or PEA (Figure 3.6B), the PHSRN synergy domain availability was significantly higher on both compared to FN on PLLA (Figure 3.6C). This indicated increased exposure of the cryptic PHSRN domain on PLLA-*b*PEA, as found on PEA, which is a hallmark of the conformational change occurring during FN fibrillogenesis (Pankov and Yamada 2002, Gee, Yueksel et al. 2013, Vanterpool, Cantini et al. 2014).

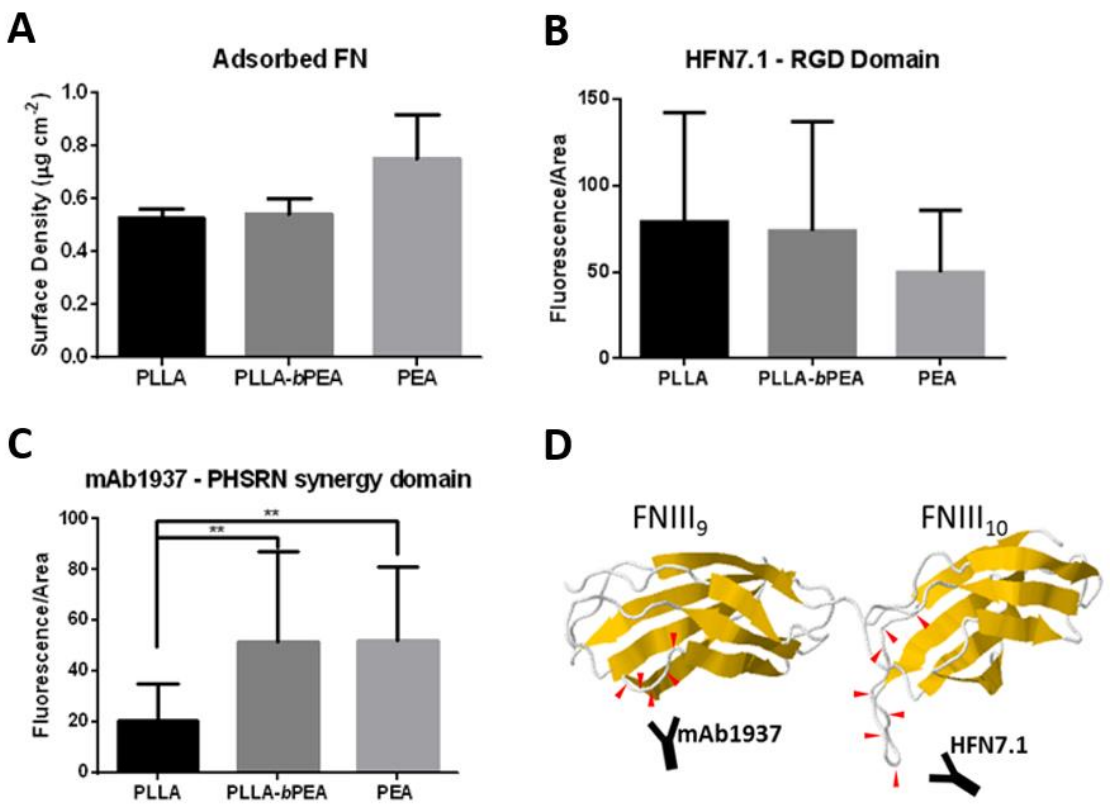

Figure 3.6. Fibronectin conformation. (A) Surface density of adsorbed FN on PLLA, PLLA-*b*PEA and PEA. **(B)** Quantification of the availability of the integrin binding domain on $FNIII_{10}$, as measured by HFN7.1 binding via ICW. **(C)** Quantification of the availability of the synergy binding domain on $FNIII_{9}$, as measured by mAb1937 binding via ICW. **(D)** 3D cartoon of FN integrin binding region ($FNIII_{9\text{-}10}$); the binding sequences (PHSRN synergy binding domain, recognised by mAb1937, and RGD binding domain, recognised by HFN7.1) are highlighted by red arrows. Adapted from PBD ID: 1FNF (Leahy, Aukhil et al.). Graphs show mean values and standard deviation, $n \geq 3$. $^{**}p < 0.01$, $^{***}p < 0.001$.

3.3.4. Cell adhesion

Having established that the fibrillar organisation of FN on PLLA-*b*PEA leads to enhanced exposure of adhesion-related binding domains, cellular assays using C2C12 cells were performed to further characterise this added functionality of SI-ATRP-treated PLLA. By conducting an adhesion assay and staining for actin and

vinculin, we aimed to investigate the PLLA-*b*PEA samples cellular interactions in comparison to untreated PLLA and spin-coated PEA (Figure 3.7A). Cells adhere to PLLA-*b*PEA samples with and without fibronectin coating, but they were observed to adhere and spread better on FN treated PLLA-*b*PEA surfaces. PLLA-*b*PEA samples generally had high density of healthy viable cells spread across a wide area of the sample surface. The PLLA-*b*PEA samples showed cellular adhesion and morphology similar to bulk PEA controls and within these cells well-defined stress fibres, indicated by the actin staining, were observed compared to PLLA. Average cell area was observed to be maintained between all surface conditions (Figure 3.7B), while circularity was significantly reduced on PEA presenting samples. This shows that while the cells cultured on PLLA-*b*PEA maintain the same size as on PLLA, they are able to adhere and spread more favourably as on PEA. This is due to the presence of FN nanonetworks and exposure of the PHRSN synergy domain.

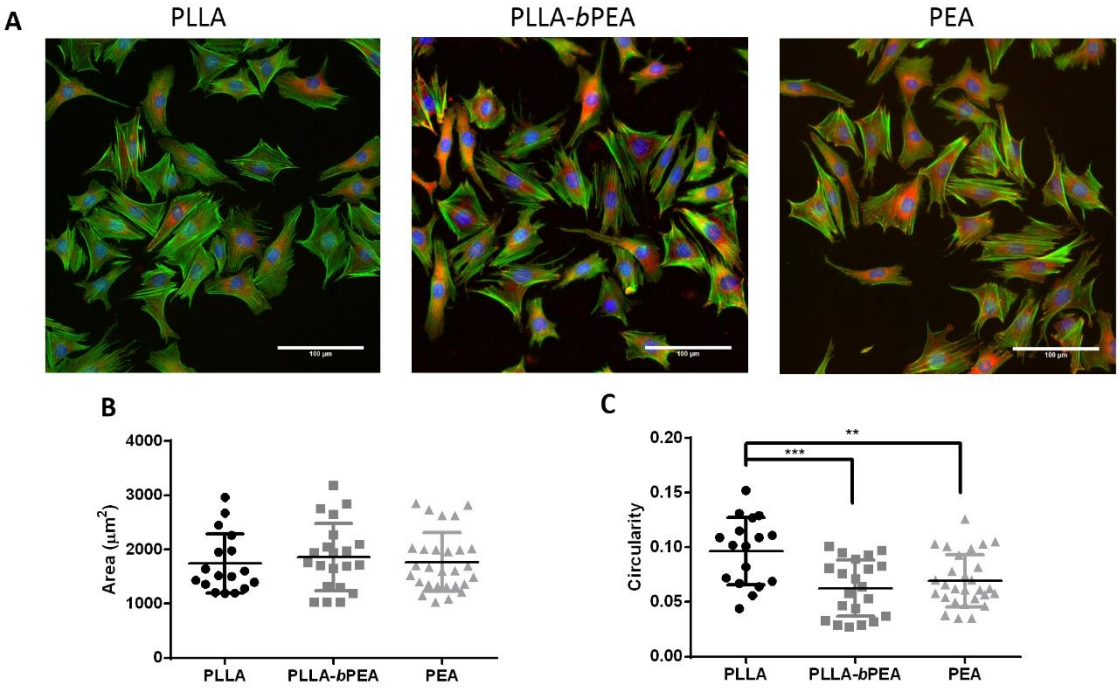

Figure 3.7. Adhesion of C2C12 cells. (A) Representative images of C2C12 cells adhering on FN-coated PLLA, PLLA-*b*PEA and PEA after 4 hours of culture. Samples were stained for actin (green), vinculin (red) and DAPI (blue). Scale bar is 100 μm. **(B)** Cell size. **(C)** Cell circularity. Graphs show mean values and standard deviation, n≥15. **p < 0.01, ***p < 0.001.

Cellular adhesion was further evaluated by investigating the focal adhesion (FAs) complexes formed on these surfaces. Number, size and distribution of focal adhesions formed were analysed by vinculin staining and analysis of images of single cells (Figure 3.8A). Single cells were observed to have a more obviously increased abundance of defined stress fibres on PLLA-*b*PEA and PEA surfaces compared to untreated PLLA. Cells seeded on both PLLA-*b*PEA and PEA were noted to possess large areas of densely packed focal adhesions at their periphery, while these areas were not noted on PLLA samples (Figure 3.8A). From thresholded vinculin images, larger concentrations of mature focal adhesions were confirmed to localise on the outer extremities of the cells on PLLA-*b*PEA and PEA surfaces (Figure 2B).

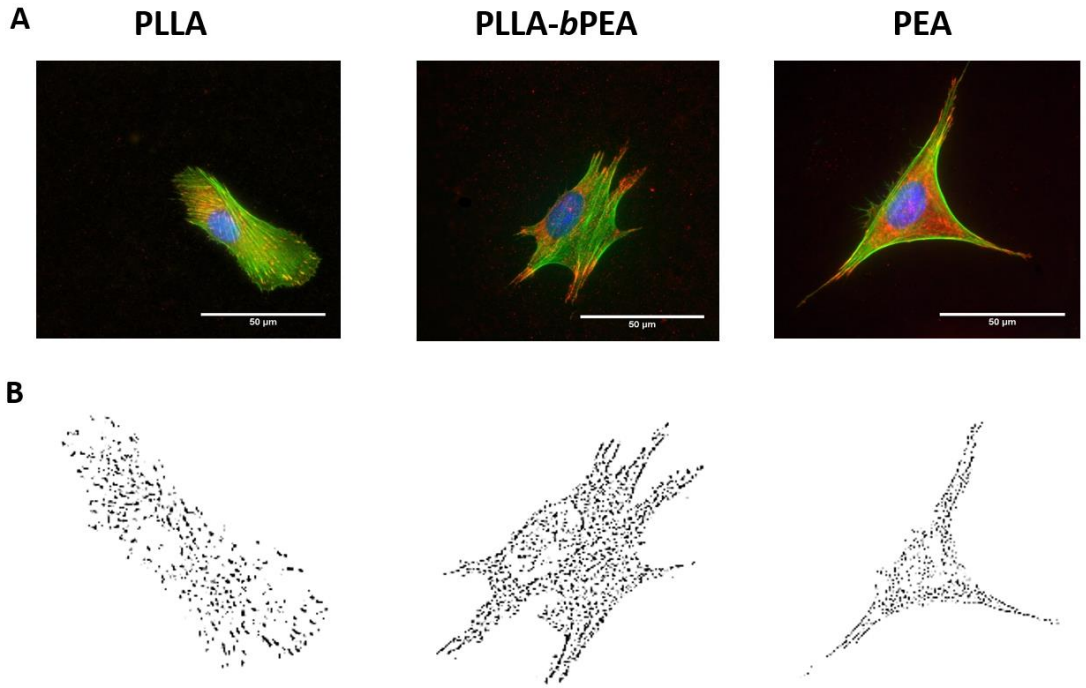

Figure 3.8. Focal adhesions of C2C12 cells. (A) Representative images of focal adhesions formed by C2C12 cells on FN-coated PLLA, PLLA-*b*PEA and PEA after 4 hours of culture. Samples were stained for actin (green), vinculin (red) and DAPI (blue). **(B)** Show thresholded binary images of the vinculin staining. Scale bar is 50 µm.

Analysis of thresholded FA images confirmed that the total number and size of FAs increased from PLLA through PLLA-*b*PEA to PEA (Figure 3.9 A and B); this

corresponds to variations in FN fractal analysis observed on these surfaces (Figure 3.9B). These FAs were measured to be larger on PEA presenting surfaces (20% and 35% of focal adhesions are longer than 2 μm on PLLA-bPEA and PEA, respectively), while on PLLA smaller FA plaques were mostly formed (95% <2 μm). These results show that SI-ATRP treatment is able to profess enhanced cellular adhesions onto PLLA surface via the incorporation of PEA brushes onto the surface, facilitating increasing focal adhesion complex formation and maturation.

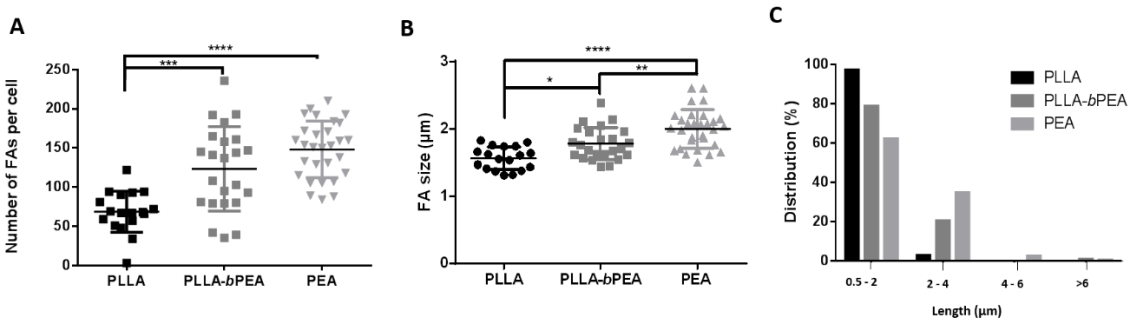

Figure 3.9. Adhesion of C2C12 cells, quantification. (A) Number of focal adhesions per cell. **(B)** Average focal adhesion size. **(C)** Frequency distribution of FA size. Graphs show mean values and standard deviation, n≥15. *p < 0.05, **p < 0.01, ***p < 0.001, ****p < 0.0001.

3.3.5. Myogenic differentiation

Further to adhesion, the differentiation of C2C12 cells towards the myogenic lineage was evaluated by staining for sarcomeric myosin after 4 days in differentiation medium (Figure 3.10). Cells were observed to differentiate predominantly on PLLA-*b*PEA and PEA, as observed from increased myotube density on these samples. Indeed, PEA and PLLA-*b*PEA presented high degrees of differentiation (~70%), while on PLLA low percentages of differentiated cells were present (~25%) (Figure 3.11B). On the other hand, cell density was calculated to be maintained independently of sample type (Figure 3.11A). Therefore, due to the similarities between surfaces, cell density is not responsible for the increased cellular differentiation on PLLA-*b*PEA samples. To further characterise whether the mechanism of differentiation observed on PLLA-*b*PEA was due to the inclusion

of PEA brushes, blebbistatin was utilised to inhibit cellular contractility. Blebbistatin is a myosin II inhibitor (Kovacs, Toth et al. 2004), which has been shown to inhibit cellular differentiation on PEA (Bathawab, Bennett et al. 2016). While cell density was not impacted (Figure 3.11A), the inclusion of blebbistatin significantly reduced the degree of differentiation on both PLLA-*b*PEA and PEA (Figure 3.11B). On the PEA presenting surfaces the degree of differentiation dropped to 25%, similar to that of PLLA. There was no difference in the number of differentiated cells on PLLA samples with blebbistatin treatment, however cellular morphology was observed to vary significantly on all surfaces with contractility inhibition. These results suggest that enhanced myogenic differentiation is facilitated by PEA brushes produced via SI-ATRP on PLLA-*b*PEA and that this supplementary characteristic is myosin II-dependent, as on PEA.

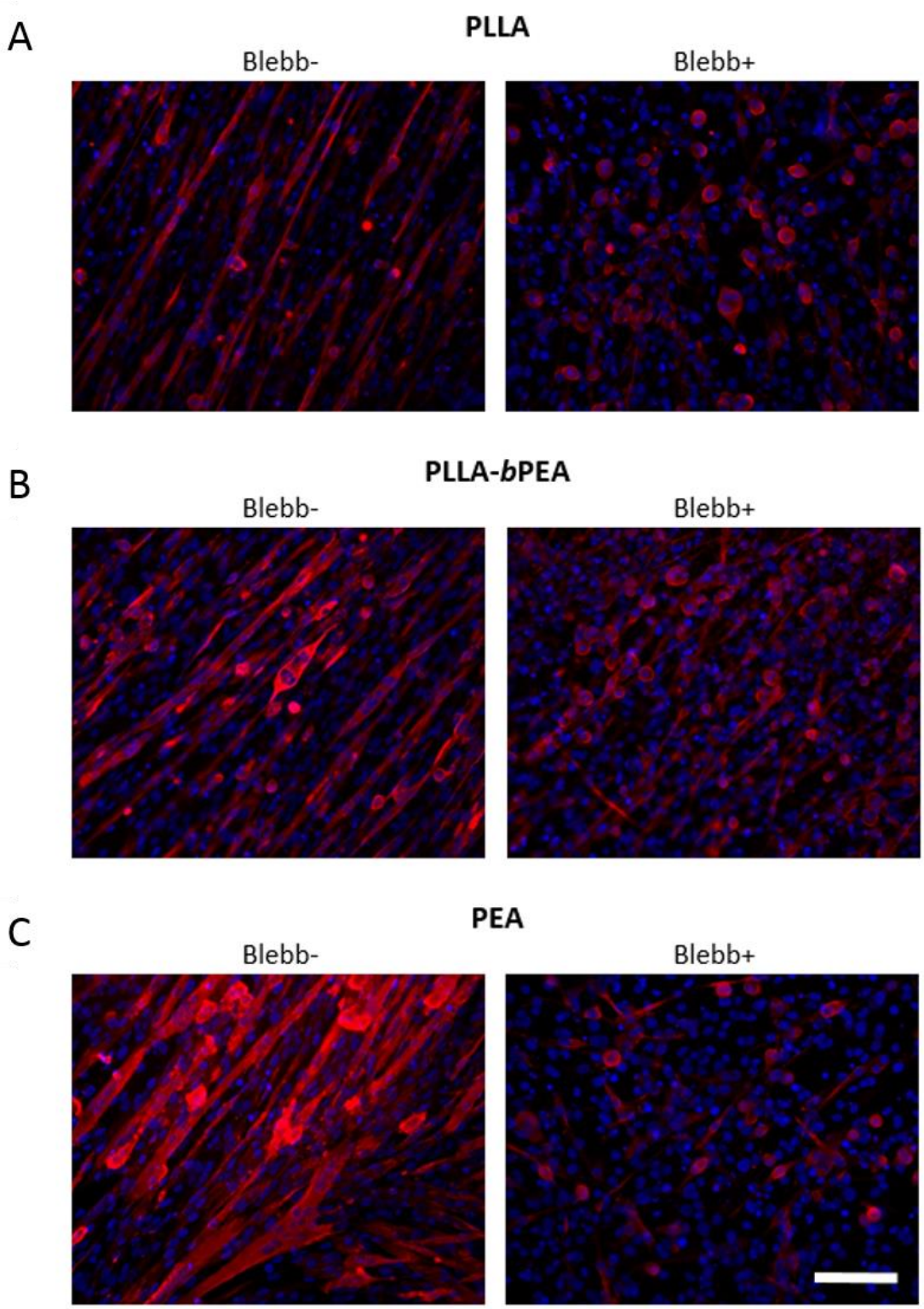

Figure 3.10. Cell differentiation. Sarcomeric myosin (red) and nuclei (blue) of C2C12 cells after 4 days of differentiation on FN-coated **(A)** PLLA, **(B)** PLLA-*b*PEA and **(C)** PEA. Blebbistatin (Blebb) 10 μM, was added in the media of Blebb+ samples as a contractility inhibitor. Scale bar is 100 μm.

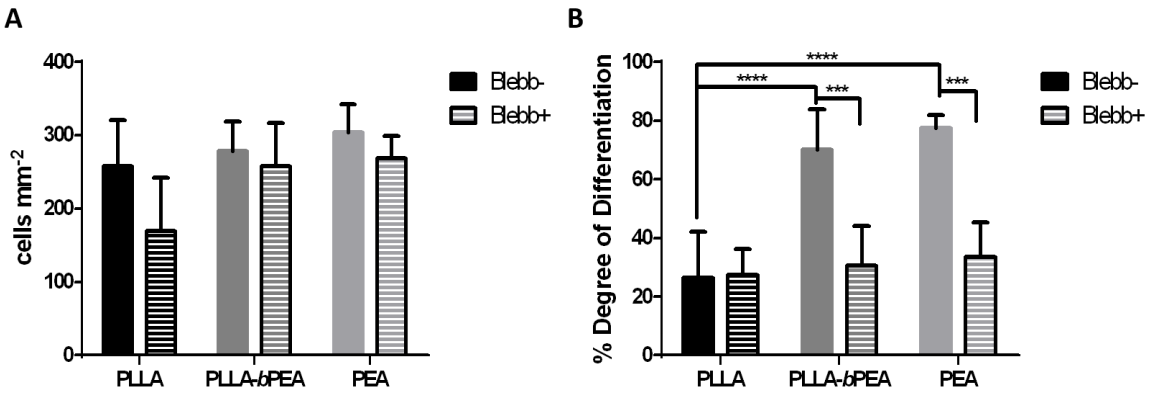

Figure 3.11. Cell differentiation analysis. (A) Cell density. **(B)** Degree of myogenic differentiation measured as percentage of sarcomeric-myosin positive cells. Blebbistatin (Blebb) was used as a contractility inhibitor. Graphs show mean values and standard deviation, n≥4. ***p < 0.001, ****p < 0.0001.

3.4. Discussion

In this chapter, having confirmed the production of PEA brushes on PLLA-*b*PEA in *Chapter 1*, we characterised fibronectin and cellular interactions on these surfaces, in order to evaluate the biological functionality of produced polymer brushes. Indeed, PEA is known to induce the assembly of FN into nanonetworks, through material-driven fibrillogenesis (Salmeron-Sanchez, Rico et al. 2011, Cantini, González-García et al. 2012); the change in the protein structure upon adsorption has been shown to induce the formation of fibrils and subsequent nanonetworks, which favourably present integrin binding domains for enhanced cellular interactions. Therefore, the aim of this project being to provide additional functionality to PLLA, we aimed to assess the improved availability of these binding domains, predominantly the cryptic PHSRN synergy domain, which has been shown to improve the binding of α5β1 integrins to the RGD domain of FN.

First, the functionality of the PEA brushes was investigated through their ability to drive changes in protein structure and fibril formation. FN coating was

observed to decrease the measured roughness and mask the differences in hydrophobicity and chemical mobility between samples (Figure 3.1). It can be suggested that FN provided a uniform coverage of all surfaces, regardless of changes in its conformation or organisation. This changes were instead detected microscopically via fluorescently tagged FN and at the molecular level via AFM. Microscopically FN networks were observed on PLLA-*b*PEA, similarly to those found on PEA. Fibronectin was observed to form fibril networks on both high and low concentrations of FN (Figure 3.2). While this suggested the biofunctionality of PEA brushes to drive fibrillogenesis, at this scale the RMS roughness introduced through the SI-ATRP process may also affect FN orientation and conformation on these surfaces.

In order to discard the effect of the nanotopography, FN molecules were examined at the nanoscale utilising AFM on smoother samples; this would further confirm changes in protein structure associated with the presence of PEA brushes on the surfaces. Indeed, on PLLA-*b*PEA FN was observed to form nanonetworks, similar to those found on bulk PEA (Figure 3.3); however on untreated PLLA this FN architecture was not present. FN was observed to remain in globular cluster conformation on pristine PLLA, due to the lack of chemical sidechains on the unmodified polymer backbone. The presence of nanonetworks on PLLA-*b*PEA shows the retention of the biological functionality of the PEA brushes produced via SI-ATRP. In fact, they provide the ability for modified PLLA surfaces to drive surface-initiated fibrillogenesis. However, FN fibrils formed on PLLA-*b*PEA samples were altered compared to those formed on bulk spin-coated PEA (Figure 3.4). These fibrils were measured as thicker and less interconnected than those found on PEA, producing wider nanonetworks with a slightly lower fractal dimension (Figure 3.3 B) (Pelta, Berry et al. 2000).

The larger fibrils on PLLA-*b*PEA can be attributed to the size of the FN protein and to the inherent nature of the polymer brushes. While FN is presented as few nanometres in thickness and with two ~40 nm stretched arms when in non-globular fibril conformation (e.g. as found on PEA), initial interactions with the surfaces is performed by globular FN, which is sized to ~30 nm (Pelta, Berry et al. 2000, Gugutkov, Gonzalez-Garcia et al. 2009). While the protein size does not affect its interaction with a homogenous microscopic layer of polymer (e.g. when

FN is adsorbed onto spin-coated PEA), this large protein initially interacts with PEA brushes that are estimated to be only few nanometres high when it is adsorbed onto PLLA-*b*PEA surfaces. These interactions are likely to cause local disruption of these small polymer brushes, inhibiting further FN interactions in the local vicinity of pre-adsorbed FN and therefore favouring FN-FN binding instead. This with FN would impact on the interconnectivity of the nanonetworks and is suspected to aid in the development of thicker fibrils compared to bulk PEA surface. Surface roughness of the treated polymer may also contribute to these differences, as nano-roughness has been previously shown to affect the protein adsorption and subsequent fibrillogenesis (Rico 2014).

It should also be noted that AFM was performed in both air and liquid conditions to investigate the potential that FN material-driven fibrillogenesis was an artefact of rapid osmotic variations on the surface during drying (Figure 3.5). Similar FN nanonetworks were observed on fixed FN-treated PEA samples in both conditions regardless of environmental conditions (Figure 3.5B); however, images obtained in liquid suffered from diminished tip-surface stability which impacted image quality. Here we have presented FN fibrillogenesis on spin-coated PEA in liquid as these surfaces presented improved tip surface stability compared to scPLLA-*b*PEA, resulting in clearer visualisation of FN nanonetworks. This could be due to slight increases in scPLLA roughness caused by SI-ATRP contributing to poor image quality as found in AFM visualisation in liquid conditions. Our results confirmed that FN nanonetworks observed on PEA samples were not a drying artefact, but rather they were induced by protein interactions with this polymer.

The conformational change of FN on PLLA-*b*PEA shows that PEA brushes have a biological functionality similar to bulk PEA. To further characterise the availability of binding domains in the FN nanonetworks assembled on the PEA brushes was investigated. As fibronectin mediates a wide range of cellular interactions with the ECM *in vivo*, the conformation and presentation of integrin binding domains on this protein are vital for the development of this, or any, tissue engineering-orientated systems (Schwarzbauer and Sechler 1999, Pankov and Yamada 2002, Martino, Tortelli et al. 2011). It has been shown that fibrillogenesis drives the presentation of different, cryptic integrin binding domains (Keselowsky, Collard et al. 2003, Keselowsky, Collard et al. 2004, Keselowsky, Collard et al. 2005, Costa

Martinez, Rodriguez Hernandez et al. 2008, Vanterpool, Cantini et al. 2014, Bathawab, Bennett et al. 2016, Grigoriou, Cantini et al. 2017); these published systems have utilised surface mobility and varying surface chemistries, such as side-chain length of acrylates or monolayers presenting defined chemistries, to expose these binding motifs, which were otherwise inaccessible on globular FN (Garcia, Vega et al. 1999, Salmeron-Sanchez, Rico et al. 2011). This subsequently facilitated enhanced cellular behaviours such as adhesion and differentiation (Garcia, Vega et al. 1999, Keselowsky, Collard et al. 2004). Here, we found that PLLA-*b*PEA surfaces present enhanced integrin binding domain availability, through increased exposure of the PHSRN synergy domain of FN (Redick, Settles et al. 2000, Vanterpool, Cantini et al. 2014), similarly to PEA (Figure 3.6C). This correlates with the observation of nanonetworks on these surfaces, as fibrillogenesis and therefore stretching of the FN molecule would present this cryptic binding domains; on the other hand on PLLA, where PHSRN availability was observed to be low, globular FN would not preferentially present this binding domain (Ballester-Beltran, Moratal et al. 2014). Availability of the RGD domain was instead observed to be similar on all surface conditions (Figure 3.6 B) due to the universal presentation of this domain on both fibril and globular FN, in line with the surface density of adsorbed FN, which was shown to be independent of nanonetwork formation (Figure 3.6 A) (Redick, Settles et al. 2000, Vanterpool, Cantini et al. 2014). This definitively shows the presence and functionality of PEA brushes produced via SI-ATRP on PLLA, and suggests potential enhanced cellular interactions favourable for tissue engineering applications of this surface modification. PEA driven FN fibrillogenesis has been utilised in similar systems via spin-coating and plasma polymerisation (Cantini, Rico et al. 2012, Llopis-Hernandez, Cantini et al. 2016), including onto the surface of biomaterials (Cheng, Alba-Perez et al. 2019). These approaches to incorporating thin layers of PEA onto the surface have shown similar enhancement of FN binding domain availabilities and formation of nanonetworks. However, spin-coating is a planar surface coating methodology and is therefore not a feasible technique for thin layer production in 3D scaffolds or other more complex systems. Plasma polymerisation is able to diffuse through complex 3D structures, this however has been shown to heterogeneously coat the surface, to produce PEA coating (Barry, Silva et al. 2005, Barry, Howard et al. 2006). However, FN nanonetworks observed on plasma polymerised PEA on glass coverslips are much more densely packed than scPEA or

scPLLA-*b*PEA (Cheng, Alba-Perez et al. 2019), resembling more FN nanonetworks on PLLA-*b*PEA films. These layer of PEA produced by spin-coating or plasma polymerisation are also not chemically bound to the surface and therefore can peel, unlike PEA brushes produced via SI-ATRP which are grafted from the PLLA and covalent bound to the surface (Matyjaszewski, Dong et al. 2007).

Indeed, cell adhesion was observed to improve on PLLA samples treated with SI-ATRP. Cells cultured on PLLA-*b*PEA spread better and showed lower circularity, resulting in improved morphologies comparatively to PLLA (Figure 3.7). Furthermore, PLLA-*b*PEA surfaces were observed to facilitate larger numbers of focal adhesions than PLLA, and of these FAs a higher concentration were longer mature focal adhesion plaques as found on PEA (Figures 8 and 9). These findings are in line with previous characterisations of cellular interactions on PEA (Vanterpool, Cantini et al. 2014), which highlighted enhanced adhesion of cells on these surfaces. This confirms that the PEA brushes formed via SI-ATRP are able to drive FN fibrillogenesis and subsequently present binding domains associated with cellular adhesion via the same mechanism as bulk PEA. Variations in number and size of focal adhesions between PLLA-*b*PEA and PEA may correspond to the diminished fractal dimension and interconnection of the FN nanonetworks formed on the brushes. In any case, the added functionality induced enhanced cellular adhesion to modified PLLA, highlighting the viability of SI-ATRP as a surface modification technique.

Additionally, PLLA-*b*PEA surfaces were observed to induce myogenic differentiation to similar degrees as control bulk PEA (Figure 3.10 and 3.11). While PLLA surfaces alone were ineffective in driving differentiation of C2C12 cells, both PLLA-*b*PEA and PEA surfaces presented high concentrations of differentiated cells after 4 days of incubation (Figure 11A). This highlights that PLLA-*b*PEA surfaces are able to facilitate more complex cellular functions than enhanced adhesion (Zhu, Gao et al. 2004). While higher cellular densities have been shown to contribute to increased degrees of myogenic differentiations (Tanaka, Sato et al. 2011), here we observed similar cellular densities in all sample conditions while increased differentiation percentages were present only on PLLA-*b*PEA and PEA. Therefore the increased myotube formation is due to the presence of functional FN nanonetworks on these samples. Moreover, C2C12 differentiation on FN

nanonetworks on PEA has been found to be contractility-dependent (Salmeron-Sanchez, Rico et al. 2011, Bathawab, Bennett et al. 2016), and here we aimed to further confirm if differentiation on PLLA-*b*PEA occurred via the same mechanism as on bulk PEA. Introduction of blebbistatin, a myosin II contractility inhibitor (Kovacs, Toth et al. 2004, Allingham, Smith et al. 2005), significantly decreased the degree of differentiated cells on PLLA-*b*PEA and PEA, whilst no decrease was observed on PLLA. This confirmed the contractility dependence of differentiation on PLLA-*b*PEA and PEA, showing that the FN nanonetworks formed on both of these surfaces activate actin-myosin contractility and drive cell fate (Cai, Rossier et al. 2010). This further shows the similarities to bulk PEA and the functionality of the SI-ATRP-produced PEA brushes, validating the potential of SI-ATRP as an avenue for tissue engineering applications.

3.5 Conclusion

In this chapter we have assessed the biological functionality of PEA brushes produced from SI-ATRP, primarily their ability to drive fibrillogenesis presenting previously inaccessible binding domains on FN to enhance cellular interactions. This retention of the functionality of PEA, similar to that of the conventionally produced bulk polymer, confirms the previous identification of chemical similarities between these two production mechanisms (Chapter 2). Therefore confirmation of nanonetwork formation and synergy domain presentation suggest PLLA-*b*PEA surfaces will favourably allow for cellular adhesion, as found for bulk PEA (Vanterpool, Cantini et al. 2014, Llopis-Hernandez, Cantini et al. 2016). This was confirmed via characterisation of PLLA-*b*PEA cellular interactions; highlighting supplementary cellular adhesion and differentiation capabilities of SI-ATRP treated PLLA. These results show that PLLA-*b*PEA is able to facilitate enhanced cellular adhesions and differentiation allowing for the potential use of stem cells and further development of this system for use in tissue regeneration.

4- Streamlining of SI-ATRP system

4.1. Introduction

In the previous chapters we have outlined the optimization of a 3-step SI-ATRP methodology. During this process a variant SI-ATRP system, which incorporates priming and initiator immobilisation in one step, was developed in tandem. While the previously described system of immobilising the SI-ATRP initiator on the PLLA surfaces involved 2-pots, first the functionalisation (aminolysis) and then the initiator immobilisation (bromination), this optimized system aims at preparing the PLLA surfaces for polymerisation within the same reaction vessel, therefore being a "1-pot SI-ATRP" system. The process was developed to produce PLLA-*b*PEA samples efficiently in a shorter time scale, avoiding the necessity to aminolyse and wash the samples before bromination. These optimization steps were undertaken based on several surface modification protocols (Charvet and Novak 2004, Min, Gao et al. 2009, Morsi, Pakzad et al. 2011, Espeel and Du Prez 2015), which outline 1-pot bromination in the presence of functionalization. Through this variant SI-ATRP protocol it was speculated that time of PLLA-*b*PEA production could be reduced alongside improved maintenance of bulk polymer characteristics, so as to allow for enhanced upscaling of the procedure while maintaining control of products specifications. However, it was also essential to ensure that the modified material was as functional as the one obtained with the previously outlined 2-pot production. Therefore, 1-pot SI-ATRP samples were produced and characterised alongside 2-pot surfaces; in this chapter, we compare the materials resulting from 1-pot and 2-pot PLLA-*b*PEA samples. While the aminolysis in the 2-pot procedure is a defined controlled reaction modulated by concentration of 1, 6 hexanediamine, temperature and time of reaction, 1-pot samples are functionalised via surface interactions with the pyridine present in the immobilisation vessel which produce complexes with α-bromoisobutyryl bromide. This manner of pyridine-based functionalisation or pyridinolysis, has been previously described in ATRP reactions (Kickelbick, Paik et al. 1999, Xia, Zhang et al. 2000, Tsarevsky and Matyjaszewski 2005, Braunecker and Matyjaszewski 2006, Tang and Matyjaszewski 2006, Iacono and Heise 2015, Kassel, Gerke et al. 2018); however, due to simultaneous inclusion of pyridine sidechains and immobilisation of initiator occurring in 1-pot reactions, it is not as controlled or definable as a separate aminolysis. Within the 2-pot reaction this pyridine based

functionalisation is suspected to be inhibited by the presence and coverage of amine groups. By characterising this pyridine based procedure, defining the alterations to the chemical and mechanical properties of the films and comparing them to 2-pot surfaces, we aim to optimize it to allow for fast and efficient PEA brush formation that may allow for easier translation into industrial or clinical applications.

4.2. Materials and methods

4.2.1. Materials: Poly (L-Lactide) films (thickness 50 μm) were purchased from Goodfellow (Huntingdon, UK). 1,6-hexanediamine (98%), 2-propanol (≥99.5%), 2-bromoisobutyryl bromide (BIBB, 98%), anhydrous pyridine (Py, 99.8%), anhydrous hexane (95%), copper(I) bromide (CuBr,99.999 %), Tris(2-pyridylmethyl)amine (TPMA, 98%), ethyl acrylate (EA, 99.5%), methanol (99.99%), ascorbic acid (AsAc) were purchased from Sigma Aldrich, Dorset, UK. Glass reaction vessels were custom-made.

4.2.2. Preparation of PLLA-bPEA films: The developed SI-ATRP system takes place in two or three steps: priming (aminolysis), initiator immobilisation (bromination) and polymerisation. These processes take place sequentially and separately within different reaction vessels for the formation of 2-pot PLLA-*b*PEA. For 1-pot PLLA-*b*PEA, samples are functionalised within the initiator immobilisation reaction vessel by available nitrogen sources during bromination (soluble pyridine), with reagent ratios hexane: BIBB: pyridine (20:1:0.4) and subsequently immobilised. They are then polymerised within a separate reaction vessel alongside the 2-pot samples. PLLA films were cut into 13.8 mm circles, with an area of 1.9 cm^2.

4.2.3. ***Atomic force microscopy:*** Atomic Force Microscopy was used to quantify surface roughness in all conditions on dried samples in air. Height and lock-in phase images were taken in AC mode using a Nanowizard 3 Bioscience AFM (JPK, Berlin Germany). Scans were made using cantilevers with a resonance frequency of 75 kHz and a force constant of 3 N m^{-1} (MPP-21120 from Bruker, Billerica, MA).

Surface area scans (n=3) of 5x5 μm (0.5Hz) were used to analyse surface roughness of each sample from any given condition. The R_{rms} was calculated using the JPK DP software after image levelling to remove variations or tilts in the background.

4.2.4. Water contact angle: Water contact angle measurements were undertaken on PLLA and functionalised samples. Static contact angles (SCA) were measured by dropping 3 μL of deionised water onto the samples. Analysis was conducted using a Theta optical tensiometer (Biolin Scientific, Stockholm, Sweden).

4.2.5. Enzymatic degradation: Individual samples were dried to constant weight under vacuum for a minimum of 2 days, samples were then submerged in 0.2 mg mL^{-1} proteinase K enzyme (Sigma, St. Louis, MO) in Tris-HCL buffer (pH 8.6) with 0.2 mg mL^{-1} sodium azide (Sigma, St. Louis, MO). Incubated samples were kept at 37°C with agitation. The degradation solution was replaced every 24 hours to maintain enzymatic activity. Samples were dried under vacuum to constant weight before final weight was established.

4.2.6. Dynamic mechanical analysis: Dynamic mechanical analysis (DMA) was performed on a DMA 8000 (Perking-Elmer) apparatus at a frequency of 1Hz in tension mode, the temperature range was -150 to 100°C at a rate of 1°C min^{-1}. Young's modulus was determined at 36-38°C on sample of 10 mm x ~6 mm x 0.05 mm.

4.2.7. Differential scanning calorimetry: Differential scanning calorimetry (DSC) was performed using a PerkinElmer 8000 apparatus. Samples were weighed to ~4mg and encapsulated within DSC pans before being cooled from 30°C to -80 °C and isothermally stabilized for 5 minutes. Samples were then heated to 200 °C at a rate of 20 °C min^{-1} (first heating) and subsequently cooled to -80 °C, this process was then repeated for the second heating. Temperature changes were at a rate of 20 °C min^{-1}, nitrogen gas rate was maintained at 20 ml^2 min^{-1}. Crystallinity percentages were obtained using the equation:

$$Crystallinity\ (\%) = \frac{\Delta \mathrm{Hm} - \Delta \mathrm{Hc}}{93.1} x100$$

Where ΔHm is the enthalpy of melting, ΔHc corresponds to the enthalpy of crystallisation and 93.1 the theoretical melting enthalpy of 100% crystalline PLLA (Ribeiro, Sencadas et al. 2011). All measurements are presented as the average of 3 replicates.

4.2.8. Thermogravimetric analysis: Thermogravimetric analysis was performed with TGA/DSC 2 STAR System (Mettler Toledo) thermobalance, at 10 °C min⁻1 from 30 to 800 °C in a nitrogen atmosphere of 50 mL min^{-1}. Samples were weighed to 4mg and encapsulated in metal casings before cooling from ambient temperature to 800 °C from ambient temperatures. Thermogram data processing and analysis was performed using the Mettler Toledo software.

4.2.9. Fourier-transform infrared spectroscopy: Attenuated total reflection (ATR) FT-IR was performed to characterise the bulk chemical composition of PLLA modified through SI-ATRP, comparatively to PLLA and PEA controls. Scans in the range of 4000- 600 cm^{-1} were acquired using a Bruker ATR device, correcting for atmospheric contamination by taking a blank scan in air conditions.

4.2.10. Dielectric relaxation spectroscopy: The molecular dynamics of the samples were determined by means of a Novocontrol Broadband Dielectric Spectrometer (Hundsagen, Germany) consisting of an Alpha analyzer to carry out measurements from 5×10^{-2} to 3×10^{6} Hz. This allows measurement of the complex dielectric permittivity, $\varepsilon^{*}(\omega)=\varepsilon'(\omega)-i\varepsilon''(\omega)$, where $\varepsilon'(\omega)$ and $\varepsilon''(\omega)$ are the storage and loss part of the dielectric permittivity. The temperature was controlled by a Novocontrol Quatro cryosystem with a precision of ±0.1 K during each sweep in frequency. The isothermal measurements were performed from -120 °C to 70 °C (step of 5 °C) in an inert N_2 atmosphere to avoid moisture uptake. Molded disc shaped samples of about 0.05 mm in thickness, with diameter of 10 mm, were mounted in the dielectric cell between two parallel gold-plated electrodes. The thickness of each sample was measured with a micrometer screw. The experimental uncertainty was less than 5% in all cases. DRS was performed by Prof. M Sanchis, Universitat Politècnica de València.

4.2.11. X-ray photoelectron spectroscopy: X-ray Photoelectron Spectroscopy was used to identify the surface chemical composition of samples. All X-ray photoelectron spectra were obtained at the National EPSRC Users' Service (NEXUS) at Newcastle University (found at: http://www.ncl.ac.uk/nexus/). Each sample was analysed at three points with a maximum beam size (400 µm x 800 µm) with a K-alpha XPS apparatus (Thermo Scientific) equipped with a monochromatic Al-K-alpha source for Carbon, Oxygen, Nitrogen, Bromine and overview spectra. X-ray energy was 1486.68 eV at a voltage of 12 kV, current of 3 mA and power of 36 W. Analysis of the XPS results was conducted with CasaXPS version 2.3.16 (Casa Software Ltd) with adjustments for transmission and escape depth included in the VAMAS block provided by NEXUS.

4.2.12. Cytotoxicity assay: a lactose dehydrogenase assay (LDH) kit (Roche; catalogue number 11644793001) was utilised to determine the cytotoxicity of polymer samples with hMSCs cells (p4, Promocell). Cells were seeded at $5x10^3$ cells cm^{-1} in a 96 well plate and polymer samples were cultured within 24 well plates for 24 hours without serum in antibiotic containing culture medium. Polymer samples were incubated with and without 2% triton X-100 within media. Cell media was replaced with media incubated with and without polymer and cells were incubated for 24 hours. The cell-free culture supernatant was collected and assayed for LDH release as directed by the kit provider. The increased concentration of enzyme activity in the supernatant represented cell permeabilization and membrane damage, and was analysed by the colour change of reagents, measured at 492nm and compared to reference media without polymer with and without 2% triton X100.

4.2.13. Cell adhesion: Mouse C2C12 myoblasts were thawed and re-suspended in Dulbecco's modified Eagle's medium (DMEM, high glucose, without pyruvate) with 1% v/v penicillin/streptomycin and 20% v/v foetal bovine serum (FBS). Cells were incubated in 37°C, 5% CO_2, and harvested by trypsinisation at 70% confluency.

For adhesion experiments, samples were sterilized under a UV lamp for 40 minutes on each side, as the samples are opaque, and coated with 10 µg mL^{-1} FN; negative controls were coated with PBS for 1 hour. Samples were then washed with PBS and seeded with 5000 cells cm^{-2} for 4 hours and then fixed with 3.7% formaldehyde

for 30 minutes at 4°C. The cells were then permeabilised with 0.1% triton X-100, washed and finally blocked (PBS/BSA1%) for 30 minutes at room temperature. Samples were first incubated with anti-vinculin primary antibody (1:400), hVIN-1 (Sigma-Aldrich), in blocking buffer for 1 hour at room temperature and subsequently washed with washing buffer, PBS/Tween 20 0.5%. Cy3-conjugated secondary antibodies (Jackson ImmunoResearch) and BODIPI FL Phallacidin (Thermo Fisher Scientific) were then added for 1 hour at RT. The samples were then washed and mounted with mounting medium containing DAPI (Vector Laboratories, Inc.) and visualised with a fluorescence microscope (Zeiss AxioObserver.Z1). Images were merged using ImageJ to localise nuclei and actin. Focal adhesions were analysed using the vinculin stain images; the procedure is described in Horzum et al (Horzum, Ozdil et al.) Images were analysed with threshold area of 0.5 μm^2 and 0-0.99 circularity.

4.2.14. Statistical analysis: Pre-processing and normalization of data are stated in the individual methods sections. Analysis of statistical differences was conducted using student T-test (Graphpad) for two sample comparison and One-way ANOVA for different groups using a Turkey HSD *post hoc* test to compare different groups. Differences were considered significant *p < 0.05, **p < 0.01, ***p < 0.001, ****p < 0.0001. All data presented are mean values, error bars are standard deviation and n numbers are noted in the figure captions.

4.3. Results

4.3.1. Surface characterisation and mechanical properties of 1- and 2-pot PLLA-*b*PEA

To characterize differences between products of SI-ATRP through a 1- or 2-pot immobilization mechanism, surface characterization was conducted. AFM showed a significant increase in RMS roughness post initiator immobilization of PLLA samples independent of pot mechanism (Figure 4.1A). Both 1- and 2-pot PLLA-*b*PEA samples have similarly increased roughness post polymerization, showing that the pot mechanism by which SI-ATRP is performed does not impact

on the topography of the samples. In contrast, 1-pot PLLA-*b*PEA surfaces were measured to have a much higher hydrophobicity than any other condition (Figure 4.1B). The increased WCA of 1-pot PLLA-*b*PEA may be a result of altered surface chemistry from the pyridinolysis immobilization mechanism. Therefore, while there are no significant topographical alterations, pyridinolysis produces distinctly altered PLLA-*b*PEA surface chemistries compared to aminolysis-based SI-ATRP.

Bulk properties were analyzed initially via dynamic mechanical analysis and enzymatic degradation. Enzymatic degradation of PLLA films showed that 1-pot PLLA-*b*PEA degraded at a slower rate than 2-pot samples and pristine PLLA (Figure 4.1C). This suggests that pyridinolysis produces a physical or hydrostatic barrier to PLLA degradation. The Young's modulus was maintained within the same mega pascal range independent of pot mechanism, however 1-pot samples were observed to possess higher stiffness values than 2-pot samples and pristine PLLA. This could indicate that the inclusion of pyridine-BIBB initiators causes a supplementary stiffening of PLLA. These results indicate that while 1-pot initiator immobilisation does not detrimentally impact on the bulk characteristics or surface topography of PLLA-*b*PEA, the altered mechanism of initiator immobilisation does result in increased surface hydrophobicity and decreased degradation at the shorter time point post treatment.

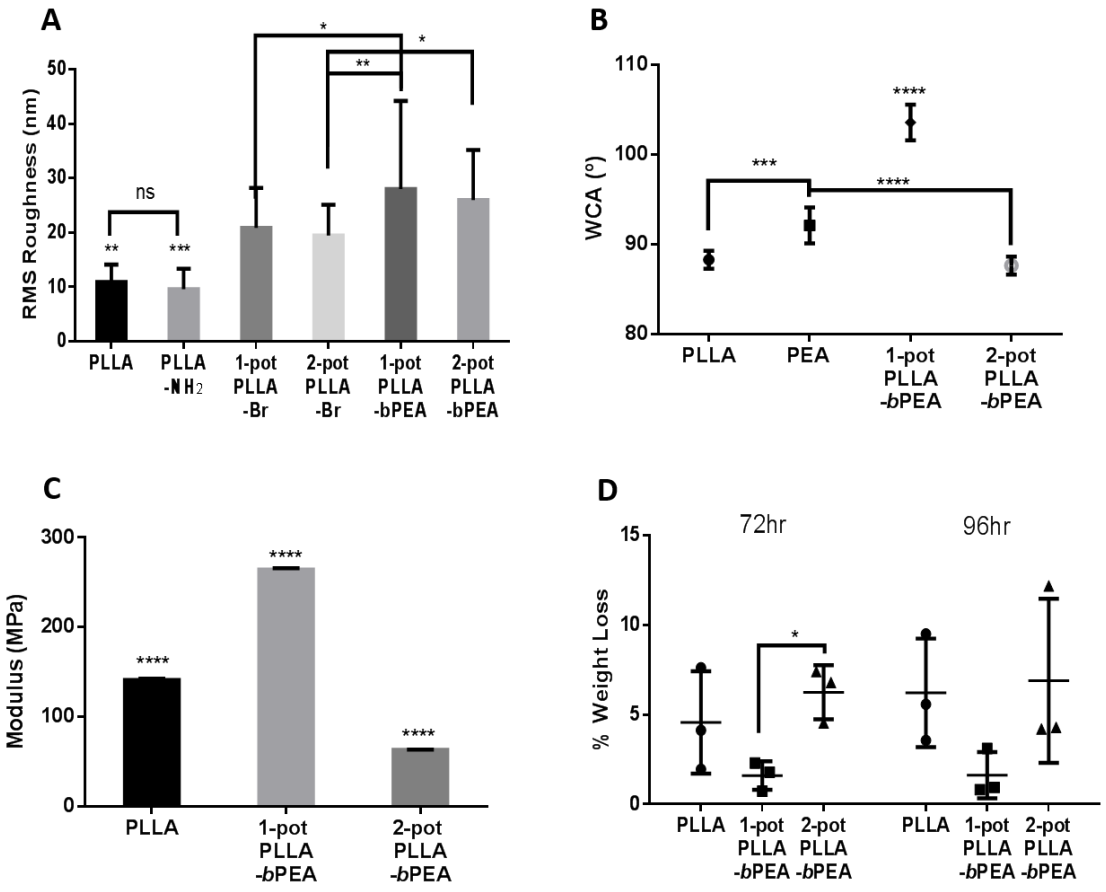

Figure 4.1. Surface and bulk properties. **(A)** Surface root mean squared roughness measurements of PLLA samples through the entire SI-ATRP process. A minimum of 20 measurements were taken from 5x5 μm^2 AFM scans of each sample. **(B)** Static water contact angle characterisation of spin-coated PEA controls, PLLA and PLLA-*b*PEA produced by either a 1-pot or 2-pot bromination. **(C)** Elastic modulus of PLLA and 1- or 2-pot PLLA-*b*PEA at 36-38 ^oC measured from dynamic mechanical analysis (DMA) using a DMA 8000 (Perking-Elmer) apparatus at a frequency of 1Hz in tension mode; the temperature range was -150 to 100^oC at a rate of 1^oC min^{-1}. Young's modulus was determined at 37^oC on samples of 10 mm x ~6 mm x 0.05 mm. **(D)** Percentage weight loss of PLLA and PLLA-*b*PEA samples after 72 hours of degradation with 0.2 mg mL^{-1} proteinase K at 37^oC. Graphs show mean values and standard deviation. *p < 0.05, **p < 0.01, ***p < 0.001, ****p < 0.0001.

4.3.2. Thermal analyses of 1- and 2-pot PLLA-bPEA

Further bulk characterisation was performed to investigate the thermal properties of 1-pot samples, in order to determine whether these immobilisation variants resulted in alterations in polymer crystallinity or resistance to thermal degradation. The DSC scans (Figure 4.2A) show the first and second heating of the samples in each condition. The first heating scans highlight the crystalline state of the polymers after each step of the SI-ATRP (Figure 4.2A). Both SI-ATRP systems drive crystallisation of the amorphous PLLA to around 40% post initiator immobilisation and 50% crystallinity in PLLA-*b*PEA (Figure 4.2B). These increases in crystallinity may be a product of heating or exposure to solvents, such as methanol during the associated reactions. The second heating scans alone indicate no distinct differences between 1-pot and 2-pot PLLA-*b*PEA, suggesting that these samples have similar heat of thermal transition and ability to crystallize (~20% crystallinity) (Figure 4.2B). While the first heating takes into account the thermal history of the analysed polymer sample, the second heating scan represents the reorganisation of polymer chains by successive melting and re-crystallization (Tamano-Machiavello, Costa et al. 2015), effectively erasing the thermal history of the polymer and resulting in an investigation into the bulk thermal capacitance. DSC scans and calculated crystallinity of both PLLA-*b*PEA conditions during the second heating indicate minor variations from the inherent crystallinity potential of pristine PLLA. These data suggest that the crystallization and chemical reactions occurring through SI-ATRP, as observed from first heating scans, do not drastically affect the availability of nucleation sites for PLLA crystallization (Figures 4.2A and B). All scans show glass transition and melting temperatures within the same range as bulk PLLA, ~60°C and ~160°C respectively, showing that neither 1-pot nor 2-pot SI-ATRP impact on these bulk characteristics. However, the inclusion of additional melting peaks at ~150°C, exclusively found in first heating scans of PLLA-Br and the second heating scan of 2-pot PLLA-Br, highlight the inclusion of the initiator. The addition of BIBB on these surfaces providing an additional melting peak in these spectra. Second heating scans of 1-pot PLLA-Br may resemble that of PLLA due to smaller concentration or chemical composition of the pyridine linked initiator providing diminished changes in thermal properties. Cooling was performed at the relatively high rate of -20 °C per minute, which may have inhibited re-crystallization at this step however

allowed for examination of crystallization properties upon second heating. Generally, these DSC analyses show no distinct differences in thermal properties between PLLA-*b*PEA pot conditions, but do indicate altered heating properties of intermediates.

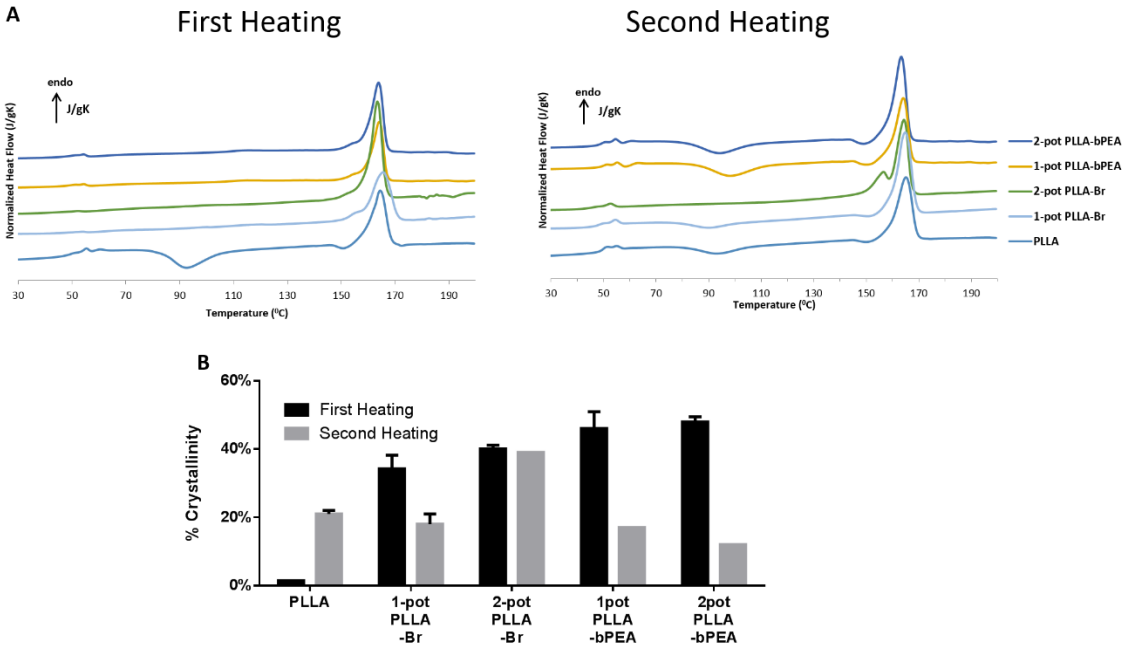

Figure 4.2. Thermal capacitance of SI-ATRP modified samples. (A) DSC heating thermographs of PLLA films treated through the SI-ATRP protocol. First heating examines the crystallinity of PLLA after each stage of treatment. Second heating investigates the heat capacity of each intermediate PLLA condition post treatment. **(B)** Crystallinity values of each step of 1-pot SI-ATRP compared to 2-pot conditions, showing both first and second heating. Calculated by measuring the change in enthalpy of heating minus crystallisation over 100% crystalline PLLA. All conditions are significantly different by at least *p < 0.05 unless otherwise stated.

Thermal stability of SI-ATRP-treated PLLA samples was further characterised via thermogravimetric analysis (TGA) (Figure 4.3). PEA thermal degradation was observed to occur at a higher temperature than PLLA, shown by the point of highest rate of weight change, at ~400°C and ~360°C respectively. Both PLLA-*b*PEA pot conditions maintained similar thermal stability to PLLA,

confirming that neither surface modification methodology significantly alters the bulk thermal stability of the PLLA films.

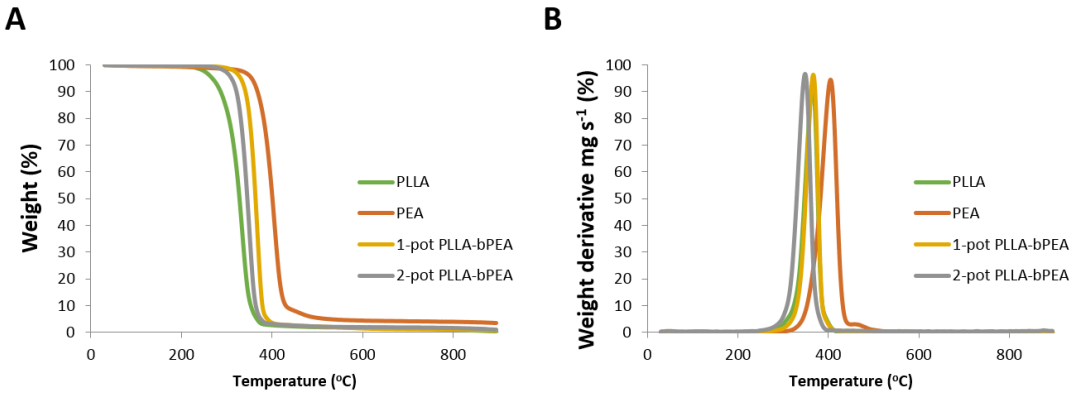

Figure 4.3. Thermogravimetric analysis. Show the percentage weight dependant on temperature and **(B)** first derivative, highlighting the temperature at which the highest weight change occurs of **PLLA**, PEA, 1-pot PLLA-*b*PEA and 2-pot PLLA-*b*PEA.

4.3.3 Physico-chemical characterisation

FT-IR, DRS and XPS were utilised to investigate the presence of nanoscale PEA brushes. While the relatively small concentration and similar chemical composition of PEA comparatively to the bulk PLLA make identifying the products of SI-ATRP difficult, some markers were identified via FT-IR (Figure 4.4A). The addition of a peak on both PLLA-*b*PEA and PLLA-Br samples at 920 cm^{-1} (Figure 4.4A and B), corresponding to a 1,2,4-trisubstituted carbon bonding, indicates the immobilized BIBB backbone maintained as an initiation point by the PEA brushes that are subsequently formed. Elongation of the peaks at 1350 and 750 cm^{-1} on 2-pot PLLA-*b*PEA, showing the presence of alcohol groups and carbon-hydrogen respectively, represent the accumulation of these groups due to the inclusion of PEA onto the surface of PLLA. This suggests that aminolysis is a more efficient functionalisation methodology, as it produces larger densities of PEA brushes onto the surface and therefore larger concentrations of these chemical groups.

By comparing the chemical composition of 1- and 2-pot products we can note differences in the initiator immobilisation mechanisms. Generally, the PLLA-Br samples have very similar FT-IR spectra, possessing peaks at 800 cm^{-1} and 1000 cm^{-1}, which are products of immobilisation of the initiator and are subsequently removed with 2-pot polymerisation. These peaks are found to be maintained on 1-pot PLLA-*b*PEA conditions (Figure 4.4B), suggesting retention of immobilised initiator post polymerisation. In fact, all 1-pot samples are observed to possess elongation of the peak found at ~1250 cm^{-1}, which may be due to the addition of nitro compound (N-O stretching) caused by the pyridinolysis of PLLA.

Generally, we are able to observe the conservation of characteristic chemical stretching of immobilisation products on 1-pot SI-ATRP-treated samples. This suggests that while immobilisation does occur on these surfaces, pyridinolysis produces a less favourable surface initiator for EA polymerisation compared to aminolysis.

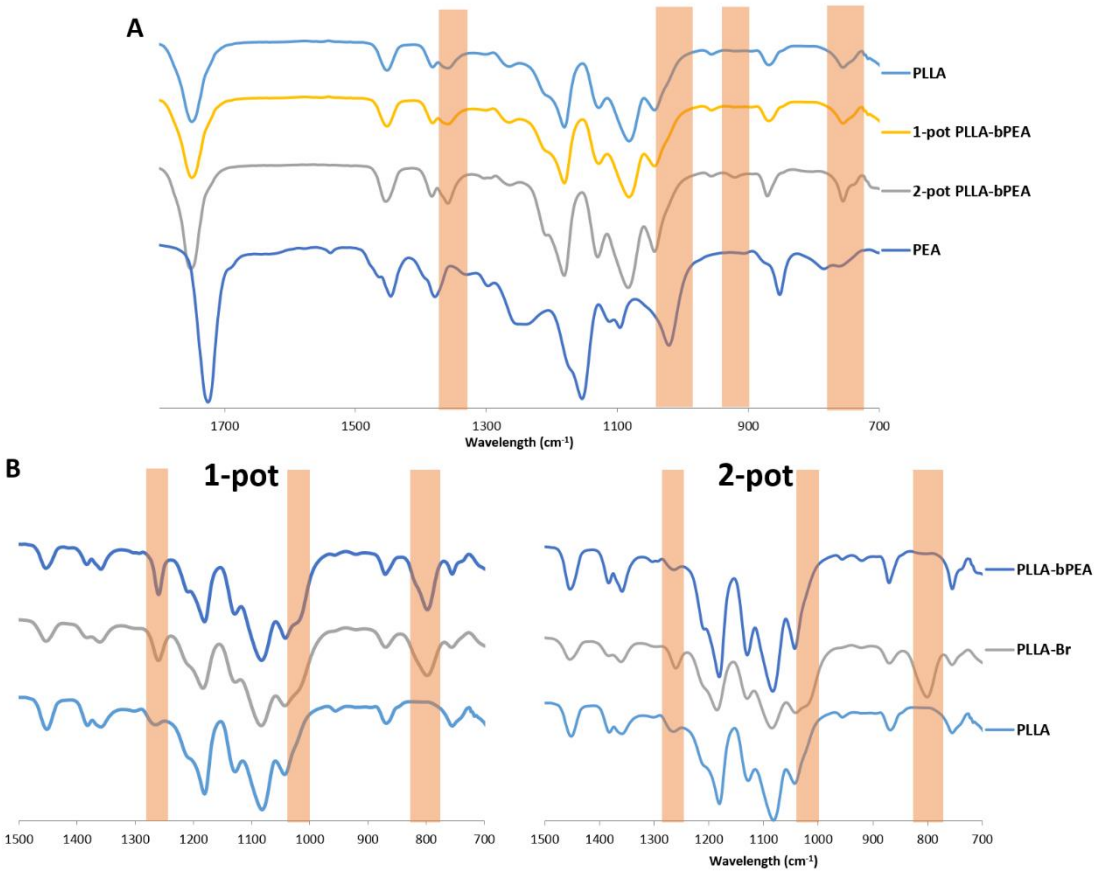

Figure 4.4. Surface chemical characterisation. (A) FT-IR analysis of PLLA, 4 hour polymerised 1- and 2-pot PLLA-*b*PEA and PEA. Highlighted areas at 750 cm^{-1}, 920 cm^{-1}, 1000 cm^{-1} and 1350 cm^{-1}. **(B)** Comparison of 4 hour polymerised, 12 hour brominated and pristine PLLA FT-IR scans of either 1-pot (left) or 2-pot (right). Highlighted areas at ~800 cm^{-1}, 1000 cm^{-1} and 1250 cm^{-1}.

Further chemical characterisation of the SI-ATRP products using dielectric relaxation spectroscopy (DRS) reveals the presence of a ß-relaxation peak on PLLA-bPEA and PEA samples (Ribelles, Duenas et al. 1989) (Figure 4.5 A). This peak found on PEA at -60°C is observed to be shifted, potentially due to the surrounding PLLA bonds, to -120°C on PLLA-*b*PEA samples (Kyritsis, Ribelles et al. 2004). The presence of PEA beta relaxation suggest that brushes have been formed on the surface of PLLA, corresponding to this additional chemical characteristic (Williams 1966). Moreover, this ß-relaxation peak is more pronounced on 2-pot PLLA-*b*PEA samples, suggesting a higher abundance of PEA chains compared to 1-pot surfaces.

Analysis of surface chemical composition via XPS showed significant differences between bromination strategies, as shown by XPS of 1- and 2-pot PLLA-Br samples (Figure 4.5B). Both surface functionalisation methodologies introduce elemental nitrogen and bromine onto the surface, showing successful aminolysis and bromination. C1s carbon spectra reveal that while 2-pot PLLA-Br samples maintain a PLLA-like spectra, 1-pot conditions have a dramatically altered carbon binding conformation, possessing predominantly carbon-carbon bonding and a significant loss of the carboxyl and ester bonding environments within the top 10 nm of the surface. The carbon-carbon peak is also shifted -0.8 eV from standard PLLA on 1-pot PLLA-Br suggesting these carbon are further bound in a stronger chemical bond, potentially in C=C sp2 hybrid as found within pyridine. A distinct loss of ester group oxygen bonding peak, suggesting a loss or masking of this PLLA binding domain.

Peak fitting PLLA-*b*PEA spectra utilising control PLLA and PEA spectra models show that while 2-pot conditions can be modelled as composites of both polymers, surfaces of 1-pot samples are distinctly chemically altered from PLLA (Figure 4.5 C and D). Additional sp2 carbon peaks on both 1-pot conditions, as observed post initiator immobilisation suggest a considerable and maintained

chemical alteration to the PLLA surface. This peak shift could be attributed to the inclusion of carbons bound in an aromatic cyclic ring, occurring with inclusion of pyridine through pyridinolysis. The carbon-carbon bonds formed from 1-pot immobilisation (Figure 4.5B) and retained on 1-pot PLLA-*b*PEA conditions (Figures 6C and D dark blue peak), represent a less favourable chemical surface modification, potentially masking the presence of PEA brushes on these surfaces. These sp2 hybrid or tertiary bound carbon molecules are abundant on all 1-pot PLLA-*b*PEA samples and a smaller amount can be speculated to be present on 2 hour 2-pot PLLA-*b*PEA (Figure 4.5C), but via polymerisation for 4 hours on 2-pot conditions these intermediates are either fully utilised or removed. This would suggest that the 1-pot mechanism produces an inefficient immobilisation of functional initiator on the surface of PLLA and that a lesser degree of pyridinolysis may occur on 2-pot samples. However, 4 hour 2-pot PLLA-*b*PEA highlights that an extended polymerisation time is able to fully quench the surface bound functionalization, producing PEA on the surface. Polymerisation exceeding 4 hours was observed to significantly decrease the structural integrity of the produced films for both functionalisation methodologies (data not shown). Therefore, increasing time of polymerisation is not a suitable methodology for attempted quenching of the initiators formed through the 1-pot mechanism.

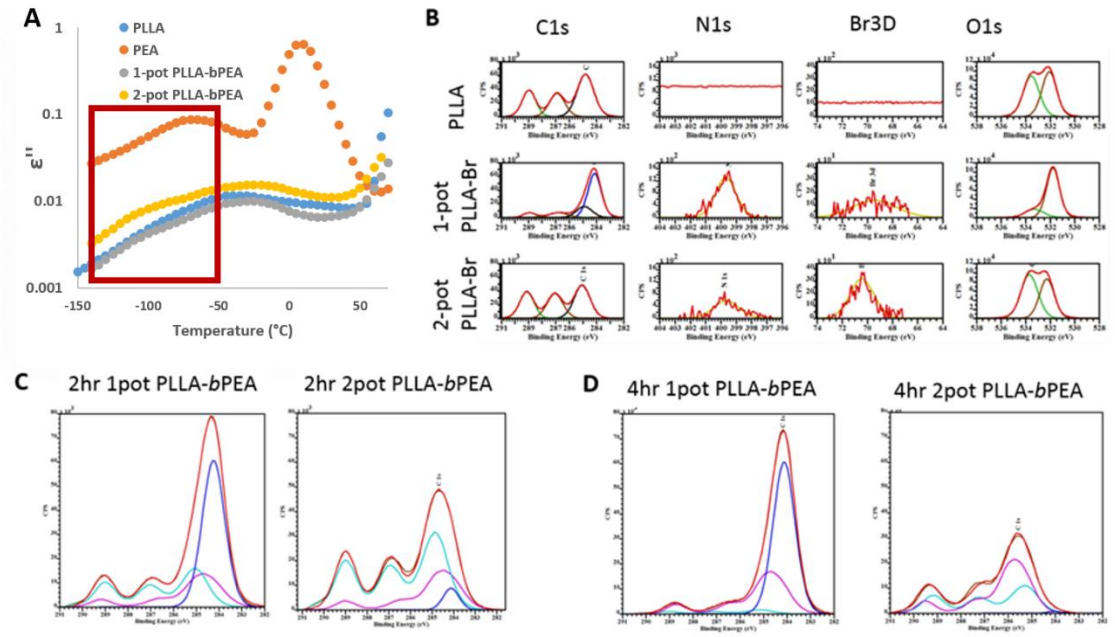

Figure 4.5. Bonding conformation of elements (A) Dielectric relaxation spectrometry analysis of PLLA, PEA, 4 hour 2-pot PLLA-*b*PEA and 4 hour 1-pot PLLA-*b*PEA. Highlighted red square shows ß relaxation peak on PLLA-bPEA and PEA but not found on PLLA. **(B)** XPS spectra of PLLA, 1-pot PLLA-Br and 2-pot PLLA-Br. Carbon, Bromine, nitrogen and oxygen spectra reveal the presence and binding conformation each element. **(C and D)** C 1s core-level showing quantification of polymer line-shape elements for PLLA-bPEA after a **(C)** 2 hour and **(D)** 4 hours polymerisation, using the spectra obtained from control PLLA and PEA as components during line fitting. The bright red line corresponds to the experimental spectra for each sample. The line shapes are as follows: teal line shows the PLLA carbon spectra, the pink line represents the PEA spectra, brown is the combined spectra of fitted peaks. The blue line shape labelled C-C corresponds to potential fragmentation found on 1-pot samples. All binding energies and CPS axes are uniform between graphs to allow comparison of peaks.

4.3.4. Cytotoxicity and cell adhesion

A cytotoxicity assay based on LDH release (Figure 4.6), measuring the cellular stress resulting from interaction with media incubated with the samples, showed that all substrates, from SI-ATRP of either mechanism, are non-cytotoxic to cells. To further assess the cell response on substrates modified with differing SI-ATRP pot conditions, the adhesion of C2C12 cells on 10 μg mL^{-1} FN-coated samples for 4 hours was investigated. Cells seeded onto PLLA and 1-pot samples were observed to have limited spreading and cluster together, whereas on 2-pot surfaces better spreading was seen (Figure 4.7). Cell area and circularity characteristics were maintained from PLLA on 1-pot PLLA-*b*PEA; conversely, on 2-pot samples cells were widely spread as on PEA (Figure 4.8 A and B). The number of focal adhesions were observed to increase on 2-pot samples relatively to PLLA and spin-coated PEA, while cells behaved on 1-pot samples as on PLLA (Figure 4.8C). This indicates that 1-pot pyridinolysis based functionalisation does not produce adequate coverage with PEA brushes to facilitate similar levels of cellular adhesion as shown by 2-pot SI-ATRP.

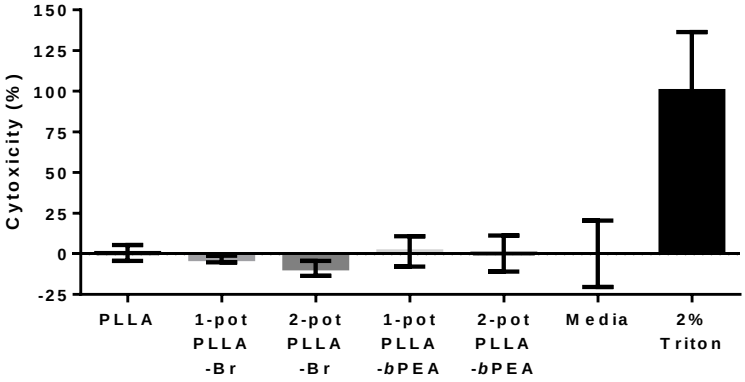

Figure 4.6. Cytotoxicity. Cytotoxicity of media incubated with each sample to cells, normalized to 2% triton x100 and media toxicities. Graphs show mean values and standard deviation, n=3.

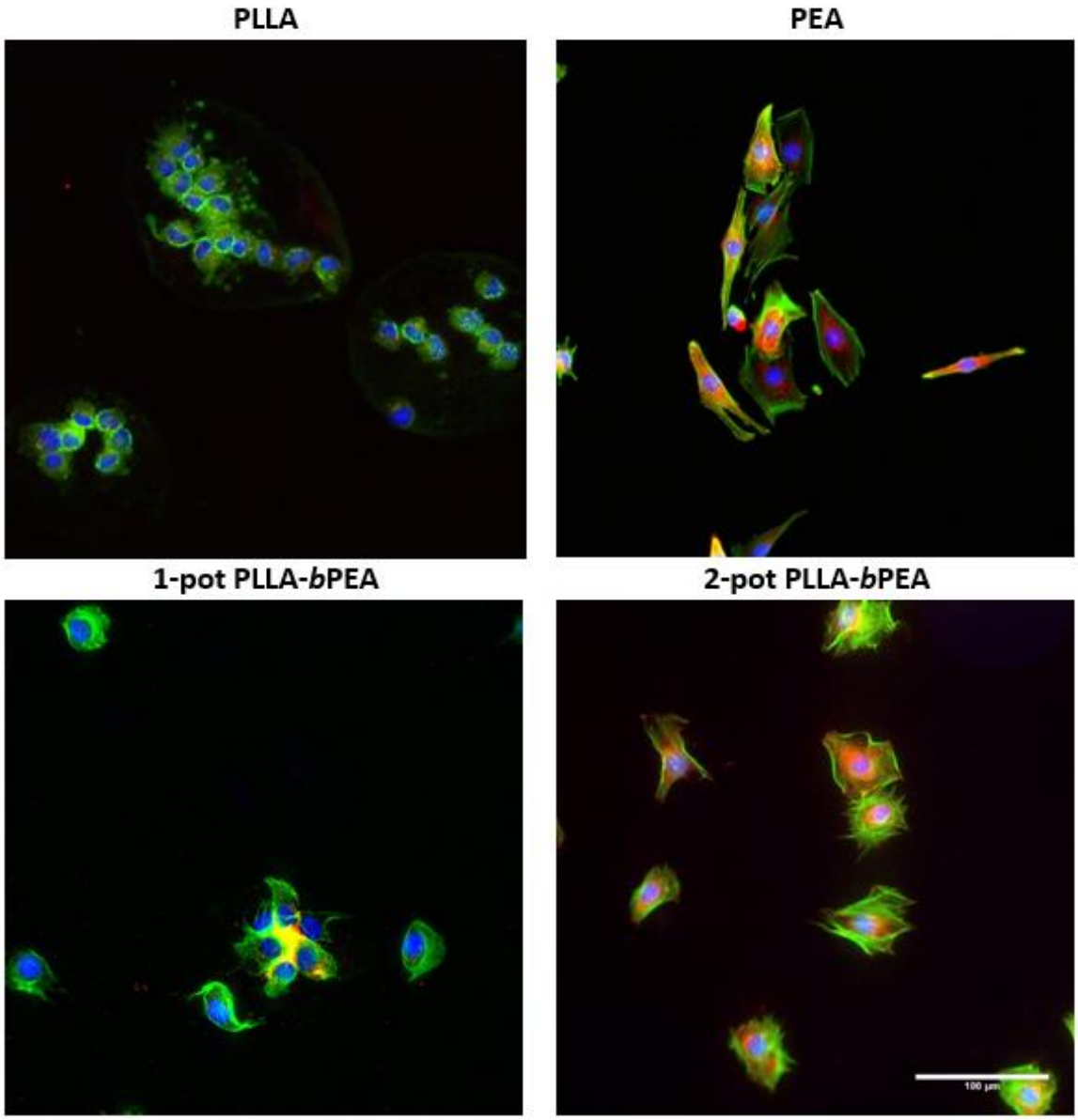

Figure 4.7. Adhesion of C2C12 cells. Representative images of adhering C2C12 cells on FN-coated PLLA, PLLA-*b*PEA and PEA after 4 hours of culture. Samples were stained for actin (green), vinculin (red) and DAPI (blue). Scale bar is 100 µm.

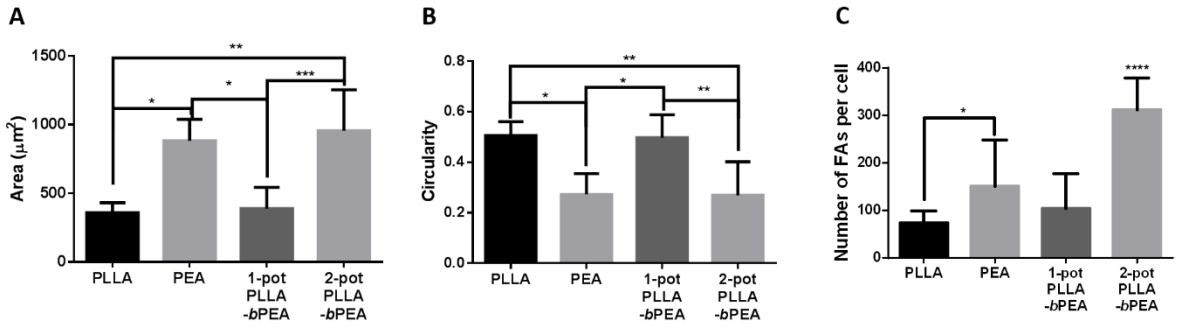

Figure 4.8. Cellular adhesion. Characterisation of representative images of C2C12 cells seeded onto 10 μg mL^{-1} coated surfaces for 4 hours. **(A)** Average cell size. **(B)** Average cell circularity. **(C)** Number of focal adhesions. **(D)** Graphs show mean values and standard deviation, n≥15. *p < 0.05, **p < 0.01, ***p < 0.001, ****p < 0.0001.

4.4. Discussion

Here we have presented the characterisation of the attempted production of an optimized SI-ATRP methodology with a 1-pot bromination, streamlined to avoid aminolysis and instead utilizing an *in situ* pyridinolysis procedure for initial surface functionalization and subsequent initiator immobilization within the same reaction vessel. We have compared this 1-pot mechanism to the 2-pot bromination (aminolysis followed by initiator immobilisation in two separate reaction vessels) to assess its efficacy in the formation of functional PEA brush formation and in the retention of favourable PLLA characteristics.

Characterisation of the modified surfaces showed that while 1-pot bromination did not impact on the RMS roughness of the PLLA-*b*PEA samples (Figure 4.1A), it did significantly increase their hydrophobicity (Figure 4.1B). This already suggests a distinct surface chemical composition compared to the previously established PLLA-*b*PEA samples obtained following a 2-pot bromination. This was further confirmed via XPS characterisation (Figure 4.5), which showed a high abundance of sp2 hybrid carbon bonding on 1-pot surfaces, corresponding to

the cyclic pyridine binding to the surface. This suggest that pyridine is directly bound instead of the amine groups in this 1-pot mechanism and that adequate amine densities on the 2-pot samples has an inhibitory impact on ATRP pyridinolysis. While these 1-pot surfaces possessed bromine and nitrogen peaks post immobilisation (Figure 4.5B), similarly to 2-pot samples, it was not clear whether PEA had successfully been polymerised onto 1-pot surfaces (Figure 4.5 C and D). This may be due to masking of the PEA spectra from excess initiator or could indicate a less abundant immobilisation providing lower surface presentation of polymerisation sites. Evaluation of the bulk film chemistry, via FT-IR (Figure 4.4), highlighted similar addition of chemical groups on both 1-pot and 2-pot PLLA-Br, however did suggest retention of these initiator immobilised groups on 1-pot PLLA-*b*PEA (Figure 4.4B). Therefore, it could be suggested that while 1-pot initiator immobilisation is functional, it does not present sufficiently activated initiator to facilitate polymerisation of EA to the same extent as amine-based SI-ATRP. This may occur due to the presentation of N-terminal ligands in pyridinolysis based ATRP, it has been shown that ligand activity depends on linking units (C4 << C3 < C2), topology (cyclic ~ linear < branched) and nature (aryl amine < aryl imine < alkyl imine < alkyl amine ~ pyridine) (Tang and Matyjaszewski 2006). Therefore, it can be speculated that diminished PEA brush production may result from poor presentation of the potentially highly linked cyclic pyridine ligands produced via pyridinolysis, in interactions with the copper (Cu) based SI-ATRP developed (Braunecker and Matyjaszewski 2007). In this case additional immobilisation reactions on the immobilised pyridine, increasing the linking units while retaining the cyclic structure would inhibit the inherent activity of pyridine based ligands. Dielectric relaxation spectroscopy for both PLLA-*b*PEA surfaces confirmed the presence of supplementary relaxation peaks on treated PLLA (Figure 4.5A); this could indicate the inclusion of PEA onto 1-pot PLLA-*b*PEA at a lower concentration that on 2-pot surfaces. However, further characterisation of these DRS measurements must be carried out to confirm that this added relaxation is exclusively conferred by PEA brushes rather than potentially retained pyridine sidechains bound to the surface (Potolinca, Buruiana et al. 2017). Hence, from chemical analysis of 1-pot SI-ATRP we are able to speculate that while PEA brushes may be formed, they are not evident in either the XPS or FT-IR spectra, which suggests the retention of initiator immobilised onto the surface of PLLA (Figure 4.9).

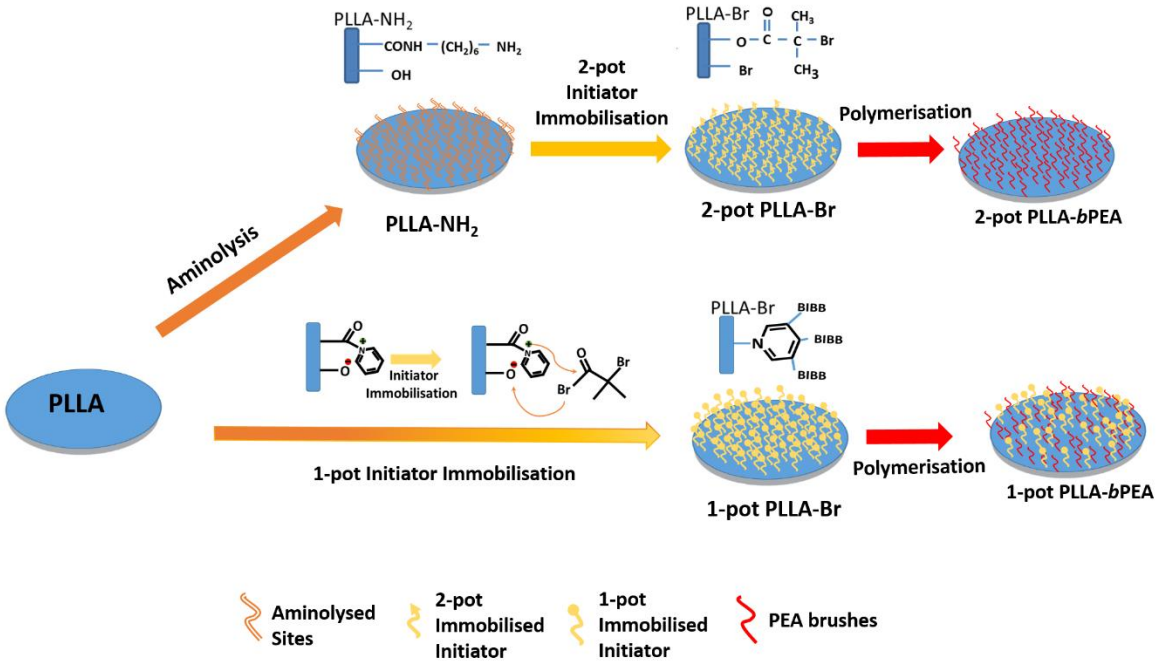

Figure 4.9. Proposed 1-pot SI-ATRP system. A general mechanism of controlled 2-pot functionalisation of PLLA and subsequently successful PEA brush polymerisation. Pyridine based functionalisation of surfaces and subsequent immobilisation of initiator (BIBB) is suspected to occur uncontrolled within the reaction vessel inhibiting the reactivity of the initiator. This results in retention of 1-pot initiator post polymerisation and inefficient PEA brush formation.

Mechanical properties of 1-pot samples also show variability compared to 2-pot samples in certain aspects. While stiffness is maintained within the same mega pascal range as pristine PLLA and 2-pot PLLA-*b*PEA, there is a distinct increase in the Young's modulus (Figure 4.1C). This is suspected to be a result of the different chemical composition of the material surface, which provides additional mechanical stiffness to the PLLA. This changed surface chemistry may also explain the diminished degradation rate (Figure 4.1D). The hydrophobic chemical composition of the 1-pot PLLA-*b*PEA surfaces may present a barrier for proteinase K to diffuse through to degrade the bulk PLLA film. To further investigate this, extended times of degradation would need to be considered, as this characteristic was not observed at 96 hours of degradation. Thermal analyses showed that PLLA-*b*PEA produced from both methodologies retain the same glass transition and melting temperatures (Figure 4.2) and possess similar thermal

stability (Figure 4.3). On the other hand, 1-pot PLLA-Br possessed similar crystallinity potential to bulk PLLA and not the increased potential measured in 2-pot PLLA-Br samples (Figure 4.2 B, second heating). This suggests again that the 1-pot pyridinolysis methodology does not immobilize initiator in the same form or density as 2-pot SI-ATRP, as was also observed via XPS (Figure 4.5B). This may suggest that bromine immobilised via the 2-pot mechanism is able to act as a nucleation point not presented by 1-pot brominated samples. Additionally increased crystallinity of 1-pot PLLA-*b*PEA samples compared to pristine PLLA, produced from SI-ATRP (Figure 4.2 B, first heating), without the degradative impact of separate 1,6-hexanediamine aminolysis-based functionalisation may result in these samples increased bulk stiffness and decreased degradation rate. Collectively, these data show that while 1-pot SI-ATRP does not significantly alter the thermal properties of produced PLLA-*b*PEA, the use of pyridinolysis for surface functionalisation does influence the early degradation rate and Young's modulus of PLLA-bPEA, and the thermal properties of the produced intermediates.

Cell behaviour also confirmed a low yield of functional PEA brush formation on 1-pot PLLA-*b*PEA. Indeed, albeit non-cytotoxic as the 2-pot system (Figure 4.6), the 1-pot samples do not promote the well-spread, focal adhesion forming phenotype that the cells adopt when seeded on 2-pot PLLA-*b*PEA or PEA (Figure 4.7). Instead, these cells interact on 1-pot samples as they do on PLLA. This suggests an insufficient surface presentation of PEA brushes able to drive fibrillogenesis and facilitate enhanced cellular interactions on 1-pot samples (Figure 4.8). Therefore, these results indicate that the 1-pot PLLA-*b*PEA is not an appropriate system for the modification of PLLA and should not be further utilised for tissue regenerative purposes. Cells were observed to be much more rounded and possessed less apparent actin filaments on PLLA treated with 10 μg mL^{-1} FN (Figures 4.7 and 4.8) compared to identical surfaces treated with 20 μg mL^{-1} FN (Figure 3.7). Additionally PLLA-*b*PEA was observed to facilitate increased numbers of FA comparatively to PEA at lower FN concentrations (Figures 3.9 and 4.8). Potentially the thicker FN nanonetworks (Figure 3.3 and 3.4) formed on these surfaces require less protein to facilitate improved cellular adhesion than PEA.

4.5. Conclusion

The alternative methodology, based on pyridinolysis, presented in this chapter to try and streamline the SI-ATRP procedure, was observed to confer to the modified samples slightly increased stiffness and resistance to short-term degradation, while maintaining thermal capacitance and stability. However, it did not provide sufficient densities of chemically functional initiation sites for polymerisation of ethyl acrylate. This short-coming of the 1-pot system is a critical issue in its development for tissue engineering applications. While potential optimization of this system and continued characterisation of the produced samples could be conducted to address this issue, these are not required since we have confirmed that 2-pot SI-ATRP is instead functional.

5. Growth factor presentation on PLLA-*b*PEA and translation from 2D to 3D scaffolds

5.1. Introduction

In order to assess the translation potential of the SI-ATRP system developed and optimised in *Chapters 2* to *3*, we aim here to apply the developed methodology to three-dimensional scaffolds composed of medical grade PLLA and relevant for future clinical use in regenerative medicine, particularly for bone regeneration. The final objective is to produce fully biocompatible and implantable 3D PLLA scaffolds on which the FN nanonetworks induced by the grafted PEA brushes would be able to interact with the cells, ideally mesenchymal stem cells of the host, enhancing their differentiation through further synergistic interaction with locally adsorbed growth factors. To achieve this aim, a 3D printing methodology was used to manufacture medical grade PLLA scaffolds with controlled architecture and key SI-ATRP-mediated characteristic variations to the polymer properties were investigated so as to ensure appropriate translation of the system from 2D films to 3D scaffolds. In order to exploit the ability of surface-initiated FN nanonetworks to sequester and locally present clinically relevant growth factors, we also aimed to further characterise our system, ensuring that FN-coated PLLA-*b*PEA retain the enhanced availability of the Heparin II binding domain of FN, in a similar way as the improved exposure of the PHSRN motif was retained. Indeed, this domain, when exposed, is able to bind and favourably present a wide range of growth factors, including BMP-2. This solid-phase presentation of BMP-2 via FN nanonetworks has been previously hypothesised and shown to synergistically improve osteogenic differentiation of MSCs *in vitro* and *in vivo* (Martino and Hubbell 2010, Martino, Tortelli et al. 2011, Cantini, Gonzalez-Garcia et al. 2012, Llopis-Hernandez, Cantini et al. 2016, Salmerón-Sánchez and Dalby 2016). To implement these characterisations several methodologies utilised with the 2D films were repeated to compare the properties of 3D scaffolds to their 2D counterparts. The Hep II growth factor binding domain availability was investigated along with the abundance and localisation of BMP-2 molecules on the PLLA-bPEA surfaces. Finally, MSCs were cultured on 2D and 3D PLLA-*b*PEA samples, with the aim to establish the potential for the developed SI-ATRP methodology to induce controlled differentiation in the cell type that would be used *in vivo*.

5.2. Material and methods

5.2.1. Preparation of 3D PLLA-bPEA scaffold: Circular scaffolds were designed (BioCAD software, Regen HU) with 90° perpendicular fibres between layers allowing for ~0.05 mm^2 pore size, to ensure sufficient diffusion of cells and solutions to the centre of the scaffold. Scaffolds were designed with a diameter of 10 mm and 1 mm height, made up of 8 individual crossing layers. Medical grade PL18 PLLA (Corbion PURAC) pellets were purchased for the production of the scaffold. Printing was performed in a RegenHU 3D Discovery bioprinter within a custom-built enclosure with an air temperature of 27°C and 35% relative humidity. First, PLLA pellets were melted at 210°C for >2 hours, extrusion was performed with a speed of 12 rpm, needle gauge of 0.33 mm, needle temperature of 200°C and 2 bar extrusion pressure to produce a fibre thickness of 0.15 mm and a line space of 0.16 mm.

Produced 3D PLLA scaffolds were SI-ATRP treated as previously described, with the exclusion of magnetic stirring during bromination and polymerisation and extension of all washing steps to a minimum of 144 hours and extensive vacuum drying for > 20 hours at room temperature to remove excess washing solutions.

5.2.2. Atomic force microscopy: Atomic Force Microscopy was used to visualise topology before and after FN coating in all conditions on samples in air conditions. FN-coated samples were rinsed with water after FN adsorption and gently dried with a nitrogen flow, for imaging in air. Height and lock-in phase images were taken in AC mode using a Nanowizard 3 Bioscience AFM (JPK, Berlin Germany). Scans were made using cantilevers with a resonance frequency of 75 kHz and a force constant of 3 N m^{-1} (MPP-21120 from Bruker, Billerica, MA).

Force spectroscopy curves were obtained, after calibration of cantilever sensitivity and spring constant, using ~30 Nm^{-1} cantilevers with a 20 µm diameter spherical silica tip. The cantilever was approached to the surface with a constant speed of 2.0 µm s^{-1}, at room temperature in ambient conditions, and the Young's modulus was calculated using a Hertz model to an indentation depth of 15 nm (JPK DP software).

***5.2.3. Ninhydrin assay*:** A ninhydrin colorimetric method was utilised to quantify the amount of available amine groups bonded onto the surface of the aminolysed PLLA samples (PLLA-NH_2). Samples were immersed in 1 ml of ninhydrin solution, prepared by mixing 40 ml of 0.35M hydrinatin dihydrate and 4.49M ninhydrin in ethylene glycol with 10 ml of 0.04M lithium acetate buffer at pH 5.2. The samples were then heated to 90°C for 20 minutes and subsequently diluted with 9ml 1:1 2-propanol: deionised water solution. The 2-propanol solution stabilised the blue compound created from the reaction between ninhydrin and amine groups on the PLLA samples. The vials were then vigorously vortexed to include any chromatic sediments and elutes were pipetted into a 96 well plate were the absorbance at 566 nm was read using Tecan NanoQuant Infinite M200 Pro plate reader (Männedorf, Switzerland).

5.2.4. Average area of pores within scaffolds: Variations in scaffold pore architecture were analysed by imaging the individual scaffolds after each step of SI-ATRP (including the related washing protocol and vacuum drying). Samples were imaged using a Carl Zeiss™ Stemi 2000-C Stereo Microscope (Zeiss) and images were analysed utilizing ImageJ to determine the cross-sectional pore area.

5.2.5. Enzymatic degradation: Individual samples were dried to constant weight under vacuum for a minimum of 2 days, samples were then submerged in 0.2 mg mL^{-1} proteinase K enzyme (Sigma, St. Louis, MO) in Tris-HCL buffer (pH 8.6) with 0.2 mg mL^{-1} sodium azide (Sigma, St. Louis, MO). Incubated samples were kept at 37ºC with agitation. The degradation solution was replaced every 24 hours to maintain enzymatic activity. Samples were dried under vacuum to constant weight before final weight was established.

5.2.6. X-ray photoelectron spectroscopy: X-ray Photoelectron Spectroscopy was used to identify the surface chemical composition of samples. All X-ray photoelectron spectra were obtained at the HarwellXPS, Cardiff University and University College London (found at: http://www.harwellxps.uk/). Each sample was analysed at three points with a maximum beam size with a Kratos SUPRA XPS fitted with a monochromatic Al kα X-ray source (1486.69 eV) (High tension: 15 kV, emission current 15 mA) and an electron flood gun charge neutraliser, for Carbon, Oxygen, Nitrogen, Bromine and overview spectra. Samples were affixed to stage

using carbon tape to attach samples to a microscope slide to ensure full electrical isolation from the system. Samples entered the analysis chamber at a pressure below 1 x 10^{-8} Torr. Survey scans were recorded at a pass energy of 160 eV. High resolution spectra were recorded using a pass energy of 20 eV. Analysis of the XPS results was conducted with CasaXPS version 2.3.16 (Casa Software Ltd) with adjustments for transmission and escape depth included in the VAMAS block provided by Harwell.

5.2.5 Growth factor adsorption: Prior to growth factor adsorption, fibronectin (R&D Systems) solutions of 20 µg mL^{-1} in Dulbecco's phosphate buffered saline (DPBS) were adsorbed onto samples for 1 hour for all applications unless otherwise stated. Samples were then rinsed with DPBS, blocked with heat inactivated BSA (Roche) for half an hour, rinsed again with DPBS and finally coated with a solution of BMP-2 (R&D Systems, 355-BM) in DPBS for 1 hour. The concentration of the BMP-2 solution was 100 ng ml^{-1} unless otherwise stated. After growth factor adsorption, samples were rinsed with DPBS before use.

5.2.7. In-Cell Western: Binding domain availability on samples was examined using in-cell western (ICW). Fibronectin coated and BMP-2 treated samples were blocked with Odyssey blocking buffer (LICOR) and incubated with primary antibody, anti-Heparin II domain (Santa Cruz Biotechnologies, sc-18827) or anti-BMP-2 (R&D Systems, MAB3551) in blocking buffer for 1 hour. Samples were then washed 5 times with agitation in 0.1% v/v Tween20/PBS. IRDye® 800CW antibodies were then prepared in blocking buffer and samples were incubated for 1 hour. After washing as before and drying, measurements were made at 800 nm using an Odyssey® system.

5.2.8. ImmunoGold staining of BMP-2: Samples were coated with FN at 20 µg ml^{-1} for 10 min, washed twice with PBS and then coated with BMP-2 (R&D Systems, 355-BM/CF) for 1 hour. Samples were then fixed (4% formaldehyde/PBS) for 30 min and washed with filtered MilliQ water. Samples were first treated with an anti–rabbit BMP-2/BMP-4 primary antibody (Santa Cruz Biotechnology, sc-9003, 1:50) for 1 hour. Samples were then washed (0.5% v/v Tween 20/PBS) repeatedly with agitation before addition of secondary antibody containing 15-nm gold particle–conjugated anti-rabbit immunoglobulin (Aurion, 815.011, 1:20) for 1

hour. Samples were then washed as before, re-fixed and washed with filtered MilliQ water before being dried with a N_2 flow. Samples were finally was visualised via AFM in AC mode using a Nanowizard 3 Bioscience AFM to localise the adsorbed BMP-2 (JPK, Berlin Germany).

5.2.9. MSC culture: human bone-marrow derived mesenchymal stem cells (Promocell) were cultured in Dulbecco's modified Eagle's medium (DMEM, high glucose, without pyruvate, Sigma-Aldrich, D5671) with 10% foetal bovine serum (FBS, ThermoFisher, 10 500-064), 1% v/v penicillin/streptomycin (Sigma-Aldrich, P0781), 1 × nonessential amino acids (ThermoFisher, 11 140-035), and an antibiotic mix consisting of sodium pyruvate (Sigma-Aldrich, S8638), L-glutamate (Sigma-Aldrich, G7513), and 0.5% Fungizone (ThermoFisher, 15 290-018). Cells were incubated in 37°C, 5% CO_2, and harvested by trypsinisation at passage 2-3, all cultures were performed in triplicate. Cells were starved of serum (media with 1% FBS) overnight before experimentation.

For MSC cultures, samples were UV sterilised and subsequently all samples were coated with 20 µg mL^{-1} FN for 1 hour, samples were blocked with heat inactivated BSA (Roche) for half an hour and then coated with 100 ng mL^{-1} BMP-2 (R&D Systems, 355-BM) for an hour. FN controls were covered in PBS-/- during BMP-2 coating. Cells were then seeded on the samples at 2 $x10^4$ cells cm^{-2} on 2D surfaces and at 1.5 x 10^6 cells ml^{-1} within 3D scaffolds for 3 hours in DMEM + 1% P/S + 0.5% fungizone. This was then replaced with media containing 1% serum after 3 hours; 25 ng mL^{-1} BMP-2 supplements were used to drive osteogenic differentiation and added with every subsequent media change, which took place every 2-3 days. After 27 days of culture the cells were washed and then fixed with 4% formaldehyde for 30 minutes at 4°C. The cells were then permeabilised with 0.1% triton X-100, washed and finally blocked (PBS/BSA1%) for 30 minutes at room temperature. Samples were first incubated with anti-OCN primary antibody (Santa Cruz Biotechnology, sc-73464, 1:50), in blocking buffer for 1 hour at room temperature and subsequently washed with washing buffer, PBS/Tween 20 0.5%. Cy3-conjugated secondary antibodies (Vector Laboratories) and BODIPI FL Phallacidin (Thermo Fisher Scientific) were then added for 1 hour at RT. The samples were then washed and mounted with mounting medium containing DAPI

(Vector Laboratories, Inc.) and visualised with a fluorescence microscope (Zeiss AxioObserver.Z1). Images were merged using ImageJ to localise nuclei and actin.

5.2.10. Calcium assay: Matrix mineralization was determined by a direct assay of total calcium produced by the seeded MSCs after 27 days. Concentration of calcium was analysed by complexing o-cresolphthalein complexone (Sigma-Aldrich, Fluka Analytical), 8-Hydroxyquinoline (Sigma-Aldrich) and alkaline buffer reagent (Sigma-Aldrich). A standard calibration curve was established to detect dilutions of 0−1600 µg/mL $CaCl_2 \cdot 6H_2O$ (Sigma-Aldrich). Measurements of calcium were performed according to the following protocol: 500 µL of 1 M HCl was added per well to lyse the cells for 24 hours at 37°C. Samples were then collected, and the o-cresolphthalein complexone solution was applied to obtain the calcium absorbance values which were then converted according to the $CaCl_2 \cdot 6H_2O$ standard curve. The solutions were pipetted into a 96 well plate were the absorbance at 566 nm was read using Tecan NanoQuant Infinite M200 Pro plate reader (Männedorf, Switzerland).

5.2.11. Statistical analysis: Pre-processing and normalization of data are stated in the individual methods sections. Analysis of statistical differences was conducted using student T-test (Graphpad) for two sample comparison and One-way ANOVA for different groups using a Turkey HSD *post hoc* test to compare different groups. Differences were considered significant *$p < 0.05$, **$p < 0.01$, ***$p < 0.001$, ****$p < 0.0001$. All data presented are mean values, error bars are standard deviation.

5.3. Results

5.3.1. Characterisation of 3D medical grade PLLA-*bPEA* Scaffolds.

Medical Grade (MG) PLLA was utilised to facilitate future translatability of the scaffolds; however, this required establishing the characteristics of this PLLA post SI-ATRP treatment. Therefore, several techniques previously used to characterise the 2D PLLA-*b*PEA surfaces (*Chapters 2 and 4*) were utilised to ensure the

successful formation of functional PEA brushes while retaining favourable mechanical properties of the bulk PLLA after SI-ATRP treatment.

Scaffolds were designed in accordance with modern literature, utilising established fibre thickness, pore size and geometry currently utilised for bone regenerative PLLA scaffolds (Patricio, Gloria et al. 2013, Serra, Mateos-Timoneda et al. 2013, Gregor, Filova et al. 2017, Ravi, Shiakolas et al. 2017, Przekora 2019). While alternative fibre geometries, such as 45/135° have been utilised in these studies the fibre geometry has not been shown to significantly impact on long term cellular density, as would be required for osteogenic regeneration (Gregor, Filova et al. 2017). Therefore, an established polymer architecture of 0/90° (Figure 5.1) interconnected fibres with ~150 nm fibre thickness was designed, to allow for sufficient cell invasion and media diffusion while producing standard mechanical integrity of the bulk scaffold (Ravi, Shiakolas et al. 2017). PLLA pellets were melted at 210°C and upon melting immediately extruded at 200°C, so as to minimize damage to the polymer. The pellets were not allowed to cool within the extruder, as re-heating and further printing was observed to produce brittle discoloured scaffolds, therefore all printing was performed immediately after polymer melting. These factors have previously been shown to impact on the thermal stability of PLLA, as increased temperature and time of thermal processing cause increased thermal degradation rates (Taubner and Shishoo 2001, Sodergard and Stolt 2002, Jamshidian, Tehrany et al. 2010). To maintain the desired fibre thickness and porosity the extruder was maintained at 12 revolutions per minute and a gas pressure of 2000 psi was utilised for printing. These parameters produced consistently uniform scaffolds, with defined fibre thickness and pore size.

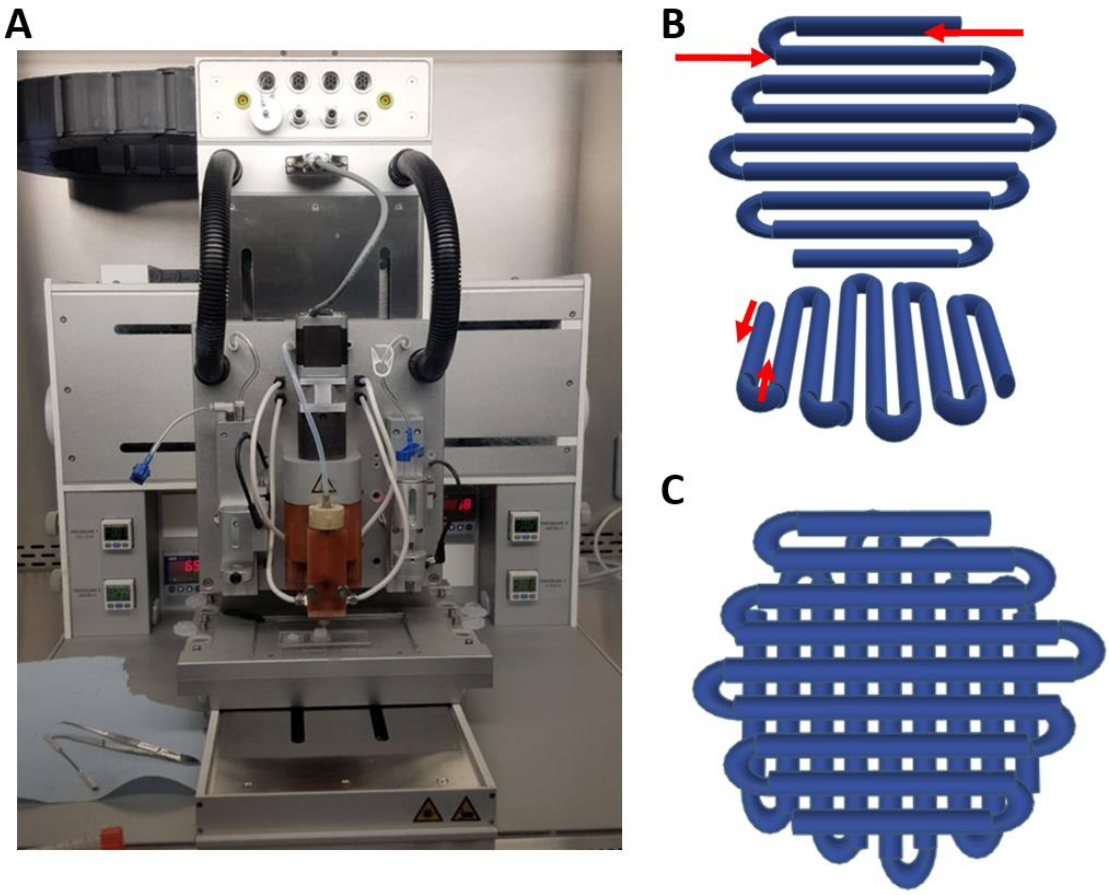

Figure 5.1. 3D printer and printing. (A) 3D printer printing scaffolds. Polymer melting chamber and extruder (orange) attached to mechanised arm controlling printing onto glass cover slips held by vacuum on gantry. **(B)** Glass slides were placed on printer gantry and polymer printed in a continuous line into layers. Red arrow representing printing direction. **(C)** Multiple layers of 90° rotated fibres created a lattice structured scaffold.

While the same principle concept of SI-ATRP was to be maintained when translating to 3D scaffolds it was imperative to ensure certain key steps and characteristics were retained when altering the bulk MG PLLA used. Therefore, firstly upon producing 3D MG PLLA scaffolds were aminolysed, as previously implemented in 2D, this produced healthy concentrations of amines introduced to the scaffolds. Aminolysis is such an important step as it provides the foundations for an abundant and uniform coverage of initiation steps and therefore produced polymer brushes on the surface. A high concentration of available surface amine groups was observed on 3D PLLA-NH_2 surfaces (Figure 5.2A). This concentration of

amine groups was higher than on untreated 3D PLLA and all 2D samples; producing a 5 fold increase in amine density compared to 2D PLLA-NH_2. Both 2D and 3D PLLA was observed to possess similar surface amine availability without treatment. The high concentration of amines indicates a successful aminolysis of the 3D scaffolds, which facilitates further SI-ATRP treatment. As we have previously noted, SI-ATRP produces physical alterations on 2D surfaces, in particular increased surface roughening; this was not observed in 3D scaffolds (Figure 5.2 B) as 3D printing was observed to produce inherently rougher untreated PLLA (2D ~10.9 nm; 3D ~46.5 nm) which did not significantly increase upon SI-ATRP treatment (PLLA-*b*PEA, 2D ~26.0 nm ; 3D ~40.9 nm). This increased surface roughness was speculated to be caused by machining and extrusion during printing, producing a rougher PLLA fibre which masks the surface roughening caused by SI-ATRP, as observed in 2D (Figure 2.4 A). Additionally, with regards to 3D scaffolds we aimed to ensure the retention of pore size so as to enable sufficient cell invasion and media diffusion into the centre of the scaffold. Therefore to characterise this property samples were treated with each step of SI-ATRP and subsequently washed and extensively vacuum dried before imaging (Figure 5.2C). The average area of pores within scaffolds was observed to vary significantly due to one process, increasing due to aminolysis and then reverting post bromination. Therefore we are able to identify that in 3D using medical grade PLLA, aminolysis produces the most significant surface alteration, as opposed to 2D in which initiator immobilisation is responsible for a significant increase in surface RMS. The Young's modulus of individual scaffold fibres, measured via nanoindentation in air with AFM (Figure 5.2D) was observed to be within the same range as 2D controls measured in the same conditions, maintaining for untreated PLLA and for PLLA-bPEA values of ~200 MPa and ~100 MPa, respectively. Degradation with proteinase K (Figure 5.2E) showed similar relationships between PLLA and PLLA-*b*PEA samples but with slightly decreased total degradation percentage with respect to 2D PLLA samples. This was unexpected as 3D scaffolds present much higher surface areas, this variation between 2D and 3D could be due to altered processing of the bulk untreated PLLA before SI-ATRP treatment or variation in the bulk molecular weights of untreated bulk PLLAs purchased from different companies. Crystallization of 3D scaffolds during printing and subsequently due to SI-ATRP treatment may decrease the abundance of amorphous regions of polymer to be enzymatically degraded by proteinase K. Overall these results show that core

surface and bulk properties are retained when SI-ATRP is performed on 3D scaffolds, similarly to what occurred on 2D films

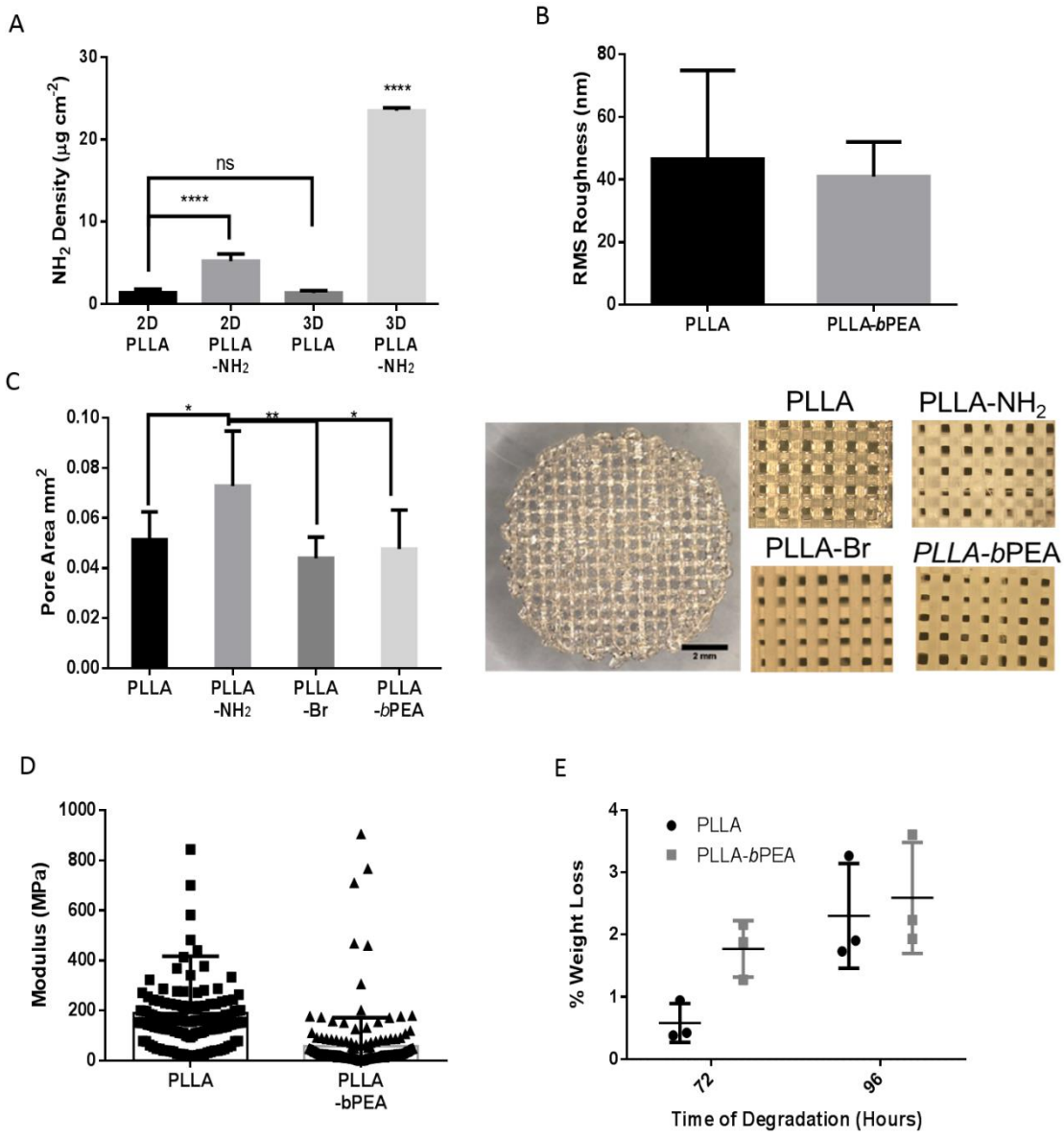

Figure 5.2. Physical characterisation of 3D scaffolds. (A) NH_2 density on 2D and 3D PLLA surfaces aminolysed for 10 minutes with 0.06 mg mL^{-1} 1, 6-hexanediamine at 40 °C normalized by surface area. **(B)** RMS roughness values of fibres from centre of PLLA and PLLA-*b*PEA scaffolds. **(C)** Average area of pores of SI-ATRP treated medical grade PLLA 3D scaffolds after each respective procedural step and extensive vacuum drying to remove excess liquids and potential polymer

swelling. Images show whole PLLA scaffold (scale bar 2mm) and examples of scaffold pores for each step of SI-ATRP. **(D)** Elastic modulus of 3D PLLA and PLLA-*b*PEA fibres measured via nanoindentation using AFM in air. **(E)** Percentage weight loss of 3D PLLA and PLLA-*b*PEA scaffolds after 72 and 96 hours of degradation with 0.2 mg mL^{-1} proteinase K at 37°C. Graphs show mean values and standard deviation. *p < 0.05, **p < 0.01, ***p < 0.001, ****p < 0.0001.

As with 2D surfaces, X-ray photoelectron spectroscopy was utilised to characterise the surface chemical composition of the top 10nm of the scaffold surface and the composition of fibres within cut cross-sections in the middle of the scaffolds (Figure 5.3). In the front facing, outer surface area carbon spectra of all samples were identical to those found in 2D, highlighting no differences between MG 3D scaffolds and 2D samples. As with 2D, PLLA-*b*PEA samples were observed to possess spectra corresponding to a mix of PLLA and PEA, confirming that PEA brushes were produced on the surface of the scaffolds. Carbon scans taken of the centre of the scaffolds were observed to have the same spectra as those on the surface, confirming that SI-ATRP is able to fully permeate the scaffold producing PEA brushes on the surface of internal PLLA fibres of the scaffold. In addition, the presence of nitrogen and bromine was observed throughout the SI-ATRP process; primarily, the addition of bromine post initiator immobilisation on both the outer surface and the internal fibres shows sufficient diffusion of SI-ATRP reagents during treatment. However, it was noted that background nitrogen peaks were present on untreated PLLA and retained post polymerisation on PLLA-*b*PEA. The presence of dual nitrogen peaks on PLLA-Br could result from this background nitrogen being retained and/or interacting with the aminolysis reagents, 1, 6-hexanediamine, or pyridine during immobilisation. The inclusion of a secondary nitrogen binding environment may result in further binding of bromine during initiator immobilisation producing the two observed Br3D peaks; however this does not produce non-functional initiator as all bromine peaks are removed post polymerisation. While this underlying nitrogen may result from the stock MG PLLA, the inclusion of a secondary peak and the presence of defined nitrogen peaks in PLLA-Br, potential due to retention of unused aminolysis sites, indicate that aminolysis is also able to fully diffuse through the entire scaffold and does not only occur on the surface of the scaffold. These XPS results are able to show the

successful production of PEA brushes on the surface and within the 3D PLLA scaffolds.

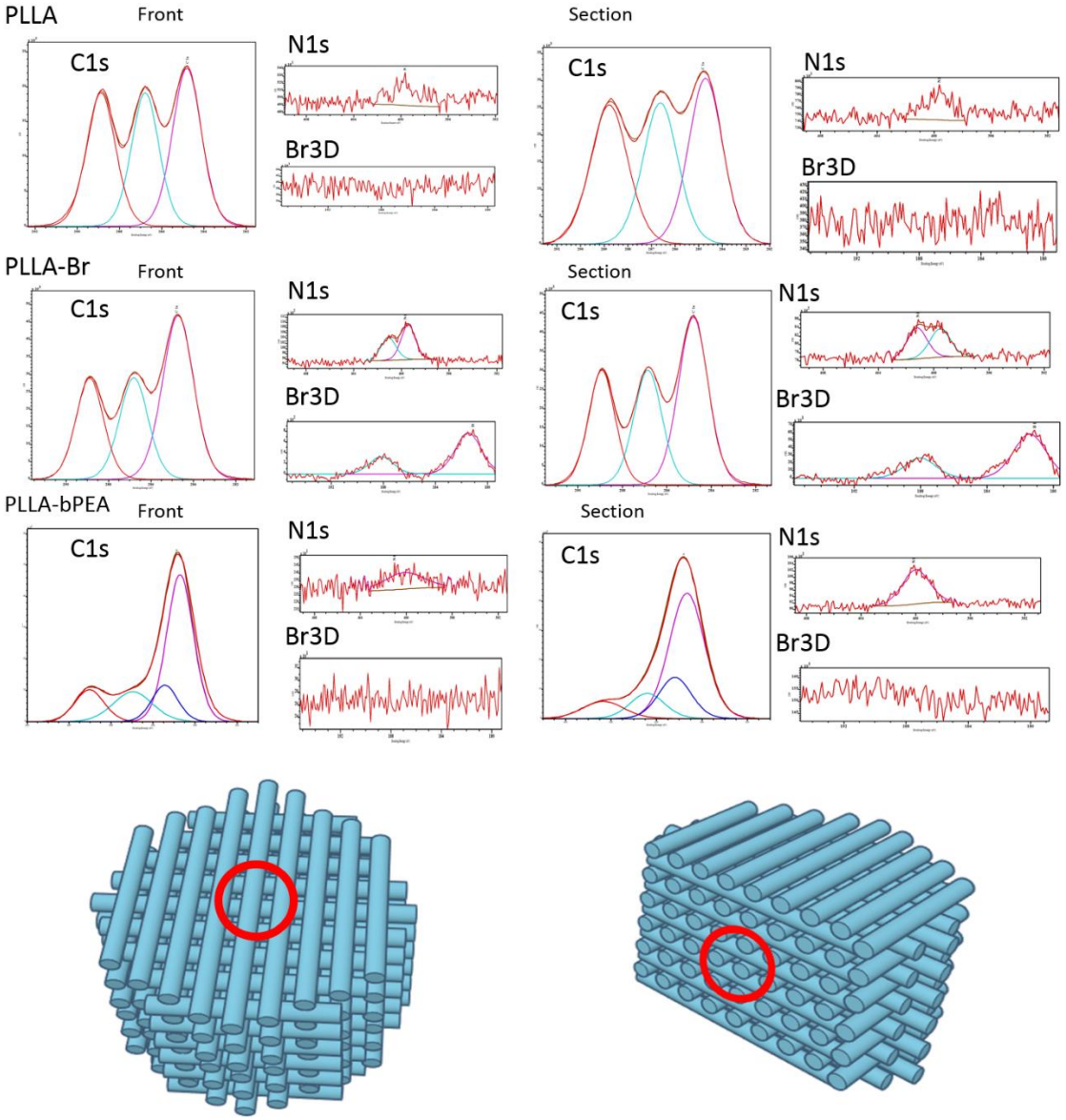

Figure 5.3. C 1s, O1s, N1s and Br3d core-level spectra. Showing the front face and segmented centre of the scaffold of PLLA, PLLA-Br and PLLA-*b*PEA. In all XPS spectra the red curve represents the experimental data. Each section shows the carbon spectra (C1s), simply peak fitted as C-C bonding (pink and blue), C-O-C bonding (blue) and O-C=O group (red). Nitrogen (N1s) and Bromine (Br3D) spectra have been peak fitted where appropriate and indicate the presence of the respective element on the top 10nm of the surface. All carbon spectra range from

281-291 eV, nitrogen from 392 – 410 eV and Bromine from 179- 196 eV, counts per second vary between samples and conditions. Each spectra is representative of 3 replicate scans from each sample, represented below in each corresponding cartoon of scaffolds. Front scans represents scanning the external surface of the scaffold, while side scans are taken from the centre of cut scaffolds, as indicated by the red circle. 3D scaffold representative images created in Tinkercad, Autodesk 123D software.

To further confirm the presence and functionality of the PEA brushes produced on the surface of the fibres of the PLLA-*b*PEA scaffolds AFM was performed to visualise FN organisation after adsorption. Fibres from the centre of the scaffolds were removed and surface topology was visualised via AFM; afterwards, these surfaces were then coated with FN. The AFM images (Figure 5.4) show rough PLLA surfaces, with areas of varying phase, most likely due to machining marks produced during extrusion in the printing process. When treated with FN no nanonetworks are observed on PLLA surfaces, however on PLLA-*b*PEA areas of interconnected nanonetworks can be observed, showing that PEA brushes are able to trigger fibrillogenesis in 3D MG PLLA-*b*PEA scaffolds.

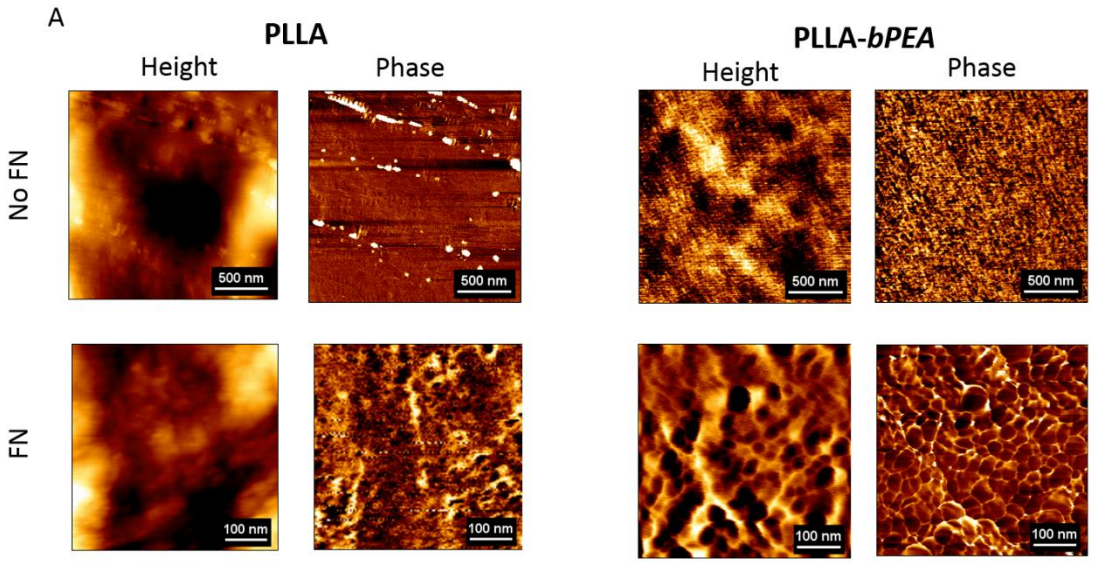

Figure 5.4. AFM of 3D printed fibres before and after FN coating. Height and phase images from tapping mode AFM of struts from 3D **(A)** PLLA and **(B)** PLLA-

*b*PEA before and after coating with 20 µg mL^{-1} FN for 1 hour at room temperature in dry conditions. Fibres were taken from centre of scaffold, see sketch Figure 5.2. Scale bar is 100 nm.

5.3.2. Growth factor binding to PLLA-*b*PEA

The ability of PEA brushes produced from SI-ATRP to drive FN fibrillogenesis has been shown to favourably expose cryptic binding domains associated with nanonetwork formation and cellular adhesion. While enhanced cellular adhesion is desirable, for regenerative medicine applications it is also important to actively drive cellular differentiation. This can be achieved by efficient binding and presentation of specific growth factors, such as BMP-2 for osteogenic differentiation. In order to assess the ability of the FN nanonetworks formed on PLLA-*b*PEA to sequester BMP-2, polymer films and 2D spin-coated SI-ATRP treated PLLA surfaces were investigated using ICW, AFM and immunogold antibody staining to determine the availability of the GF binding domain on FN, the binding of BMP-2, and the location of the bound GF. The availability of the growth factor binding domain (Hep II) of FN on PEA and PLLA-*b*PEA was observed to be higher than on PLLA (Figure 5.5A), indicating that this cryptic FN region is favourably exposed when FN is in fibrillar conformation (Martino, Tortelli et al. 2011, Llopis-Hernandez, Cantini et al. 2016). The relative concentration of BMP-2 on PLLA-bPEA samples was also higher than on both PLLA and PEA (Figure 5.5B), which was unexpected as we have previously shown that the total amount of adsorbed BMP-2 is not impacted by the formation of a FN nanonetwork (Llopis-Hernandez, Cantini et al. 2016). This suggests that the nanonetworks formed via PEA brushes, having shown to be composed by thicker and less interconnected fibrils than on PEA are potentially able to bind higher amounts of BMP-2. To further investigate BMP-2 binding on PLLA-*b*PEA, samples were treated with FN and BMP-2 before being fixed and immunostained with 15 nm immunogold nanoparticles targeting BMP-2 molecules (Figure 5.5 E and D). The co-localisation of BMP-2 to the FN nanonetworks was analysed via AFM. On scPLLA-*b*PEA samples, BMP-2 could be observed to clump onto the FN fibrils, while these large features were not observed on stained PLLA-*b*PEA samples without BMP-2. The BMP-2-immunogold complexes are much more pronounced than FN nanonetworks and show altered

phase profiles than FN fibres. This shows that FN fibrils formed via adsorption of the protein on PLLA-*b*PEA samples are able to favourably present the growth factor binding domain, similarly to those found on PEA, but are also able to bind a higher concentration of BMP-2 molecules, which co-localise with the FN nanonetworks.

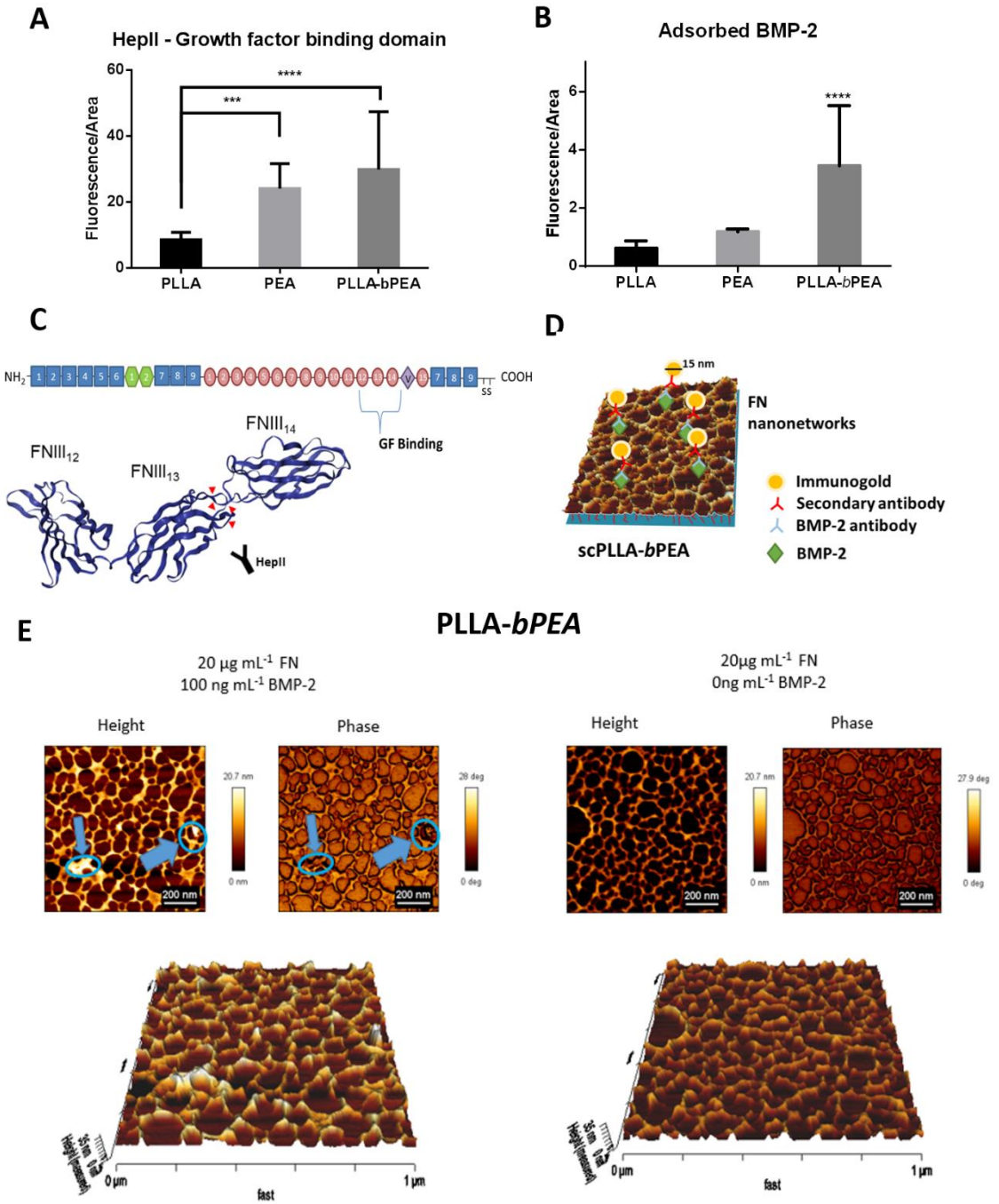

Figure 5.5. Growth factor binding on 2D scPLLA-*b*PEA surfaces. (C) Sketch of fibrillar FN highlighting growth factor binding domain and 3D cartoon of FN GF binding region ($FNIII_{12-14}$); the binding sequence of Heparin II domain, recognised by HepII is highlighted by red arrows. Adapted from PBD ID: 1FNF (Leahy, Aukhil et al. 1996). **(A)** Quantification of the availability of the growth factor binding domain on $FNIII_{12-14}$, as measured by HepII binding via ICW. Performed on spin-coated PEA, PLLA films and PLLA-*b*PEA films. **(B)** Relative surface density of adsorbed BMP-2 on FN treated PLLA, PLLA-*b*PEA and PEA measured via ICW. Performed on spin-coated PEA, PLLA films and PLLA-*b*PEA films. **(C)** Sketch of fibrillar FN highlighting growth factor binding domain and 3D cartoon of FN GF binding region ($FNIII_{12-14}$); the binding sequence of Heparin II domain, recognised by HepII is highlighted by red arrows. Adapted from PBD ID: 1FNF (Leahy, Aukhil et al. 1996). **(D)** Sketch of spin-coated PLLA-*b*PEA surfaces, treated with 20 µg mL^{-1} FN and 100 ng mL^{-1} BMP-2 and subsequently immunostained for BMP-2 with Immunogold nanoparticles. These nanoparticles protrude from the surface highlighting the localisation of BMP-2. **(E)** Height and Phase AFM images of 20 µg mL^{-1} FN treated PLLA-*b*PEA samples with and without BMP-2 adsorption. 3D images show the areas of increased height caused by the presence of BMP-2-bound gold particles of 15 nm diameter. AFM height and phase relative scales have been modified to be within the same range so as to allow for visual comparison. Scale bars are 200 nm and 1 µm. Performed on spin-coated PLLA and PLLA-*b*PEA. Graphs show mean values and standard deviation. ***$p < 0.001$, ****$p < 0.0001$.

5.3.3. MSC differentiation

Having identified that PLLA-*b*PEA is able to favourably induce exposure of GF binding domains, bind BMP-2 and that 3D MG scaffolds are not cytotoxic to cells (Figure 5.6), both 2D and 3D samples were utilised in MSC differentiation assays, to ascertain whether SI-ATRP-treated samples were able to facilitate controlled osteogenic differentiation via the presentation of BMP-2. Due to the opacity and mechanical properties of PLLA and PLLA-*b*PEA scaffolds, immunostaining was not performed on 3D scaffolds, as neither confocal imaging

nor histological sectioning were available as potential methodologies to visualise cells within the scaffolds. Therefore, immunostaining of actin (green), osteocalcin (OCN) (red) and nuclei (blue) were performed on 2D surfaces (Figure 5.7 and 5.8). MSC cells were observed to spread on all surfaces, although the actin cytoskeleton was more developed on PEA containing surfaces, suggesting that as with myoblast cells the FN nanonetworks are able to improve cellular interactions. BMP-2 treated surfaces were noted to possess increased deposition of osteocalcin, a signalling protein indicating mature osteoblast differentiation and bone matrix production (Aubin 2001). Clusters of OCN can be noted in both PEA and PLLA-*b*PEA samples coated with BMP-2 (Figure 5.7); these are clearer at higher magnification (Figure 5.8). These results show that PLLA-*b*PEA surfaces coated with FN and subsequently with BMP-2 are able to drive osteogenic differentiation of MSCs similarly to bulk PEA. `

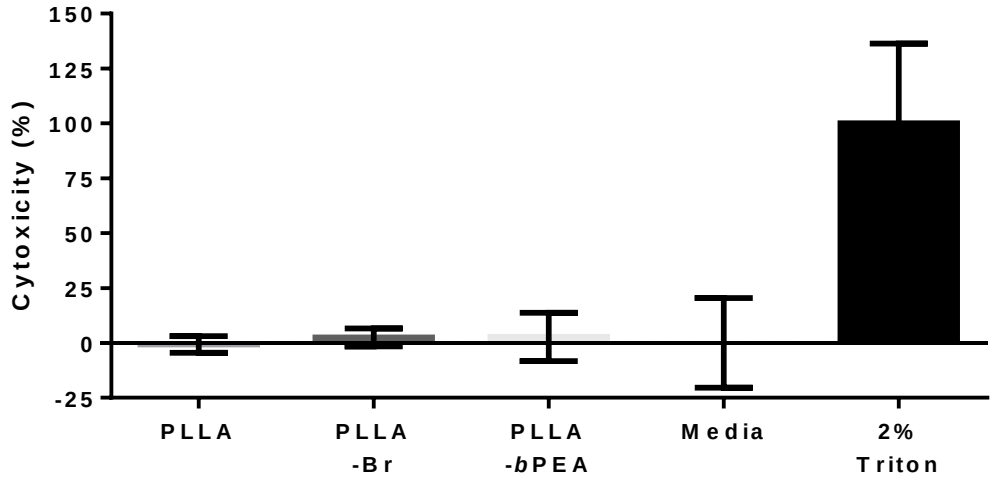

Figure 5.6. Cytotoxicity. Cytotoxicity of media incubated with each 3D sample to MSC cells, normalized to 2% triton x100 and media toxicities. Graphs show mean values and standard deviation, n=3.

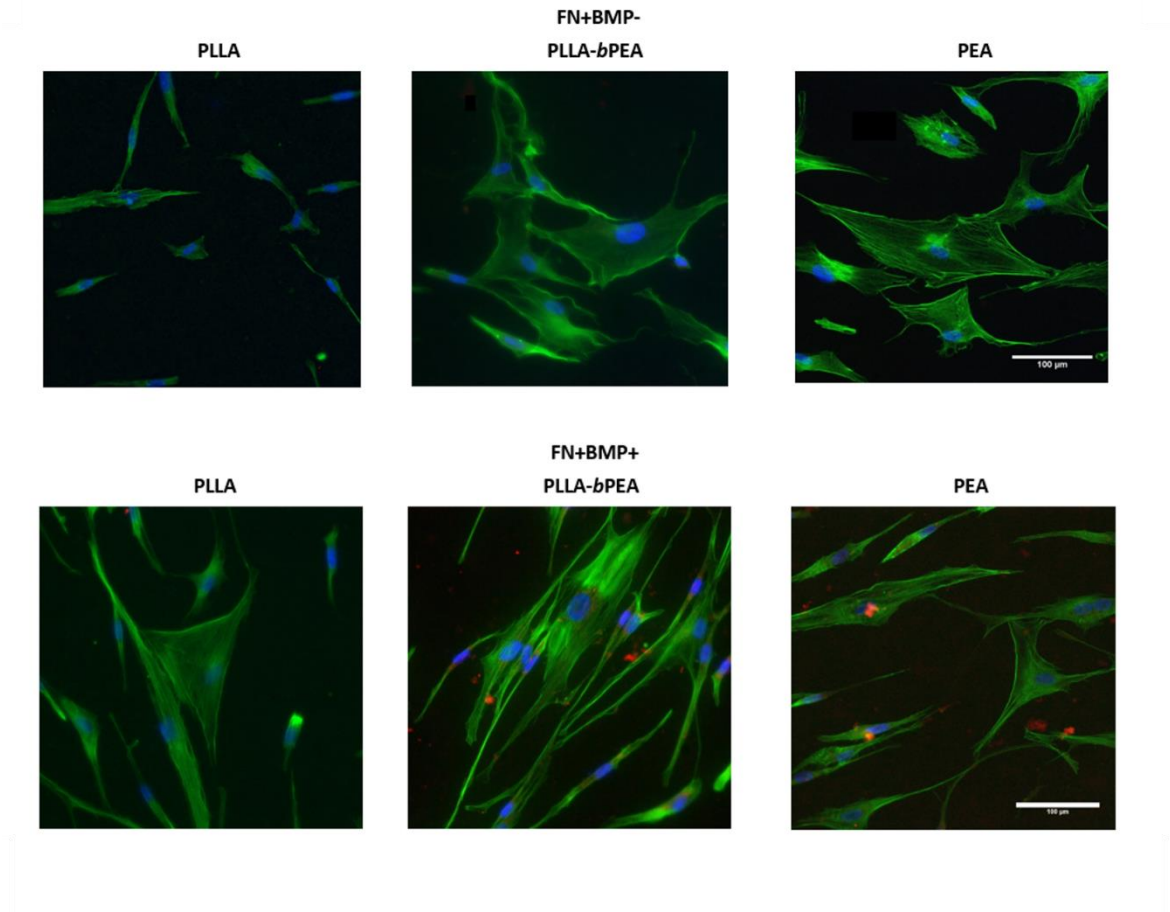

Figure 5.7. Osteogenic differentiation of hMSCs on 2D surfaces. Representative images of MSCs on FN or FN and BMP-2 coated PLLA and PLLA-*b*PEA after 27 days of culture. Samples were stained for actin (green), osteocalcin (red) and DAPI (blue). Scale bar is 100 µm.

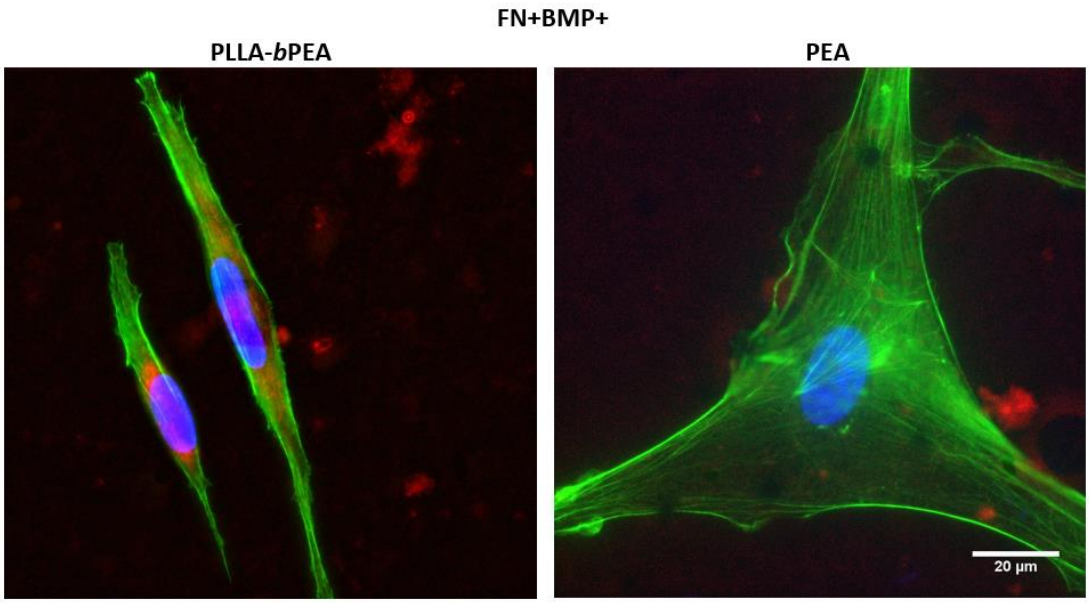

Figure 5.8. Secretion of osteocalcin by hMSCs on 2D surfaces. Representative images of MSCs on FN and BMP-2 coated PLLA and PLLA-*b*PEA after 27 days of culture. Samples were stained for actin (green), osteocalcin (red) and DAPI (blue).

To characterise osteogenic differentiation in 3D scaffolds a calcium assay was performed to analyse the mineralization potential of the differentiated MSCs. No significant amounts of calcium phosphates were observed on 2D surfaces, or in 3D PLLA-*b*PEA scaffolds without GFs (Figure 5.9). The concentration of calcium phosphates was observed to significantly increase when cells were incubated within 3D PLLA-*b*PEA scaffolds pre-treated with BMP-2. This increased mineralization in 3D can be correlated to FN nanonetwork-mediated BMP-2 presentation, as PLLA coated with FN and BMP-2 does not show this increase. This suggests that 3D PLLA-*b*PEA scaffolds are able to outperform their 2D counterparts by presenting increased surface area of produced brushes to individual cells.

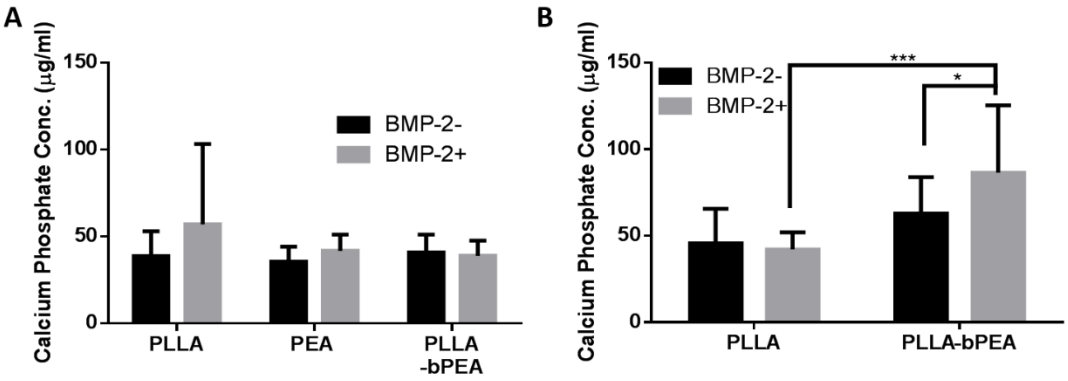

Figure 5.9. Mineralisation by MSCs on 2D and 3D biomaterials. Deposition of calcium phosphates by MSCs cultured on **(A)** 2D surfaces and **(B)** 3D scaffolds after 27 days with and without initial BMP-2 (BMP-2-/+) coating of 100 ng mL^{-1} and subsequent supplements of 25 ng mL^{-1} with each media change. Cells were removed via freeze-thawing and matrix calcium phosphate was solubilized via overnight incubation in 1M HCL. Calcium phosphate concentrations are quantified via comparison to a standard curve. Graphs show mean values and standard deviation. *$p < 0.05$, ***$p < 0.001$.

5.4. Discussion

In this chapter, we have translated our ARGET SI-ATRP from a 2D model system to 3D medical grade scaffolds able to support the growth and differentiation of MSCs, with the objective of establishing the potential of this methodology for regenerative medicine applications.

Initially, the design and production of 3D PLLA-*b*PEA scaffolds was optimized to maintain key surface properties such as initial amine group functionalisation and pore size. The developed printing programme produced consistently uniform medical grade PLLA scaffolds with a defined pore size that maintained their mechanical strength as compared to PLLA films. Application of the established SI-ATRP process, firstly utilising aminolysis, showed successful incorporation of amine groups allowing for a significantly higher density of available amine comparatively to 2D surfaces. The bulk surface modification was

investigated so as to maintain a similar pore size post treatment allowing for effective cellular invasion and media diffusion into the centre of scaffold. The retention of interconnectivity and porosity, signified by the average area of pores are vital for ensuring that the produced polymer architecture of the scaffold is able to facilitate cellular proliferation, migration, nutrient transfer and *in vivo* tissue colonization, which have been shown to be ideal for tissue engineering purposes (Polo-Corrales, Latorre-Esteves et al. 2014, Velasco, Narvaez-Tovar et al. 2015, Gregor, Filova et al. 2017).

The mechanical properties were examined by AFM nanoindentation and enzymatic degradation, these showed comparably similar results to 2D PLLA and PLLA-*b*PEA. Nanoindentation, performed on individual polymer fibres, showed Young's moduli within the same general range as 2D films, both before and after SI-ATRP treatment. This suggests that while a different medical grade polymer was utilised, the core mechanical properties are maintained and SI-ATRP does not dramatically alter this characteristic, as we have previously shown in 2D. As we found with the 2D characterisation the slight decrease in Young's modulus can be correlated to the chemical lysis of the lactide backbone during the aminolysis procedure (Zhu, Gao et al. 2004). Therefore, while there is an increased amine group deposition comparatively to 2D surfaces, due to increased surface area, there is no distinguishable deterioration of mechanical stiffness. Enzymatic degradation, utilising proteinase K, resulted in a similar degradation profile as found in 2D, but the 3D scaffold were observed to degrade slightly slower than their 2D counterparts. Maintenance of the degradation rate is vital when developing an implantable scaffold as it allows for the scaffold to structurally support the tissue to be regenerated after implantation, while gradually reintroducing physical function to cells *in situ* through tuneable degradation (Armentano, Dottori et al. 2010, Ulery, Nair et al. 2011, Saito, Liao et al. 2013, Velasco, Narvaez-Tovar et al. 2015). The surface and bulk characterisation show a clear and successful translation of the SI-ATRP. Generally, the conservation of the bulk characteristics of the printed PLLA scaffolds suggests that SI-ATRP is able to facilitate the desired surface modification while maintaining both stiffness values and degradation profiles, therefore allowing for the continued optimization of the system for regenerative medicine applications. Additionally, mechanical testing of the full scaffold, could be performed to further evaluate bulk

mechanical properties. Porosity and geometry of the scaffold have been shown to impact on the mechanical strength and degradation and therefore modification of these architectural properties may provide a potential further optimisation potential for this system (Ravi, Shiakolas et al. 2017). Therefore, maintenance of these mechanical characteristics post-SI-ATRP modification, unlike photo-induced grafting reactions of PLLA blends (Rasal and Hirt 2009, Hoglund, Hakkarainen et al. 2010), provides the potential for modulation of scaffold stiffness dependant to polymer architecture.

Chemical analysis via XPS confirmed successful grafting of PEA brushes within the entirety of the scaffold. To ensure that SI-ATRP reagents and reactions were able to diffuse and produce PEA brushes, cross sections of the samples were made, allowing for chemical analysis of the central part of the scaffold. As found in 2D, carbon binding regions of the surface closely resembled those of bulk PEA, highlighting that SI-ATRP had been performed on the outer extremities of the scaffold. PEA C1s spectra were also present within the scaffold, which confirmed that SI-ATRP is able to diffuse throughout the scaffold fibres and present PEA brushes in a 3D environment to enclosed cells. The presence of nitrogen and bromine peaks within PLLA-Br scaffolds reinforces the utility and versatility of SI-ATRP, as these data show that all key steps of SI-ATRP occur homogenously throughout the scaffold. The inclusion of additional N1s and Br3D peaks on both PLLA and PLLA-Br, comparatively to 2D PLLA films, are suspected to be chemical remnants from increased aminolysis on 3D samples. This would suggest that not all available amine groups are utilized during bromination, potentially requiring longer times of initiator immobilisation. In either case, these supplementary peaks are removed post polymerisation and corresponding carbon peaks are not drastically altered as they were observed to be in 1-pot SI-ATRP. Therefore we are able to identify that SI-ATRP is able to successfully produce PEA binding motifs both on the surface and within the scaffold. The diffusion of SI-ATRP through the entire scaffold, producing PEA brushes within the centre, shows the viability of this system, allowing for the control of external and internal scaffold surface features, which has previously been an issue for polymeric scaffold (Kosik-Koziol, Graham et al. 2019).

Biological functionality of the PEA brushes on the 3D scaffolds was evaluated via AFM, and demonstrated by the presence of FN nanonetworks. Tightly packed FN nanonetworks were observed on 3D printed fibres from the central part of the scaffold. These densely packed networks may be more clustered than found on scPLLA-bPEA, due to the increased surface roughness or curvature of the fibre. However, the presence of these networks on 3D scaffolds highlights the efficient translation of the SI-ATRP to 3D and indicates a potentially improved modification allowing for the identification of FN nanonetworks from rougher polymer surfaces rather than on relatively smooth spin-coated PLLA, as was observed in 2D. Fibronectin has been shown to improve cellular adhesion on PLLA scaffolds previously (Cronin, Thurmond et al. 2004, Islami, Mortazavi et al. 2018), although these studies did not aim to define or modify the secondary structure of the ECM protein. Surface modification to further improve the biofunctionality of PLLA and similar polymers (Wan, Yang et al. 2003, Ding, Chen et al. 2004, Ho, Hou et al. 2006), such as PCL (Declercq, Desmet et al. 2013, Cheng, Alba-Perez et al. 2019), has shown enhanced FN-related activity and thus growth factor presentation and cellular interactions. SI-ATRP, as a surface modification methodology has been shown to homogenously modify surfaces, producing whole PEA brushes and defined FN nanonetworks within the centre of the scaffolds. This has been highlighted as an issue for plasma polymerisation due to fragmentation of polymer (Cantini, Rico et al. 2012), removal of surface modification due to plasma induced etching (Ding, Chen et al. 2004) or penetrance of plasma treatment into 3D scaffolds (Barry, Silva et al. 2005, Canal, Khurana et al. 2016). Indeed, penetrance of surface modification techniques through scaffolds has been shown to be an issue for both plasma and wet-chemical deposition (Barry, Howard et al. 2006, Cools, Mota et al. 2018), which we have shown via XPS and the presence of FN nanonetworks on fibres taken from the centre of scaffolds to not apply to this SI-ATRP system.

While we had shown a direct translation of the SI-ATRP system to a 3D scaffold, the ability of the *b*PEA-driven FN nanonetworks to sequester and synergistically present BMP-2 had still to be demonstrated. This is fundamental to further characterise the functionality of the SI-ATRP-treated samples for bone regeneration (Figure 5.10). Hence, the availability of the growth factor binding domain on FN and the binding and co-localisation of BMP-2 was examined on 2D scPLLA-*b*PEA samples. InCell Western results showed that both PEA and PLLA-*b*PEA

samples are able to drive enhanced availability of the heparin II growth factor binding domain. While this increased binding domain availability does not facilitate higher concentrations of bound BMP-2 on PEA comparatively to PLLA controls, on PLLA-*b*PEA a higher concentration of BMP-2 is found. Potentially the increased thickness and height of FN nanonetworks as found on PLLA-*b*PEA may allow for improved accessibility of GF binding domains on these networks facilitating increased concentrations of BMP-2 binding. This increase in GF binding comparatively to spin-coated PEA has been shown previously on PEA plasma coated PCL surfaces (Cheng, Alba-Perez et al. 2019), which also produced thicker nanonetworks than on scPEA. Suggesting that much like as plasma surface modification has shown to introduce enhanced GF presentation properties to PCL, SI-ATRP may profess similar properties to PLLA.

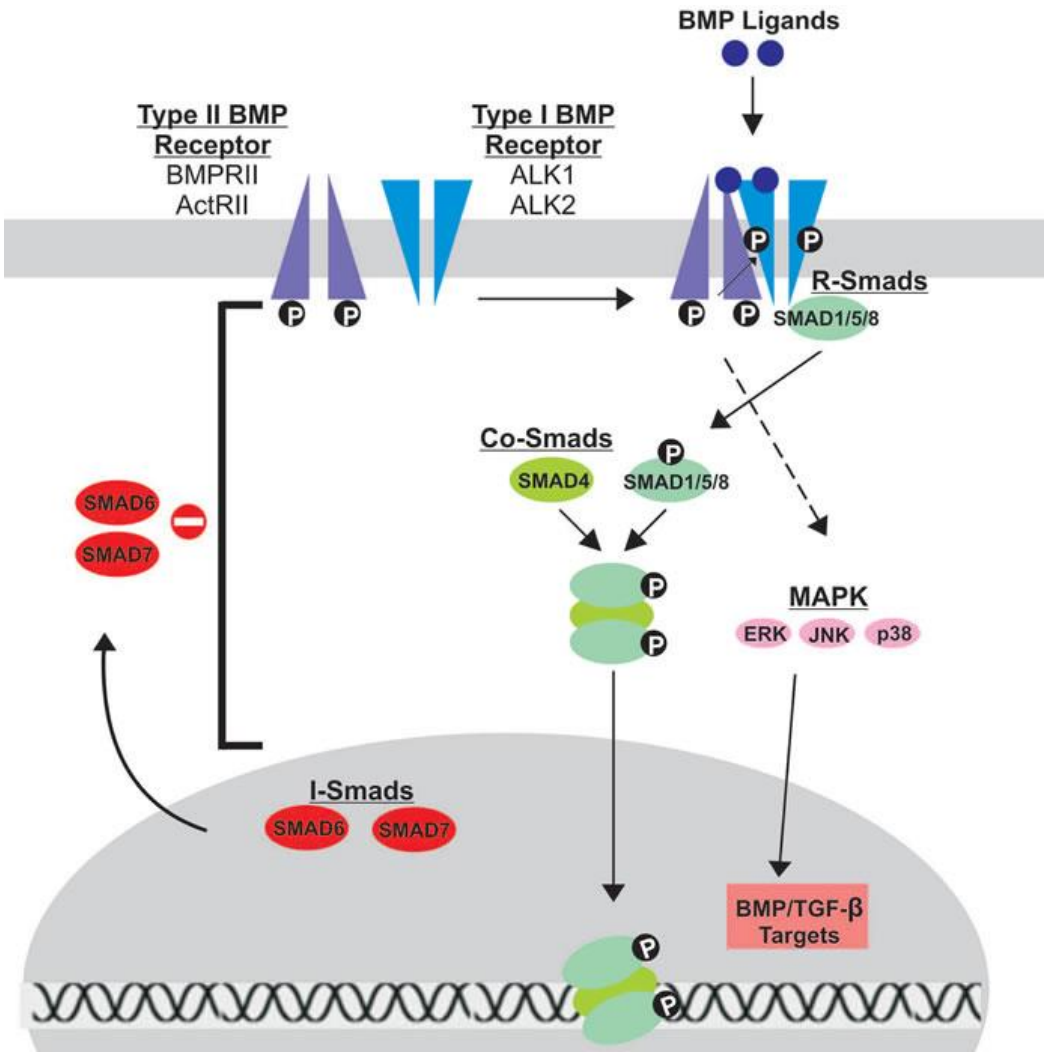

Figure 5.10. Outline of general BMP-2 signalling transduction. From Beederman et al, 2013, BMP signaling in mesenchymal stem cell differentiation

and bone formation, Journal of Biomedical Science and Engineering volume 6(8A): 32–52. (2013)(Beederman, Lamplot et al. 2013)

To characterise the localisation of BMP-2 on these nanonetworks, samples were fixed and stained with BMP-2 targeted immunogold particles of 15 nm diameter. BMP-immunogold nanoparticles were observed to bind in high densities on FN, identified by areas of dramatically increased height and altered phase, no such immunogold particles were observed on samples without BMP-2 treatment. This correlates with previous surface modification techniques utilised for BMP-2 recruitment on FN (Llopis-Hernandez, Cantini et al. 2016, Cheng, Alba-Perez et al. 2019), however unlike on these surfaces thicker FN nanonetworks, produced from conglomeration of FN fibrils on individual PEA brushes may produce areas of BMP-2-immunogold clumping. Generally from 2D scPLLA-*b*PEA samples we are able to show that SI-ATRP is able to increase the availability of fibronectin GF binding domain subsequently facilitating increased concentrations of BMP-2 co-localisation on FN fibrils. This material solid-state presentation of GF has been shown to be more effective than administration of soluble GF for tissue engineering (Martino, Briquez et al. 2015). The site specific binding of BMP-2 on FN allows for synergistic crosstalk between the GFs and integrin receptors, enhancing osteogenic regeneration (Martino, Tortelli et al. 2011). This co-localisation and subsequent synergistic crosstalk, resulting from surface modification aimed at whole FN, professes additional benefits compared to systems utilising heparin binding peptide fragments as it allows for the induction of additional signalling, such as integrin-dependant Smad signalling (Fourel, Valat et al. 2016, Llopis-Hernandez, Cantini et al. 2016).

Having characterised GF binding to SI-ATRP treated FN samples, hMSCs were cultured on 2D surfaces and 3D scaffolds. FN and BMP-2 coated 2D PLLA-*b*PEA samples were able to drive osteogenic differentiation after 27 days, as shown via identification of extracellular OCN clusters showing mature bone matrix formation. These clusters of OCN were abundant on both PLLA-*b*PEA and PEA and not present on PLLA samples, showing that nanonetwork formation and subsequent BMP-2 presentation was able to drive cellular differentiation towards the osteogenic fate. This is in accordance with previous studies showing the osteogenic potential of material-driven fibrillogenesis of FN and subsequent

presentation of BMP-2 (Llopis-Hernandez, Cantini et al. 2016, Cheng, Alba-Perez et al. 2019), allowing for enhanced transduction of the BMP-2 signalling cascade (Figure 5.10). In the 3D scaffolds mineralisation was observed to increase significantly only in the presence of FN-mediated BMP-2 presentation via the PEA brushes, compared to unmodified PLLA scaffolds with or without FN/BMP-2 coating or to PLLA-*b*PEA scaffolds coated only with FN and no BMP-2. This high concentration of calcium phosphates indicates formation of mineral bone matrix, a process performed by osteoblasts. Research has shown that while high calcium concentrations in scaffolds can signify osteogenic differentiation (Raghavendran, Puvaneswary et al. 2014, Al-Jarsha, Moulisova et al. 2018), it can also stimulate further osteogenic activity in PLLA scaffolds (Niu, Liu et al. 2017). This difference was not measurable on 2D samples, suggesting that while PLLA-*b*PEA is able to favourably bind and present BMP-2 in 2D, this presentation is not as effective as in 3D. This suggests that 3D scaffolds may be a more favourable system to direct cellular differentiation, as the 3D presentation of PEA brushes, FN nanonetworks and BMP-2 molecules may enhance or quicken the osteogenic differentiation potential of the system. This behaviour has been shown in other polymer osteogenic systems, where the same surface was utilised in both 2D surfaces and 3D scaffold (Tian, Heng et al. 2008, Persson, Lehenkari et al. 2018). These results indicate that osteogenic differentiation is enhanced by the improved biomimicry provided by the 3D architecture (Sikavitsas, Temenoff et al. 2001). Indeed, these results are similar to plasma polymerisation of PEA onto PCL surfaces to induce osteogenesis (Cheng, Alba-Perez et al. 2019). Both these systems utilise BMP-2 at lower concentrations than established murine osteogenic models (Shekaran, Garcia et al. 2014) and the current clinical gold standard (Woo 2012, Llopis-Hernandez, Cantini et al. 2016), highlighting the potential for SI-ATRP as a methodology for inclusion of additional biofunctionality on established biomaterials. In general, long term MSCs differentiation and mineralisation of the surrounding extracellular matrix have shown that the 3D PLLA-*b*PEA scaffolds are able to facilitate and drive growth factor-regulated osteogenic differentiation.

5.5 Conclusion

In conclusion, here we have presented the translation of SI-ATRP to 3D scaffolds using medical grade PLLA. The PEA brushes produced from this process are able to induce favourable presentation of the cryptic growth factor binding domains on the adsorbed FN, the binding and subsequent presentation of BMP-2 to drive mesenchymal stem cell differentiation through the osteogenic pathway. This results in an implantable scaffold able to drive osteogenic differentiation and mineralisation, further establishing the utility of SI-ATRP for the surface modification of biodegradable biomaterials in regenerative medicine.

6. Thesis conclusion and future perspectives

6.1. General discussion

The aim of this PhD project has been to supplement the functionality of an established biodegradable polymer, poly L-lactic acid with polymer brushes of poly (ethyl acrylate), which are able to drive fibrillogenesis of fibronectin and facilitate enhanced cellular interactions. In this dissertation we have presented the development of a surface initiated atomic transfer radical polymerisation procedure, utilising an activator regenerated electron transfer mechanism for cost-effective, quick and efficient surface modification. We have then demonstrated the ability of the produced polymer brushes to control protein organisation and growth factor presentation, consequently driving cell response in scaffolds for tissue engineering applications.

The production and optimization of this system entailed tailoring the SI-ATRP system to drive brush formation while maintaining favourable bulk PLLA characteristics. Preservation of these properties, predominantly the mechanical strength and degradation rate, needed for tissue engineering purposes, ensures that produced PLLA-*b*PEA surfaces can be utilised as implantable functional and bioactive scaffolds (Ulery, Nair et al. 2011). Initially, the procedure was developed and established using 2D PLLA films. Bulk properties of the films were maintained. PEA brush formation was optimised by tuning each step of SI-ATRP; aminolysis, initiator immobilisation and polymerisation. Initially, aminolysis was optimised with respect to duration, temperature and concentration of treatment, and a procedure which produced a sufficient coverage of available amine groups on the least altered PLLA topography was established (Xu, Zhao et al. 2007, Xu, Yang et al. 2011). These aminolysis functionalisation parameters were observed to decrease the hydrophobicity of PLLA films, through the incorporation of hydrophilic surface amine groups (Zhu, Gao et al. 2004, Tokiwa and Calabia 2006). Incorporation of the bromine based initiator was observed to revert the hydrophobicity to similar levels as PLLA films although was noted to significantly increase surface roughness (Yu and Luo 2011, Kang, An et al. 2018). This change in topography was hypothesised to arise from the exothermic bromination reaction, which also increased the crystallinity of the bulk PLLA films. While crystallinity increased post initiator immobilisation, thermal stability of PLLA was not dramatically impacted by SI-ATRP treatment. Ultimately, maintenance of the

degradation rate and Young's modulus of PLLA and PLLA-*b*PEA confirmed that SI-ATRP is functionally able to maintain the favourable characteristics of bulk PLLA ideal for tissue engineering applications, while implementing controlled surface modification.

Validation of polymer brush formation was performed via chemical analysis of SI-ATRP-treated samples. Chemical analysis confirmed the presence PEA on the surface of PLLA by incorporation of additional bonding domains attributed to PEA as observed via FT-IR, introduction of ß relaxation spectra measured via DRS, like those found on PEA, and surface chemical composition via XPS corresponding to a mix of both polymers. The accumulation of hydroxyl and alkane groups attributed to both PLLA and PEA on PLLA-*b*PEA highlights the addition of similar polymer chains via SI-ATRP. By investigating the brominated intermediates via FT-IR, chemical modification during initiator immobilisation was confirmed and subsequent utilisation of these chemical primer sidechains confirmed post polymerisation. XPS surface analysis showed that aminolysis and initiator immobilisation were both observed to incorporate elemental nitrogen and bromine onto the PLLA, highlighting the efficacy of these reactions. Post polymerisation these elements were not present on PLLA-*b*PEA spectra, which presented carbon spectra corresponding to a combination of PEA on a PLLA backbone. This PEA formation was observed to be time-dependent, as longer time of polymerisation was estimated to increase the total PEA percentage on the surface (Ma, Textor et al. 2006). These spectra also confirm fully intact PEA polymer formation, showing that SI-ATRP does not result in fragmented or damaged chemical chains during polymerisation. The introduction of a ß relaxation peak on PLLA-*b*PEA, at approximately -120°C at 11349 Hz, not found on PLLA, shows additional chemical chain mobility confirming the incorporation of PEA (Ribelles, Duenas et al. 1989). Additionality, it should also be noted that brush formation induced increased roughness and produced surfaces with increased chemical mobility, comparable to spin-coated PEA controls (Zhu, Zhang et al. 2002, Liu, Du et al. 2007). We also attempted to streamline the SI-ATRP protocol by incorporating initial surface functionalisation and initiator immobilisation in a 1-pot bromination procedure via pyridinolysis, but the procedure did not yield a functional surface modification and was not carried forward in this work.

To further develop this system, the SI-ATRP methodology was translated from 2D PLLA films to 3D printed biomedical grade PLLA scaffolds. This involved the establishment of polymer processing protocols to produce 3D scaffolds. Then, the established SI-ATRP protocol was adapted to be used on the scaffolds and the resulting materials analysed to ensure, once again, that while PEA brushes are being produced, the alterations to the PLLA backbone properties are minimized. 3D scaffolds were observed to maintain similar mechanical strength and degradability to 2D PLLA even after SI-ATRP treatment and PEA brush formation was observed on these PLLA-*b*PEA scaffolds. Indeed, SI-ATRP was noted to penetrate the entirety of the porous scaffold, as PEA spectra were observed within its centre.

The biological functionality of produced PEA brushes was assessed via their ability to drive fibrillogenesis of fibronectin, a unique property of PEA within this system (Salmeron-Sanchez, Rico et al. 2011, Llopis-Hernandez, Rico et al. 2013). Fibronectin was observed to form fibrils, which in turn formed nanonetworks on both control PEA and PLLA-*b*PEA, as revealed by imaging via AFM. While these nanonetworks possessed slightly diminished fractal dimensions to bulk PEA, their presence on SI-ATRP treated PLLA confirms the previously observed chemical similarities of brush to bulk PEA. Biologically the FN fibres formed on PLLA-*b*PEA were observed to present binding domains similarly to those exposed upon adsorption on conventional radically polymerised PEA (Pankov and Yamada 2002, Llopis-Hernandez, Rico et al. 2013). While total protein density and RGD cellular binding domain availability were conserved between all sample types (Vanterpool, Cantini et al. 2014), the exposure of the PHSRN cell binding synergy motif and of the HepII domain, known to recruit and regulate the activity of many growth factors, was upregulated on both PEA-presenting surfaces. This confirms that PLLA-*b*PEA surfaces have the potential to support enhanced cell response, via cell adhesion strengthening of α5β1 integrins due to PHSRN exposure and via enhanced differentiation through synergistic signalling between integrins and growth factors receptors due to the proximity of their ligands. While no significant difference was noted in the presentation of the synergy or growth factor binding domains between PLLA-*b*PEA and bulk PEA, the density of adsorbed growth factor, specifically BMP-2, on SI-ATRP-reacted samples was observed to be significantly higher compared to PEA. This could be attributed to the increased thickness of

the FN fibres on these surfaces (Rico 2014), providing a higher surface area for BMP-2 molecules to bind to. This presentation of the cryptic synergy integrin binding domain and of the growth factor binding region, not exposed on PLLA, highlights the biological functionality of PEA brushes.

To confirm the ability of these functional PEA brushes to enhance cellular interactions on PLLA, cellular assays were performed utilising C2C12 mouse myoblasts and human mesenchymal stem cells. Myoblasts were observed to spread better and present better morphology on all PEA-presenting 2D surfaces post FN adsorption. While less and smaller focal adhesions were formed on pristine PLLA samples, PLLA-*b*PEA and PEA samples presented improved binding microenvironments due to the presence of FN nanonetworks (Keselowsky, Collard et al. 2003, Keselowsky, Collard et al. 2004, Keselowsky, Collard et al. 2005), and increased PHSRN domain binding (Vanterpool, Cantini et al. 2014). On these samples higher numbers of mature focal adhesion plaques were observed, highlighting that SI-ATRP provides the additional benefit of PEA-induced cellular adhesion to PLLA surfaces. Myogenic differentiation was also observed to be enhanced on PLLA-*b*PEA, with the same contractile-dependent mechanism as on bulk PEA (Salmeron-Sanchez, Rico et al. 2011, Bathawab, Bennett et al. 2016). This shows that SI-ATRP-treated surfaces can drive higher order cellular functions than simple adhesion (Ulery, Nair et al. 2011). Finally, osteogenic differentiation was investigated with MSCs on 2D PLLA-*b*PEA surfaces and in 3D PLLA-*b*PEA scaffolds. Prior to cell culture, these materials were coated not only with FN, but also with BMP2, to take advantage of the ability of the FN nanonetworks to recruit the GF and boost its activity via presentation in synergy with cell binding domains. Indeed, solid-phase presentation of the GF via FN on PLLA-*b*PEA induced osteogenic differentiation, as demonstrated by the presence of osteocalcin, a marker of mature osteogenic differentiation (Aubin 2001). Moreover, PLLA-*b*PEA 3D scaffolds supported enhanced mineralisation of the matrix, a sign of late stage osteogenesis (Schindeler, McDonald et al. 2008), compared to untreated PLLA. These results, as well as the absence of cytotoxicity, demonstrate the ability of SI-ATRP-treated samples to enhance cell adhesion and facilitate differentiation both in 2D and within 3D scaffolds. This establishes the potential for these biodegradable 3D medical grade PLLA-*b*PEA scaffolds to be utilised in tissue engineering as, for example, an implantable biomaterial for bone regeneration.

While other techniques, plasma polymerisation and spin-coating, have previously been shown to provide similar functionality to biomaterials (Cantini, Gonzalez-Garcia et al. 2012, Llopis-Hernandez, Cantini et al. 2015, Llopis-Hernandez, Cantini et al. 2016, Cheng, Alba-Perez et al. 2019), SI-ATRP provides a surface modification which is chemically bound to the surface, homogenous, produces un-fragmented polymer chains and is fully translatable to 3D scaffolds. Due to these benefits and the tuneable nature of SI-ATRP, this system presents an improved methodology for the incorporation of thin layers of PEA and therefore enhanced biological functionality on established biomaterials.

6.2 Thesis conclusions

- The developed SI-ATRP system is able to produce functional poly (ethyl acrylate) brushes on 2D and 3D PLLA.

Chemical analysis highlighted the production of fully intact poly (ethyl acrylate) chains producing a uniform coverage over the entire film; this was shown to cover both 2D surfaces as well as fully penetrate 3D scaffolds. The production of PEA on PLLA-*b*PEA was shown to be dependent on the time of polymerisation.

- The produced PLLA-*b*PEA samples possess similar physical properties as pristine PLLA.

While new functionality was added to PLLA, the bulk polymer mechanical and physical properties were maintained through processing. Maintenance of bulk PLLA stiffness and biodegradability rate ensure that the produced scaffolds are able to initially provide structural support to the damaged tissue while gradually re-introducing physical strain to regenerating cells *in situ*.

- The PEA brushes are able to drive fibrillogenesis of fibronectin, producing nanonetworks and favourably presenting the PHSRN synergy motif and the HepII growth factor binding domain.

The produced PEA brushes were able to drive the re-organisation of globular FN molecules into physiological-like nanonetworks, made of individual FN fibrils. These nanofibrils exposed additional cryptic binding domains and were able to bind growth factors in close proximity to the integrin binding region of fibronectin, unlike pristine PLLA, enhancing cellular interactions.

- PLLA-*b*PEA samples are able to facilitate enhanced cellular adhesion and drive differentiation due to the PEA brushes.

Successful cellular cultures of both C2C12 cells and hMSCs, for 5 days and a month respectively, alongside cytotoxicity assays, have shown that the produced PLLA-*b*PEA surfaces are viable for cellular incubation and long term culture. The additional functionality of the produced polymer brushes provide enhanced cellular adhesion and facilitate controlled myogenic and osteogenic differentiation. Osteogenic differentiation was induced by enhanced solid-state presentation, promoting GF-integrin synergy, of ultra-low concentrations of BMP-2 due to material-driven fibrillogenesis of FN on PLLA-*b*PEA samples.

6.3 Future work

The addition of specific biological functionalities to established biomaterials presents extensive possibilities for improved regenerative medicine applications. Here we have achieved enhanced cellular adhesion and osteogenic potential on PLLA surfaces, improving the initial biological performance of the implant and its long term bone regenerative ability via the inclusion of PEA brushes. PEA driven fibrillogenesis has also been shown to enhance other tissue engineering regenerative applications, such as vascularisation via synergistic presentation of vascular endothelial growth factor (VEGF) (Moulisova, Gonzalez-Garcia et al. 2017). Highlighting the potential for utilisation of this PLLA-bPEA system for more than just bone tissue engineering. However, the process that we have developed has the potential to be translated to modify countless other polymers; such as poly (lactic-co-glycolic acid), poly caprolactone or polystyrene, for either the enhancement of cellular interactions or to improve their biocompatibility. Additionally, the SI-ATRP system itself may be further developed to decrease the time of treatment, utilising a 1-pot methodology which has yet to

be optimized to a sufficient degree. Further characterisation and fine tuning of this 1-pot system may provide a faster, more accessible methodology for further scaling up of the system. In fact, the SI-ATRP treatment of different bulk backbone polymers, for example those possessing aromatic hydrocarbon rings like polystyrene, would not require the initial aminolysis step to functionalize the surface for initiator immobilisation (Vivek and Dhamodharan 2007).

With regards to the system for bone regeneration presented in this thesis, while PLLA-*b*PEA scaffolds were observed to facilitate osteogenic differentiation, further characterisation of the mechanisms involved and of their osteogenic potential should be performed. qPCR, to evaluate RNA levels of osteogenic factors, such as osteocalcin or osteopontin, and further 3D scaffold imaging, utilising histological sections and immunostaining, will further highlight the functionality of these surfaces. While enzymatic degradation assays have been performed, long-term hydrolytic degradation in simulated body fluid could be also studied, with analysis of the degradative products via gel permeable chromatography. Finally, a key development in the utilisation of this system will be its use in *in vivo* models, which would definitively show the validity of and enhanced functionality of PLLA-*b*PEA as a system for bone regeneration. Characterisation of this system utilising animal models, in line with current regulatory requirements, would aim to further establish the efficacy and biocompatibility shown *in vitro*. Demonstrating the regenerative potential of the system in these models would further the development of SI-ATRP system for production of nanoscale PEA brushes, enhancing the functionality of established polymer biomaterials as a potential clinical application for non-union bone defect healing.

7. References

Al-Jarsha, M., V. Moulisova, A. Leal-Egana, A. Connell, K. B. Naudi, A. F. Ayoub, M. J. Dalby and M. Salmeron-Sanchez (2018). "Engineered Coatings for Titanium Implants To Present Ultralow Doses of BMP-7." Acs Biomaterials Science & Engineering **4**(5): 1812-1819.

Allingham, J. S., R. Smith and I. Rayment (2005). "The structural basis of blebbistatin inhibition and specificity for myosin II." Nature Structural & Molecular Biology **12**(4): 378-379.

Ambrosio, A. M. A., J. S. Sahota, Y. Khan and C. T. Laurencin (2001). "A novel amorphous calcium phosphate polymer ceramic for bone repair: 1. Synthesis and characterization." Journal of Biomedical Materials Research **58**(3): 295-301.

Anderson, H. J., J. K. Sahoo, R. V. Ulijn and M. J. Dalby (2016). "Mesenchymal Stem Cell Fate: Applying Biomaterials for Control of Stem Cell Behavior." Frontiers in Bioengineering and Biotechnology **4**.

Anthis, N. J. and I. D. Campbell (2011). "The tail of integrin activation." Trends in Biochemical Sciences **36**(4): 191-198.

Aota, S., M. Nomizu and K. M. Yamada (1994). "THE SHORT AMINO-ACID-SEQUENCE PRO-HIS-SER-ARG-ASN IN HUMAN FIBRONECTIN ENHANCES CELL-ADHESIVE FUNCTION." Journal of Biological Chemistry **269**(40): 24756-24761.

Armentano, I., M. Dottori, E. Fortunati, S. Mattioli and J. M. Kenny (2010). "Biodegradable polymer matrix nanocomposites for tissue engineering: A review." Polymer Degradation and Stability **95**(11): 2126-2146.

Athanasiou, K. A., G. G. Niederauer and C. M. Agrawal (1996). "Sterilization, toxicity, biocompatibility and clinical applications of polylactic acid polyglycolic acid copolymers." Biomaterials **17**(2): 93-102.

Aubin, J. E. (2001). "Regulation of osteoblast formation and function." Reviews in endocrine & metabolic disorders **2**(1): 81-94.

Auras, R., Lim, L., Selke, S. E. M.,Tsuji, H. (2010). Poly(Lactic Acid): Synthesis, Structures, Properties, Processing, and Applications, John Wiley & Sons, Inc.

Bachman, H., J. Nicosia, M. Dysart and T. H. Barker (2015). "Utilizing Fibronectin Integrin-Binding Specificity to Control Cellular Responses." Advances in Wound Care **4**(8): 501-511.

Badia, A., R. B. Lennox and L. Reven (2000). "A dynamic view of self-assembled monolayers." Accounts of Chemical Research **33**(7): 475-481.

Baharvand, H., S. M. Hashemi, S. Kazemi Ashtian and A. Farrokhi (2006). "Differentiation of human embryonic stem cells into hepatocytes in 2D and 3D culture systems in vitro." International Journal of Developmental Biology **50**(7): 645-652.

Ballester-Beltran, J., D. Moratal, M. Lebourg and M. Salmeron-Sanchez (2014). "Fibronectin-matrix sandwich-like microenvironments to manipulate cell fate." Biomaterials Science **2**(3): 381-389.

Baneyx, G. and V. Vogel (1999). "Self-assembly of fibronectin into fibrillar networks underneath dipalmitoyl phosphatidylcholine monolayers: Role of lipid matrix and tensile forces." Proceedings of the National Academy of Sciences of the United States of America **96**(22): 12518-12523.

Barry, J. J. A., D. Howard, K. M. Shakesheff, S. M. Howdle and M. R. Alexander (2006). "Using a core-sheath distribution of surface chemistry through 3D tissue engineering scaffolds to control cell ingress." Advanced Materials **18**(11): 1406-+.

Barry, J. J. A., M. Silva, K. M. Shakesheff, S. M. Howdle and M. R. Alexander (2005). "Using plasma deposits to promote cell population of the porous interior

of three-dimensional poly(D,L-lactic acid) tissue-engineering scaffolds." Advanced Functional Materials **15**(7): 1134-1140.
Basu, A., K. R. Kunduru, S. Doppalapudi, A. J. Domb and W. Khan (2016). "Poly(lactic acid) based hydrogels." Advanced Drug Delivery Reviews **107**: 192-205.
Bathawab, F., M. Bennett, M. Cantini, J. Reboud, M. J. Dalby and M. Salmeron-Sanchez (2016). "Lateral Chain Length in Polyalkyl Acrylates Determines the Mobility of Fibronectin at the Cell/Material Interface." Langmuir **32**(3): 800-809.
Beederman, M., J. D. Lamplot, G. Nan, J. Wang, X. Liu, L. Yin, R. Li, W. Shui, H. Zhang, S. H. Kim, W. Zhang, J. Zhang, Y. Kong, S. Denduluri, M. R. Rogers, A. Pratt, R. C. Haydon, H. H. Luu, J. Angeles, L. L. Shi and T.-C. He (2013). "BMP signaling in mesenchymal stem cell differentiation and bone formation." Journal of biomedical science and engineering **6**(8A): 32-52.
Benoit, D. S. W., M. P. Schwartz, A. R. Durney and K. S. Anseth (2008). "Small functional groups for controlled differentiation of hydrogel-encapsulated human mesenchymal stem cells." Nature Materials **7**(10): 816-823.
Benya, P. D. and J. D. Shaffer (1982). "DEDIFFERENTIATED CHONDROCYTES REEXPRESS THE DIFFERENTIATED COLLAGEN PHENOTYPE WHEN CULTURED IN AGAROSE GELS." Cell **30**(1): 215-224.
Bhushan, B. (2009). "Biomimetics: lessons from nature - an overview." Philosophical Transactions of the Royal Society a-Mathematical Physical and Engineering Sciences **367**(1893): 1445-1486.
Bonnans, C., J. Chou and Z. Werb (2014). "Remodelling the extracellular matrix in development and disease." Nature Reviews Molecular Cell Biology **15**(12): 786-801.
Borges, E., Y. W. Jan and E. Ruoslahti (2000). "Platelet-derived growth factor receptor beta and vascular endothelial growth factor receptor 2 bind to the beta(3) integrin through its extracellular domain." Journal of Biological Chemistry **275**(51): 39867-39873.
Bossard, C., L. Van den Berghe, H. Laurell, C. Castano, M. Cerutti, A. C. Prats and H. Prats (2004). "Antiangiogenic properties of fibstatin, an extracellular FGF-2-binding polypeptide." Cancer Research **64**(20): 7507-7512.
Braunecker, W. A. and K. Matyjaszewski (2006). "Recent mechanistic developments in atom transfer radical polymerization." Journal of Molecular Catalysis a-Chemical **254**(1-2): 155-164.
Braunecker, W. A. and K. Matyjaszewski (2007). "Controlled/living radical polymerization: Features, developments, and perspectives." Progress in Polymer Science **32**(1): 93-146.
Brown, R. A., G. W. Blunn and O. S. Ejim (1994). "PREPARATION OF ORIENTATED FIBROUS MATS FROM FIBRONECTIN - COMPOSITION AND STABILITY." Biomaterials **15**(6): 457-464.
Cai, Y., O. Rossier, N. C. Gauthier, N. Biais, M.-A. Fardin, X. Zhang, L. W. Miller, B. Ladoux, V. W. Cornish and M. P. Sheetz (2010). "Cytoskeletal coherence requires myosin-IIA contractility." Journal of Cell Science **123**(3): 413-423.
Calderwood, D. A. (2004). "Integrin activation." Journal of Cell Science **117**(5): 657-666.
Calderwood, D. A., I. D. Campbell and D. R. Critchley (2013). "Talins and kindlins: partners in integrin-mediated adhesion." Nature Reviews Molecular Cell Biology **14**(8): 503-517.
Calderwood, D. A., Y. Fujioka, J. M. de Pereda, B. Garcia-Alvarez, T. Nakamoto, B. Margolis, C. J. McGlade, R. C. Liddington and M. H. Ginsberg (2003). "Integrin beta cytoplasmic domain interactions with phosphotyrosine-binding domains: A

structural prototype for diversity in integrin signaling." Proceedings of the National Academy of Sciences of the United States of America **100**(5): 2272-2277.
Caliari, S. R. and J. A. Burdick (2016). "A practical guide to hydrogels for cell culture." Nature Methods **13**(5): 405-414.
Canal, C., K. Khurana, S. Gallinetti, S. Bhatt, J. Pulpytel, F. Arefi-Khonsari and M.-P. Ginebra (2016). "Design of calcium phosphate scaffolds with controlled simvastatin release by plasma polymerisation." Polymer **92**: 170-178.
Cantini, M., C. Gonzalez-Garcia, V. Llopis-Hernandez and M. Salmeron-Sanchez (2012). "Material-Driven Fibronectin Fibrillogenesis." Proteins at Interfaces Iii: State of the Art **1120**: 471-496.
Cantini, M., C. González-García, V. Llopis-Hernández and M. Salmerón-Sánchez (2012). "Material-Driven Fibronectin Fibrillogenesis." Proteins at Interfaces III State of the Art.(**January 1, 2012**): 471-496.
Cantini, M., P. Rico, D. Moratal and M. Salmeron-Sanchez (2012). "Controlled wettability, same chemistry: biological activity of plasma-polymerized coatings." Soft Matter **8**(20): 5575-5584.
Carletti, E., A. Motta and C. Migliaresi (2011). Scaffolds for Tissue Engineering and 3D Cell Culture. 3D Cell Culture: Methods and Protocols. J. W. Haycock. Totowa, NJ, Humana Press**:** 17-39.
Castillo, R. C., M. J. Bosse, E. J. MacKenzie, B. M. Patterson and L. S. Grp (2005). "Impact of smoking on fracture healing and risk of complications in limb-threatening open tibia fractures." Journal of Orthopaedic Trauma **19**(3): 151-157.
Charvet, R. and B. M. Novak (2004). "One-pot, one-catalyst synthesis of graft copolymers by controlled ROMP and ATRP polymerizations." Macromolecules **37**(23): 8808-8811.
Chen, J.-P. and C.-H. Su (2011). "Surface modification of electrospun PLLA nanofibers by plasma treatment and cationized gelatin immobilization for cartilage tissue engineering." Acta Biomaterialia **7**(1): 234-243.
Cheng, Z. A., A. Alba-Perez, C. Gonzalez-Garcia, H. Donnelly, V. Llopis-Hernandez, V. Jayawarna, P. Childs, D. W. Shields, M. Cantini, L. Ruiz-Cantu, A. Reid, J. F. C. Windmill, E. S. Addison, S. Corr, W. G. Marshall, M. J. Dolby and M. Salmeron-Sanchez (2019). "Nanoscale Coatings for Ultralow Dose BMP-2-Driven Regeneration of Critical-Sized Bone Defects." Advanced Science **6**(2).
Chu, P. K., J. Y. Chen, L. P. Wang and N. Huang (2002). "Plasma-surface modification of biomaterials." Materials Science & Engineering R-Reports **36**(5-6): 143-206.
Cools, P., C. Mota, I. Lorenzo-Moldero, R. Ghobeira, N. De Geyter, L. Moroni and R. Morent (2018). "Acrylic Acid Plasma Coated 3D Scaffolds for Cartilage tissue engineering applications." Scientific Reports **8**.
Corey, J. M., C. C. Gertz, B.-S. Wang, L. K. Birrell, S. L. Johnson, D. C. Martin and E. L. Feldman (2008). "The design of electrospun PLLA nanofiber scaffolds compatible with serum-free growth of primary motor and sensory neurons." Acta Biomaterialia **4**(4): 863-875.
Costa Martinez, E., J. C. Rodriguez Hernandez, M. Machado, J. F. Mano, J. L. Gomez Ribelles, M. Monleon Pradas and M. Salmeron Sanchez (2008). "Human Chondrocyte Morphology, Its Dedifferentiation, and Fibronectin Conformation on Different PLLA Microtopographies." Tissue Engineering Part A **14**(10): 1751-1762.
Critchley, D. R. (2004). "Cytoskeletal proteins talin and vinculin in integrin-mediated adhesion." Biochemical Society Transactions **32**: 831-836.
Cronin, E. M., F. A. Thurmond, R. Bassel-Duby, R. S. Williams, W. E. Wright, K. D. Nelson and H. R. Garner (2004). "Protein-coated poly(L-lactic acid) fibers provide

a substrate for differentiation of human skeletal muscle cells." Journal of Biomedical Materials Research Part A **69A**(3): 373-381.
Curran, J. M., R. Chen and J. A. Hunt (2005). "Controlling the phenotype and function of mesenchymal stem cells in vitro by adhesion to silane-modified clean glass surfaces." Biomaterials **26**(34): 7057-7067.
Curran, J. M., R. Chen and J. A. Hunt (2006). "The guidance of human mesenchymal stem cell differentiation in vitro by controlled modifications to the cell substrate." Biomaterials **27**(27): 4783-4793.
Dalby, M. J., N. Gadegaard and R. O. C. Oreffo (2014). "Harnessing nanotopography and integrin-matrix interactions to influence stem cell fate." Nature Materials **13**(6): 558-569.
Dalby, M. J., N. Gadegaard, R. Tare, A. Andar, M. O. Riehle, P. Herzyk, C. D. W. Wilkinson and R. O. C. Oreffo (2007). "The control of human mesenchymal cell differentiation using nanoscale symmetry and disorder." Nature Materials **6**(12): 997-1003.
Dalby, M. J., A. J. Garcia and M. Salmeron-Sanchez (2018). "Receptor control in mesenchymal stem cell engineering." Nature Reviews Materials **3**(3).
Dalby, M. J., A. Hart and S. J. Yarwood (2008). "The effect of the RACK1 signalling protein on the regulation of cell adhesion and cell contact guidance on nanometric grooves." Biomaterials **29**(3): 282-289.
Datta, H., A. K. Bhowmick and N. K. Singha (2008). "Tailor-made hybrid nanostructure of poly(ethyl acrylate)/clay by surface-initiated atom transfer radical polymerization." Journal of Polymer Science Part a-Polymer Chemistry **46**(15): 5014-5027.
Declercq, H. A., T. Desmet, E. E. M. Berneel, P. Dubruel and M. J. Cornelissen (2013). "Synergistic effect of surface modification and scaffold design of bioplotted 3-D poly-epsilon-caprolactone scaffolds in osteogenic tissue engineering." Acta Biomaterialia **9**(8): 7699-7708.
Ding, Z., J. N. Chen, S. Y. Gao, J. B. Chang, J. F. Zhang and E. T. Kang (2004). "Immobilization of chitosan onto poly-L-lactic acid film surface by plasma graft polymerization to control the morphology of fibroblast and liver cells." Biomaterials **25**(6): 1059-1067.
Discher, D. E., P. Janmey and Y. L. Wang (2005). "Tissue cells feel and respond to the stiffness of their substrate." Science **310**(5751): 1139-1143.
Dominici, M., K. Le Blanc, I. Mueller, I. Slaper-Cortenbach, F. C. Marini, D. S. Krause, R. J. Deans, A. Keating, D. J. Prockop and E. M. Horwitz (2006). "Minimal criteria for defining multipotent mesenchymal stromal cells. The International Society for Cellular Therapy position statement." Cytotherapy **8**(4): 315-317.
Donnelly, H., M. J. Dalby, M. Salmeron-Sanchez and P. E. Sweeten (2018). "Current approaches for modulation of the nanoscale interface in the regulation of cell behavior." Nanomedicine-Nanotechnology Biology and Medicine **14**(7): 2455-2464.
Donnelly, H., M. Salmeron-Sanchez and M. J. Dalby (2018). "Designing stem cell niches for differentiation and self-renewal." Journal of the Royal Society Interface **15**(145).
Donnelly, H., C.-A. Smith, P. E. Sweeten, N. Gadegaard, R. M. D. Meek, M. D'Este, A. Mata, D. Eglin and M. J. Dalby (2017). "Bone and cartilage differentiation of a single stem cell population driven by material interface." Journal of Tissue Engineering **8**.
E Golub, E. and K. Boesze-Battaglia (2007). The role of alkaline phosphatase in mineralization.

Edmondson, R., J. J. Broglie, A. F. Adcock and L. Yang (2014). "Three-Dimensional Cell Culture Systems and Their Applications in Drug Discovery and Cell-Based Biosensors." Assay and Drug Development Technologies **12**(4): 207-218.
Einhorn, T. A. (1995). "ENHANCEMENT OF FRACTURE-HEALING." Journal of Bone and Joint Surgery-American Volume **77A**(6): 940-956.
El-Sherbiny, I. M. and M. H. Yacoub (2013). "Hydrogel scaffolds for tissue engineering: Progress and challenges." Global cardiology science & practice **2013**(3): 316-342.
Elosegui-Artola, A., R. Oria, Y. Chen, A. Kosmalska, C. Perez-Gonzalez, N. Castro, C. Zhu, X. Trepat and P. Roca-Cusachs (2016). "Mechanical regulation of a molecular clutch defines force transmission and transduction in response to matrix rigidity." Nature Cell Biology **18**(5): 540-+.
Engler, A. J., S. Sen, H. L. Sweeney and D. E. Discher (2006). "Matrix elasticity directs stem cell lineage specification." Cell **126**(4): 677-689.
Espeel, P. and F. E. Du Prez (2015). "One-pot multi-step reactions based on thiolactone chemistry: A powerful synthetic tool in polymer science." European Polymer Journal **62**: 247-272.
Faia-Torres, A. B., M. Charnley, T. Goren, S. Guimond-Lischer, M. Rottmar, K. Maniura-Weber, N. D. Spencer, R. L. Reis, M. Textor and N. M. Neves (2015). "Osteogenic differentiation of human mesenchymal stem cells in the absence of osteogenic supplements: A surface-roughness gradient study." Acta Biomaterialia **28**: 64-75.
Farah, S., D. G. Anderson and R. Langer (2016). "Physical and mechanical properties of PLA, and their functions in widespread applications - A comprehensive review." Advanced Drug Delivery Reviews **107**: 367-392.
Fernandez-Yague, M. A., S. A. Abbah, L. McNamara, D. I. Zeugolis, A. Pandit and M. J. Biggs (2015). "Biomimetic approaches in bone tissue engineering: Integrating biological and physicomechanical strategies." Advanced Drug Delivery Reviews **84**: 1-29.
Fourel, L., A. Valat, E. Faurobert, R. Guillot, I. Bourrin-Reynard, K. Ren, L. Lafanechere, E. Planus, C. Picart and C. Albiges-Rizo (2016). "beta 3 integrin-mediated spreading induced by matrix-bound BMP-2 controls Smad signaling in a stiffness-independent manner." Journal of Cell Biology **212**(6): 693-706.
Frantz, C., K. M. Stewart and V. M. Weaver (2010). "The extracellular matrix at a glance." Journal of Cell Science **123**(24): 4195-4200.
Frydrych, M., S. Roman, S. MacNeil and B. Chen (2015). "Biomimetic poly(glycerol sebacate)/poly(L-lactic acid) blend scaffolds for adipose tissue engineering." Acta Biomaterialia **18**: 40-49.
Garcia, A. J., M. D. Vega and D. Boettiger (1999). "Modulation of cell proliferation and differentiation through substrate-dependent changes in fibronectin conformation." Molecular Biology of the Cell **10**(3): 785-798.
Gee, E. P. S., D. Yueksel, C. M. Stultz and D. E. Ingber (2013). "SLLISWD Sequence in the 10FNIII Domain Initiates Fibronectin Fibrillogenesis." Journal of Biological Chemistry **288**(29): 21329-21340.
Gentile, P., V. Chiono, I. Carmagnola and P. V. Hatton (2014). "An Overview of Poly(lactic-co-glycolic) Acid (PLGA)-Based Biomaterials for Bone Tissue Engineering." International Journal of Molecular Sciences **15**(3): 3640-3659.
Gomez-Barrena, E., P. Rosset, D. Lozano, J. Stanovici, C. Ermthaller and F. Gerbhard (2015). "Bone fracture healing: Cell therapy in delayed unions and nonunions." Bone **70**: 93-101.

Gonzalez-Garcia, C., D. Moratal, R. O. C. Oreffo, M. J. Dalby and M. Salmeron-Sanchez (2012). "Surface mobility regulates skeletal stem cell differentiation." Integrative Biology **4**(5): 531-539.
Green, J. J. and J. H. Elisseeff (2016). "Mimicking biological functionality with polymers for biomedical applications." Nature **540**(7633): 386-394.
Greenbaum, A., Y.-M. S. Hsu, R. B. Day, L. G. Schuettpelz, M. J. Christopher, J. N. Borgerding, T. Nagasawa and D. C. Link (2013). "CXCL12 in early mesenchymal progenitors is. required for haematopoietic stem-cell maintenance." Nature **495**(7440): 227-230.
Gregor, A., E. Filova, M. Novak, J. Kronek, H. Chlup, M. Buzgo, V. Blahnova, V. Lukasova, M. Bartos, A. Necas and J. Hosek (2017). "Designing of PLA scaffolds for bone tissue replacement fabricated by ordinary commercial 3D printer." Journal of Biological Engineering **11**.
Grigoriou, E., M. Cantini, M. J. Dalby, A. Petersen and M. Salmeron-Sanchez (2017). "Cell migration on material-driven fibronectin microenvironments." Biomaterials Science **5**(7): 1326-1333.
Gugutkov, D., C. Gonzalez-Garcia, J. C. R. Hernandez, G. Altankov and M. Salmeron-Sanchez (2009). "Biological Activity of the Substrate-Induced Fibronectin Network: Insight into the Third Dimension through Electrospun Fibers." Langmuir **25**(18): 10893-10900.
Haers, P. E., R. Suuronen, C. Lindqvist and H. F. Sailer (1999). "Biodegradable polylactide plates and screws in orthognathic surgery: technical note - Piet Eduard Haers, Riitta Suuronen, Christian Lindqvist, Hermann Sailer - Journal of Cranio-maxillofacial Surg 1998; 26: 87-91. Reply." Journal of Cranio-Maxillofacial Surgery **27**(3): 198-200.
Harrison, G., I. M. Shapiro and E. E. Golub (1995). "THE PHOSPHATIDYLINOSITOL-GLYCOLIPID ANCHOR ON ALKALINE-PHOSPHATASE FACILITATES MINERALIZATION INITIATION IN-VITRO." Journal of Bone and Mineral Research **10**(4): 568-573.
Hauschka, P. V., J. B. Lian, D. E. C. Cole and C. M. Gundberg (1989). "OSTEOCALCIN AND MATRIX GLA PROTEIN - VITAMIN K-DEPENDENT PROTEINS IN BONE." Physiological Reviews **69**(3): 990-1047.
Hay, J. J., A. Rodrigo-Navarro, M. Petaroudi, A. V. Bryksin, A. J. Garcia, T. H. Barker, M. J. Dalby and M. Salmeron-Sanchez (2018). "Bacteria-Based Materials for Stem Cell Engineering." Advanced Materials **30**(43).
He, Y., W. Wang and J. Ding (2013). "Effects of L-lactic acid and D,L-lactic acid on viability and osteogenic differentiation of mesenchymal stem cells." Chinese Science Bulletin **58**(20): 2404-2411.
Hench, L. L. (1993). "BIOCERAMICS - FROM CONCEPT TO CLINIC." American Ceramic Society Bulletin **72**(4): 93-98.
Hernlund, E., A. Svedbom, M. Ivergard, J. Compston, C. Cooper, J. Stenmark, E. V. McCloskey, B. Jonsson and J. A. Kanis (2013). "Osteoporosis in the European Union: medical management, epidemiology and economic burden." Archives of Osteoporosis **8**(1-2).
Hiemstra, C., Z. Zhong, L. Li, P. J. Dijkstra and J. Feijen (2006). "In-situ formation of biodegradable hydrogels by stereocomplexation of PEG-(PLLA)(8) and PEG-(PDLA)(8) star block copolymers." Biomacromolecules **7**(10): 2790-2795.
Ho, M. H., L. T. Hou, C. Y. Tu, H. J. Hsieh, J. Y. Lai, W. J. Chen and D. M. Wang (2006). "Promotion of cell affinity of porous PLLA scaffolds by immobilization of RGD peptides via plasma treatment." Macromolecular Bioscience **6**(1): 90-98.
Hoglund, A., M. Hakkarainen, U. Edlund and A.-C. Albertsson (2010). "Surface Modification Changes the Degradation Process and Degradation Product Pattern of Polylactide." Langmuir **26**(1): 378-383.

Hollister, S. J. and W. L. Murphy (2011). "Scaffold Translation: Barriers Between Concept and Clinic." Tissue Engineering Part B-Reviews **17**(6): 459-474.
Hopkins, A. M., E. DeSimone, K. Chwalek and D. L. Kaplan (2015). "3D in vitro modeling of the central nervous system." Progress in Neurobiology **125**: 1-25.
Horzum, U., B. Ozdil and D. Pesen-Okvur (2014). "Step-by-step quantitative analysis of focal adhesions." MethodsX **1**: 56-59.
Howard, D., L. D. Buttery, K. M. Shakesheff and S. J. Roberts (2008). "Tissue engineering: strategies, stem cells and scaffolds." Journal of Anatomy **213**(1): 66-72.
Hughes, P. E., F. DiazGonzalez, L. Leong, C. Y. Wu, J. A. McDonald, S. J. Shattil and M. H. Ginsberg (1996). "Breaking the integrin hinge - A defined structural constraint regulates integrin signaling." Journal of Biological Chemistry **271**(12): 6571-6574.
Huh, D., Y.-s. Torisawa, G. A. Hamilton, H. J. Kim and D. E. Ingber (2012). "Microengineered physiological biomimicry: Organs-on-Chips." Lab on a Chip **12**(12): 2156-2164.
Humphries, J. D., A. Byron and M. J. Humphries (2006). "Integrin ligands at a glance." Journal of Cell Science **119**(19): 3901-3903.
Humphries, J. D., P. Wang, C. Streuli, B. Geiger, M. J. Humphries and C. Ballestrem (2007). "Vinculin controls focal adhesion formation by direct interactions with talin and actin." Journal of Cell Biology **179**(5): 1043-1057.
Hynes, R. O. (1999). "The dynamic dialogue between cells and matrices: Implications of fibronectin's elasticity." Proceedings of the National Academy of Sciences of the United States of America **96**(6): 2588-2590.
Hynes, R. O. (2002). "Integrins: Bidirectional, allosteric signaling machines." Cell **110**(6): 673-687.
Iacono, M. and A. Heise (2015). "Stable Poly(methacrylic acid) Brush Decorated Silica Nano-Particles by ARGET ATRP for Bioconjugation." Polymers **7**(8): 1427-1443.
Iaquinta, M. R., E. Mazzoni, M. Manfrini, A. D'Agostino, L. Trevisiol, R. Nocini, L. Trombelli, G. Barbanti-Brodano, F. Martini and M. Tognon (2019). "Innovative Biomaterials for Bone Regrowth." International journal of molecular sciences **20**(3).
Islami, M., Y. Mortazavi, M. Soleimani and S. Nadri (2018). "In vitro expansion of CD 133+cells derived from umbilical cord blood in poly-L-lactic acid (PLLA) scaffold coated with fibronectin and collagen." Artificial Cells Nanomedicine and Biotechnology **46**(5): 1025-1033.
Jacobs, T., H. Declercq, N. De Geyter, R. Cornelissen, P. Dubruel, C. Leys, A. Beaurain, E. Payen and R. Morent (2013). "Plasma surface modification of polylactic acid to promote interaction with fibroblasts." Journal of Materials Science-Materials in Medicine **24**(2): 469-478.
James, A. W., G. LaChaud, J. Shen, G. Asatrian, V. Nguyen, X. Zhang, K. Ting and C. Soo (2016). "A Review of the Clinical Side Effects of Bone Morphogenetic Protein-2." Tissue Engineering Part B-Reviews **22**(4): 284-297.
Jamshidian, M., E. A. Tehrany, M. Imran, M. Jacquot and S. Desobry (2010). "Poly-Lactic Acid: Production, Applications, Nanocomposites, and Release Studies." Comprehensive Reviews in Food Science and Food Safety **9**(5): 552-571.
Janorkar, A. V., A. T. Metters and D. E. Hirt (2007). "Degradation of Poly(L-Lactide) films under ultravioletInduced photografting and sterilization conditions." Journal of Applied Polymer Science **106**(2): 1042-1047.

Jarvelainen, H., A. Sainio, M. Koulu, T. N. Wight and R. Penttinen (2009). "Extracellular Matrix Molecules: Potential Targets in Pharmacotherapy." Pharmacological Reviews **61**(2): 198-223.
Jones, D. L. and A. J. Wagers (2008). "No place like home: anatomy and function of the stem cell niche." Nature Reviews Molecular Cell Biology **9**(1): 11-21.
Kang, C., R. M. Crockett and N. D. Spencer (2014). "Molecular-Weight Determination of Polymer Brushes Generated by SI-ATRP on Flat Surfaces." Macromolecules **47**(1): 269-275.
Kang, H., S. An, W. J. Lee, G. R. Kang, S. Kim, S.-M. Hur, K. Paeng and M. Kim (2018). "Stable polymer brushes with effectively varied grafting density synthesized from highly crosslinked random copolymer thin films." Rsc Advances **8**(43): 24166-24174.
Kassel, M., J. Gerke, A. Ley and P. Vana (2018). "Surface Modification of Wood Flour via ARGET ATRP and Its Application as Filler in Thermoplastics." Polymers **10**(4).
Kaur, A., T. G. Ribelli, K. Schroder, K. Matyjaszewski and T. Pintauer (2015). "Properties and ATRP Activity of Copper Complexes with Substituted Tris(2-pyridylmethyl)amine-Based Ligands." Figshare.
Keselowsky, B. G., D. M. Collard and A. J. Garcia (2003). "Surface chemistry modulates fibronectin conformation and directs integrin binding and specificity to control cell adhesion." Journal of Biomedical Materials Research Part A **66A**(2): 247-259.
Keselowsky, B. G., D. M. Collard and A. J. Garcia (2004). "Surface chemistry modulates focal adhesion composition and signaling through changes in integrin binding." Biomaterials **25**(28): 5947-5954.
Keselowsky, B. G., D. M. Collard and A. J. Garcia (2005). "Integrin binding specificity regulates biomaterial surface chemistry effects on cell differentiation." Proceedings of the National Academy of Sciences of the United States of America **102**(17): 5953-5957.
Khabibullin, A., E. Mastan, K. Matyjaszewski and S. Zhu (2016). "Surface-Initiated Atom Transfer Radical Polymerization." Controlled Radical Polymerization at and from Solid Surfaces **270**: 29-76.
Khan, F. and M. Tanaka (2017). "Designing Smart Biomaterials for Tissue Engineering." International journal of molecular sciences **19**(1).
Khan, F., M. Tanaka and S. R. Ahmad (2015). "Fabrication of polymeric biomaterials: a strategy for tissue engineering and medical devices." Journal of Materials Chemistry B **3**(42): 8224-8249.
Khandare, J. and T. Minko (2006). "Polymer-drug conjugates: Progress in polymeric prodrugs." Progress in Polymer Science **31**(4): 359-397.
Khetan, S., M. Guvendiren, W. R. Legant, D. M. Cohen, C. S. Chen and J. A. Burdick (2013). "Degradation-mediated cellular traction directs stem cell fate in covalently crosslinked three-dimensional hydrogels." Nature Materials **12**(5): 458-465.
Kickelbick, G., H. J. Paik and K. Matyjaszewski (1999). "Immobilization of the copper catalyst in atom transfer radical polymerization." Macromolecules **32**(9): 2941-2947.
Kilian, K. A., B. Bugarija, B. T. Lahn and M. Mrksich (2010). "Geometric cues for directing the differentiation of mesenchymal stem cells." Proceedings of the National Academy of Sciences of the United States of America **107**(11): 4872-4877.
Kimizuka, F., Y. Ohdate, Y. Kawase, T. Shimojo, Y. Taguchi, K. Hashino, S. Goto, H. Hashi, I. Kato, K. Sekiguchi and K. Titani (1991). "ROLE OF TYPE-III HOMOLOGY

REPEATS IN CELL ADHESIVE FUNCTION WITHIN THE CELL-BINDING DOMAIN OF FIBRONECTIN." Journal of Biological Chemistry **266**(5): 3045-3051.
Kirkpatrick, C. A. and S. B. Selleck (2007). "Heparan sulfate proteoglycans at a glance." Journal of Cell Science **120**(11): 1829-1832.
Kosik-Koziol, A., E. Graham, J. Jaroszewicz, A. Chlanda, P. T. S. Kumar, S. Ivanovski, W. Swieszkowski and C. Vaquette (2019). "Surface Modification of 3D Printed Polycaprolactone Constructs via a Solvent Treatment: Impact on Physical and Osteogenic Properties." Acs Biomaterials Science & Engineering **5**(1): 318-328.
Kostenuik, P. and F. M. Mirza (2017). "Fracture healing physiology and the quest for therapies for delayed healing and nonunion." Journal of Orthopaedic Research **35**(2): 213-223.
Kovacs, M., J. Toth, C. Hetenyi, A. Malnasi-Csizmadia and J. R. Sellers (2004). "Mechanism of blebbistatin inhibition of myosin II." Journal of Biological Chemistry **279**(34): 35557-35563.
Kramer, E., B. Kunkemoeller and M. Wei (2014). "Evaluation of alkaline pre-treatment of PLLA fibers for biomimetic hydroxyapatite coating." Surface & Coatings Technology **244**: 23-28.
Kreyling, W. G., A. M. Abdelmonem, Z. Ali, F. Alves, M. Geiser, N. Haberl, R. Hartmann, S. Hirn, D. Jimenez de Aberasturi, K. Kantner, G. Khadem-Saba, J.-M. Montenegro, J. Rejman, T. Rojo, I. Ruiz de Larramendi, R. Ufartes, A. Wenk and W. J. Parak (2015). "In vivo integrity of polymer-coated gold nanoparticles." Nature Nanotechnology **10**(7): 619-+.
Kuhl, P. R. and L. G. GriffithCima (1997). "Tethered epidermal growth factor as a paradigm for growth factor-induced stimulation from the solid phase (vol 2, pg 1022, 1996)." Nature Medicine **3**(1): 93-93.
Kyritsis, A., J. L. G. Ribelles, J. M. M. Duenas, N. S. Campillo, G. G. Ferrer and M. M. Pradas (2004). "alpha-beta splitting region in the dielectric relaxation spectrum of PEA-PEMA sequential IPNs." Macromolecules **37**(2): 446-452.
Lane, S. W., D. A. Williams and F. M. Watt (2014). "Modulating the stem cell niche for tissue regeneration." Nature Biotechnology **32**(8): 795-803.
Langer, R. and J. P. Vacanti (1993). "Tissue engineering." Science **260**(5110): 920.
Leahy, D. J., I. Aukhil and H. P. Erickson (1996). "2.0 A crystal structure of a four-domain segment of human fibronectin encompassing the RGD loop and synergy region." Cell **84**(1): 155-164.
Lee, J. Y., J. K. Chang, A. A. Dominguez, H.-p. Lee, S. Nam, J. Chang, S. Varma, L. S. Qi, R. B. West and O. Chaudhuri (2019). "YAP-independent mechanotransduction drives breast cancer progression." Nature Communications **10**(1): 1848.
Lee, K., E. A. Silva and D. J. Mooney (2011). "Growth factor delivery-based tissue engineering: general approaches and a review of recent developments." Journal of the Royal Society Interface **8**(55): 153-170.
Lemmon, C. A. and S. H. Weinberg (2017). "Multiple Cryptic Binding Sites are Necessary for Robust Fibronectin Assembly: An In Silico Study." Scientific Reports **7**.
Li, L.-J., N. Liu, J.-G. Shi, Q. Liu, L.-S. Jia and W. Yuan (2012). "Osteogenic scaffolds for bone reconstruction." BioResearch open access **1**(3): 137-144.
Li, Y. and K. A. Kilian (2015). "Bridging the Gap: From 2D Cell Culture to 3D Microengineered Extracellular Matrices." Advanced Healthcare Materials **4**(18): 2780-2796.
Lin, F., X.-D. Ren, Z. Pan, L. Macri, W.-X. Zong, M. G. Tonnesen, M. Rafailovich, D. Bar-Sagi and R. A. F. Clark (2011). "Fibronectin Growth Factor-Binding Domains

Are Required for Fibroblast Survival." Journal of Investigative Dermatology **131**(1): 84-98.
Liu, F., C. H. Du, B. K. Zhu and Y. Y. Xu (2007). "Surface immobilization of polymer brushes onto porous poly(vinylidene fluoride) membrane by electron beam to improve the hydrophilicity and fouling resistance." Polymer **48**(10): 2910-2918.
Liu, H. and K. Roy (2005). "Biomimetic three-dimensional cultures significantly increase hematopoietic differentiation efficacy of embryonic stem cells." Tissue Engineering **11**(1-2): 319-330.
Liu, P. and Z. X. Su (2005). "Surface-initiated atom transfer radical polymerization (SI-ATRP) of n-butyl acrylate from starch granules." Carbohydrate Polymers **62**(2): 159-163.
Liu, Q., S. Tian, C. Zhao, X. Chen, I. Lei, Z. Wang and P. X. Ma (2015). "Porous nanofibrous poly(L-lactic acid) scaffolds supporting cardiovascular progenitor cells for cardiac tissue engineering." Acta Biomaterialia **26**: 105-114.
Liu, S. Q., Q. Tian, J. L. Hedrick, J. H. P. Hui, P. L. R. Ee and Y. Y. Yang (2010). "Biomimetic hydrogels for chondrogenic differentiation of human mesenchymal stem cells to neocartilage." Biomaterials **31**(28): 7298-7307.
Llopis-Hernandez, V., M. Cantini, C. Gonzalez-Garcia, Z. A. Cheng, J. Yang, P. M. Tsimbouri, A. J. Garcia, M. J. Dalby and M. Salmeron-Sanchez (2016). "Material-driven fibronectin assembly for high-efficiency presentation of growth factors." Science Advances **2**(8).
Llopis-Hernandez, V., M. Cantini, C. Gonzalez-Garcia and M. Salmeron-Sanchez (2015). "Material-based strategies to engineer fibronectin matrices for regenerative medicine." International Materials Reviews **60**(5): 245-263.
Llopis-Hernandez, V., P. Rico, D. Moratal, G. Altankov and M. Salmeron-Sanchez (2013). "Role of material-driven fibronectin fibrillogenesis in protein remodeling." Biores Open Access **2**(5): 364-373.
Lozano Picazo, P., M. Perez Garnes, C. Martinez Ramos, A. Valles-Lluch and M. Monleon Pradas (2015). "New Semi-Biodegradable Materials from Semi-Interpenetrated Networks of Poly(epsilon-caprolactone) and Poly(ethyl acrylate)." Macromolecular Bioscience **15**(2): 229-240.
Ma, H., M. Textor, R. L. Clark and A. Chilkoti (2006). "Monitoring kinetics of surface initiated atom transfer radical polymerization by quartz crystal microbalance with dissipation." Biointerphases **1**(1): 35-39.
Makadia, H. K. and S. J. Siegel (2011). "Poly Lactic-co-Glycolic Acid (PLGA) as Biodegradable Controlled Drug Delivery Carrier." Polymers **3**(3): 1377-1397.
Mao, Y. and J. E. Schwarzbauer (2005). "Fibronectin fibrillogenesis, a cell-mediated matrix assembly process." Matrix Biology **24**(6): 389-399.
Marom, R., I. Shur, R. Solomon and D. Benayahu (2005). "Characterization of adhesion and differentiation markers of osteogenic marrow stromal cells." Journal of Cellular Physiology **202**(1): 41-48.
Martino, M. M., P. S. Briquez, K. Maruyama and J. A. Hubbell (2015). "Extracellular matrix-inspired growth factor delivery systems for bone regeneration." Advanced Drug Delivery Reviews **94**: 41-52.
Martino, M. M. and J. A. Hubbell (2010). "The 12th-14th type III repeats of fibronectin function as a highly promiscuous growth factor-binding domain." Faseb Journal **24**(12): 4711-4721.
Martino, M. M., F. Tortelli, M. Mochizuki, S. Traub, D. Ben-David, G. A. Kuhn, R. Mueller, E. Livne, S. A. Eming and J. A. Hubbell (2011). "Engineering the Growth Factor Microenvironment with Fibronectin Domains to Promote Wound and Bone Tissue Healing." Science Translational Medicine **3**(100).

Mason, B. N., J. P. Califano and C. A. Reinhart-King (2012). "Matrix Stiffness: A Regulator of Cellular Behavior and Tissue Formation." Bhatia S. (eds) Engineering Biomaterials for Regenerative Medicine. Springer, New York, NY: pp 19-37.
Matyjaszewski, K. (2012). "Atom Transfer Radical Polymerization (ATRP): Current Status and Future Perspectives." Macromolecules **45**(10): 4015-4039.
Matyjaszewski, K., H. Dong, W. Jakubowski, J. Pietrasik and A. Kusumo (2007). "Grafting from surfaces for "Everyone": ARGET ATRP in the presence of air." Langmuir **23**(8): 4528-4531.
Mayer, G. (2005). "Rigid biological systems as models for synthetic composites." Science **310**(5751): 1144-1147.
Meng, B., X. H. Wang, F. Z. Cui, H. Y. Dong and F. Yu (2004). "A new method of heparinizing PLLA film by surface entrapment." Journal of Bioactive and Compatible Polymers **19**(2): 131-143.
Meves, A., C. Stremmel, K. Gottschalk and R. Faessler (2009). "The Kindlin protein family: new members to the club of focal adhesion proteins." Trends in Cell Biology **19**(10): 504-513.
Min, K., H. Gao, J. A. Yoon, W. Wu, T. Kowalewski and K. Matyjaszewski (2009). "One-Pot Synthesis of Hairy Nanoparticles by Emulsion ATRP." Macromolecules **42**(5): 1597-1603.
Mohammadi, M., S. K. Olsen and R. Goetz (2005). "A protein canyon in the FGF-FGF receptor dimer selects from an a la carte menu of heparan sulfate motifs." Current Opinion in Structural Biology **15**(5): 506-516.
Morrison, S. J. and A. C. Spradling (2008). "Stem cells and niches: Mechanisms that promote stem cell maintenance throughout life." Cell **132**(4): 598-611.
Morshed, S. (2014). "Current Options for Determining Fracture Union." Advances in medicine **2014**: 708574-708574.
Morsi, S. M., A. Pakzad, A. Amin, R. S. Yassar and P. A. Heiden (2011). "Chemical and nanomechanical analysis of rice husk modified by ATRP-grafted oligomer." Journal of Colloid and Interface Science **360**(2): 377-385.
Moulisova, V., C. Gonzalez-Garcia, M. Cantini, A. Rodrigo-Navarro, J. Weaver, M. Costell, R. Sabater i Serra, M. J. Dalby, A. J. Garcia and M. Salmeron-Sanchez (2017). "Engineered microenvironments for synergistic VEGF - Integrin signalling during vascularization." Biomaterials **126**: 61-74.
Mpoyi, E. N., M. Cantini, P. M. Reynolds, N. Gadegaard, M. J. Dalby and M. Salmeron-Sanchez (2016). "Protein Adsorption as a Key Mediator in the Nanotopographical Control of Cell Behavior." ACS Nano **10**(7): 6638-6647.
Muellner, M., S. J. Dodds, N. Tri-Hung, D. Senyschyn, C. J. H. Porter, B. J. Boyd and F. Caruso (2015). "Size and Rigidity of Cylindrical Polymer Brushes Dictate Long Circulating Properties In Vivo." Acs Nano **9**(2): 1294-1304.
Nadig, R. R. (2009). "Stem cell therapy - Hype or hope? A review." Journal of conservative dentistry : JCD **12**(4): 131-138.
Nampoothiri, K. M., N. R. Nair and R. P. John (2010). "An overview of the recent developments in polylactide (PLA) research." Bioresource Technology **101**(22): 8493-8501.
Nelea, V. and M. T. Kaartinen (2010). "Periodic beaded-filament assembly of fibronectin on negatively charged surface." Journal of Structural Biology **170**(1): 50-59.
Nemani, S. K., R. K. Annavarapu, B. Mohammadian, A. Raiyan, J. Heil, M. A. Haque, A. Abdelaal and H. Sojoudi (2018). "Surface Modification of Polymers: Methods and Applications." Advanced Materials Interfaces **5**(24).
Niu, X., Z. Liu, F. Tian, S. Chen, L. Lei, T. Jiang, Q. Feng and Y. Fan (2017). "Sustained delivery of calcium and orthophosphate ions from amorphous calcium

phosphate and poly(L-lactic acid)-based electrospinning nanofibrous scaffold." Scientific Reports **7**.
Noda, M. and D. T. Denhardt (2008). "Osteopontin." Principles of Bone Biology, Vol 1, 3rd Edition: 351-366.
O'Brien, F. J. (2011). "Biomaterials & scaffolds for tissue engineering." Materials Today **14**(3): 88-95.
Obara, M., M. S. Kang and K. M. Yamada (1988). "SITE-DIRECTED MUTAGENESIS OF THE CELL-BINDING DOMAIN OF HUMAN FIBRONECTIN - SEPARABLE, SYNERGISTIC SITES MEDIATE ADHESIVE FUNCTION." Cell **53**(4): 649-657.
Ohno, S. and K. Matyjaszewski (2006). "Controlling grafting density and side chain length in poly(n-butyl acrylate) by ATRP copolymerization of macromonomers." Journal of Polymer Science Part a-Polymer Chemistry **44**(19): 5454-5467.
Oldberg, A., A. Franzen and D. Heinegard (1988). "THE PRIMARY STRUCTURE OF A CELL-BINDING BONE SIALOPROTEIN." Journal of Biological Chemistry **263**(36): 19430-19432.
Pankov, R. and K. M. Yamada (2002). "Fibronectin at a glance." Journal of Cell Science **115**(20): 3861-3863.
Patricio, T., A. Gloria and P. Bartolo (2013). "Mechanical and Biological Behaviour of PCL and PCL/PLA Scaffolds for Tissue Engineering Applications." Icheap-11: 11th International Conference on Chemical and Process Engineering, Pts 1-4 **32**: 1645-1650.
Pelta, J., H. Berry, G. C. Fadda, E. Pauthe and D. Lairez (2000). "Statistical conformation of human plasma fibronectin." Biochemistry **39**(17): 5146-5154.
Perez, J. R., D. Kouroupis, D. J. Li, T. M. Best, L. Kaplan and D. Correa (2018). "Tissue Engineering and Cell-Based Therapies for Fractures and Bone Defects." Frontiers in Bioengineering and Biotechnology **6**.
Persson, M., P. P. Lehenkari, L. Berglin, S. Turunen, M. A. J. Finnila, J. Risteli, M. Skrifvars and J. Tuukkanen (2018). "Osteogenic Differentiation of Human Mesenchymal Stem cells in a 3D Woven Scaffold." Scientific Reports **8**.
Phillips, J. E., T. A. Petrie, F. P. Creighton and A. J. Garcia (2010). "Human mesenchymal stem cell differentiation on self-assembled monolayers presenting different surface chemistries." Acta Biomaterialia **6**(1): 12-20.
Phinney, D. G. and D. J. Prockop (2007). "Concise review: Mesenchymal stem/multipotent stromal cells: The state of transdifferentiation and modes of tissue repair - Current views." Stem Cells **25**(11): 2896-2902.
Platt, M. O., A. J. Roman, A. Wells, D. A. Lauffenburger and L. G. Griffith (2009). "Sustained Epidermal Growth Factor Receptor Levels and Activation by Tethered Ligand Binding Enhances Osteogenic Differentiation of Multi-Potent Marrow Stromal Cells." Journal of Cellular Physiology **221**(2): 306-317.
Plow, E. F., T. K. Haas, L. Zhang, J. Loftus and J. W. Smith (2000). "Ligand binding to integrins." Journal of Biological Chemistry **275**(29): 21785-21788.
Polo-Corrales, L., M. Latorre-Esteves and J. E. Ramirez-Vick (2014). "Scaffold Design for Bone Regeneration." Journal of Nanoscience and Nanotechnology **14**(1): 15-56.
Potolinca, V. O., E. C. Buruiana and S. Oprea (2017). "The effects of different positions of the pyridine functional groups on the dielectric relaxation of the heterocyclic polyurethane-urea elastomers." Materials Today Communications **10**: 25-33.
Prasad, K., O. Bazaka, M. Chua, M. Rochford, L. Fedrick, J. Spoor, R. Symes, M. Tieppo, C. Collins, A. Cao, D. Markwell, K. Ostrikov and K. Bazaka (2017). "Metallic Biomaterials: Current Challenges and Opportunities." Materials **10**(8).

Przekora, A. (2019). "Current Trends in Fabrication of Biomaterials for Bone and Cartilage Regeneration: Materials Modifications and Biophysical Stimulations." International Journal of Molecular Sciences **20**(2).
Raghavendran, H. R. B., S. Puvaneswary, S. Talebian, M. R. Murali, S. V. Naveen, G. Krishnamurithy, R. McKean and T. Kamarul (2014). "A Comparative Study on In Vitro Osteogenic Priming Potential of Electron Spun Scaffold PLLA/HA/Col, PLLA/HA, and PLLA/Col for Tissue Engineering Application." Plos One **9**(8).
Rasal, R. M. and D. E. Hirt (2009). "Toughness decrease of PLA-PHBHHx blend films upon surface-confined photopolymerization." Journal of Biomedical Materials Research Part A **88A**(4): 1079-1086.
Ravi, P., P. S. Shiakolas and T. R. Welch (2017). "Poly-L-lactic acid: Pellets to fiber to fused filament fabricated scaffolds, and scaffold weight loss study." Additive Manufacturing **16**: 167-176.
Redick, S. D., D. L. Settles, G. Briscoe and H. P. Erickson (2000). "Defining fibronectin's cell adhesion synergy site by site-directed mutagenesis." Journal of Cell Biology **149**(2): 521-527.
Ribeiro, C., V. Sencadas, C. Miguel Costa, J. L. Gomez Ribelles and S. Lanceros-Mendez (2011). "Tailoring the morphology and crystallinity of poly(L-lactide acid) electrospun membranes." Science and Technology of Advanced Materials **12**(1).
Ribelles, J. L. G., J. M. M. Duenas and M. M. Pradas (1989). "DIELECTRIC RELAXATIONS IN POLY(METHYL ACRYLATE), POLY(ETHYL ACRYLATE), AND POLY(BUTYL ACRYLATE)." Journal of Applied Polymer Science **38**(6): 1145-1157.
Rico, P. T., Cantini, M., Altankov, A., Salmeron-Sanchez, M. (2014). Matrix Protein Interactions with Synthetic Surfaces Polymers in Regenerative Medicine: Biomedical Applications from Nano- to Macro-Structures. M. M. P. M. J. Vicent, John Wiley & Sons, Inc.**:** 91-146.
Rincon Lasprilla, A. J., G. A. Rueda Martinez, B. H. Lunelli, J. E. Jaimes Figueroa, A. L. Jardini and R. Maciel Filho (2011). "Synthesis and Characterization of Poly (Lactic Acid) for Use in Biomedical Field." Icheap-10: 10th International Conference on Chemical and Process Engineering, Pts 1-3 **24**: 985-990.
Roach, P., D. Eglin, K. Rohde and C. C. Perry (2007). "Modern biomaterials: a review-bulk properties and implications of surface modifications." Journal of Materials Science-Materials in Medicine **18**(7): 1263-1277.
Rodrigues, M., H. Blair, L. Stockdale, L. Griffith and A. Wells (2013). "Surface Tethered Epidermal Growth Factor Protects Proliferating and Differentiating Multipotential Stromal Cells from FasL-Induced Apoptosis." Stem Cells **31**(1): 104-116.
Rosenzweig, D. H., E. Carelli, T. Steffen, P. Jarzem and L. Haglund (2015). "3D-Printed ABS and PLA Scaffolds for Cartilage and Nucleus Pulposus Tissue Regeneration." International Journal of Molecular Sciences **16**(7): 15118-15135.
Saito, E., E. E. Liao, W.-W. Hu, P. H. Krebsbach and S. J. Hollister (2013). "Effects of designed PLLA and 50:50 PLGA scaffold architectures on bone formation in vivo." Journal of Tissue Engineering and Regenerative Medicine **7**(2): 99-111.
Sakai, K., T. Fujii and T. Hayashi (1994). "CELL-FREE FORMATION OF DISULFIDE-BONDED MULTIMER FROM ISOLATED PLASMA FIBRONECTIN IN THE PRESENCE OF A LOW CONCENTRATION OF SH REAGENT UNDER A PHYSIOLOGICAL CONDITION." Journal of Biochemistry **115**(3): 415-421.
Salmerón-Sánchez, M. and M. Dalby, J (2016). "Synergistic growth factor microenvironments." Chem. Commun., 2016, 52, 13327.
Salmeron-Sanchez, M., P. Rico, D. Moratal, T. T. Lee, J. E. Schwarzbauer and A. J. Garcia (2011). "Role of material-driven fibronectin fibrillogenesis in cell differentiation." Biomaterials **32**(8): 2099-2105.

Savioli Lopes, M., A. L. Jardini and R. Maciel Filho (2012). "Poly (lactic acid) production for tissue engineering applications." Chisa 2012 **42**: 1402-1413.
Schindeler, A., M. M. McDonald, P. Bokko and D. G. Little (2008). "Bone remodeling during fracture repair: The cellular picture." Seminars in Cell & Developmental Biology **19**(5): 459-466.
Schofield, R. (1978). "RELATIONSHIP BETWEEN SPLEEN COLONY-FORMING CELL AND HEMATOPOIETIC STEM-CELL - HYPOTHESIS." Blood Cells **4**(1-2): 7-25.
Schulz, A. S., H. Gojzewski, J. Huskens, W. L. Vos and G. J. Vancso (2018). "Controlled sub-10-nanometer poly(N-isopropyl-acrylamide) layers grafted from silicon by atom transfer radical polymerization." Polymers for Advanced Technologies **29**(2): 806-813.
Schwartz, M. A. (2010). "Integrins and Extracellular Matrix in Mechanotransduction." Cold Spring Harbor Perspectives in Biology **2**(12).
Schwarzbauer, J. E. and D. W. DeSimone (2011). "Fibronectins, Their Fibrillogenesis, and In Vivo Functions." Cold Spring Harbor Perspectives in Biology **3**(7).
Schwarzbauer, J. E. and J. L. Sechler (1999). "Fibronectin fibrillogenesis: a paradigm for extracellular matrix assembly." Current Opinion in Cell Biology **11**(5): 622-627.
Serra, T., M. A. Mateos-Timoneda, J. A. Planell and M. Navarro (2013). "3D printed PLA-based scaffolds A versatile tool in regenerative medicine." Organogenesis **9**(4): 239-244.
Shekaran, A., J. R. Garcia, A. Y. Clark, T. E. Kavanaugh, A. S. Lin, R. E. Guldberg and A. J. Garcia (2014). "Bone regeneration using an alpha 2 beta 1 integrin-specific hydrogel as a BMP-2 delivery vehicle." Biomaterials **35**(21): 5453-5461.
Siegwart, D. J., J. K. Oh and K. Matyjaszewski (2012). "ATRP in the design of functional materials for biomedical applications." Progress in Polymer Science **37**(1): 18-37.
Sikavitsas, V. I., J. S. Temenoff and A. G. Mikos (2001). "Biomaterials and bone mechanotransduction." Biomaterials **22**(19): 2581-2593.
Simakova, A., S. E. Averick, D. Konkolewicz and K. Matyjaszewski (2012). "Aqueous ARGET ATRP." Macromolecules **45**(16): 6371-6379.
Singh, P., C. Carraher and J. E. Schwarzbauer (2010). "Assembly of Fibronectin Extracellular Matrix." Annual Review of Cell and Developmental Biology, Vol 26 **26**: 397-419.
Sodek, J., B. Ganss and M. D. McKee (2000). "Osteopontin." Critical Reviews in Oral Biology & Medicine **11**(3): 279-303.
Sodergard, A. and M. Stolt (2002). "Properties of lactic acid based polymers and their correlation with composition." Progress in Polymer Science **27**(6): 1123-1163.
Sotiropoulou, P. A., S. A. Perez, M. Salagianni, C. N. Baxevanis and M. Papamichail (2006). "Characterization of the optimal culture conditions for clinical scale production of human mesenchymal stem cells." Stem Cells **24**(2): 462-471.
Soucacos, P. N., Z. Dailiana, A. E. Beris and E. O. Johnson (2006). "Vascularised bone grafts for the management of non-union." Injury-International Journal of the Care of the Injured **37**: S41-S50.
Sprott, M. R., G. Gallego-Ferrer, M. J. Dalby, M. Salmeron-Sanchez and M. Cantini (2019). "Functionalization of PLLA with Polymer Brushes to Trigger the Assembly of Fibronectin into Nanonetworks." Advanced healthcare materials: e1801469-e1801469.
Suuronen, R., T. Pohjonen, J. Hietanen and C. Lindquist (1998). "A 5-year in vitro and in vivo study of the biodegradation of polylactide plates." Journal of Oral and Maxillofacial Surgery **56**(5): 604-614.

Takagi, J. and T. A. Springer (2002). "Integrin activation and structural rearrangement." Immunological Reviews **186**: 141-163.
Takahashi, S., M. Leiss, M. Moser, T. Ohashi, T. Kitao, D. Heckmann, A. Pfeifer, H. Kessler, J. Takagi, H. P. Erickson and R. Faessler (2007). "The RGD motif in fibronectin is essential for development but dispensable for fibril assembly." Journal of Cell Biology **178**(1): 167-178.
Takahashi, Y. and Y. Tabata (2004). "Effect of the fiber diameter and porosity of non-woven PET fabrics on the osteogenic differentiation of mesenchymal stem cells." Journal of Biomaterials Science-Polymer Edition **15**(1): 41-57.
Tamano-Machiavello, M. N., C. M. Costa, J. Molina-Mateo, C. Torregrosa-Cabanilles, J. M. Meseguer-Duenas, S. N. Kalkura, S. Lanceros-Mendez, R. Sabater i Serra and J. L. Gomez Ribelles (2015). "Phase morphology and crystallinity of poly(vinylidene fluoride)/poly(ethylene oxide) piezoelectric blend membranes." Materials Today Communications **4**: 214-221.
Tanaka, K., K. Sato, T. Yoshida, T. Fukuda, K. Hanamura, N. Kojima, T. Shirao, T. Yanagawa and H. Watanabe (2011). "Evidence for cell density affecting C2C12 myogenesis: possible regulation of myogenesis by cell-cell communication." Muscle Nerve **44**(6): 968-977.
Tang, W. and K. Matyjaszewski (2006). "Effect of Ligand Structure on Activation Rate Constants in ATRP." Macromolecules **39**(15): 4953-4959.
Taubner, V. and R. Shishoo (2001). "Influence of processing parameters on the degradation of poly(L-lactide) during extrusion." Journal of Applied Polymer Science **79**(12): 2128-2135.
Tian, X. F., B. C. Heng, Z. Ge, K. Lu, A. J. Rufaihah, V. T. W. Fan, J. F. Yeo and T. Cao (2008). "Comparison of osteogenesis of human embryonic stem cells within 2D and 3D culture systems." Scandinavian Journal of Clinical & Laboratory Investigation **68**(1): 58-67.
Tokiwa, Y. and B. P. Calabia (2006). "Biodegradability and biodegradation of poly(lactide)." Appl Microbiol Biotechnol **72**(2): 244-251.
Tozzi, G., A. De Mori, A. Oliveira and M. Roldo (2016). "Composite Hydrogels for Bone Regeneration." Materials **9**(4).
Tsarevsky, N. V. and K. Matyjaszewski (2005). "Synthesis of well-defined (bio)degradable polymeric materials with disulfide bonds by atom transfer radical polymerization." Abstracts of Papers of the American Chemical Society **229**: U930-U930.
Tzioupis, C. and P. V. Giannoudis (2007). "Prevalence of long-bone non-unions." Injury-International Journal of the Care of the Injured **38**: S3-S9.
Ulery, B. D., L. S. Nair and C. T. Laurencin (2011). "Biomedical Applications of Biodegradable Polymers." Journal of Polymer Science Part B-Polymer Physics **49**(12): 832-864.
Ulman, A. (1996). "Formation and structure of self-assembled monolayers." Chemical Reviews **96**(4): 1533-1554.
Ulmer, J., B. Geiger and J. P. Spatz (2008). "Force-induced fibronectin fibrillogenesis in vitro." Soft Matter **4**(10): 1998-2007.
Vanterpool, F. A., M. Cantini, F. P. Seib and M. Salmeron-Sanchez (2014). "A material-based platform to modulate fibronectin activity and focal adhesion assembly." Biores Open Access **3**(6): 286-296.
Vartio, T. (1986). "DISULFIDE-BONDED POLYMERIZATION OF PLASMA FIBRONECTIN IN THE PRESENCE OF METAL-IONS." Journal of Biological Chemistry **261**(20): 9433-9437.

Velasco, M. A., C. A. Narvaez-Tovar and D. A. Garzon-Alvarado (2015). "Design, Materials, and Mechanobiology of Biodegradable Scaffolds for Bone Tissue Engineering." Biomed Research International.
Vivek, A. V. and R. Dhamodharan (2007). "Grafting of methacrylates and styrene on to polystyrene backbone via a "Grafting from" ATRP process at ambient temperature." Journal of Polymer Science Part a-Polymer Chemistry **45**(17): 3818-3832.
Wan, Y. Q., J. Yang, J. L. Yang, J. Z. Bei and S. G. Wang (2003). "Cell adhesion on gaseous plasma modified poly-(L-lactide) surface under shear stress field." Biomaterials **24**(21): 3757-3764.
Wang, M. (2003). "Developing bioactive composite materials for tissue replacement." Biomaterials **24**(13): 2133-2151.
Wang, R. N., J. Green, Z. Wang, Y. Deng, M. Qiao, M. Peabody, Q. Zhang, J. Ye, Z. Yan, S. Denduluri, O. Idowu, M. Li, C. Shen, A. Hu, R. C. Haydon, R. Kang, J. Mok, M. J. Lee, H. L. Luu and L. L. Shi (2014). "Bone Morphogenetic Protein (BMP) signaling in development and human diseases." Genes & diseases **1**(1): 87-105.
Wang, Y., X. Wang, J. Shi, R. Zhu, J. Zhang, Z. Zhang, D. Ma, Y. Hou, F. Lin, J. Yang and M. Mizuno (2016). "A Biomimetic Silk Fibroin/Sodium Alginate Composite Scaffold for Soft Tissue Engineering." Scientific Reports **6**.
Wang, Z., Y. Wang, Y. Ito, P. Zhang and X. Chen (2016). "A comparative study on the in vivo degradation of poly(L-lactide) based composite implants for bone fracture fixation." Scientific Reports **6**.
Watanabe, Y., N. Harada, K. Sato, S. Abe, K. Yamanaka and T. Matushita (2016). "Stem cell therapy: is there a future for reconstruction of large bone defects?" Injury-International Journal of the Care of the Injured **47**: S47-S51.
Webb, D. J., K. Donais, L. A. Whitmore, S. M. Thomas, C. E. Turner, J. T. Parsons and A. F. Horwitz (2004). "FAK-Src signalling through paxillin, ERK and MLCK regulates adhesion disassembly." Nature Cell Biology **6**(2): 154-+.
Wen, J. H., L. G. Vincent, A. Fuhrmann, Y. S. Choi, K. C. Hribar, H. Taylor-Weiner, S. Chen and A. J. Engler (2014). "Interplay of matrix stiffness and protein tethering in stem cell differentiation." Nature Materials **13**(10): 979-987.
Westrick, E., B. Hamilton, P. Toogood, B. Henley and R. Firoozabadi (2017). "Humeral shaft fractures: results of operative and non-operative treatment." International Orthopaedics **41**(2): 385-395.
Wierzbicka-Patynowski, I., Y. Mao and J. E. Schwarzbauer (2004). "Analysis of fibronectin matrix assembly." Current protocols in cell biology **Chapter 10**: Unit 10.12-Unit 10.12.
Wijelath, E. S., S. Rahman, M. Namekata, J. Murray, T. Nishimura, Z. Mostafavi-Pour, Y. Patel, Y. Suda, M. J. Humphries and M. Sobel (2006). "Heparin-II domain of fibronectin is a vascular endothelial growth factor-binding domain - Enhancement of VEGF biological activity by a singular growth factor/matrix protein synergism." Circulation Research **99**(8): 853-860.
Williams, E. C., P. A. Janmey, R. B. Johnson and D. F. Mosher (1983). "FIBRONECTIN - EFFECT OF DISULFIDE BOND REDUCTION ON ITS PHYSICAL AND FUNCTIONAL-PROPERTIES." Journal of Biological Chemistry **258**(9): 5911-5914.
Williams, G. (1966). "DIPOLE RELAXATION IN POLYETHYL METHACRYLATE AND POLYETHYL ACRYLATE AS A FUNCTION OF FREQUENCY TEMPERATURE AND PRESSURE - ALPHA BETA AND ALPHABETA RELAXATIONS." Transactions of the Faraday Society **62**(524P): 2091-&.
Wolfenson, H., A. Bershadsky, Y. I. Henis and B. Geiger (2011). "Actomyosin-generated tension controls the molecular kinetics of focal adhesions." Journal of Cell Science **124**(9): 1425-1432.

Woo, E. J. (2012). "Recombinant human bone morphogenetic protein-2: adverse events reported to the Manufacturer and User Facility Device Experience database." Spine Journal **12**(10): 894-899.
Wozniak, M. A., K. Modzelewska, L. Kwong and P. J. Keely (2004). "Focal adhesion regulation of cell behavior." Biochimica Et Biophysica Acta-Molecular Cell Research **1692**(2-3): 103-119.
Xia, J., X. Zhang and K. Matyjaszewski (2000). The Effect of Ligands on Copper-Mediated Atom Transfer Radical Polymerization. Transition Metal Catalysis in Macromolecular Design, American Chemical Society. **760:** 207-223.
Xiao, D. Q. and M. J. Wirth (2002). "Kinetics of surface-initiated atom transfer radical polymerization of acrylamide on silica." Macromolecules **35**(8): 2919-2925.
Xiao, G. Z., D. Jiang, R. Gopalakrishnan and R. T. Franceschi (2002). "Fibroblast growth factor 2 induction of the osteocalcin gene requires MAPK activity and phosphorylation of the osteoblast transcription factor, Cbfa1/Runx2." Journal of Biological Chemistry **277**(39): 36181-36187.
Xiao, L., B. Wang, G. Yang and M. Gauthier (2011). "Poly(Lactic Acid)-Based Biomaterials: Synthesis, Modification and Applications." Biomedical Science, Engineering and Technology: 247-282.
Xiong, J. P., T. Stehle, B. Diefenbach, R. G. Zhang, R. Dunker, D. L. Scott, A. Joachimiak, S. L. Goodman and M. A. Arnaout (2001). "Crystal structure of the extracellular segment of integrin alpha V beta 3." Science **294**(5541): 339-345.
Xu, F., X. Yang, C. Li and W. Yang (2011). "Functionalized Polylactide Film Surfaces via Surface-Initiated ATRP." Macromolecules **44**(7): 2371-2377.
Xu, F. J., J. P. Zhao, E. T. Kang and K. G. Neoh (2007). "Surface functionalization of polyimide films via chloromethylation and surface-initiated atom transfer radical polymerization." Industrial & Engineering Chemistry Research **46**(14): 4866-4873.
Yasuda, H. and T. Yasuda (2000). "The competitive ablation and polymerization (CAP) principle and the plasma sensitivity of elements in plasma polymerization and treatment." Journal of Polymer Science Part a-Polymer Chemistry **38**(6): 943-953.
Younger, E. M. and M. W. Chapman (1989). "Morbidity at bone graft donor sites." Journal of orthopaedic trauma **3**(3): 192-195.
Yu, H.-J. and Z.-H. Luo (2011). "Silica/Polystyrene and Silica/Polystyrene-b-polymethacryloxypropyltrimethoxysilane Hybrid Nanoparticles via Surface-Initiated ATRP and Comparison of Their Wettabilities." Polymer Engineering and Science **51**(2): 218-224.
Yu, Q., L. M. Johnson and G. P. Lopez (2014). "Nanopatterned Polymer Brushes for Triggered Detachment of Anchorage-Dependent Cells." Advanced Functional Materials **24**(24): 3751-3759.
Yu, X., X. Tang, S. V. Gohil and C. T. Laurencin (2015). "Biomaterials for Bone Regenerative Engineering." Advanced Healthcare Materials **4**(9): 1268-1285.
Zadpoor, A. A. and J. Malda (2017). "Additive Manufacturing of Biomaterials, Tissues, and Organs." Annals of Biomedical Engineering **45**(1): 1-11.
Zhang, G. (2012). "Biomimicry in biomedical research." Organogenesis **8**(4): 101-102.
Zhao, M., S. E. Harris, D. Horn, Z. P. Geng, R. Nishimura, G. R. Mundy and D. Chen (2002). "Bone morphogenetic protein receptor signaling is necessary for normal murine postnatal bone formation." Journal of Cell Biology **157**(6): 1049-1060.
Zhong, C. L., M. Chrzanowska-Wodnicka, J. Brown, A. Shaub, A. M. Belkin and K. Burridge (1998). "Rho-mediated contractility exposes a cryptic site in fibronectin and induces fibronectin matrix assembly." Journal of Cell Biology **141**(2): 539-551.

Zhu, A. P., M. Zhang, J. Wu and J. Shen (2002). "Covalent immobilization of chitosan/heparin complex with a photosensitive hetero-bifunctional crosslinking reagent on PLA surface." Biomaterials **23**(23): 4657-4665.
Zhu, J. and R. A. F. Clark (2014). "Fibronectin at Select Sites Binds Multiple Growth Factors and Enhances their Activity: Expansion of the Collaborative ECM-GF Paradigm." Journal of Investigative Dermatology **134**(4): 895-901.
Zhu, Y., C. Gao, X. Liu, T. He and J. Shen (2004). "Immobilization of biomacromolecules onto aminolyzed poly(L-lactic acid) toward acceleration of endothelium regeneration." Tissue Eng **10**(1-2): 53-61.
Zhu, Y. B., C. Y. Gao, X. Y. Liu, T. He and J. C. Shen (2004). "Immobilization of biomacromolecules onto aminolyzed poly(L-lactic acid) toward acceleration of endothelium regeneration." Tissue Engineering **10**(1-2): 53-61.
Zoppe, J. O., N. C. Ataman, P. Mocny, J. Wang, J. Moraes and H.-A. Klok (2017). "Surface-Initiated Controlled Radical Polymerization: State-of-the-Art, Opportunities, and Challenges in Surface and Interface Engineering with Polymer Brushes." Chemical Reviews **117**(3): 1105-1318.